3-26-2021

Electron Field Emission and Electrochemical Lithiation Properties of Vertically Aligned Carbon Nanotube Arrays Grown Directly on Metal Substrates

Arun Thapa
Florida International University, athap002@fiu.edu

FLORIDA INTERNATIONAL UNIVERSITY

Miami, Florida

ELECTRON FIELD EMISSION AND ELECTROCHEMICAL LITHIATION PROPERTIES OF VERTICALLY ALIGNED CARBON NANOTUBE ARRAYS GROWN DIRECTLY ON METAL SUBSTRATES

A dissertation submitted in partial fulfillment of

the requirements for the degree of

DOCTOR OF PHILOSOPHY

in

PHYSICS

by

Arun Thapa

2021

To: Dean Michael R. Heithaus
College of Arts, Sciences and Education

This dissertation, written by Arun Thapa, and entitled Electron Field Emission and Electrochemical Lithiation Properties of Vertically Aligned Carbon Nanotube Arrays Grown Directly on Metal Substrates, having been approved in respect to style and intellectual content, is referred to you for judgment.

We have read this dissertation and recommend that it be approved.

_____
Xuewen Wang

_____
Chunlei Wang

_____
Prem P. Chapagain

_____
Yi Xiao

_____
Wenzhi Li, Major Professor

Date of Defense: March 26, 2021

The dissertation of Arun Thapa is approved.

_____
Dean Michael R. Heithaus
College of Arts, Sciences and Education

_____
Andrés G. Gil
Vice President for Research and Economic Development
and Dean of the University Graduate School

Florida International University, 2021

DEDICATION

To my beloved mother late Bishnu Maya Thapa.

ACKNOWLEDGMENTS

I would like to express my sincere gratitude to my advisor, Dr. Wenzhi Li, for his mentoring, relentless support, and encouragement during my Ph.D. study, without which this dissertation would not have been possible. I am deeply indebted to his invaluable guidance and endless time in reviewing and proofreading my papers. His constructive approach has led me through these years, and I am sure it will be a guiding factor towards my future research accomplishments.

I would like to extend my sincere thanks to Dr. Xuewen Wang for his expert guidance in developing my theoretical simulation skills. I must thank Dr. Chunlei Wang for letting me use her lab for the electrochemical test of my samples and her timely support at various stages of my Ph.D. research. I would also like to thank Dr. Prem Chapagain and Dr. Yi Xiao for their timely support, insightful suggestions, and comments.

I am also grateful to Dr. Katherine L. Jungjohann for in situ TEM experiments and insightful comments on my manuscripts. I would like to thank Dr. Jun Su and Prof. Yihua Gao for their help with the TEM experiment. My special gratitude goes to all the group members in the NanoPhysics lab at Florida International University. I very much appreciate my lab mates Yuba Raj Poudel and Rui Guo for their help and cooperation. I owe special appreciation to Amin Rabiei, who taught me battery fabrication and basic test skills during my initial days in Dr. Wang's Lab.

I would like to acknowledge the assistance and support provided by Florida International University Graduate School through their Dissertation Year Fellowship award program.

I gratefully acknowledge the Department of Physics for the financial assistance, the Graduate and Professional Student Committee for travel funding, and the Florida International University for copyright permissions. I am also thankful to all the faculties and support staff members in the Physics Department at Florida International University. I would like to acknowledge the support from the Advanced Materials Engineering Research Institutes (AMERI) at Florida International University.

I am grateful to my parents, brothers, sisters, and in-laws for their support during this challenging journey.

Finally, I would like to thank my beloved wife, Puspa, for her unconditional love and support which helped me get through difficult times without giving up.

ABSTRACT OF THE DISSERTATION

ELECTRON FIELD EMISSION AND ELECTROCHEMICAL LITHIATION PROPERTIES OF VERTICALLY ALIGNED CARBON NANOTUBE ARRAYS GROWN DIRECTLY ON METAL SUBSTRATES

by

Arun Thapa

Florida International University, 2021

Miami, Florida

Professor Wenzhi Li, Major Professor

Carbon nanotubes (CNTs) represent one of the critical inventions that have triggered new science and technology in many fields because of their distinctive mechanical, thermal, electrical, electrochemical, and optical properties. Despite the tremendous potential of CNTs, challenges in synthesizing and processing continue to hinder their applications. This dissertation is devoted to synthesizing vertically aligned CNT arrays on metal substrates via plasma-enhanced chemical vapor deposition and the study of their electron field emission (FE) and electrochemical lithiation properties.

Vertically aligned CNTs (VACNTs) are promising electron field emitters for vacuum micro/nano-electronics. Improved control over the morphology and a successful direct-growth of the VACNTs on a metal substrate will greatly improve their emission current and temporal stability. Coating the VACNTs with metal oxides or filling the interior hollow channels of the VACNTs with metals will boost both their mechanical

strength and electrical conductivity. The first part of this dissertation is focused on the controlled synthesis, surface modification, metal filling, and FE properties measurement of VACNT arrays grown over several metal substrates, including stainless steel, copper, and nickel. Compared to pristine VACNT array, the SnO_2 coated VACNTs (SnO_2-VACNTs), VACNT pillars, and copper-filled VACNT array exhibited enhanced FE properties because of the unique structural change caused by the coating procedure, the protection against the structural failure of VACNTs provided by SnO_2 nanoparticles, the low contact resistance between the substrate and the VACNTs, the increased active electron emitting sites in pillar structures, and the improved thermal and electrical conductivities of VACNTs caused by a highly conductive copper core filled inside the VACNTs.

Vertically aligned CNTs have great potential applications for developing high-energy and high-power density lithium-ion batteries (LIBs). In the second part of the dissertation, the electrochemical lithiation property of the free-standing binder-free SnO_2-VACNTs was investigated. Compared to the conventional graphite-based LIB anode, the SnO_2-VACNTs exhibited superior Li^+ storage performance with a high specific capacity of 1891 mAh/g at a current density of 0.1 Ah/g after 100 cycles and 900 mAh/g at the current density of 1 A/g after 200 cycles with excellent coulombic efficiency and rate capability, showing potential anode material for developing future LIBs.

TABLE OF CONTENTS

LIST OF TABLES

LIST OF FIGURES

CHAPTER 1

Introduction

The purpose of the present research is to investigate the correlation between synthesis, structure, and electronic/electrochemical properties of vertically aligned carbon nanotube (VACNT) arrays and their composites for potential applications in electron field emission devices and lithium-ion batteries. In the dissertation, the field emission performance of VACNT arrays, the VACNTs encased within shells of tin-oxide nanoparticles (SnO_2-VACNTs), and copper filled VACNT arrays has been extensively studied to develop an understanding of the field emission process and hence to overcome the shortcomings of existing field emitters. Besides, key electrochemical lithiation parameters of the SnO_2-VACNTs have been investigated to understand the lithiation property of the hybrid material, which may hold the promise of developing high-performance lithium-ion batteries.

1.1 Overview

Since the discovery of carbon nanotubes (CNTs) by Iijima in 1991 [1], a vast amount of time, money, and effort have been expended on exploiting their unique and excellent properties to develop new devices and to improve many components of current technologies. Carbon nanotubes have demonstrated great potential in plentiful applications, such as field emitters, lithium-ion batteries, supercapacitors, sensors, fuel cells, and solar cells, because of their unique physical, electrical, electronic, mechanical, and thermal properties [2-9]. Carbon nanotubes are one of the most researched materials in physics, chemistry, materials science, and related fields, evidenced by the steady

increase in the number of journal publications and patents related to CNTs from 1991 to 2019, as shown in Figure 1.1(a) [10]. Figure 1.1(b) represents the number of annual publications in CNTs research in the field of materials science, chemistry, and physics over the period 1991-2019.

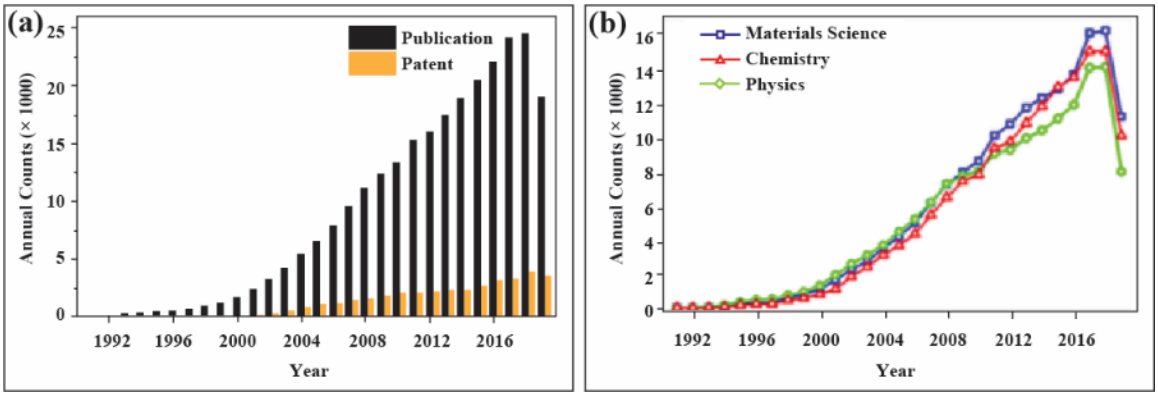

Figure 1.1. Research trends of CNTs from 1991 to 2019. (a) The number of publications and patents related to CNTs over the last two decades. (b) The number of journal publications annually in the fields of Materials Science, Chemistry, and Physics over the period 1991-2019 [adapted from ref. 10].

1.1.1 Carbon nanotubes as field emitters

Field emission (FE) is the escape of electrons from a conductor's surface as a result of the quantum mechanical tunneling effect in the presence of a very high electric field. Carbon nanotubes are exceptional electron emitters because of their small tip dimensions, large aspect ratio, and chemical stability. Since the first report of FE from a single CNT by Rinzler et al. [11] and from a CNT film by de Heer et al. [5] in 1995, CNTs have been exploited as electron sources in many applications such as flat panel displays [12], vacuum tube x-rays [13], electron microscopy [14], and vacuum microelectronic devices [15]. The morphology of the single CNT and its arrays, such as tip structure, length, degree of defects, number density, alignment, and geometrical arrangement, play a crucial role in their FE properties, including turn-on field, threshold field, field enhancement factor, total

current density, and current stability. The FE process involves the transportation of electrons from the substrate through the interface between the substrate and CNT, along the CNT, and final emission out into the vacuum. So, the contact resistance between the CNT and the substrate, as well as the electrical and thermal conductivity of both the CNT and the substrate, becomes important in device applications.

The main drawback of currently available CNT emitters is the lack of direct connection of CNTs on the conducting substrates and their vertical alignment with an appropriate inter-CNT separation. Most experimental work focuses on synthesizing dense forests of VACNTs on conducting substrates with pre-deposited buffer and metal catalyst layers [16-18]. The method of synthesizing VACNTs using buffer layer adds an extra electrical resistance between CNTs and the substrate, which can hinder the FE performance by increasing the turn-on and threshold field and hence lowering the total current density and field enhancement factor. Besides, high contact resistance can cause resistive heating, which in turn results in sublimation or melting of VACNTs at the higher electric field, thereby reducing electron-emitting sites and producing subdued FE properties. The most efficient techniques commonly used to deposit the buffer layer and catalyst onto the substrate are sputtering and e-beam evaporation. Unfortunately, these techniques are limited to a research laboratory scale because of the high cost and the limited chamber size, inhibiting mass production at a commercial scale. Hence, it is necessary to grow VACNTs directly on the conducting substrates without the aid of an extra catalyst. However, the main problem with the direct synthesis techniques lies in an absolute requirement of substrate pretreatments with acids and a series of oxidation-reduction processes and non-uniform and non-reproducible CNT growth [19-21]. Also, the direct fabrication of VACNT

arrays on metal substrates generally produces a dense forest of VACNTs, which suffers significant screening effect by the adjacent VACNTs, reducing field enhancement at VACNT apices.

The critical aspect of the CNT growth is the decomposition of the carbon precursor on a catalytic surface, dissolution of carbon atoms or clusters into the catalyst particles, and their precipitation in a certain crystalline form, namely, graphite [22]. The deposition of a thin layer of catalyst materials on the substrate surface is a crucial stage. Therefore, the availability of substrate materials showing catalytic activity to CNTs synthesis and adequate techniques to synthesize and align CNTs are essential for the direct growth of VACNTs on conducting substrates by eliminating a vital step, namely, catalyst preparation. Stainless steel can be used as the catalytic substrate for CNTs growth as it is an economic material with a high content of iron, and iron is an excellent catalyst for CNTs growth. Besides, plasma-enhanced chemical vapor deposition (PECVD) for VACNTs synthesis facilitates control over the alignment, length, diameter, and density of the CNTs by adjusting the synthesis parameters [23]. The plasma sheath possesses an abundant number of highly energetic species that help in activating catalyst nanoparticles by etching the substrate surface and amorphous carbon from the catalyst surface, which can eliminate the necessity of substrate pre-treatment by various means. The energetic plasma species also contribute to the efficient decomposition of hydrocarbon gas, leading to the graphitization even when the substrate is not heat-treated externally.

The FE properties of dense arrays of VACNTs can be enhanced by synthesizing separated VACNTs with a spacing of about twice their height to minimize the screening

effect [24]. Pillar arrays of VACNTs, an alternative to separated VACNT arrays, have shown improved FE properties over their dense array counterpart [25]. Current pillar emitters lack direct contact with the substrates and rely heavily on the complex photolithographic techniques since they require careful catalyst patterning before VACNTs synthesis. It is important to note that these pillars have a cross-section typically ranging from a few μm to tens of μm in diameter. Therefore, field screening within a single pillar emitter still occurs dominantly during the FE process. Hence, it is more desirable to synthesize the VACNT pillar of smaller lateral dimensions in an array structure with controlled inter-pillar distance directly on the conducting substrates.

The FE properties of VACNT arrays can be improved by decorating the CNT wall with metal/metal-oxide nanoparticles, such as Al, Cu, In, ZnO, RuO_2, and MgO, which can lead to highly conductive, as well as mechanically and chemically more stable CNT composite [26-30]. To date, plenty of research has been done to understand the FE properties of various field emitters, including pristine and morphology controlled-VACNT arrays, vertically aligned metal nanowire arrays, and CNTs coated with metal/metal-oxide nanoparticles. However, there are no reports on the FE behavior of the copper filled VACNT arrays synthesized directly on the bulk copper substrate. The lack of reports is fairly understandable because it is challenging to grow VACNT arrays directly on the copper substrate because of the poor carbon solubility in copper [16]. The FE properties of VACNTs can be significantly improved by filling their interior hollow space with a metal nanowire such as copper. The presence of a highly conductive metal nanowire at the core of VACNTs can enhance the overall electronic and thermal conductivity of the emitters, thereby improving the FE performance.

1.1.2 Carbon nanotubes as anode materials for lithium-ion batteries

The quest for highly efficient, economic, and environmentally friendly energy storage means for powering electronic devices, as well as electric vehicles, has remained a challenge for a long time. Lithium-ion battery (LIB) is one of the energy storage and power devices that operate on the basis of electrochemical energy storage and conversion mechanism. To improve the lower energy density and power capacity of current LIBs, significant research has been carried out towards developing new and high-performance materials for LIB components. Carbon nanotubes have demonstrated the potential for application as the LIB anode because of their unique one-dimensional tubular structure, large surface area, short diffusion length of Li^+ ions, and high electrical and thermal conductivity [31]. Also, CNTs are considered to have a high theoretical specific capacity of ~1000 mAh/g [32] compared to the-state-of-art graphite anode material (372 mAh/g). Also, CNTs have been used as an excellent additive material to improve the electrochemical performance of electrode materials with much-improved energy conversion, storage capacities, and charge transfer ability. Several groups have researched the possibility of using CNTs, in different forms and architectures, as an anode in LIBs for charge storage [33, 34].

Despite a high theoretical Li^+ ion storage capacity, several reports have shown that the specific capacity of CNT anodes is well below 400 mAh/g [33, 35]. One of the main reasons to the low specific capacity of the CNT anode is its conventional bilayer design in which a thin layer of CNTs is glued onto a copper foil current collector with the help of a binder. The binder limits the potential application of batteries above 200 ºC. Reports have

shown that the bilayer design of anode materials can reduce the usable capacity by ~47% [32], making it necessary to use free-standing binder-free CNTs grown directly on current collectors.

High capacity metal and semiconductor materials, such as Al (800 mAh/g), Sn (994 mAh/g), Li (3860 mAh/g), Si (4000 mAh/g), and Ge (1600 mAh/g), have been explored to improve the specific and volumetric capacity of LIB anodes [36]. Despite having such a high Li^+ storage capacity of these materials, colossal volume instability during the lithiation/delithiation leads to pulverization of the anode materials and loss of inter-particle contact, resulting in rapid capacity fading and severe safety issues. Recent research of anode materials has been motivated mainly by hybrid materials consisting of high capacity nanoparticles (<100 nm) and CNTs to address the inherent concerns of bulk electrode materials [37-39]. The reduction of particle size may potentially modify the mechanism of volumetric alteration, and simultaneous use of CNTs can absorb the considerable stress developed during the lithiation and delithiation process. Also, the high electrical conductivity of CNTs can enhance the performance of LIBs by offering a quick pathway for charged particles during the battery operation. Hence, using CNTs coated with SnO_2 nanoparticles (SnO_2-CNTs) as an anode of LIBs is an attractive strategy since the theoretical charge storage capacity of SnO_2 (781 $mAhg^{-1}$) is over twice as much as graphite anodes. Several groups have researched on SnO_2-CNTs composite material to explore its potential as anode materials of LIBs [39-41].

Most of the reports for fabricating SnO_2-CNTs composite as anode materials mainly focus on using wet chemical methods on randomly oriented CNTs. However, SnO_2-

VACNTs can significantly improve the performance of anode materials by offering proper electrolyte accessibility and charge transfer capability owing to the regular pore structure and inter-tube space of the VACNTs array [42]. Improved contact resistance between VACNTs and current collectors achieved through the direct synthesis of VACNTs on conducting substrates and anisotropic conductivities of VACNTs may enhance the charge transfer and dissipation of heat caused by resistive heating. A proper inter-tube distance in an array of VACNTs can alleviate the stress developed during the lithiation/delithiation process. Therefore, it is highly desirable to develop binder-free VACNT templates with minimum contact resistance to accommodate a uniform coating of ultra-fine SnO_2 nanoparticles for achieving high-performance LIB anodes.

1.2 Objectives and scope of the research

The primary goal of the research is to fabricate arrays of VACNTs, in different forms and architectures, directly on conductive substrates and to study how their morphology affects their field emission and electrochemical properties. The central part of the research is focused on the controlled synthesis of VACNT arrays on popular metal substrates and their surface modification. Our aim of synthesizing VACNTs directly on conductive substrates without using an external catalyst layer inspired us to choose metals such as stainless steel, copper, and nickel, which are well-known catalysts for CNT growth. In my dissertation work, three different approaches were used to enhance the FE properties of VACNT emitter arrays. (i) Coating VACNTs with SnO_2 nanoparticles (SnO_2-VACNTs core-shell structure) and modifying VACNT arrays into uniquely bundled structures formed by the solution phase coating process. After the coating process, the resulting

morphology is expected to reduce the field screening effect and enhance the mechanical stability of the VACNT emitters, thereby improving the FE properties. (ii) Fabricating micro-pillar arrays of VACNTs with an appropriate size and inter-pillar distance to increase the number of active field emitters and reduce the screening effect, thus increasing the total emission current density. (iii) Synthesizing vertically aligned and mechanically self-supported pure copper-filled CNT arrays directly connected to the copper substrate. The highly conductive crystalline copper at the core of VACNTs is expected to increase the electrical and thermal conductivities of VACNT emitters, which can be vital in increasing the field enhancement factor of VACNT emitters. To understand the effect of VACNT emitter morphology on FE properties, simulation on the electrostatic field distribution of VACNT field emitters has been performed.

Another focus of the research is on synthesizing binder-free self-standing VACNTs on 3-dimensional (3D) nickel foam and coating the wall of the VACNTs with SnO_2 nanoparticles to form core-shell structures. Further, the electrochemical lithiation properties of the pristine VACNTs and SnO_2-VACNTs grown on 3D nickel foam were investigated when they are used as anode materials in LIB coin cells. The SnO_2-VACNTs composite with uniquely bundled morphology fabricated on 3D nickel foam has shown high energy density and improved cyclability at high current rates with excellent capacity retention.

1.3 Outline of the dissertation

This dissertation is organized into eight chapters. Chapter 2 presents the background literature review on basic structures, synthesis methods, properties, and

applications of CNTs. In chapter 2, only the properties of CNTs relevant to the dissertation's scope have been discussed. While reviewing the applications of CNTs, particular care has been concentrated on field emission and energy storage devices. Chapter 3 is dedicated to the detailed description of the experimental procedures involved, including substrate preparation, consequent synthesis of VACNTs by PECVD, and SnO_2-VACNTs composite synthesis by a wet-chemical method. Chapter 3 also describes various tools and techniques for structural and properties characterization of as-synthesized samples. Chapter 4 discusses the results of direct synthesis of VACNT arrays on stainless steel, structural modification of VACNT arrays by solution-phase SnO_2 coating process, and its effect on FE properties. Efforts to enhance the FE properties of VACNT arrays by synthesizing unique VACNT pillar arrays on stainless steel and crystalline copper-filled VACNT arrays on the copper substrate have been reported in chapters 5 and 6, respectively. A complete explanation of the synthesis, structural characterization, and electrochemical lithiation properties of pristine VACNTs and SnO_2-VACNTs composite fabricated on nickel foam is presented in chapter 7. Finally, research results with future perspectives have been summarized in chapter 8.

References

[1] Iijima S., Helical microtubules of graphitic carbon. *Nature* **1991,** 354 (6348), 56.

[2] Bockrath M., Cobden D.H., McEuen P.L., Chopra N.G., Zettl A., Thess A. and Smalley R.E., Single-electron transport in ropes of carbon nanotubes. *Science* **1997,** 275 (5308), 1922.

[3] Qian D., Wagner G.J., Liu W.K., Yu M.F. and Ruoff R.S., Mechanics of carbon nanotubes. *Applied Mechanics Reviews* **2002,** 55 (6), 495.

[4] Hone J., Llaguno M.C., Biercuk M.J., Johnson A.T., Batlogg B., Benes Z. and Fischer J.E., Thermal properties of carbon nanotubes and nanotube-based materials. *Applied Physics A: Materials Science & Processing* **2002,** 74 (3), 339.

[5] De Heer W.A., Chatelain A. and Ugarte D., A carbon nanotube field-emission electron source. *science* **1995,** 270 (5239), 1179.

[6] Ng S.H., Wang J., Guo Z.P., Chen J., Wang G.X. and Liu H.K., Single wall carbon nanotube paper as anode for lithium-ion battery. *Electrochimica Acta* **2005,** 51 (1), 23.

[7] Chen Y.M., Cai J.H., Huang Y.S., Lee K.Y. and Tsai D.S., Preparation and characterization of iridium dioxide-carbon nanotube nanocomposites for supercapacitors. *Nanotechnology* **2011,** 22 (11), 115706.

[8] Chopra S., Pham A., Gaillard J., Parker A. and Rao A.M., Carbon-nanotube-based resonant-circuit sensor for ammonia. *Applied Physics Letters* **2002,** 80 (24), 4632.

[9] Chen Y., Lv Z., Xu J., Peng D., Liu Y., Chen J., Sun X., Feng C. and Wei C., Stainless steel mesh coated with MnO2/carbon nanotube and polymethylphenyl siloxane as low-cost and high-performance microbial fuel cell cathode materials. *Journal of Power Sources* **2012,** 201, 136.

[10] Yang F., Wang M., Zhang D., Yang J., Zheng M. and Li Y., Chirality Pure Carbon Nanotubes: Growth, Sorting, and Characterization. *Chemical Reviews* **2020,** 120 (5), 2693.

[11] Rinzler A., Hafner J., Nikolaev P., Nordlander P., Colbert D., Smalley R., Lou L., Kim S. and Tománek D., Unraveling nanotubes: field emission from an atomic wire. *Science* **1995,** 269 (5230), 1550.

[12] Wang Q., Yan M. and Chang R.P., Flat panel display prototype using gated carbon nanotube field emitters. *Applied Physics Letters* **2001,** 78 (9), 1294.

[13] Saito Y., Hata K., Takakura A., Yotani J. and Uemura S., Field emission of carbon nanotubes and its application as electron sources of ultra-high luminance light-source devices. *Physica B: Condensed Matter* **2002,** 323 (1-4), 30.

[14] Saito Y. and Uemura S., Field emission from carbon nanotubes and its application to electron sources. *Carbon* **2000,** 38 (2), 169.

[15] Fursey G., Field emission in vacuum micro-electronics. *Applied Surface Science* **2003,** 215 (1-4), 113.

[16] Neupane S., Lastres M., Chiarella M., Li W., Su Q. and Du G., Synthesis and field emission properties of vertically aligned carbon nanotube arrays on copper. *Carbon* **2012,** 50 (7), 2641.

[17] Chen G., Neupane S., Li W., Chen L. and Zhang J., An increase in the field emission from vertically aligned multiwalled carbon nanotubes caused by NH3 plasma treatment. *Carbon* **2013,** 52, 468.

[18] Lahiri I., Seelaboyina R., Hwang J.Y., Banerjee R. and Choi W., Enhanced field emission from multi-walled carbon nanotubes grown on pure copper substrate. *Carbon* **2010,** 48 (5), 1531.

[19] Hashempour M., Vicenzo A., Zhao F. and Bestetti M., Direct growth of MWCNTs on 316 stainless steel by chemical vapor deposition: Effect of surface nano-features on CNT growth and structure. *Carbon* **2013,** 63, 330.

[20] Sano N., Hori Y., Yamamoto S. and Tamon H., A simple oxidation–reduction process for the activation of a stainless steel surface to synthesize multi-walled carbon nanotubes and its application to phenol degradation in water. *Carbon* **2012,** 50 (1), 115.

[21] Neupane S., Yang Y., Li W. and Gao Y., Synthesis and enhanced electron field emission of vertically aligned carbon nanotubes grown on stainless steel substrate. *Journal of Nanoscience Letters* **2014,** 4, 14.

[22] Esconjauregui S., Whelan C.M. and Maex K., The reasons why metals catalyze the nucleation and growth of carbon nanotubes and other carbon nanomorphologies. *Carbon* **2009,** 47 (3), 659.

[23] Meyyappan M.D., L.; Cassell, A. and Has, D., Carbon nanotube growth by PECVD: a review. *Plasma Sources Science and Technology* **2003,** 12, 205.

[24] Nilsson L., Groening O., Emmenegger C., Kuettel O., Schaller E., Schlapbach L., Kind H., Bonard J. and Kern K., Scanning field emission from patterned carbon nanotube films. *Applied Physics Letters* **2000,** 76 (15), 2071.

[25] Gupta B.K., Kedawat G., Gangwar A.K., Nagpal K., Kashyap P.K., Srivastava S., Singh S., Kumar P., Suryawanshi S.R. and Seo D.M., High-performance field emission device utilizing vertically aligned carbon nanotubes-based pillar architectures. *AIP Advances* **2018,** 8 (1), 015117.

[26] Sridhar S., Tiwary C., Vinod S., Taha-Tijerina J.J., Sridhar S., Kalaga K., Sirota B., Hart A.H.C., Ozden S., Sinha R.K., Harsh, Vajtai R., Choi W., Kordas K. and Ajayan P.M., Field Emission with Ultralow Turn On Voltage from Metal Decorated Carbon Nanotubes. *ACS Nano* **2014,** 8 (8), 7763.

[27] Sreekanth M., Ghosh S., Barman S., Sadhukhan P. and Srivastava P., Field emission properties of indium-decorated vertically aligned carbon nanotubes: an interplay between type of hybridization, density of states and metal thickness. *Applied Physics A* **2018,** 124 (8), 528.

[28] Green J.M., Dong L., Gutu T., Jiao J., Conley J.F. and Ono Y., ZnO-nanoparticle-coated carbon nanotubes demonstrating enhanced electron field-emission properties. *Journal of Applied Physics* **2006,** 99 (9), 094308.

[29] Chen C.A., Lee K.Y., Chen Y.M., Chi J.G., Lin S.S. and Huang Y.S., Field emission properties of RuO2 thin film coated on carbon nanotubes. *Vacuum* **2010,** 84 (12), 1427.

[30] Chakrabarti S., Pan L., Tanaka H., Hokushin S. and Nakayama Y., Stable field emission property of patterned MgO coated carbon nanotube arrays. *Japanese Journal of Applied Physics* **2007,** 46 (7R), 4364.

[31] Liu X.M., Huang Z.D., Oh S.W., Zhang B., Ma P.C., Yuen M.M. and Kim J.K., Carbon nanotube (CNT)-based composites as electrode material for rechargeable Li-ion batteries: a review. *Composites Science and Technology* **2012,** 72 (2), 121.

[32] Landi B.J., Ganter M.J., Cress C.D., DiLeo R.A. and Raffaelle R.P., Carbon nanotubes for lithium ion batteries. *Energy & Environmental Science* **2009,** 2 (6), 638.

[33] Kang C., Lahiri I., Baskaran R., Kim W.G., Sun Y.K. and Choi W., 3-dimensional carbon nanotube for Li-ion battery anode. *Journal of Power Sources* **2012,** 219, 364.

[34] De las Casas C. and Li W., A review of application of carbon nanotubes for lithium ion battery anode material. *Journal of Power Sources* **2012,** 208, 74.

[35] Yehezkel S., Auinat M., Sezin N., Starosvetsky D. and Ein-Eli Y., Bundled and densified carbon nanotubes (CNT) fabrics as flexible ultra-light weight Li-ion battery anode current collectors. *Journal of Power Sources* **2016,** 312, 109.

[36] Larcher D., Beattie S., Morcrette M., Edstroem K., Jumas J.C. and Tarascon J.M., Recent findings and prospects in the field of pure metals as negative electrodes for Li-ion batteries. *Journal of Materials Chemistry* **2007,** 17 (36), 3759.

[37] Park G.D., Choi J.H., Jung D.S., Park J.-S. and Kang Y.C., Three-dimensional porous pitch-derived carbon coated Si nanoparticles-CNT composite microsphere with superior electrochemical performance for lithium ion batteries. *Journal of Alloys and Compounds* **2020,** 821, 153224.

[38] Gao C., Kim N.D., Salvatierra R.V., Lee S.-K., Li L., Li Y., Sha J., Silva G.A.L., Fei H. and Xie E., Germanium on seamless graphene carbon nanotube hybrids for lithium ion anodes. *Carbon* **2017,** 123, 433.

[39] Noerochim L., Wang J.Z., Chou S.L., Wexler D. and Liu H.K., Free-standing single-walled carbon nanotube/SnO2 anode paper for flexible lithium-ion batteries. *Carbon* **2012,** 50 (3), 1289.

[40] Zhang B., Huang J. and Kim J.K., Ultrafine Amorphous SnOx Embedded in Carbon Nanofiber/Carbon Nanotube Composites for Li-Ion and Na-Ion Batteries. *Advanced Functional Materials* **2015,** 25 (32), 5222.

[41] Ma C., Zhang W., He Y.-S., Gong Q., Che H. and Ma Z.-F., Carbon coated SnO 2 nanoparticles anchored on CNT as a superior anode material for lithium-ion batteries. *Nanoscale* **2016,** 8 (7), 4121.

[42] Jiang Y., Wang P., Zang X., Yang Y., Kozinda A. and Lin L., Uniformly embedded metal oxide nanoparticles in vertically aligned carbon nanotube forests as pseudocapacitor electrodes for enhanced energy storage. *Nano Lett* **2013,** 13 (8), 3524.

CHAPTER 2

Progress and trends in carbon nanotubes research

The current chapter presents a summary of the literature review in the field of carbon nanotubes.

2.1 Structure of CNTs

Carbon is one of the most abundant and is an extremely versatile element. It has several allotropes, each with different chemical and physical traits. Various arrangements of carbon-carbon bonds result in the allotropes having different properties. Carbon nanotube (CNT) is one of the allotropes of carbon, which can be considered a hollow cylindrical structure formed by rolling graphene sheets. A graphene sheet is an extended planar honeycomb lattice of purely sp^2-bonded carbon atoms, Figure 2.1(a). In general, CNTs can be classified into single-walled CNTs (SWCNTs) and multi-walled CNTs (MWCNTs) on the basis of the number of graphene layers on the tube structure. A chiral vector ($\mathbf{C_h}$), an intrinsic geometrical property, is expressed as a linear combination of two basis vectors $\mathbf{a_1}$ and $\mathbf{a_2}$ in real space as $\mathbf{C_h} = n\mathbf{a_1} + m\mathbf{a_2}$, where n and m are integers can completely describe an SWCNT except its length [1]. Different values of n and m set up different chirality, such as (n, 0), (n, m = n), or (n, m), forming three different types of SWCNTs, which are zig-zag, armchair, and chiral tubes, respectively (Figure 2.1(b)).

In other words, the vector $\mathbf{C_h}$ makes a chiral angle θ with vector $\mathbf{a_1}$ which defines the mode of graphene layer wrapping, such as zig-zag when $\theta = 0^o$ and armchair when $\theta = 30^o$. All other chiral angles (i.e., $0^o < \theta < 30^o$) represent the chiral tubes. Besides, these integers (n, m) also determine the electronic band structure of the SWCNTs and hence their

optical, magnetic, and electronic properties [2]. The SWCNTs are metallic if the (n, m) indices satisfy the relationship n – m = 3j and they are semiconducting when n – m = 3j +1 or 3j + 2, where j is an integer [1]. Additionally, the chiral indices (n, m) can also determine the diameter of the SWCNT as $d = \frac{a}{\pi}\sqrt{(n^2 + nm + m^2)}$, where a = 0.246 nm. In contrast, an MWCNT is a more complex system of a few to a few tens of coaxial cylindrical graphene sheets separated by a distance of about 0.34 nm, as shown in the inset of Figure 2.1(a). Experimental measurements suggest that MWCNTs are one-dimensional conductors, and electronic transport occurs on the tube's outer wall [3].

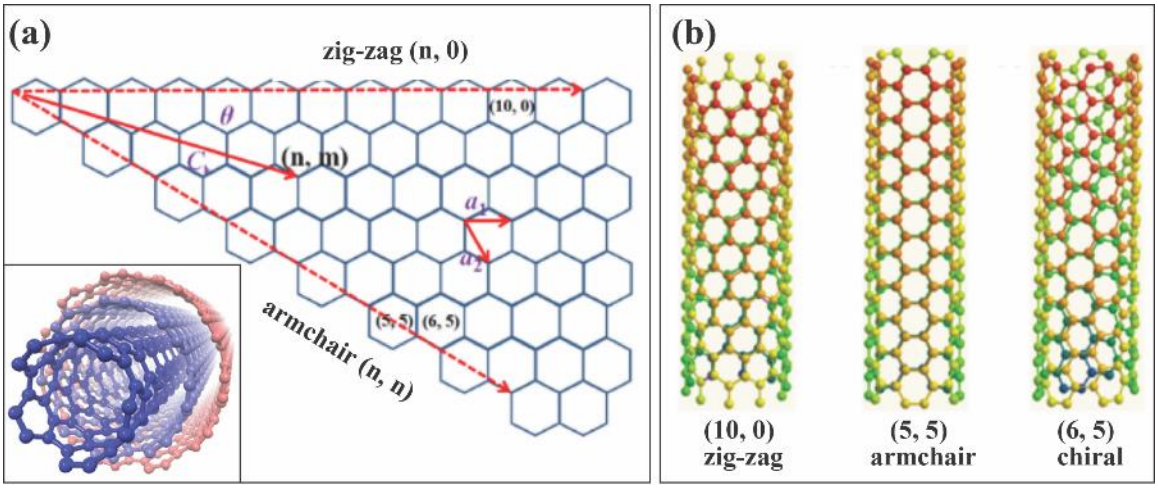

Figure 2.1. Schematics of (a) a graphene sheet and (b) three types of single-walled CNTs. The inset in Figure 2.1(a) shows a multi-walled CNT [adapted from ref. 1].

2.2 Synthesis methods of CNTs

To date, various methods have been used to synthesize CNTs. The following section presents a comprehensive description of some widely used synthesis techniques, including the arc-discharge method, laser ablation method, chemical vapor deposition (CVD) method, and plasma-enhanced chemical vapor deposition (PECVD) method. A few other synthesis techniques are also summarized.

2.2.1 Arc-discharge

Iijima reported the discovery of a new type of finite carbon structure consisting of needle-like tubes, now known as CNTs, by using the arc-discharge evaporation technique [4]. As shown in the schematic in Figure 2.2(a), the arc-discharge apparatus consists of two carbon rods as the cathode and the anode separated by a distance of about 1mm [5]. A high direct current (50–200 A) is applied between two carbon rods; meanwhile, the whole apparatus is enclosed inside a chamber filled with inert gas (Ar or He) at 100 Torr. The arc created between the electrodes at a high current vaporizes the carbon rod, and the cathode deposit contains CNTs. The diameter of CNTs was in the range of 4 to 30 nm and the length of about 1 μm [4]. Figure 2.2(b) represents the transmission electron micrograph of CNTs with 5, 2, and 7 concentric cylindrical graphene layers. Furthermore, Iijima *et al.*

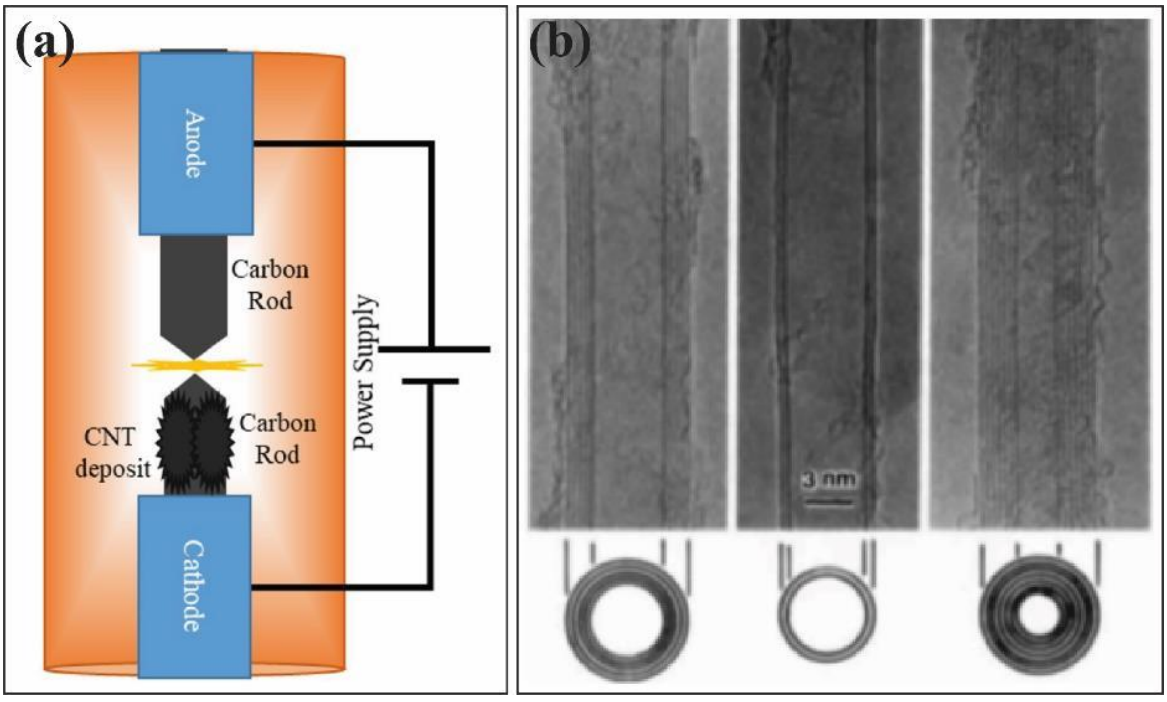

Figure 2.2. (a) Schematic of the arc-discharge apparatus for synthesizing CNTs [adapted from ref. 5]. (b) Transmission electron micrograph of MWCNTs having 5, 2, and 7 walls [adapted from ref. 4].

reported the growth of SWCNTs by adding an iron catalyst to the graphite electrode in the presence of a gas mixture of Ar (40 Torr) and CH_4 (10 Torr) [6]. The length of the SWCNTs was about 700 nm; whereas, the diameter was in the range of 0.7 to 1.6 nm. Ebbesen and Ajayan reported a large-scale synthesis of MWCNTs by employing a potential of about 18 V between two graphite rods of diameter 6 and 9 mm and in the presence of the He gas pressure of 500 Torr [7]. It was shown that a large-scale synthesis of SWCNTs could be achieved by using a mixture of metal catalysts and graphite powder in the presence of He gas at 495 Torr [8].

2.2.2 Laser ablation

In the laser ablation method, a high-energy pulse or continuous laser vaporizes a mixture of catalysts and a graphite target at a high temperature in an inert atmosphere. CNTs are formed upon condensation. Figure 2.3(a) shows a schematic of the laser ablation apparatus for synthesizing CNTs. A research group at Rice University reported a large-scale (gram quantities) synthesis of SWCNTs at 1200 ºC by using Ni/Co (1.2 at. %) catalyst in the presence of He or Ar at a pressure of 500 Torr inside a quartz tube (50 cm long and 2.5 cm diameter) [9]. The SWCNTs were self-organized into ropes consisting of 100–500 SWCNTs in a two-dimensional triangular lattice. Figures 2.3(b-c) show transmission electron micrographs of SWCNTs synthesized by using the laser ablation method. These SWCNTs were more than 100 μm long and very uniform in diameter of about 1.4 nm. *Chen et al.* reported a novel method for large-scale synthesis of MWCNTs by using Nd:YAG laser pulses over a graphite target at normal temperature and pressure in metal nano-sol [10]. The metal nano-sol was prepared by laser ablation of Fe or Ni targets in

ethanol and used as catalysts for growing CNTs. The randomly oriented MWCNTs were 15–45 nm in diameter and a few μm in length. They found that the metal nano-sol was critical in their method to synthesize MWCNTs, and obtained carbon nanofibers instead of CNTs in the absence of metal nano-sol.

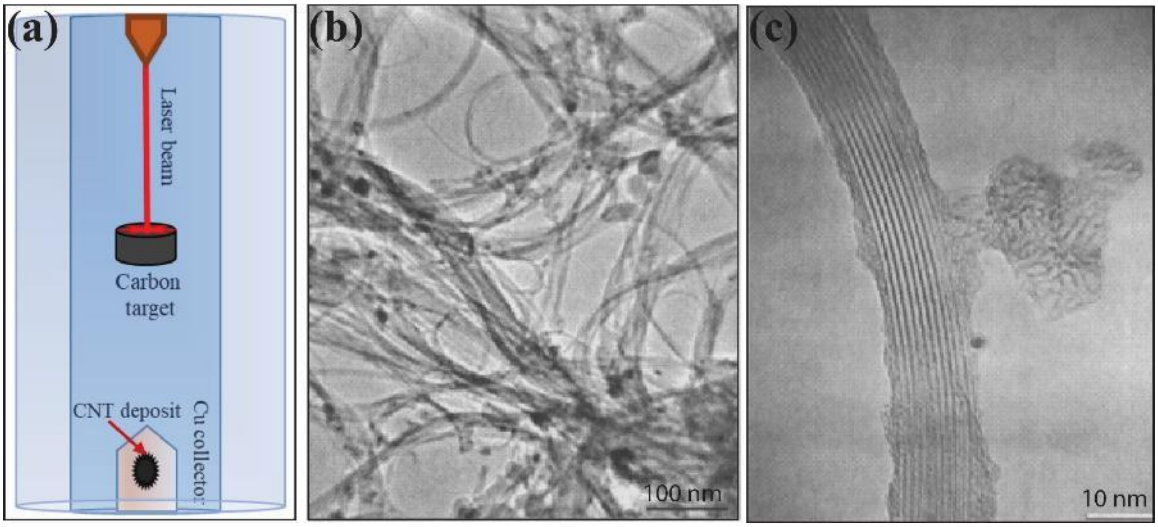

Figure 2.3. (a) Schematic of the laser ablation apparatus for synthesizing CNTs [adapted from ref. 5]. (b) low resolution and (c) high-resolution transmission electron micrographs showing ropes of SWCNTs synthesized by laser ablation method [adapted from ref. 9].

2.2.3 Chemical vapor deposition

Fundamentally, arc-discharge and laser ablation methods are plasma-based syntheses; however, chemical vapor deposition (CVD) entirely relies on thermal energy and never exceeds temperature above 1200 ºC. Figure 2.4(a) shows a schematic of the set up for a typical CVD method. Synthesis of CNTs via the CVD method involves nucleation of CNTs on catalyst nanoparticles (Fe, Ni, Co) at elevated temperatures (400–1100 ºC) in a controlled hydrocarbon gas environment [11-13]. Catalytically active nanoparticles are formed through a crucial thermal annealing step under a reducing gas environment, such as H_2 and NH_3. Hydrocarbon precursor gas is catalytically decomposed at the catalyst sites

which allow to dissolve, precipitate upon saturation, and graphitize carbon atoms into crystalline CNTs.

Li *et al.* reported a large-scale synthesis of vertically aligned CNTs via CVD on mesoporous silica containing Fe nanoparticles using a mixture of C_2H_2 and N_2 as precursor gas [14]. The growth direction of high-quality CNTs was controlled by the pores available on the silica surface. The highly aligned arrays of isolated CNTs were about 50 μm long, 30 nm in diameter, and separated by a distance of about 100 nm. Jung *et al.* synthesized both randomly and vertically aligned CNTs on Ni (2–7 nm) coated Si substrate by using C_2H_2 (2.4–20 vol. %) as carbon precursor gas in the presence of various carrier and etching gases, such as N_2, H_2, Ar, and NH_3 (200 sccm except for NH_3 100 sccm) [15]. The formation of Ni nanoparticles (15–90 nm) after the heat pretreatment at 850 ºC under the reducing environment was crucial for the successful growth of CNTs, Figure 2.4(b-c). The CNTs were measured to be about 10–20 μm long and about 35 nm in diameter.

There are several reports of synthesizing horizontally aligned CNTs by the CVD method. Joselevich *et al.* reported the growth of horizontally aligned CNTs on ferrihydrite nanoparticles (3–5 nm) deposited on the surface of Si substrate between two electrodes [16]. The SWCNTs were grown for 10 min at 800 ºC in the presence of a gas mixture of C_2H_2 (0.2 vol. %), H_2 (40 vol. %), and Ar (60 vol. %). The length of SWCNTs was in the range of 100 nm to several μm, and the diameter was about 2 nm. The alignment was achieved by applying an electric field of 4×10^6 V/m parallel to the plane of the substrate. Furthermore, the horizontal alignment of CNTs has also been achieved through directed gas-flow and lattice-directed growth [17-19].

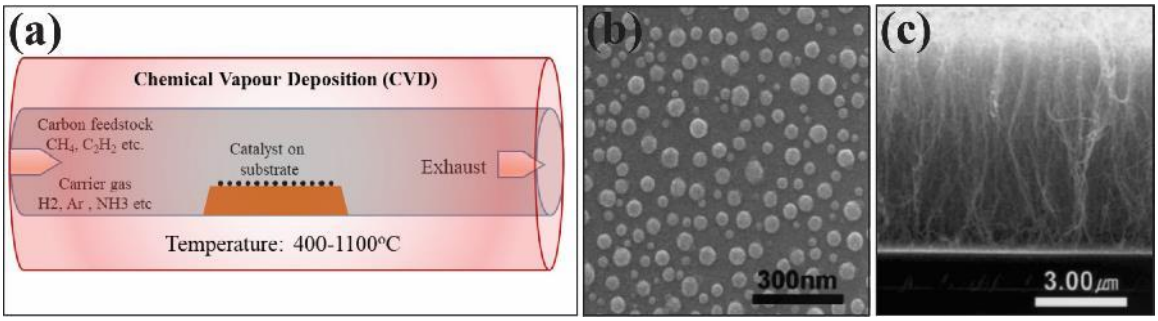

Figure 2.4. (a) Schematic of the set-up for a typical CVD apparatus [adapted from ref. 5]. Scanning electron micrograph of (b) Ni nanoparticles after heat pretreatment in the mixture of N_2 and H_2 environment and (c) CNTs synthesized for 20 minutes [adapted from ref 15].

2.2.4 Plasma-enhanced chemical vapor deposition

Plasma-enhanced chemical vapor deposition (PECVD) enables the growth of well-aligned CNTs at lower temperatures than thermally driven CVD [20]. The synthesis of aligned CNTs is achieved by facilitating the decomposition of hydrocarbon precursor gas at lower temperatures. In the PECVD method, a high-frequency potential applied to the electrodes generates a plasma that consists of highly energetic gas species such as radicals, ions, and electrons. These energetic plasma species help to decompose carbon feedstock (e.g., C_2H_2, CH_4, C_2H_4, and C_2H_6.), and the electric field in the plasma aligns CNTs along the direction of the applied electric field [21]. Besides, plasma enhances the CNT growth rate by etching away amorphous carbon from the catalyst surface during the CNT growth process. Figure 2.5(a) represents a schematic of the set-up for a typical PECVD apparatus consisting of two parallel plates separated by a distance and enclosed by a chamber.

Ren *et al.* reported the synthesis of vertically aligned CNTs (VACNTs) at 666 ºC on Ni-coated glass substrate by using C_2H_2 as carbon source and NH_3 as dilution gas [22]. Figure 2.5(b) shows a scanning electron micrograph of VACNTs synthesized by the PECVD method. The VACNTs measured 0.1 to 50 µm in length and 20 to 400 nm in

diameter. They found that the morphology of the CNTs can be controlled by synthesis parameters such as growth time, plasma intensity, flow rates of precursor gases, and the thickness of metal catalysts deposited on the substrate. Chhowalla *et al.* synthesized VACNTs by direct current PECVD method at 550–900 ºC on Ni-coated Si substrate [23]. They studied growth properties, such as the diameter, growth rate, and areal density of the VACNTs, as a function of the Ni catalyst layer thickness, bias voltage, deposition temperature, C_2H_2:NH_3 ratio, and pressure. Besides, they concluded that the alignment of the VACNTs strongly depends on the applied electric field.

Bell *et al.* investigated the role of plasma in aligning the CNTs in the direction of the applied electric field by synthesizing VACNTs via PECVD on Ni-coated Si substrate using C_2H_2/NH_3 feedstock [24]. They also studied the role of NH_3 in the plasma and found

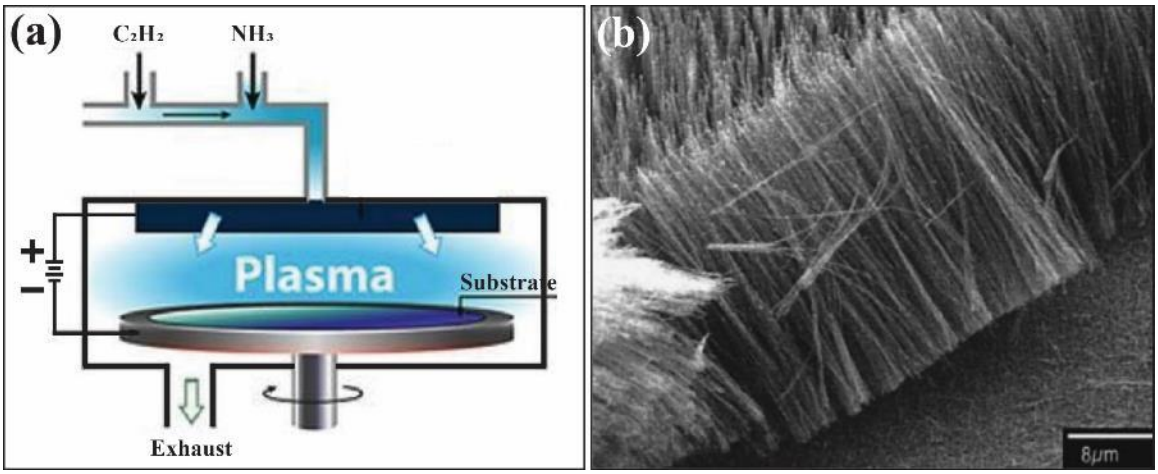

Figure 2.5. (a) Schematic of the set-up for a typical PECVD apparatus. (b) Vertically aligned CNTs synthesized on quartz substrate [adapted from ref. 22].

that it can suppress the excess decomposition of carbon precursor and remove unnecessary amorphous carbon during the CNTs growth. Furthermore, PECVD has been used to synthesize VACNTs on metal substrates with and without external catalysts to use them in

various field emission devices [25-29]. Various types of PECVD, such as microwave PECVD, radio-frequency PECVD, inductive PECVD, and hot filament PECVD, have been developed to fabricate VACNTs with controlled morphology and high yield at lower temperatures [25, 30-32].

2.2.5 Other methods

A few techniques, other than the above-explained commonly used methods, have been developed to synthesize CNTs. The most notable methods are diffusion flame synthesis and electrochemical synthesis. Wal *et al.* reported the synthesis of SWCNTs by using a simple laboratory-scale diffusion flame method at temperatures above 1200 ºC [33]. The C_2H_2, diluted with N_2, was used as the carbon precursor gas, and metal nanoparticles formed from a metallocene were used as catalysts in the floating catalyst approach at atmospheric pressure. The SWCNTs were 1.4 nm in diameter, and the growth rate of CNTs was observed as 200–2000 nm/s. Yuan *et al.* synthesized randomly oriented and partially aligned MWCNTs on the stainless steel grid by using ethylene–air diffusion flame at temperatures between 1200–1500 ºC at normal pressure [34]. The addition of N_2 to the ethylene–air flame was crucial for aligning entangled MWCNTs by lowering the flame temperature. Multi-walled VACNTs of uniform diameter (15 nm) can also be synthesized by using methane inverse diffusion flame in the presence of an external electric field on metal alloy substrates [35].

The MWCNTs can be synthesized below room temperature by using electrolysis of C_2H_2, which is mixed with NH_3 cooled to -40 ºC in a glass vessel [36]. The electrolysis was performed at a direct current bias of 150 V between Si electrodes for 5–10 hours.

Principally, the formation of MWCNTs on the cathode was initiated by the decomposition of carbon precursor C_2H_2 with the help of atomic hydrogen generated on the negative electrode. The MWCNTs were measured to be 15 nm in diameter and more than 15 μm in length.

2.3 Growth mechanism

For synthesizing CNTs, the most common precursors are CH_4, C_2H_4, C_2H_2, C_6H_6, C_8H_8, and CO; whereas, typical metal catalysts are Fe, Co, and Ni because of their high carbon solubility and high carbon diffusion rate [37]. Furthermore, metal catalysts in the form of nanoparticles are essential for decomposing precursor gases at a temperature lower than their spontaneous decomposition temperature. Once carbon precursor gas decomposes into carbon and hydrogen species at the surface of catalyst particles, carbon atoms dissolve. As a result, carbon atoms precipitate out upon the super-saturation of the metal catalyst and graphitizes into an energetically stable, crystalline cylinder. A thermal gradient created inside the catalyst particle triggered by exothermic precursor decomposition and endothermic carbon crystallization processes maintains the whole process active [38].

Two widely accepted and most general CNT growth mechanism is shown in Figure 2.6 [38]. If the catalyst particle is loosely attached to the substrate, carbon atoms precipitate out across the particle bottom and push the catalyst particle off the substrate, stage (i) Figure 2.6(a). As long as the catalyst particle remains active for further hydrocarbon decomposition and dissolution of carbon atoms, CNT grows continuously (stage (ii) Figure 2.6(a)). Eventually, CNT growth is stopped once the particle loses its catalytic activity, stage (iii) Figure 2.6(a), and the process is familiar as a tip-growth model [38, 39]. In

contrast, if the catalyst particle is strongly attached to the substrate, precipitation of carbon atoms occurs at the top of the catalyst particle. As a result, carbon atoms graphitize out as a hemispherical dome (stage (i) Figure 2.6(b)), which eventually elongates to form a CNT with a catalyst particle rooted on its base (stage (ii) Figure 2.6(b)). The process is known as the base-growth model [39].

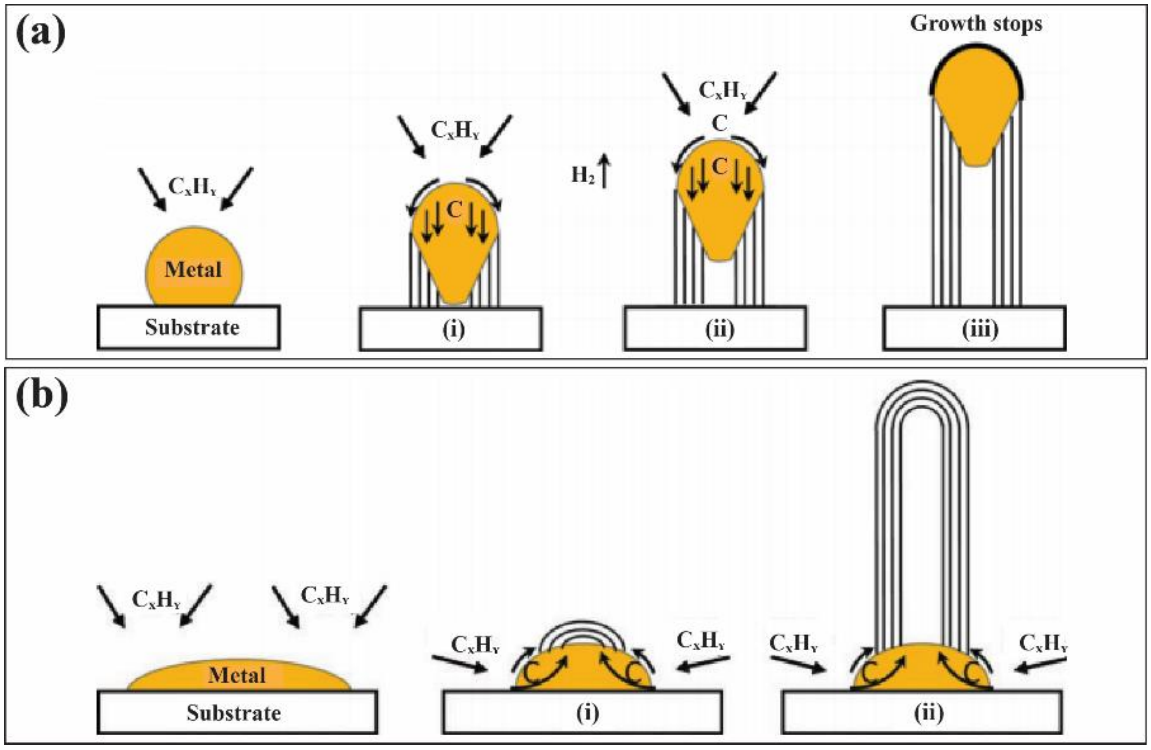

Figure 2.6. Growth mechanisms for CNTs: (a) tip-growth model and (b) base-growth model [adapted from ref. 38].

2.4 Properties of CNTs

Since the discovery of CNTs in 1991, significant success has been achieved in understanding the unique and excellent properties of CNTs. The following section reviews the properties of CNTs in brief.

2.4.1 Electrical conductivity

The measurements, performed both in air and in high vacuum, have demonstrated that CNTs behave as ballistic conductors at room temperature, with mean free paths of the order of tens of microns. Frank *et al.* demonstrated for the first time that CNTs conduct current ballistically without dissipating heat [40]. The conductance of multi-walled CNTs (MWCNTs), 4 μm long and 15 nm wide, was measured by using the MWCNT as the tip of the scanning probe microscope, which could be lowered into mercury (Hg) to make electrical contact with the MWCNT, Figure 2.7(a). The conductance of MWCNTs was one unit of the conductance quantum, and the current density through the nanowire was measured to be more than 10^7 A/cm^2. Poncharal *et al.* followed up on the research conducted by Frank *et al.* by using in-situ electron microscopy experiments and further confirmed the ballistic conduction of CNTs [3]. They also investigated the CNT length dependence of the resistance. Figure 2.7(b–c) shows an MWCNT in contact with Hg completing a closed circuit to measure the conductance and the MWCNT failure at a high applied voltage of 4 V. The measurement revealed that the conductance increases linearly with the increasing voltage at high voltages because of the opening of higher conducting channels, as shown in Figure 2.7(d) and its inset. Furthermore, as shown in Figure 2.7(e), the variation in length did not show a significant change in the conductance of CNTs.

Langer *et al.* measured the electrical resistance of bundles of MWCNTs in a temperature range from room temperature to 0.3 K in magnetic fields of up to 14 T [41]. The MWCNTs showed semi-metallic properties with a similar band structure to rolled graphene sheets. The resistance of the nanotube bundle was decreased as a magnetic field

was applied perpendicular to the CNT axis. Langer *et al.* further studied the electrical properties of individual MWCNTs down to a very low temperature of 20 mK [42]. The conductance measurements of the MWCNT revealed a logarithmic dependence on the temperature and its saturation at low temperatures. The MWCNT displayed increased conductance upon applying a magnetic field normal to the tube axis.

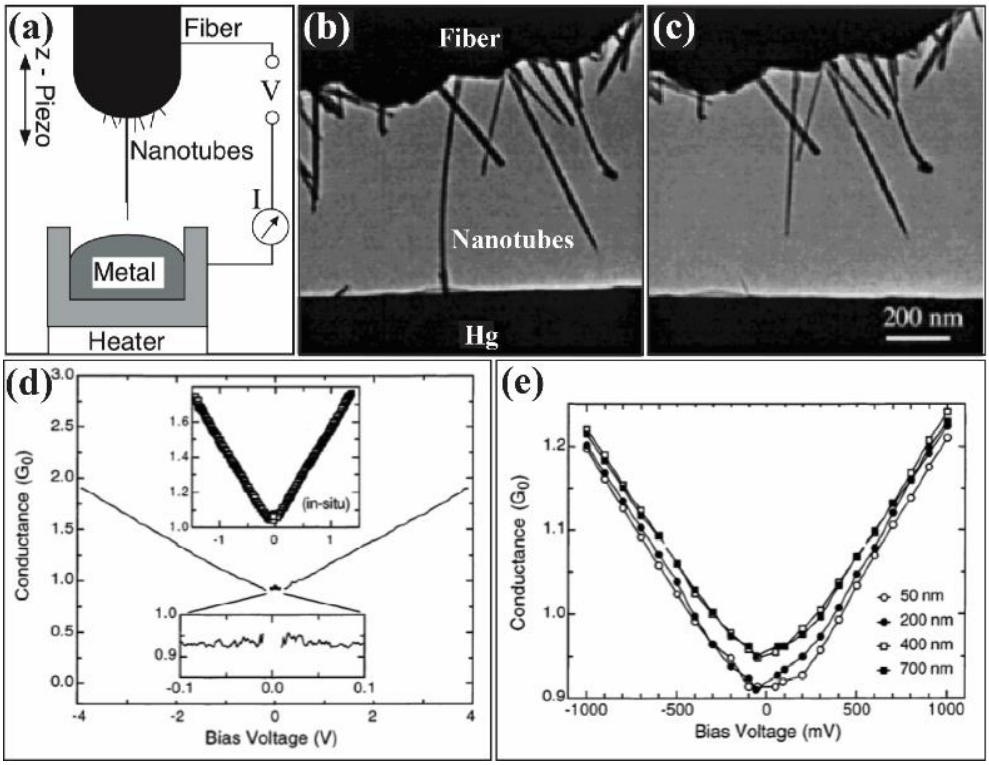

Figure 2.7. (a) Schematic diagram of the experimental setup for measuring the conductance of an MWCNT. (b-c) Transmission electron micrographs of contacted nanotubes and their failure at the applied voltage of 4 V. (d) Conductance of an MWCNT as a function of the bias voltage. (e) The conductance of a MWCNT as a function of the position of the nanotube contact into the Hg [adapted from ref. 3].

2.4.2 Electron field emission

Carbon nanotubes are considered the most suitable source of electrons for future nano-electronic devices through the process of field emission because of their small tip dimension and large aspect ratio. The FE from CNTs can be described by the Fowler-Nordheim (F-N) theory on the basis of a simplified one-dimensional free electron model

and Wentzel-Kramers-Brillouin (WKB) approximation. According to the F-N theory, the emission current density from the CNT emitter can be given as:

$$J = \left(\frac{A\, E_{local}^2}{\phi}\right) \exp\left(-\frac{B\, \phi^{\frac{3}{2}}}{E_{local}}\right) \tag{2.1}$$

where A (1.56×10^{-6} A V^{-2} eV) and B (6.83×10^{9} $eV^{3/2}$ V m^{-1}) are constant quantities. ϕ is the work function of the field emitter. An expression relates the local electric field (E_{local}) and an applied electric field (E) as:

$$\beta = \frac{E_{local}}{E} \tag{2.2}$$

where β is the field enhancement factor. The FE properties of CNTs are measured typically by using a diode configuration method under a high vacuum of ~10^{-6} to 10^{-7} Torr. The diode configuration includes a cathode consisting of CNT emitters and an anode, and a voltage bias can be applied between the anode and the cathode.

Rinzler *et al.* in 1995 reported, for the first time, the FE from a single CNT and found that the emission current significantly enhanced when the nanotube tips were opened [43]. The emission currents of 0.1 to 1 µA were recorded at room temperature with bias voltages of less than 80 V. In the same year, De Heer *et al.* fabricated a high-intensity and highly stable electron gun with the FE at low voltages from a thin film of vertically aligned CNTs [44]. Current densities up to 0.1 mA/cm^2 were observed for applied voltages as low as 200 V, and high current densities more than 100 mA/cm^2 were recorded at 700 V.

In the case of FE from CNTs film, one of the fundamental parameters is the number density of the emitters. Typically, CNTs density is reported to be in the range between 10^8 to 10^9 cm^{-2} in a dense CNTs film; however, the number density of effective emitters for

randomly oriented CNTs usually is much lower, in the range between 10^3 to 10^7 cm^{-2} [45, 46]. It is expected a number density of the emitters more than 10^6 cm^{-2} and a total emission current density of more than 80 μA cm^{-2} are appropriate for CNT films to be used in real FE applications [47]. Therefore, vertically aligned CNTs (VACNTs) are preferred over randomly oriented CNTs as field emitters because of their high number density of effective electron-emitting sites.

It is a well-known fact that the tip of the CNT releases the electron during the FE process. The VACNTs can facilitate the FE process because the apex of each CNT experiences the same constant electric field to emit the electrons. However, typical dense VACNT arrays suffer from the screening effect because of the close proximity of neighboring VACNTs, which adversely affects the field emission performance by increasing the turn-on field and decreasing the total emission current density [48]. Nilsson *et al.* suggested an optimum ratio of intertube distance (R) to the VACNT height (H) to be 2 (R/H = 2) for the maximum possible field enhancement from the emitter array [49].

The VACNT arrays can be patterned to form various morphologies such as circular, square, and toroidal pillar-shaped structures with appropriate inter-pillar distances through optical or electron beam lithography to achieve high emission current density, which can garner values up to a few amperes per cm^2 [50-52]. It has also been observed that the length and diameter (cross-section size) of the pillar structure and inter-pillar distance play a vital role in FE properties.

Hazra *et al.* reported an extremely low turn-on field (0.16 V μm^{-1} at 10 μA cm^{-2}) and impressively high emission current density of about 1.5 A cm^{-2} at 0.3 V μm^{-1} for the VACNT-based pillar structure after the plasma treatment had been applied to the pillars to

create an extremely sharp-tipped pillar structure (tip diameter < 1 μm) [53]. It is reported that a post-growth structural modification of the CNT-based emitters by coating the CNTs with a wide-bandgap semiconducting metal oxide or metal nanoparticles, such as TiO_2, ZnO, RuO_2, MgO, SnO_2, Al, and Cu, can enhance the FE properties through modifying the electronic and the physical structure of the CNT-based field emitters [54-58].

2.4.3 Thermal properties

The thermal properties of CNTs are technologically crucial for controlling the performance and stability of electronic and micromechanical devices. The phonon energy spectrum at different temperatures completely describes the thermal transport behavior of CNTs, specifically SWCNTs. Hone *et al.* observed the linear dependence of specific heat of SWCNTs in the temperature range from 300 to 2 K and found it completely different from the specific heat of two-dimensional graphene or three-dimensional graphite [59]. The calculation of the lowest quantized phonon subband energy (4.3 meV) and tube-tube Debye energy (1.1 meV) through theoretical modeling indicated a weak coupling interaction between the tubes in SWCNT bundles, which was evidence of 1D quantized phonon subbands.

Yi *et al.* reported the measurement of the specific heat and thermal conductivity of millimeter-long aligned MWCNTs over the temperature range of 10 to 300 K [60]. The MWCNTs exhibited a linear temperature-dependent specific heat and a weak inter-wall coupling, similar to the SWCNTs. However, they observed a low thermal conductivity caused by the highly defective MWCNTs prepared by a chemical vapor deposition.

Lasjaunias *et al.* further extended the low-temperature heat capacity measurements of SWCNTs down to 0.1 K. They tested the role of adsorbed helium (He) on the heat capacity of the nanotubes [61]. Figure 2.8(a) shows the specific heat of an SWCNT rope for three different runs in the temperature range of 0.1 to 7 K. The specific heat exhibited three different influences, mainly from nuclear hyperfine interactions in residual ferromagnetic catalyst particles (0.7–1.0 at. % Co), represented by a well-defined T^{-2} term. Also, the specific heat showed a monotonously varying vibrational contribution raised from the He adsorption. After completely outgassing the He, as shown in run C of Figure 2.8(a), the specific heat displayed an inter-tube coupling evidenced by the T^3 term. Finally, the specific heat showed linear temperature dependence from 4.5 K onward.

Kim *et al.* reported the measurement of the thermal conductivity of an individual MWCNT by using a microfabricated suspended device, as shown in the SEM image at the upper corner of Figure 2.8(b) [62]. The suspended device consists of two islands of silicon nitride membranes connected by an MWCNT and a platinum thin-film resistor on each island for heating the sample. Figure 2.8(b) shows the thermal conductance of an MWCNT of diameter 14 nm measured in a temperature range of 8 to 370 K. The measurement displayed an increase in the thermal conductance significantly as the temperature was increased while reaching a maximum (1.6×10^{-7} W/K) near room temperature. As shown in the lower inset of Figure 2.8(b), the thermal conductivity of a single MWNT (solid line) exhibited an interesting temperature-dependent behavior that was absent in bulk material. At low temperatures (8–50 K), the thermal conductivity increased with a power law $T^{2.50}$, while it varied almost quadratically ($T^{1.98}$) at intermediate temperatures (50–150 K). Above 150 K, the thermal conductivity deviated from quadratic temperature dependence and

peaked at 320 K. The thermal conductivity decreased rapidly beyond the peak temperature. The MWNT bundles (broken and dotted line) did not show such behavior, and thermal conductivity became similar to that of a mat sample. The thermal conductivity was measured to be more than 3000 W/m K at room temperature, which is two orders of magnitudes greater than the thermal conductivity of CNT films [60].

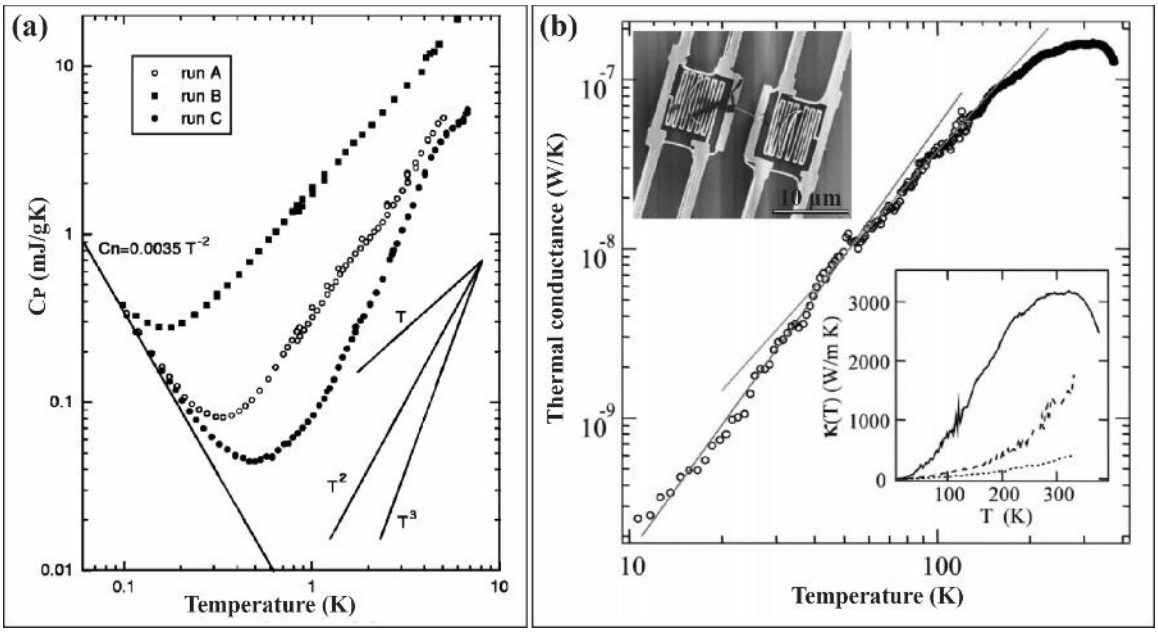

Figure 2.8. (a) Specific heat of the SWCNT rope for three different runs A, B, and C. The effect of the He adsorption is maximum in run B and minimum in run C. Power-law straight lines are illustrative only [adapted from ref. 61]. (b) Thermal conductance of an MWCNT. The inset at the upper corner shows a SEM image of the microfabricated device with the individual MWNT. The inset at the lower corner represents the thermal conductivity of an individual MWNT with diameter 14 nm (solid line), 80 nm (broken line) and 200 nm (dotted line) [adapted from ref. 62].

2.4.4 Mechanical properties

The mechanical properties of CNTs are strongly related to the chemical bonding of the constituent carbon atoms. In the seamless cylindrical graphitic structure of CNTs, each carbon atom is bonded to three neighboring carbon atoms as a result of the in-plane sp^2 hybridization through σ-bond (see section 2.1 for detail). The σ-bond is considered the strongest chemical bond in nature and crucial for the excellent mechanical properties of

CNTs [63]. Knowledge of Young's modulus of CNTs is essential for their use as a structural element for various applications. Treacy *et al.* evaluated Young's modulus of individual CNTs by measuring the amplitude of their intrinsic thermal vibrations in the temperature range of 25 ºC to 800 ºC inside a transmission electron microscope, as shown in Figure 2.9 [64]. Measurements on various nanotubes of diameter in the range of 5.6 to 24.8 nm and a length ranging from 1.2 to 5.8 µm revealed an average Young's modulus of 1.8 TPa. Figure 2.9(a–b) shows the transmission electron micrographs of free-standing CNTs showing the thermal vibration at different temperatures. Figure 2.9(c) represents the mean-square vibration amplitude of a 5.60 µm long and 16.6 nm wide free-standing CNT. The Young's modulus of the CNT calculated by using the slope of the plot was 3.7 Tpa.

Wong *et al.* measured Young's modulus of MWCNTs to be 1.3 TPa by using atomic force microscopy [65]. A comparative study revealed that the MWNTs were about two times stiffer than silicon carbide nanorods. Further application of bending force on the silicon carbide nanorod eventually led to fracture, whereas the MWNTs demonstrated a remarkable elastic buckling. Various theoretical and experimental measurements have demonstrated Young's modulus of an individual SWCNT and SWCNT rope in the range of 0.4–1 TPa [66-68]. Li *et al.* reported the direct tensile strength measurements of 20 mm long ropes consisting of highly aligned SWCNTs synthesized by the catalytic CVD [69]. The average tensile strength of SWNT rope composites was as high as 3.6 ± 0.4 GPa, similar to that of carbon fibers. Yu *et al.* measured the tensile strengths of individual MWCNTs to be ranged from 11 to 63 GPa by using a nano-stressing stage inside a scanning electron microscope [70]. They observed a fascinating multi-step breaking mechanism of MWCNTs, which initiated in the outermost layer called sword-in-sheath failure.

Additional analysis of the stress-strain curve of MWCNTs revealed Young's modulus of the outermost layer to be in the range of 0.27 to 0.95 TPa.

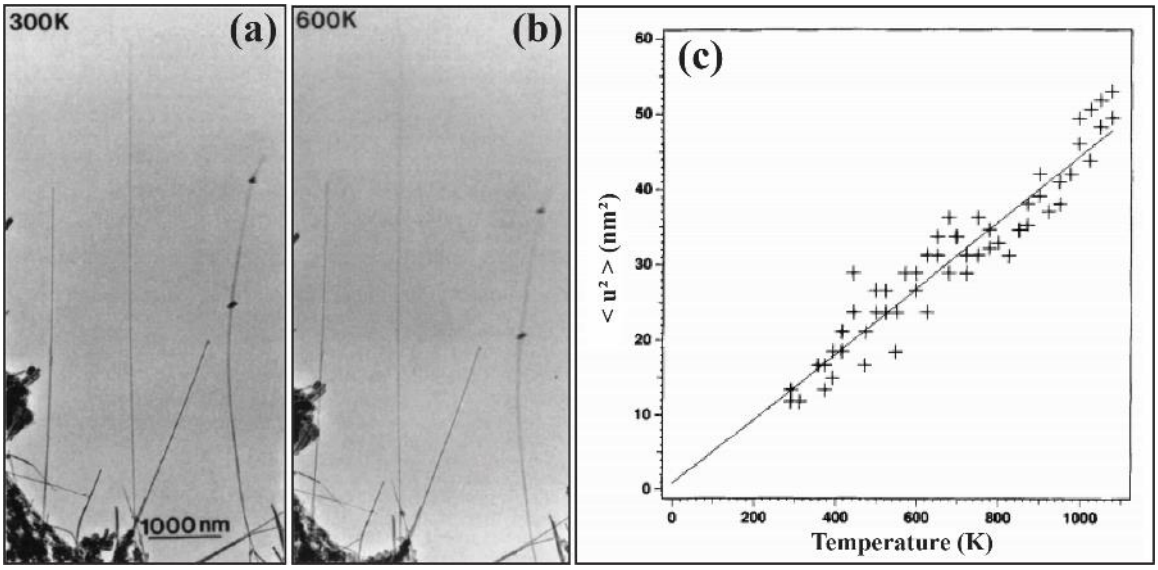

Figure 2.9. (a-b) Transmission electron micrographs of free-standing CNTs showing the blurring at the tips caused by thermal vibration at different temperatures. (c) Plot of mean-square vibration amplitude of a free-standing CNT at different temperatures to calculate Young's modulus [adapted from ref. 64].

2.5 Applications of CNTs

Because of the exceptional properties described in the previous section, CNTs have potential in various applications, including field emission displays, energy storage, and sensors. The following section describes the application of CNTs in various fields.

2.5.1 Field emission displays

CNTs are promising materials for macroelectronic devices such as field emission display (FED) because of their excellent field emission properties. The CNT-based FEDs can exhibit superior display performances such as fast response time, wide viewing angles, wide temperature range of operation, ultra-slim features, low power consumption, bright displays with excellent color and contrast resolution [71]. The vertical alignment of CNTs

is essential for their application as field emitters in FEDs. Wang *et al.* reported the fabrication of a 32×32 matrix addressable diode FED (200×200 μm^2) by using a CNT–epoxy composite as the electron emission source, which exhibited excellently-lit pixels under the bias of ±150 V [72]. Each pixel of the FEDs was carefully analyzed by measuring the current versus applied voltage curves across the panel.

Lee *et al.* fabricated large-area FEDs by using an electron emission layer of SWCNT paste printed on a glass substrate to demonstrate moving color images [73]. Figure 2.10(a) and (b) show a schematic of the CNT-based FED panel with the diode structure and a 4.5-inch CNT-FED display, respectively. The panel consists of a glass plate cathode with stripes of CNTs and a phosphorus coated glass plate anode separated from the cathode by a distance of 200 μm. Pixels of 20 μm size, consisting of vertically aligned CNTs, were fabricated on the cathode plate by screen printing and subsequent heat treatment at 350 ºC for 20 min. In contrast, the anode was prepared by screen printing the low voltage phosphors of different colors with a thickness of 6–10 μm on ITO-coated soda-lime glass. The FED exhibited excellent field emission performance of a threshold electric field of about 2 V/μm, as shown in Figure 2.10(c).

Nakayama and Akita fabricated FEDs on the basis of vertically oriented CNTs by using the electrophoresis method [74]. The CNT field emitters were attached to the substrate using conductive and non-conductive polysilane films. The device in diode configuration showed a low turn-on voltage of 180 V for the conductive film while the non-conductive film exhibited the bistability with the turn-on voltage of 380 V and turn-off voltage of 250 V. The CNT-based and diode-type FED displayed strong luminescence;

however, the stability was very poor. Various research groups have reported the fabrication of FEDs using CNTs, which show a promising future in economical, energy-efficient, and performance-enhanced displays [75-78].

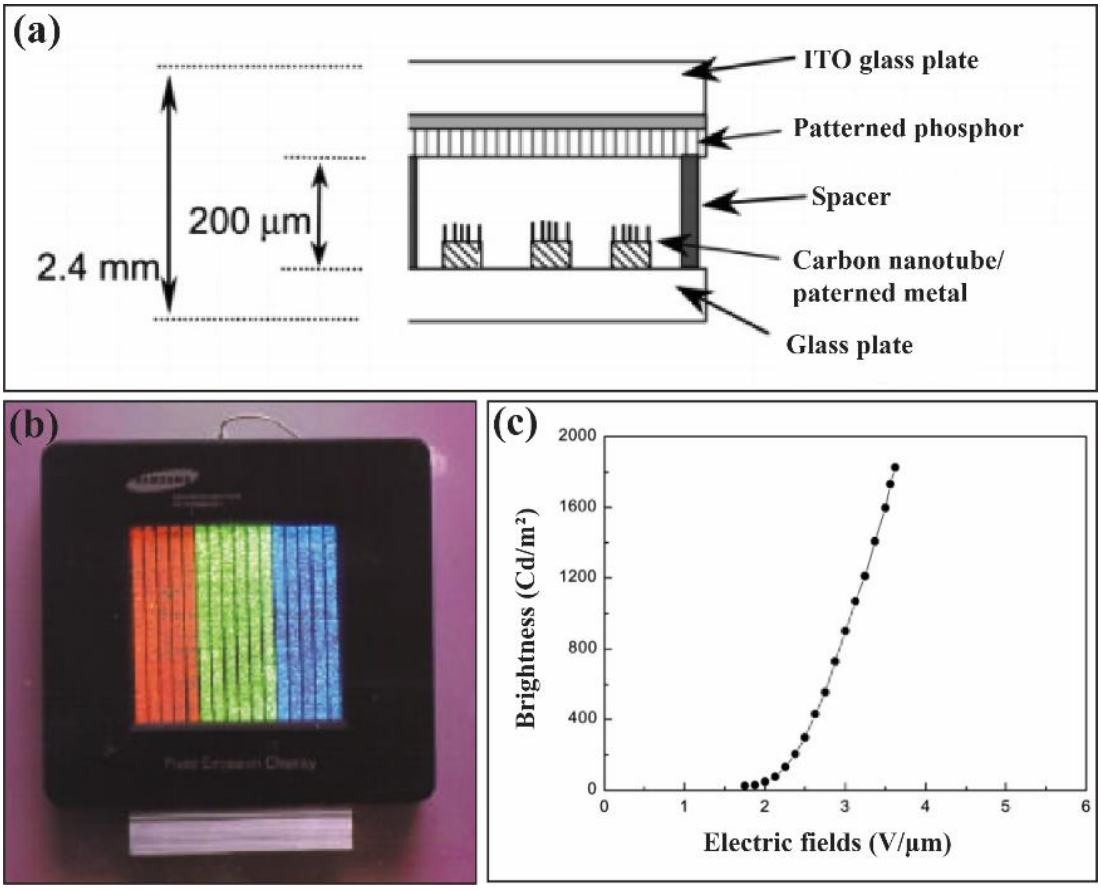

Figure 2.10. (a) Schematic of a carbon nanotube field emission display with the diode configuration. (b) 4.5-inch carbon nanotube field emission display. (c) Plot of brightness versus electric fields [adapted from ref 73].

2.5.2 Lithium-ion batteries and supercapacitors

Properties of CNTs such as unique one-dimensional tubular structure, large surface area, short diffusion length of Li^+ ions, and high electrical and thermal conductivity make them efficient electrode materials for high-performance energy storage devices [79]. Theoretical lithiation/delithiation predictions show that SWCNTs can facilitate charge

transfer with relatively small structure deformation during electrochemical energy storage and conversion mechanism [80]. It has been speculated that both the interstitial sites and the inner wall of the nanotubes may be energetically favorable sites for Li^+ ion storage. Furthermore, theoretical computations predicted that every two carbon atoms in a graphene plane intercalate with a single Li^+ ion [81]. Therefore, CNTs exhibit higher Li^+ ion storage capacity (~1000 mAh/g) than graphite (372 mAh/g). Figure 2.11(a) shows a schematic diagram of a typical lithium-ion battery (LIB) consisting of a graphite anode and a $LiCoO_2$ cathode, separated by a polymer separator [82].

Yang *et al.* conducted a comparative study of two kinds of CNTs, i.e., short CNTs-1 (150–400 nm long and 35–65 nm wide) synthesized by pyrolysis method and long CNTs-2 (several μm long and 15–30 nm wide) fabricated by a CVD method as anode materials for LIBs [83]. Figure 2.11(b-c) represents the charge/discharge curves of type 1 and type 2 CNTs anode at the current density of 0.2 mAh/g. Besides, Figure 2.11(d-e) compares the cycle stability of CNT anodes of type 1 and 2 at the current densities of 0.2 and 0.8 mAh/g. The reversible capacities of the CNTs-1 anode were nearly double compared to the CNTs-2 anode at both the high and low current densities. The poor electrochemical performance of the longer CNT anodes was caused by the larger voltage hysteresis related to the surface functional groups on CNTs and the surface resistance of CNTs. The surface resistance caused the limited charge transport and higher overvoltage during Li^+ ions extraction from electrodes.

Lu *et al.* fabricated high-performance and high-safety LIBs by using vertically aligned CNTs (VACNTs) and V_2O_5 coated vertically aligned CNTs (V_2O_5-VACNTs) as

both anode and cathode electrode, respectively [84]. The VACNT anode and V_2O_5-VACNTs cathode exhibited a high specific capacity of 600 mAh/g and 368 mAh/g, respectively, leading to a high energy density of 297 Wh/kg and power density of 12 kW/kg. Recent research of electrode materials is mainly focused on composite materials consisting of CNTs and high Li^+ ion storage capacity materials (e.g., Si, Ge, SnO_2, and Li) to address the inherent concerns such as tremendous volume expansion, capacity fading, low energy density, and safety issues [85-88]. These CNT-based electrodes have pushed LIBs well above 1000 mAh/g, some reaching even more than 2000 mAh/g with excellent cycling capacity for hundreds of cycles at the higher current density.

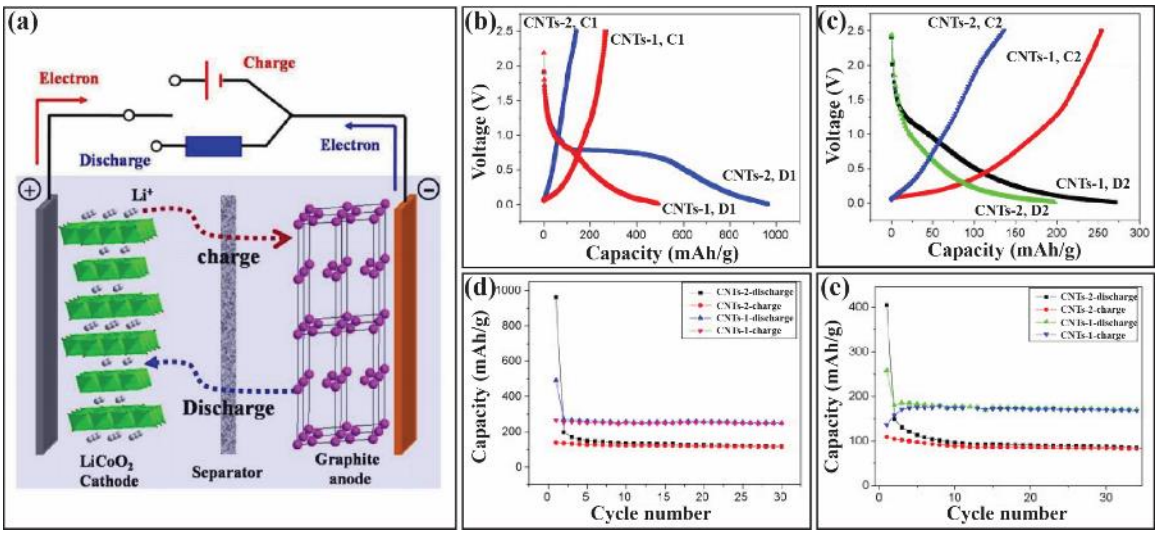

Figure 2.11. Electrochemical properties of CNTs anode. (a) Schematic of a LIB with graphite anode and $LiCoO_2$ cathode [adapted from ref. 82]. (b-c) Charge/discharge properties of type 1 and type 2 CNTs anode at the current density of 0.2 mA/h. (d-e) Cycle stability of type 1 and type 2 CNTs anode at current densities of 0.2 and 0.8 mA/h [adapted from ref. 83].

Carbon nanotubes have also been significantly investigated as electrodes of supercapacitors because of their ability to store and deliver a tremendous amount of energy in a short period of time for a long-life cycle through a simple charge separation process. Niu *et al.* assembled a supercapacitor by using free-standing mats of entangled nanotubes

as electrodes and reported that a power density of more than 8 kW/kg was achieved [89]. A single cell capacitor assembly with 38 wt % H_2SO_4 as the electrolyte produced high specific capacitances of 102 and 49 F/g at 1 and 100 Hz, respectively. An *et al.* fabricated supercapacitors by using CNTs grown on polished nickel foil as electrodes [90, 91]. A low contact resistance resulted from the direct growth of CNTs on conducting substrate was observed. A reduced internal resistance as a result of a heat-treatment to the CNT electrode at high temperatures was crucial for delivering high power densities. A maximum specific capacitance of 180 F/g and a high-power density of 20 kW/ kg at energy densities in the range of 7 to 6.5 Wh/kg were recorded [91].

Cheng *et al.* reported the fabrication of supercapacitors by using flexible and binder-free CNTs-graphene-MnO_2 nanocomposite electrodes [92]. The measurements revealed a high specific capacitance of 372 F/g with excellent rate capability for supercapacitors without current collectors and binders. Several research groups have recently reported the fabrication of high-performance supercapacitors with different CNT-based composite electrodes such as nitrogen-doped CNTs, CNTs-graphene nanocomposites, and NiO-CNTs composite [93-95].

2.5.3 Photovoltaic devices

Carbon nanotubes have demonstrated potential applications in photovoltaic devices such as solar cells for harvesting clean solar energy because of their high electron mobility essential for efficiently collecting photo-generated electrons. Lee *et al.* reported the fabrication of novel dye-sensitized solar cells using nitrogen-doped vertically aligned CNTs (N-VACNTs) on a rigid glass substrate or flexible plastic substrate as counter

electrodes [96]. Cyclic voltammetry analysis revealed much higher cathodic and anodic current densities of the N-VACNT counter electrode than those of the platinum (Pt) electrode. Improved current densities indicated that the N-VACNT counter electrode offers a much faster reaction and electron transfer rate from the substrate than in the Pt electode. Figure 2.12(a-b) represent a schematic of a dye-sensitized solar cell with N-VACNT counter electrode and current density (J) versus voltage (V) characteristics of solar cells with N-VACNT or Pt counter electrodes. Under illumination, the N-VACNT based solar cell exhibited comparatively similar performance to that of the Pt-based solar cell with a fill factor of 0.67, a current density (Jsc) of 14 mA/cm^2, an open circuit voltage (Voc) of 0.767 V, and a conversion efficiency of 7.04 %.

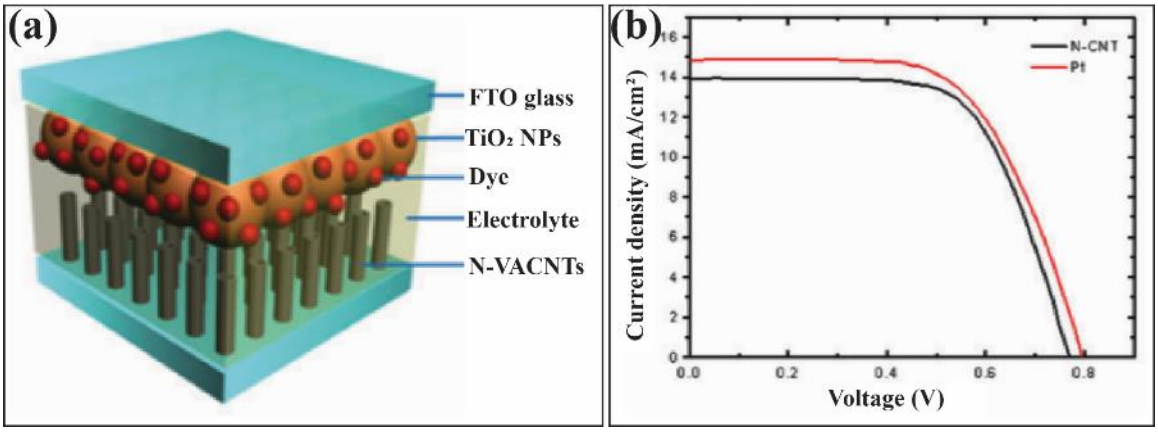

Figure 2.12. CNTs for solar cells. (a) Schematic of a dye-sensitized solar cell with N-VACNT counter electrode. (b) J–V characteristics of solar cells with N-VACNT or Platinum (Pt) counter electrodes [adapted from ref. 96].

Dang *et al.* report the fabrication of the dye-sensitized solar cells with TiO_2-SWCNTs nanocrystal core-shell nanocomposites as photoanodes [97]. The addition of a small fraction of SWCNTs improved the power conversion efficiency of the solar cells to 10.6% by increasing the electron collection efficiency. Yue *et al.* synthesized MWCNTs decorated with tungsten sulfide (WS_2-MWCNTs) for use as a low-cost platinum-free

counter electrode in dye-sensitized solar cells [98]. The solar cell showed a conversion efficiency of 6.41% under a simulated solar illumination of 100 mW/cm^2, comparable to 6.56% for a dye-sensitized solar cell with a Pt counter electrode. Li *et al.* reported the synthesis of VACNTs directly onto a free-standing graphene paper (GP-VACNTs) by using CVD and used the composite as counter electrodes in dye-sensitized solar cells [99]. The solar cell with GP-VACNTs counter electrode exhibited the closed-circuit current density of ~14.6 mA/cm^2 and the conversion efficiency of 6.05%, comparable to that of the Pt counter electrode.

2.5.4 Sensors

Carbon nanotubes are considered excellent chemical and biological sensors because of their unique electrochemical and adsorption properties. These sensors work according to feedbacks shown in the I–V curves upon adsorption of specific molecules on the CNT's wall. It has been demonstrated that the use of CNTs in sensor devices improves sensitivity and selectivity, as well as response rate and recovery time. Sayago *et al.* synthesized SWCNTs by the arc-discharge method. They investigated them as resistive gas sensors for H_2 detection at room and elevated temperatures after functionalizing with palladium (Pd) nanoparticles of diameter 3–5 nm [100]. Figure 2.13 (a) shows a typical transmission electron micrograph of the Pd-SWCNT composite used for H_2 detection at room temperature. Figure 2.13(b) represents the dc electrical measurements (resistances) of the sensor at the detection concentrations of H_2 from 0.5 to 4% in the mixture with pure N_2. The measurement showed a small variation in resistance as a function of gas concentration. The slow rate of adsorption-desorption processes was accredited to the low

operating temperature; however, the sensor sensitivity ($S = 100 \times (\Delta R)/R_{N2}$) was significantly increased and reached about 20% at the temperature of 250 ºC.

Star *et al.* used a network of SWCNTs decorated with metal nanoparticles (e.g., Pd, Pt, Rh, and Au) in the form of a field-effect transistor to detect toxic/combustible gases such as H_2, CH_4, CO, and H_2S [101]. The decoration of CNTs with metal nanoparticles dramatically improved the selectivity and sensitivity of the sensor at less than 5 ppm (parts-per-million) concentrations of gases. It has been reported that various materials such as NH_3, H_2O_2, DNA, glucose, and protein can be detected by recording their electrical or optical response to the CNT-based sensors before and after introducing the detection materials [102-106].

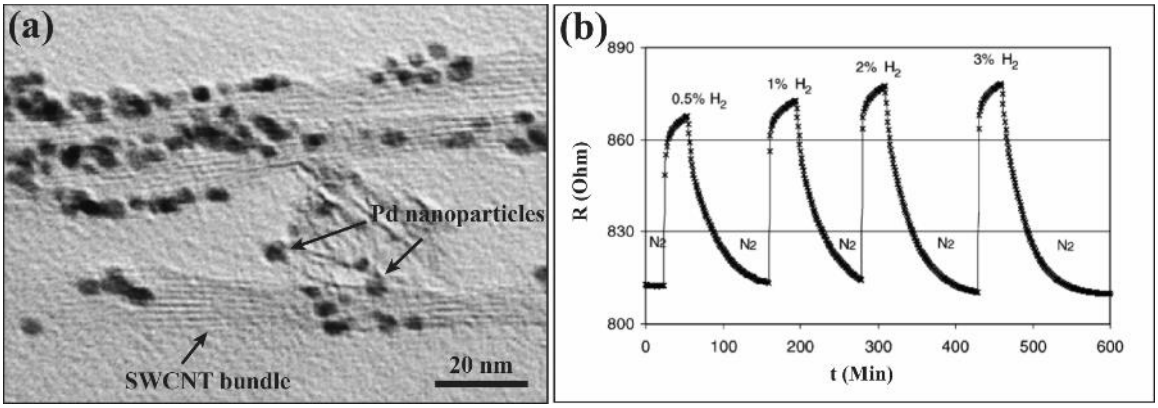

Figure 2.13. Application of CNTs as a gas sensor. (a) Transmission electron micrograph of Pd-SWCNT composite. (b) Response curve of the Pd-SWCNTs at room temperature [adapted from ref. 100].

2.5.5 Hydrogen storage

Hydrogen has demonstrated tremendous potential as a fuel to power transport vehicles and electronic devices. However, a lack of proper hydrogen storage has remained a problem for a long time, limiting its use as a power source. A large number of theoretical and experimental research have revealed that CNTs can store a significant amount of

hydrogen at an extensive temperature range because of their chemical stability, large surface area, low density, hollowness, and nanometer-scale diameters. Research performed by Dillion *et al.* showed the possibility of storing impressive 5–10 wt.% molecular hydrogen at room temperature in SWCNTs of diameter 1.2 nm, which were synthesized by the arc-discharge method [107]. Shiraishi *et al.* investigated molecular hydrogen desorption from SWCNT bundles at about 350 K by using the temperature-programmed-desorption (TPD) method [108]. The SWCNTs treated with NaOH exhibited the storage of the hydrogen molecule in an inter-tube space and sub-nanometer sized spaces in the bundle. Since the hydrogen desorption measurement was performed under high vacuum conditions, only a small amount (0.01 wt%) of molecular hydrogen was desorbed into the host SWCNT bundle at the moderate temperature.

It has been reported that the hydrogen storage capacity of the CNTs can be improved significantly by impregnating Ni nanoparticles on MWCNTs [109]. The improved hydrogen storage capacity was accredited to the effective dissociation of hydrogen molecules in the gas phase by Ni catalysts, supplying atomic hydrogen promising for adsorbing on the walls of MWCNTs. Hydrogen desorption measurements revealed ~2.8 wt % hydrogen storage into MWCNTs in the temperature range of 340–520 K. Seenithurai *et al.* performed a theoretical analysis of Al-decorated SWCNT for possible hydrogen storage applications by Density Functional Theory [110]. The investigation revealed that the Al decoration on the CNT's wall significantly increased the gravimetric hydrogen storage capacity up to 6.15 wt% since Al atoms adsorbed H_2 molecules by polarizing them. The improved hydrogen storage capacity was accredited to the enhanced

interaction between the CNT and aluminum caused by the enhanced charge transfer from the aluminum to the CNT.

2.5.6 Other applications

Carbon nanotube yarns can convert mechanical energy into electrical energy from torsional and tensile motion. It has been reported that these CNT yarn harvesters can be used in the ocean to harvest wave energy on a large scale and combined with artificial muscles to generate electrical energy from a temperature gradient [111]. The CNTs have potential applications on scanning probe instruments because of their small dimension, high electrical conductivity, high tensile strength, and flexibility. The CNTs have exhibited an improved resolution when used as the tips of an atomic force microscope or scanning tunneling microscope [112, 113]. The CNTs and their derivatives have shown excellent biocompatibility and emerged as a new alternative and efficient tool for transporting remedial drug molecules [114, 115]. The key to drug delivery applications is that CNTs can be functionalized with protein or drug molecules, and the bio-composite can be delivered to cells and organs. Furthermore, because of CNT's extremely high tensile strength, high Young's modulus, large aspect ratio, low density, chemical stability, and high thermal and electrical conductivity, CNTs-based composites have shown potential applications for various structural applications [116]. In short, the excellent properties of CNTs have facilitated their applications in various fields, which will be crucial in nanotechnology.

References

[1] Zhang F., Hou P.X., Liu C. and Cheng H.M., Epitaxial growth of single-wall carbon nanotubes. *Carbon* **2016,** 102, 181.

[2] Dresselhaus M.S. and Eklund P.C., Phonons in carbon nanotubes. *Advances in physics* **2000,** 49 (6), 705.

[3] Poncharal P., Berger C., Yi Y., Wang Z. and de Heer W.A., Room temperature ballistic conduction in carbon nanotubes. *Journal of Physical Chemistry B* **2002,** 106, 12104.

[4] Iijima S., Helical microtubules of graphitic carbon. *Nature* **1991,** 354 (6348), 56.

[5] Ahmad M. and Silva S.R.P., Low Temperature Growth of Carbon Nanotubes–A Review. *Carbon* **2019,** 158, 24.

[6] Iijima S. and Ichihashi T., Single-shell carbon nanotubes of 1-nm diameter. *nature* **1993,** 363 (6430), 603.

[7] Ebbesen T. and Ajayan P., Large-scale synthesis of carbon nanotubes. *Nature* **1992,** 358 (6383), 220.

[8] Journet C., Maser W., Bernier P., Loiseau A., de La Chapelle M.L., Lefrant d.S., Deniard P., Lee R. and Fischer J., Large-scale production of single-walled carbon nanotubes by the electric-arc technique. *nature* **1997,** 388 (6644), 756.

[9] Thess A., Lee R., Nikolaev P., Dai H., Petit P., Robert J., Xu C., Lee Y.H., Kim S.G. and Rinzler A.G., Crystalline ropes of metallic carbon nanotubes. *Science* **1996,** 273 (5274), 483.

[10] Chen C., Chen W. and Zhang Y., Synthesis of carbon nano-tubes by pulsed laser ablation at normal pressure in metal nano-sol. *Physica E: Low-dimensional Systems and Nanostructures* **2005,** 28 (2), 121.

[11] Li J., Papadopoulos C., Xu J. and Moskovits M., Highly-ordered carbon nanotube arrays for electronics applications. *Applied physics letters* **1999,** 75 (3), 367.

[12] Cassell A.M., Raymakers J.A., Kong J. and Dai H., Large scale CVD synthesis of single-walled carbon nanotubes. *The Journal of Physical Chemistry B* **1999,** 103 (31), 6484.

[13] Kukovitsky E., L'vov S., Sainov N., Shustov V. and Chernozatonskii L., Correlation between metal catalyst particle size and carbon nanotube growth. *Chemical Physics Letters* **2002,** 355 (5-6), 497.

[14] Li W., Xie S., Qian L.X., Chang B., Zou B., Zhou W., Zhao R. and Wang G., Large-scale synthesis of aligned carbon nanotubes. *Science* **1996,** 274 (5293), 1701.

[15] Jung M., Eun K.Y., Lee J.-K., Baik Y.-J., Lee K.-R. and Park J.W., Growth of carbon nanotubes by chemical vapor deposition. *Diamond and Related Materials* **2001,** 10 (3-7), 1235.

[16] Joselevich E. and Lieber C.M., Vectorial growth of metallic and semiconducting single-wall carbon nanotubes. *Nano Letters* **2002,** 2 (10), 1137.

[17] Huang S., Cai X. and Liu J., Growth of millimeter-long and horizontally aligned single-walled carbon nanotubes on flat substrates. *Journal of the American Chemical Society* **2003,** 125 (19), 5636.

[18] Jin Z., Chu H., Wang J., Hong J., Tan W. and Li Y., Ultralow feeding gas flow guiding growth of large-scale horizontally aligned single-walled carbon nanotube arrays. *Nano letters* **2007,** 7 (7), 2073.

[19] Kocabas C., Hur S.H., Gaur A., Meitl M.A., Shim M. and Rogers J.A., Guided growth of large-scale, horizontally aligned arrays of single-walled carbon nanotubes and their use in thin-film transistors. *small* **2005,** 1 (11), 1110.

[20] Baro M., Gogoi D., Pal A.R., Adhikary N.C., Bailung H. and Chutia J., Pulsed PECVD for Low-temperature Growth of Vertically Aligned Carbon Nanotubes. *Chemical Vapor Deposition* **2014,** 20 (4-5-6), 161.

[21] Bo Z., Yang Y., Chen J., Yu K., Yan J. and Cen K., Plasma-enhanced chemical vapor deposition synthesis of vertically oriented graphene nanosheets. *Nanoscale* **2013,** 5 (12), 5180.

[22] Ren Z.F., Huang Z.P., Xu J.W., Wang J.H., Bush P., Siegal M.P. and Provencio P.N., Synthesis of large arrays of well aligned carbon nanotubes on glass. *Science* **1998,** 282 (5391), 1105.

[23] Chhowalla M., Teo K.B.K., Ducati C., Rupesinghe N.L., Amaratunga G.A.J., Ferrari A.C., Roy D., Robertson J. and Milne W.I., Growth process conditions of vertically aligned carbon nanotubes using plasma enhanced chemical vapor deposition. *Journal of Applied Physics* **2001,** 90 (10), 5308.

[24] Bell M.S., Teo K.B.K., Lacerda R.G., Milne W.I., Hash D.B. and Meyyappan M., Carbon nanotubes by plasma-enhanced chemical vapor deposition. *Pure and Applied Chemistry* **2006,** 78 (6), 1117.

[25] Park D., Hoon Kim Y. and Kee Lee J., Synthesis of carbon nanotubes on metallic substrates by a sequential combination of PECVD and thermal CVD. *Carbon* **2003,** 41 (5), 1025.

[26] Neupane S., Lastres M., Chiarella M., Li W., Su Q. and Du G., Synthesis and field emission properties of vertically aligned carbon nanotube arrays on copper. *Carbon* **2012,** 50 (7), 2641.

[27] Chen G., Neupane S., Li W., Chen L. and Zhang J., An increase in the field emission from vertically aligned multiwalled carbon nanotubes caused by NH3 plasma treatment. *Carbon* **2013,** 52, 468.

[28] Lin C.L., Chen C.F. and Shi S.C., Field emission properties of aligned carbon nanotubes grown on stainless steel using CH4/CO2 reactant gas. *Diamond and Related Materials* **2004,** 13 (4-8), 1026.

[29] Thapa A., Guo J., Jungjohann K.L., Wang X. and Li W., Density control of vertically aligned carbon nanotubes and its effect on field emission properties. *Materials Today Communications* **2020,** 22, 100761.

[30] Wang N. and Yao B.D., Nucleation and growth of well-aligned, uniform-sized carbon nanotubes by microwave plasma chemical vapor depositon. *Applied Physics Letters* **2001,** 78 (25), 4028.

[31] Park D K.Y., Lee J. , Pretreatment of stainless steel substrate surface for the growth of carbon nanotubes by PECVD. *J Mater Sci* **2003,** 38, 4933–9.

[32] Okuyama H., Iwata N. and Yamamoto H., Growth of Vertically Aligned Carbon Nanotubes Depending on Thickness of Catalyst Films by Plasma-Enhanced Chemical Vapor Deposition. *Molecular Crystals and Liquid Crystals* **2007,** 472 (1), 209.

[33] Vander Wal R.L., Ticich T.M. and Curtis V.E., Diffusion flame synthesis of single-walled carbon nanotubes. *Chemical Physics Letters* **2000,** 323 (3-4), 217.

[34] Yuan L., Saito K., Hu W. and Chen Z., Ethylene flame synthesis of well-aligned multi-walled carbon nanotubes. *Chemical physics letters* **2001,** 346 (1-2), 23.

[35] Xu F., Liu X. and Stephen D.T., Synthesis of carbon nanotubes on metal alloy substrates with voltage bias in methane inverse diffusion flames. *Carbon* **2006,** 44 (3), 570.

[36] Matveev A.T., Golberg D., Novikov V., Klimkovich L. and Bando Y., Synthesis of carbon nanotubes below room temperature. *Carbon* **2001,** 39 (1), 155.

[37] Esconjauregui S., Whelan C.M. and Maex K., The reasons why metals catalyze the nucleation and growth of carbon nanotubes and other carbon nanomorphologies. *Carbon* **2009,** 47 (3), 659.

[38] Kumar M. and Ando Y., Chemical vapor deposition of carbon nanotubes: a review on growth mechanism and mass production. *Journal of nanoscience and nanotechnology* **2010,** 10 (6), 3739.

[39] Meyyappan M.D., L.; Cassell, A. and Has, D., Carbon nanotube growth by PECVD: a review. *Plasma Sources Science and Technology* **2003,** 12, 205.

[40] Frank S., Poncharal P., Wang Z. and De Heer W.A., Carbon nanotube quantum resistors. *Science* **1998,** 280 (5370), 1744.

[41] Langer L., Stockman L., Heremans J., Bayot V., Olk C., Van Haesendonck C., Bruynseraede Y. and Issi J.-P., Electrical resistance of a carbon nanotube bundle. *Journal of Materials Research* **1994,** 9 (4), 927.

[42] Langer L., Bayot V., Grivei E., Issi J.-P., Heremans J., Olk C., Stockman L., Van Haesendonck C. and Bruynseraede Y., Quantum transport in a multiwalled carbon nanotube. *Physical review letters* **1996,** 76 (3), 479.

[43] Rinzler A., Hafner J., Nikolaev P., Nordlander P., Colbert D., Smalley R., Lou L., Kim S. and Tománek D., Unraveling nanotubes: field emission from an atomic wire. *Science* **1995,** 269 (5230), 1550.

[44] De Heer W.A., Chatelain A. and Ugarte D., A carbon nanotube field-emission electron source. *science* **1995,** 270 (5239), 1179.

[45] Bonard J.M., Weiss N., Kind H., Stöckli T., Forró, Lμszló and Kern K.C.t., Andre, Tuning the Field Emission Properties of Patterned Carbon Nanotube Films. *Avanced Materials* **2001,** 13 (3), 184.

[46] Bonard J.-M., Kind H., Stöckli T. and Nilsson L.-O., Field emission from carbon nanotubes: the first five years. *Solid-State Electronics* **2001,** 45 (6), 893.

[47] Bonard J.M., Croci M., Klinke C., Kurt R., Noury O. and Weiss N., Carbon nanotube films as electron field emitters. *Carbon* **2002,** 40 (10), 1715.

[48] Pandey A., Prasad A., Moscatello J., Ulmen B. and Yap Y.K., Enhanced field emission stability and density produced by conical bundles of catalyst-free carbon nanotubes. *Carbon* **2010,** 48 (1), 287.

[49] Nilsson L., Groening O., Emmenegger C., Kuettel O., Schaller E., Schlapbach L., Kind H., Bonard J. and Kern K., Scanning field emission from patterned carbon nanotube films. *Applied Physics Letters* **2000,** 76 (15), 2071.

[50] Wang K.-Y., Liao C.-Y. and Cheng H.-C., Field-Emission Characteristics of the Densified Carbon Nanotube Pillars Array. *ECS Journal of Solid State Science and Technology* **2016,** 5 (9), 99.

[51] Li Z., Yang X., He F., Bai B., Zhou H., Li C. and Dai Q., High current field emission from individual non-linear resistor ballasted carbon nanotube cluster array. *Carbon* **2015,** 89, 1.

[52] Silan J.L., Niemann D.L., Ribaya B.P., Rahman M., Meyyappan M. and Nguyen C.V., Carbon nanotube pillar arrays for achieving high emission current densities. *Applied Physics Letters* **2009,** 95 (13), 133111.

[53] Hazra K.S., Rai P., Mohapatra D.R., Kulshrestha N., Bajpai R., Roy S. and Misra D., Dramatic enhancement of the emission current density from carbon nanotube based nanosize tips with extremely low onset fields. *ACS nano* **2009,** 3 (9), 2617.

[54] Li X., Niu J., Zhang J., Li H. and Liu Z., Labeling the Defects of Single-Walled Carbon Nanotubes Using Titanium Dioxide Nanoparticles. *J. Phys. Chem. B* **2003,** 107, 2453.

[55] Green J.M., Dong L., Gutu T., Jiao J., Conley J.F. and Ono Y., ZnO-nanoparticle-coated carbon nanotubes demonstrating enhanced electron field-emission properties. *Journal of Applied Physics* **2006,** 99 (9), 094308.

[56] Chen C.A., Lee K.Y., Chen Y.M., Chi J.G., Lin S.S. and Huang Y.S., Field emission properties of RuO2 thin film coated on carbon nanotubes. *Vacuum* **2010,** 84 (12), 1427.

[57] Chakrabarti S., Pan L., Tanaka H., Hokushin S. and Nakayama Y., Stable field emission property of patterned MgO coated carbon nanotube arrays. *Japanese Journal of Applied Physics* **2007,** 46 (7R), 4364.

[58] Sridhar S., Tiwary C., Vinod S., Taha-Tijerina J.J., Sridhar S., Kalaga K., Sirota B., Hart A.H.C., Ozden S., Sinha R.K., Harsh, Vajtai R., Choi W., Kordas K. and Ajayan P.M., Field Emission with Ultralow Turn On Voltage from Metal Decorated Carbon Nanotubes. *ACS Nano* **2014,** 8 (8), 7763.

[59] Hone J., Batlogg B., Benes Z., Johnson A. and Fischer J., Quantized phonon spectrum of single-wall carbon nanotubes. *Science* **2000,** 289 (5485), 1730.

[60] Yi W., Lu L., Dian-Lin Z., Pan Z. and Xie S., Linear specific heat of carbon nanotubes. *Physical Review B* **1999,** 59 (14), 9015.

[61] Lasjaunias J.-C., Biljaković K., Benes Z., Fischer J. and Monceau P., Low-temperature specific heat of single-wall carbon nanotubes. *Physical Review B* **2002,** 65 (11), 113409.

[62] Kim P., Shi L., Majumdar A. and McEuen P.L., Thermal transport measurements of individual multiwalled nanotubes. *Physical review letters* **2001,** 87 (21), 215502.

[63] Ruoff R.S., Qian D. and Liu W.K., Mechanical properties of carbon nanotubes: theoretical predictions and experimental measurements. *Comptes Rendus Physique* **2003,** 4 (9), 993.

[64] Treacy M.J., Ebbesen T.W. and Gibson J.M., Exceptionally high Young's modulus observed for individual carbon nanotubes. *nature* **1996,** 381 (6584), 678.

[65] Wong E.W., Sheehan P.E. and Lieber C.M., Nanobeam mechanics: elasticity, strength, and toughness of nanorods and nanotubes. *science* **1997,** 277 (5334), 1971.

[66] Hernandez E., Goze C., Bernier P. and Rubio A., Elastic properties of C and B x C y N z composite nanotubes. *Physical Review Letters* **1998,** 80 (20), 4502.

[67] Gao G., Cagin T. and Goddard III W.A., Energetics, structure, mechanical and vibrational properties of single-walled carbon nanotubes. *Nanotechnology* **1998,** 9 (3), 184.

[68] Yu M.-F., Files B.S., Arepalli S. and Ruoff R.S., Tensile loading of ropes of single wall carbon nanotubes and their mechanical properties. *Physical review letters* **2000,** 84 (24), 5552.

[69] Li F., Cheng H., Bai S., Su G. and Dresselhaus M., Tensile strength of single-walled carbon nanotubes directly measured from their macroscopic ropes. *Applied physics letters* **2000,** 77 (20), 3161.

[70] Yu M.-F., Lourie O., Dyer M.J., Moloni K., Kelly T.F. and Ruoff R.S., Strength and breaking mechanism of multiwalled carbon nanotubes under tensile load. *Science* **2000,** 287 (5453), 637.

[71] Wang R., Xie L., Hameed S., Wang C. and Ying Y., Mechanisms and applications of carbon nanotubes in terahertz devices: A review. *Carbon* **2018,** 132, 42.

[72] Wang Q., Setlur A., Lauerhaas J., Dai J., Seelig E. and Chang R.P., A nanotube-based field-emission flat panel display. *Applied Physics Letters* **1998,** 72 (22), 2912.

[73] Lee N.S., Chung D.S., Han I.T., Kang J.H., Choi Y.S., Kim H.Y., Park S.H., Jin Y.W., Yi W.K. and Yun M.J., Application of carbon nanotubes to field emission displays. *Diamond and related materials* **2001,** 10 (2), 265.

[74] Nakayama Y. and Akita S., Field-emission device with carbon nanotubes for a flat panel display. *Synthetic Metals* **2001,** 117 (1-3), 207.

[75] Guo P., Chen T., Chen Y., Zhang Z., Feng T., Wang L., Lin L., Sun Z. and Zheng Z., Fabrication of field emission display prototype utilizing printed carbon nanotubes/nanofibers emitters. *Solid-state electronics* **2008,** 52 (6), 877.

[76] Lee J., Jung Y., Song J., Kim J.S., Lee G.-W., Jeong H.J. and Jeong Y., High-performance field emission from a carbon nanotube carpet. *Carbon* **2012,** 50 (10), 3889.

[77] Zeng F.-g., Zhu C.-c., Liu W. and Liu X., The fabrication and operation of fully printed carbon nanotube field emission displays. *Microelectronics journal* **2006,** 37 (6), 495.

[78] Choi W.B., Jin Y.W., Kim H.Y., Lee S.J., Yun M.J., Kang J.H., Choi Y.S., Park N.S., Lee N.S. and Kim J.M., Electrophoresis deposition of carbon nanotubes for triode-type field emission display. *Applied Physics Letters* **2001,** 78 (11), 1547.

[79] Liu X.M., Huang Z.D., Oh S.W., Zhang B., Ma P.C., Yuen M.M. and Kim J.K., Carbon nanotube (CNT)-based composites as electrode material for rechargeable Li-ion batteries: a review. *Composites Science and Technology* **2012,** 72 (2), 121.

[80] Landi B.J., Ganter M.J., Cress C.D., DiLeo R.A. and Raffaelle R.P., Carbon nanotubes for lithium ion batteries. *Energy & Environmental Science* **2009,** 2 (6), 638.

[81] Zhao J., Buldum A., Han J. and Lu J.P., First-principles study of Li-intercalated carbon nanotube ropes. *Physical review letters* **2000,** 85 (8), 1706.

[82] Xu G.L., Wang Q., Fang J.C., Xu Y.F., Li J.T., Huang L. and Sun S.G., Tuning the structure and property of nanostructured cathode materials of lithium ion and lithium sulfur batteries. *Journal of Materials Chemistry A* **2014,** 2 (47), 19941.

[83] Yang S., Huo J., Song H. and Chen X., A comparative study of electrochemical properties of two kinds of carbon nanotubes as anode materials for lithium ion batteries. *Electrochimica Acta* **2008,** 53 (5), 2238.

[84] Lu W., Goering A., Qu L. and Dai L., Lithium-ion batteries based on vertically-aligned carbon nanotube electrodes and ionic liquid electrolytes. *Physical Chemistry Chemical Physics* **2012,** 14 (35), 12099.

[85] Park G.D., Choi J.H., Jung D.S., Park J.-S. and Kang Y.C., Three-dimensional porous pitch-derived carbon coated Si nanoparticles-CNT composite microsphere with superior electrochemical performance for lithium ion batteries. *Journal of Alloys and Compounds* **2020,** 821, 153224.

[86] Gao C., Kim N.D., Salvatierra R.V., Lee S.-K., Li L., Li Y., Sha J., Silva G.A.L., Fei H. and Xie E., Germanium on seamless graphene carbon nanotube hybrids for lithium ion anodes. *Carbon* **2017,** 123, 433.

[87] Noerochim L., Wang J.Z., Chou S.L., Wexler D. and Liu H.K., Free-standing single-walled carbon nanotube/SnO2 anode paper for flexible lithium-ion batteries. *Carbon* **2012,** 50 (3), 1289.

[88] Li Q., Sheng J., Wei Q., An Q., Wei X., Zhang P. and Mai L., A unique hollow Li 3 VO 4/carbon nanotube composite anode for high rate long-life lithium-ion batteries. *Nanoscale* **2014,** 6 (19), 11072.

[89] Niu C., Sichel E.K., Hoch R., Moy D. and Tennent H., High power electrochemical capacitors based on carbon nanotube electrodes. *Applied Physics Letters* **1997,** 70 (11), 1480.

[90] An K.H., Kim W.S., Park Y.S., Choi Y.C., Lee S.M., Chung D.C., Bae D.J., Lim S.C. and Lee Y.H., Supercapacitors using single-walled carbon nanotube electrodes. *Advanced Materials* **2001,** 13 (7), 497.

[91] An K.H., Kim W.S., Park Y.S., Moon J.M., Bae D.J., Lim S.C., Lee Y.S. and Lee Y.H., Electrochemical properties of high-power supercapacitors using single-walled carbon nanotube electrodes. *Advanced functional materials* **2001,** 11 (5), 387.

[92] Cheng Y., Lu S., Zhang H., Varanasi C.V. and Liu J., Synergistic effects from graphene and carbon nanotubes enable flexible and robust electrodes for high-performance supercapacitors. *Nano letters* **2012,** 12 (8), 4206.

[93] Wang Y., Fugetsu B., Wang Z., Gong W., Sakata I., Morimoto S., Hashimoto Y., Endo M., Dresselhaus M. and Terrones M., Nitrogen-doped porous carbon monoliths from polyacrylonitrile (PAN) and carbon nanotubes as electrodes for supercapacitors. *Scientific reports* **2017,** 7, 40259.

[94] Trigueiro J.P.C., Lavall R.L. and Silva G.G., Nanocomposites of graphene nanosheets/multiwalled carbon nanotubes as electrodes for in-plane supercapacitors. *Electrochimica Acta* **2016,** 187, 312.

[95] Yi H., Wang H., Jing Y., Peng T. and Wang X., Asymmetric supercapacitors based on carbon nanotubes@ NiO ultrathin nanosheets core-shell composites and MOF-derived porous carbon polyhedrons with super-long cycle life. *Journal of Power Sources* **2015,** 285, 281.

[96] Lee K.S., Lee W.J., Park N.-G., Kim S.O. and Park J.H., Transferred vertically aligned N-doped carbon nanotube arrays: use in dye-sensitized solar cells as counter electrodes. *Chemical communications* **2011,** 47 (14), 4264.

[97] Dang X., Yi H., Ham M.-H., Qi J., Yun D.S., Ladewski R., Strano M.S., Hammond P.T. and Belcher A.M., Virus-templated self-assembled single-walled carbon nanotubes for highly efficient electron collection in photovoltaic devices. *Nature Nanotechnology* **2011,** 6 (6), 377.

[98] Yue G., Wu J., Lin J.-Y., Xiao Y., Tai S.-Y., Lin J., Huang M. and Lan Z., A counter electrode of multi-wall carbon nanotubes decorated with tungsten sulfide used in dye-sensitized solar cells. *Carbon* **2013,** 55, 1.

[99] Li S., Luo Y., Lv W., Yu W., Wu S., Hou P., Yang Q., Meng Q., Liu C. and Cheng H.M., Vertically Aligned Carbon Nanotubes Grown on Graphene Paper as Electrodes in Lithium-Ion Batteries and Dye-Sensitized Solar Cells. *Advanced Energy Materials* **2011,** 1 (4), 486.

[100] Sayago I., Terrado E., Lafuente E., Horrillo M.C., Maser W.K., Benito A.M., Navarro R., Urriolabeitia E.P., Martinez M.T. and Gutierrez J., Hydrogen sensors based on carbon nanotubes thin films. *Synthetic Metals* **2005,** 148 (1), 15.

[101] Star A., Joshi V., Skarupo S., Thomas D. and Gabriel J.-C.P., Gas sensor array based on metal-decorated carbon nanotubes. *The Journal of Physical Chemistry B* **2006,** 110 (42), 21014.

[102] Lee H., Shaker G., Naishadham K., Song X., McKinley M., Wagner B. and Tentzeris M., Carbon-nanotube loaded antenna-based ammonia gas sensor. *IEEE Transactions on Microwave Theory and Techniques* **2011,** 59 (10), 2665.

[103] Šljukić B., Banks C.E. and Compton R.G., Iron oxide particles are the active sites for hydrogen peroxide sensing at multiwalled carbon nanotube modified electrodes. *Nano letters* **2006,** 6 (7), 1556.

[104] Tang X., Bansaruntip S., Nakayama N., Yenilmez E., Chang Y.-l. and Wang Q., Carbon nanotube DNA sensor and sensing mechanism. *Nano letters* **2006,** 6 (8), 1632.

[105] Ye J.-S., Wen Y., De Zhang W., Gan L.M., Xu G.Q. and Sheu F.-S., Nonenzymatic glucose detection using multi-walled carbon nanotube electrodes. *Electrochemistry Communications* **2004,** 6 (1), 66.

[106] Landry M.P., Ando H., Chen A.Y., Cao J., Kottadiel V.I., Chio L., Yang D., Dong J., Lu T.K. and Strano M.S., Single-molecule detection of protein efflux from microorganisms using fluorescent single-walled carbon nanotube sensor arrays. *Nature nanotechnology* **2017,** 12 (4), 368.

[107] Dillon A.C., Gennett T., Alleman J., Jones K., Parilla P. and Heben M., Carbon nanotube materials for hydrogen storage. *Proc. 2000 DOE/NREL Hydrogen program review* **2000,** 8.

[108] Shiraishi M., Takenobu T., Yamada A., Ata M. and Kataura H., Hydrogen storage in single-walled carbon nanotube bundles and peapods. *Chemical physics letters* **2002,** 358 (3-4), 213.

[109] Kim H.S., Lee H., Han K.S., Kim J.H., Song M.S., Park M.S., Lee J.Y. and Kang J.K., Hydrogen storage in Ni nanoparticle-dispersed multiwalled carbon nanotubes. *The Journal of Physical Chemistry B* **2005,** 109 (18), 8983.

[110] Seenithurai S., Pandyan R.K., Kumar S.V., Saranya C. and Mahendran M., Al-decorated carbon nanotube as the molecular hydrogen storage medium. *International journal of hydrogen energy* **2014,** 39 (23), 11990.

[111] Kim S.H., Haines C.S., Li N., Kim K.J., Mun T.J., Choi C., Di J., Oh Y.J., Oviedo J.P., Bykova J., Fang S., Jiang N., Liu Z., Wang R., Kumar P., Qiao R., Priya S., Cho K.,

Kim M., Lucas M.S., Drummy L.F., Maruyama B., Lee D.Y., Lepro X., Gao E., Albarq D., Ovalle-Robles R., Kim S.J. and Baughman R.H., Harvesting electrical energy from carbon nanotube yarn twist. *Science* **2017,** 357 (6353), 773.

[112] Dai H., Hafner J.H., Rinzler A.G., Colbert D.T. and Smalley R.E., Nanotubes as nanoprobes in scanning probe microscopy. *Nature* **1996,** 384 (6605), 147.

[113] Hafner J.H., Cheung C.L. and Lieber C.M., Direct growth of single-walled carbon nanotube scanning probe microscopy tips. *Journal of the American Chemical Society* **1999,** 121 (41), 9750.

[114] Bianco A., Kostarelos K. and Prato M., Applications of carbon nanotubes in drug delivery. *Current opinion in chemical biology* **2005,** 9 (6), 674.

[115] Hilder T.A. and Hill J.M., Carbon nanotubes as drug delivery nanocapsules. *Current Applied Physics* **2008,** 8 (3-4), 258.

[116] Zhang X., Li Q., Tu Y., Li Y., Coulter J.Y., Zheng L., Zhao Y., Jia Q., Peterson D.E. and Zhu Y., Strong carbon-nanotube fibers spun from long carbon-nanotube arrays. *small* **2007,** 3 (2), 244.

CHAPTER 3

Experimental procedure and characterization technique

Chapter 3 presents the detailed description of the techniques used for synthesis, characterization, and properties measurement of the materials in the dissertation work.

3.1 Substrate preparation

3.1.1 Substrate for dense arrays of vertically aligned CNTs

Vertically aligned CNT (VACNT) arrays growth experiments were performed on stainless steel (SS 304 type, Fe 72, Cr 18, Ni 8, Mn 2 wt.%) and copper (Cu 99.95 wt.%). The as-received metal sheets were cut into slabs of dimension 1 cm × 1 cm × 0.63 mm or circular disks of diameter and thickness of ~1.5 cm and 0.60 mm, respectively. Then substrates were polished with different sandpapers (Norton 120, 1200, 2400, and 4000 grits successively) to a smooth finish. Furthermore, free-standing, binder-free VACNT anodes for coin cell lithium-ion batteries were synthesized on nickel foam (Ni 99.99 wt.%). The as-received Ni foam was cut into circular disks of diameter and thickness of ~1 cm and 1.6 mm, respectively. Subsequently, metal substrates were cleaned ultrasonically with acetone and isopropyl alcohol (IPA) baths, each for 10 minutes to remove organic/inorganic contaminants. Then, varied synthesis parameter tests were performed in a plasma-enhanced chemical vapor deposition (PECVD) system, as described in section 3.2.1.

3.1.2 Substrate for morphology-controlled arrays of vertically aligned CNTs

Figure 3.1 shows a schematic of the nanosphere lithography (NSL) procedure using polystyrene (PS) spheres for the selective synthesis of VACNT pillars or individual self-

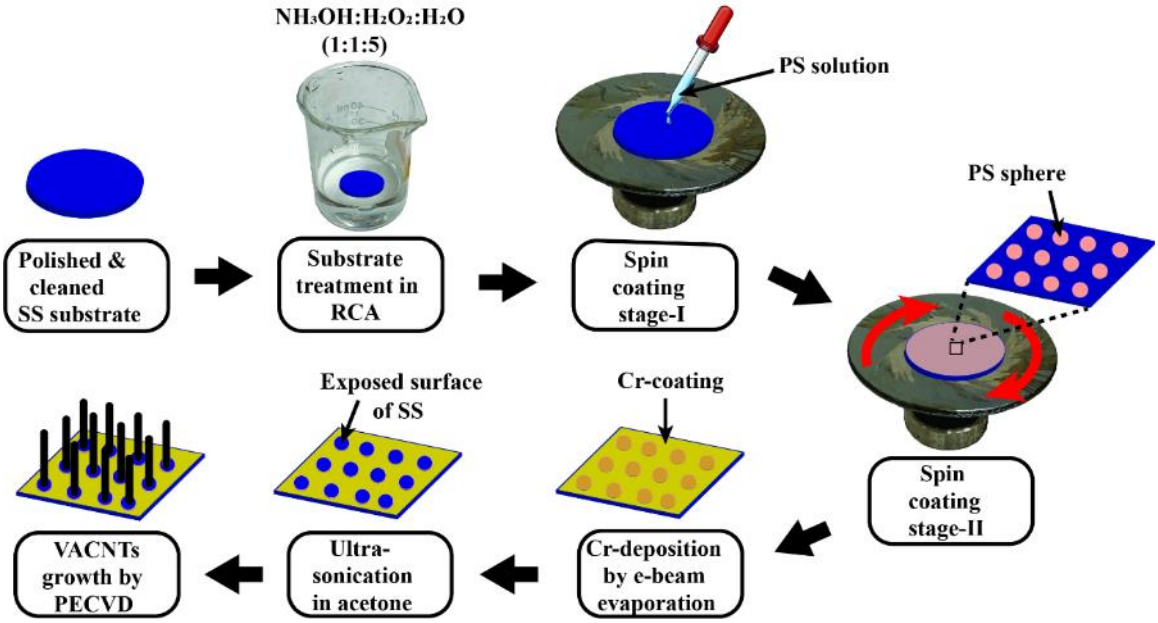

Figure 3.1. Schematic diagram showing the stepwise process of the NSL using polystyrene (PS) spheres to create optimum spaces on the Cr-coated SS surface before growing individual/pillar VACNTs on them.

standing VACNT array on the bulk catalytic metal substrate. A brief description of the NSL procedure is as follows. As-received SS sheet with a thickness of 0.6 mm was cut into circular disks of diameter ~1.5 cm. They were sequentially polished with sandpapers (Norton 120, 600, 800, 1200, 2400, and 4000 grits) to a smooth, shiny finish followed by a 10 minutes ultrasonication in acetone and IPA bath, respectively. The clean SS disks were treated with RCA solution ($NH_4OH:H_2O_2:H_2O$ in the ratio 1:1:5) for 30 seconds to make their surface hydrophilic.

The PS sphere solutions were prepared by mixing commercially available PS sphere suspensions (5% w/v, Spherotech Inc.) with spheres of sizes (nominal diameter) 110, 200, 450, 950, and 1500 nm with IPA at a volume ratio of 1:20, 1:15, 1:10, 1:4, and 1:2, respectively. The different PS solution concentrations were used to achieve a uniform distribution of individual spheres on the substrate without forming clusters of the PS

spheres and maintaining the number density of VACNT emitters constant for different samples. A drop of the PS sphere solution about 30 µL was cast on the substrate surface, followed by a spin coating process at 2000 rpm for 35 seconds. Chromium (Cr) layer (CNT inhibitor layer) of different thicknesses, such as 15, 50, 150, and 300 nm, were deposited on the substrate surfaces patterned with PS spheres of sizes 110, 200, 450, 950, and 1500 nm, respectively using the e-beam evaporation method. Finally, the Cr-coated substrates were ultrasonicated in an acetone bath for 3 minutes to remove the PS spheres and obtain open circular areas on the SS substrate. Figure 3.2(a) shows a scanning electron micrograph of the SS substrate after the dispersion of PS spheres of diameter 200 nm. Figure 3.2(b) represents the Cr-coated (50 nm) SS surface after removing PS spheres by ultrasonication in an acetone bath.

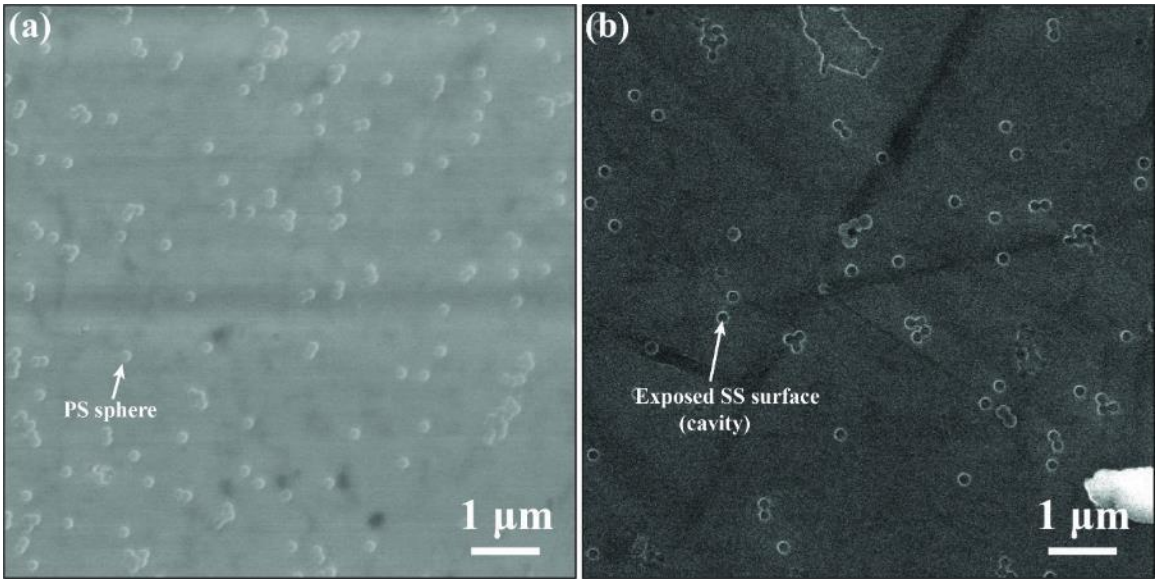

Figure 3.2. Scanning electron micrographs of the Cr-coated SS surface (a) before and (b) after the removal of PS spheres of diameter 200 nm. The removal of PS spheres results in the small circular cavities to expose the native surface of the SS, which are the potential sites for the growth of VACNTs.

3.2 Material synthesis techniques

3.2.1 Plasma-enhanced chemical vapor deposition

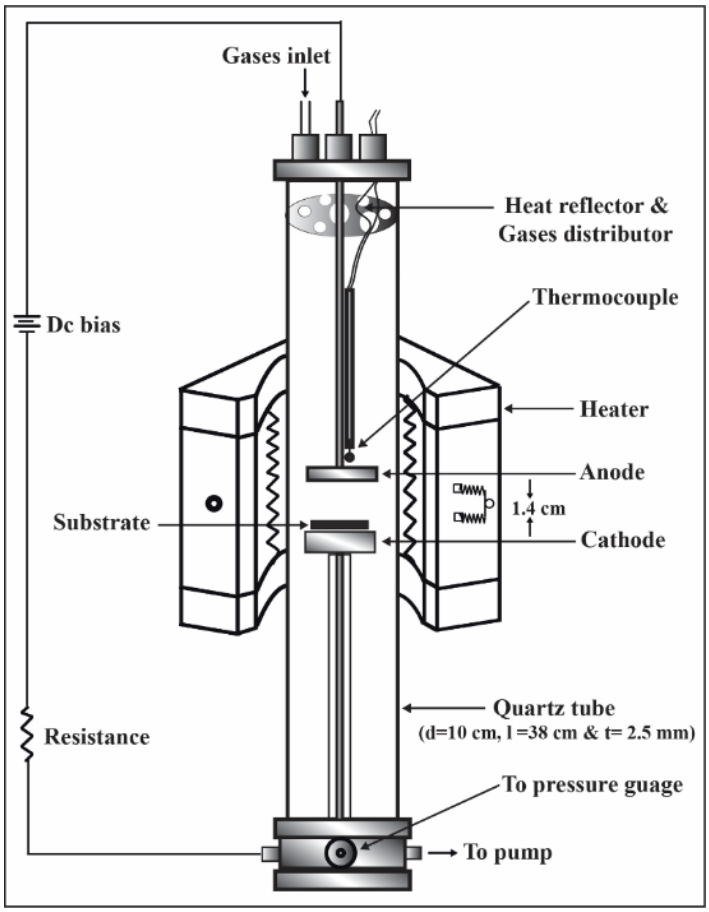

Figure 3.3. Schematic diagram of the PECVD system used to synthesize VACNT arrays.

Vertically aligned CNT arrays were synthesized by using an in-house designed plasma-enhanced chemical vapor deposition (PECVD) system, as shown in the schematic diagram of Figure 3.3. It consists of a quartz tube of diameter 10 cm and length 43 cm wrapped around by an infrared heater (RHL-P65CP, ULVAC-RICO, INC.) to concentrate heat onto the substrate. A solid cylindrical copper rod (diameter = 25.5 mm and height = 17.8 mm) was used as the sample (substrate) holder and a cathode, on which a negative bias was applied to generate plasma. The gas inlet and outlet lines were present at the two

closed ends of the quartz tube for the carbon source and carrier gases. These lines could be pumped down if necessary.

The VACNT growth parameters were optimized according to the results of previously published literature [1, 2]. A brief description of the VACNT growth procedure is as follows. The cleaned metal substrates were placed on top of the sample holder and the reaction chamber was pumped down to 0.01 Torr (base pressure). Then ammonia gas (NH_3) as an etch and reduction gas was introduced at a flow rate of 400 or 600 standard cubic centimeters per minute (sccm). The substrates were heated to growth temperatures (Table 3.1) at a rate of 50 ºC/min under the NH_3 environment at a constant pressure of 7 Torr. It should be pointed out that during the temperature increase to the targeted temperatures, the substrates were simultaneously treated by the NH_3 gas, resulting in the change of the substrate surface structure. The surface treatment is not a separate process from the VACNT growth. Once the growth temperature reached the targeted value, DC plasma was turned on and adjusted to the desired powers (Table 3.1).

Acetylene (C_2H_2) as a carbon source was introduced immediately for VACNT growth as soon as the plasma became stable. The flow rate of C_2H_2 was kept constant at 15 or 25 sccm throughout the VACNTs growth time. The VACNTs were grown for different time durations, as indicated in Table 3.1, then allowed to cool down to about room temperature under the base pressure. To study the surface morphology just before introducing the carbon source (C_2H_2), two different SS substrates were prepared by heating to 760 °C at the rate of 50 °C/min under the NH_3 environment and Ar environment both at 400 sccm and 7 Torr. To study the surface morphology of Cu substrates before introducing

the C_2H_2, the substrates were prepared by heating to 650 °C, 700 °C, or 750 °C in the presence of the NH_3 (600 sccm) at the pressure of 7 Torr. Table 3.1 represents the typical synthesis parameters for synthesizing VACNTs on different metal substrates.

Table 3.1. Typical parameters for the growth of VACNTs on different metal substrates.

Substrate	Temperature (°C)	Time (min.)	Plasma (W)	Flow rate (sccm)	
				C_2H_2	NH_3
SS	650, 700, 760, 800	2, 5, 10, 15, 20	9, 40, 70, 92	15	400
Patterned SS	600	10	70	25	400
Cu	600, 650, 700, 750, 800	30	70	25	600
Ni-foam	600	7	70	25	400

3.2.2 Wet-chemical method

The VACNT arrays were coated with tin oxide (SnO_2) nanoparticles to study their electron field emission and electrochemical properties. A simple wet-chemical method similar to that reported by Han and Zettl [3] was used to synthesize SnO_2 nanoparticles on the external surface of the VACNTs to form core-shell (SnO_2-VACNTs) structured composite material. The as-synthesized VACNT array (not separated from the original substrate) was treated with nitric acid (HNO_3, 40%) at room temperature for two hours to clean the surface of nanotubes and to create the oxygen-containing functional groups on the VACNT wall. However, the acid treatment to the VACNT array synthesized on Ni-foam was performed in a weak HNO_3 (20%) for 15 min to protect the Ni fibers from dissolving into the acid. A solution was prepared at room temperature by mixing 1 g of tin (II) chloride ($SnCl_2$, 98%, anhydrous) in 80 mL of deionized water, and then 1.4 mL of hydrochloric acid (HCl, 38%) was added. Finally, the acid-treated VACNTs sample, first

rinsed with deionized water, was submerged into the solution for different coating periods. The solution was stirred by the gentle flow of air through the solution continuously to facilitate the coating process. Once the sample was coated for the desired time, it was taken out from the solution and dried at 95 °C for 15 min.

3.3 Examination techniques for structural characterization

3.3.1 Atomic force microscopy

Atomic force microscopy (AFM) is a powerful surface analysis technique for characterizing micro/nanostructures down to a sub-nanometer resolution. This flexible technique can be used in ambient air or liquid media to precisely scan the local features of the samples. The AFM scans the surface of a specimen by using a sharp tip of a size of ~10 to 20 nm attached to a cantilever. While scanning the surface, the tip moves in response to tip-surface interactions caused by the van der Waals forces [4]. This defection of the cantilever is projected to a photodiode with the help of a laser beam, which finally maps the surface features at nanoscopic precision. The AFM images the sample by touching the surface continuously with the tip (contact mode) or vibrating the cantilever above the sample surface such that the tip is only in intermittent contact with the surface (tapping mode) [5]. Many physical properties, including size, morphology, surface texture, and roughness of the samples before C_2H_2 introduction, were analyzed by the AFM in tapping mode (Veeco Multimode Nanoscope III D) with Si tip (spring constant = 42 N/m and resonance frequency = 250–300 kHz). Raw data were processed and analyzed using Nanoscope Control and Gwyddion software.

3.3.2 Focused ion beam method

Focused ion beam (FIB) is an extremely useful technique for scanning and cutting the substrate surface at the micro/nanoscale inside a vacuum chamber. The FIB uses highly focused ion beams such as Ga^+ beam to cut the specimen for sample preparation in electron microscopy. However, it can also be used to remove/deposit materials from/to a specific site of the sample surface for creating MEMS/NEMS devices [6]. During the FIB micromachining, chemical interactions and heating caused by the powerful ion beam can induce damages in the sample. So, removing neutral and ionized atoms from the substrate is essential for FIB application. It is also critical to cover the substrate surface with a metallic or carbon layer for protecting the surface damage caused by energetic ion beams [7, 8]. The surface evolution and chemical composition of the SS substrate induced by the heat treatment under the reducing environment before introducing hydrocarbon precursor gas were analyzed using dual-beam FIB (Ga+) system equipped with an energy dispersive

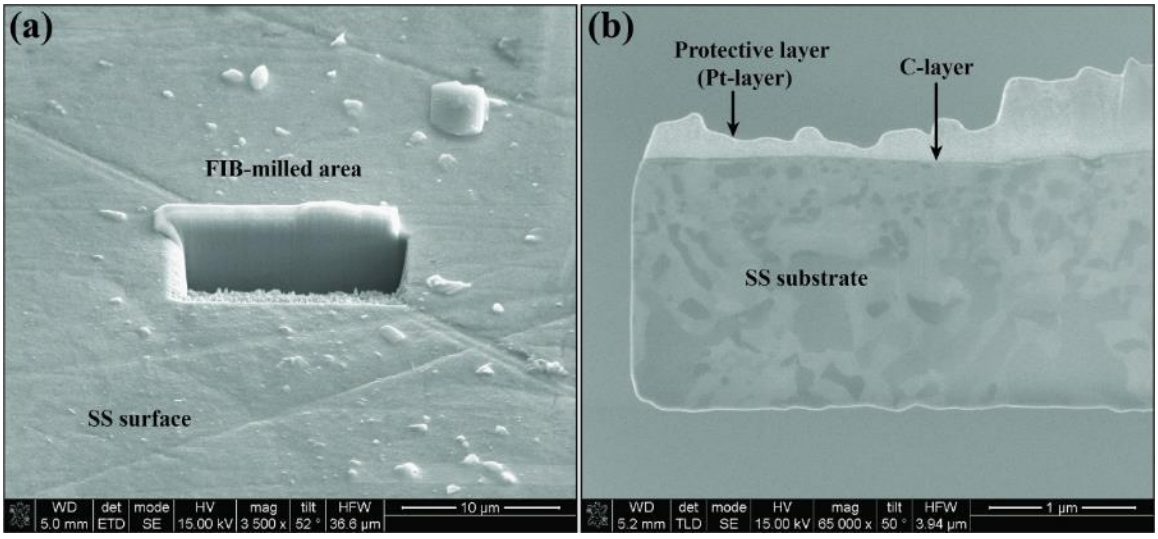

Figure 3.4. Sample preparation by FIB technique to study surface evolution and chemical composition of the SS substrate before introducing the carbon precursor gas. (a) Scanning electron micrograph showing the FIB-milled area. (b) Scanning electron micrograph of a cross-section of the SS substrate.

dispersive X-ray spectrometer (EDS) and scanning electron microscope. Figure 3.4(a-b) represent the scanning electron micrographs of the substrate surface after the FIB milling and the cross-sectional structure of the sample, coated with a platinum (Pt) layer to protect the surface features.

3.3.3 Scanning electron microscopy

Scanning electron microscopy (SEM) is a common technique used to study the texture, chemical composition, and orientation of materials composing the sample. The secondary electrons and back-scattered electrons, resulting from electron-sample interactions upon the introduction of high-energy electrons focused beam on the sample surface, generate the specimen's information in the form of two-dimensional images [9]. An SEM is regarded as a non-destructive method for probing the sample, so the same materials can be examined repeatedly if necessary. In my research, the surface morphology of the as-synthesized samples was examined by using a field emission Scanning Electron Microscope (SEM, JEOL JSM–6330F) operated at an accelerating voltage of 25 kV. The samples were directly glued to the sample holder using conducting (copper or carbon) tape to inspect through the SEM.

3.3.4 Transmission electron microscopy

Transmission electron microscopy (TEM) is an efficient technique for generating highly magnified atomic-scale resolution images in real space that uses a high-energy electron beam to visualize the sample. During the TEM operation, an electron beam strikes the sample, and an image is formed by using the information contained in the electron waves transmitted through the specimen [10]. The nano-structural analyses of samples

were carried out by using an FEI Tecnai F30 TEM operated at 300 kV equipped with an Energy Dispersive X-ray spectrometer (EDS). A Tecnai G^2 20 U-Twin high-resolution TEM with an acceleration voltage of 200 kV was used to acquire the images in the case of VACNTs synthesized on the Cu substrate. Crystal structure and chemical composition of samples were investigated through high-resolution TEM images (HRTEM), selected area diffraction (SAED) pattern, and EDS. The TEM sample preparation was performed on the as-synthesized VACNTs, by being scratched off the substrate using tweezers and then dispersed ultrasonically in IPA for 5 min and deposited on to the TEM grid. The TEM raw data were processed and analyzed using Gatan Microscopy Suite (GMS3) and ImageJ software.

3.3.5 X-ray diffraction analysis

X-ray diffraction (XRD) is a rapid and non-destructive technique used to identify phases of crystalline materials that determine the atomic and molecular structure. The XRD identifies the crystal structure on the basis of Bragg's diffraction pattern formation upon striking the crystalline sample by monochromatic X-rays. In the dissertation, the crystal structure of the Cu filled inside the VACNT and SnO_2 present in SnO_2-VACNTs core-shell structure was established via XRD experiments in Siemens Diffraktometer D5000 using Cu (Kα) radiation (λ = 1.54 Å) operated at 40 kV and 40 mA with the step size of 0.02° ranging from 20° to 80° at a speed of 0.5°/min. During the XRD experiment, the substrate with as-synthesized samples was placed directly on the sample stage and targeted with the X-ray beam. The crystal phases of Cu at the core of VACNTs and SnO_2 were identified by comparing them with the ICDD PDF standard database.

3.3.6 Raman spectroscopy

Raman spectroscopy is a useful non-destructive real-time material analysis technique that depends on the inelastic scattering of light according to the Raman effect. The Raman spectrometer's main components include a monochromator, sample holder, detector, and a light source. A monochromatic light incident on the sample interacts with the molecules during the spectral measurement, inducing a redshift of the photon's energy [11]. The induced change in energy reflects the internal vibrational energy of molecules, which is observed as a change in the reflected photon energy. Analysis of this energy change provides detailed information about chemical structure, crystallinity, defects, and molecular interactions. In my dissertation, the degree of structural defect on the as-synthesized VACNT samples was characterized by a Raman spectrometer equipped with an Ar^+ laser of wavelength 632.8 nm, operated at a maximum power of 15 mV. The relative intensity of two Raman characteristic peaks (I_D/I_G) was used to analyze the degree of defects present in the materials [12]. A higher value of I_D/I_G interprets into the presence of a large number of defects.

3.3.7 Fourier transform infrared spectroscopy

Fourier transform infrared spectroscopy (FTIR) is an efficient method to identify and characterize different functional groups, contaminants, and additives associated with the material (organic/inorganic) under investigation. The FTIR technique uses the Fourier transform, a mathematical tool, for translating the raw data recorded over a wide frequency range in the infra-red region into the actual high-resolution infrared spectrum of transmission or absorption. In the FTIR experiment, a beam of light containing many

frequencies is incident on the sample, and the spectrometer collects photons transmitted/absorbed by the specimen. The process is repeated many times with the light beam containing a different combination of frequencies, and the data are compiled to produce the spectrum. In the dissertation, the functional groups created after the acid treatment and SnO_2 coating on the CNT wall were analyzed using an FTIR (Jasco, FT/IR-4100) in the frequency range between 4000 and 550 cm^{-1} with the spectral resolution of 4 cm^{-1}.

3.4 Properties measurement

3.4.1 Field emission properties measurement

The field emission (FE) properties of VACNT emitters were measured inside a vacuum chamber using a diode configuration method under the pressure of ~1×10^{-6} Torr. Figure 3.5 shows a schematic diagram of the set up for field emission measurement. In diode configuration, the as-synthesized VACNT samples were glued onto a stainless steel plate by silver paste and were used as the cathode. In contrast, a solid cylindrical stainless steel rod of cross-section area 0.803 cm^2 was used as the anode. A fixed distance of 500 µm separated the anode and cathode. A Keithley 236 SMU was used to measure the emission current; meanwhile, a Matsusada AU–15P20 DC power supply was used to apply the voltage bias during the experiments. A pair of general-purpose interface bus (GPIB) were used to communicate between the computer, power supply, and SMU. The voltage was increased in steps of 50 V, and the corresponding current was measured until the emission current was saturated. The field emission properties of the samples were tested multiple times to confirm the repeatability and reliability of the recorded data.

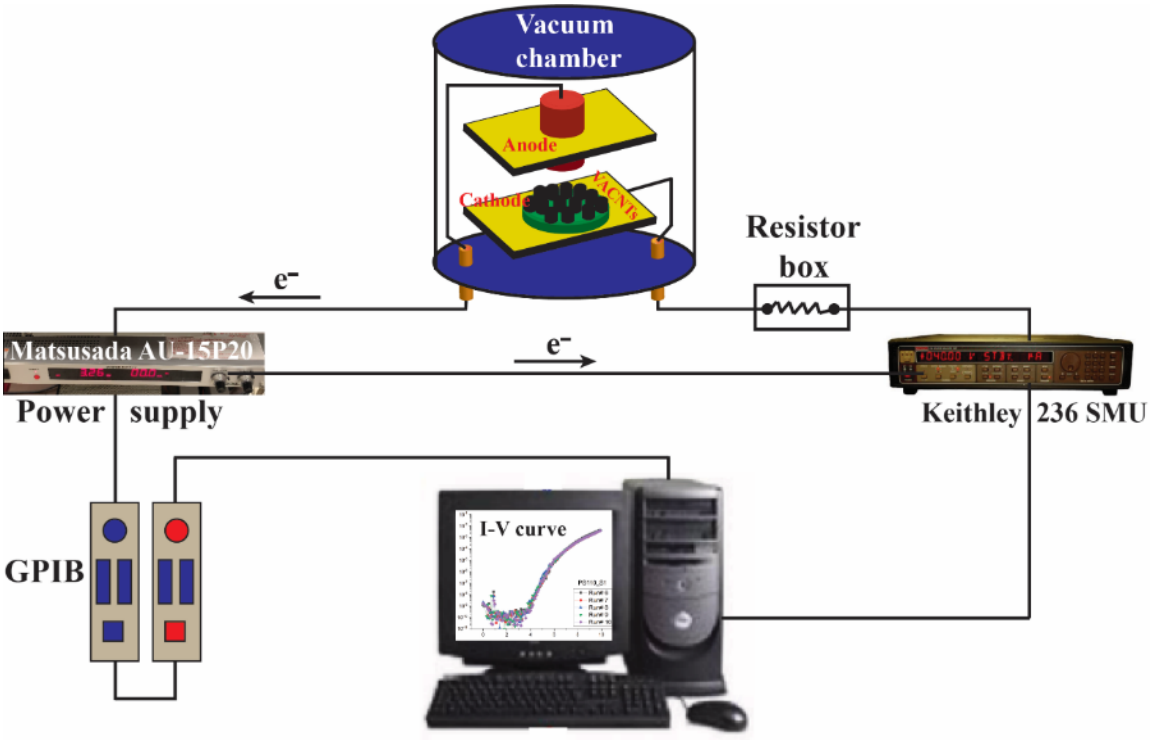

Figure 3.5. A simplified schematic diagram of electron field emission properties measurement set up.

3.4.2 Electrochemical lithiation properties measurement

3.4.2.1 Via coin cell fabrication

Electrochemical lithiation properties of pristine VACNTs and SnO_2 coated VACNTs (SnO_2-VACNTs core-shell structure) anode synthesized directly on the three-dimensional Ni foam were measured by fabricating lithium-ion coin cells. Figure 3.6 represents the schematic diagram of the coin cell assembly of a lithium-ion battery (CR2032 coin type), showing its constituents. Coin cells were assembled inside an argon-filled glove box with both moisture and oxygen levels less than 1 ppm. The coin cells were fabricated in half-cell configuration with lithium foil (99.9 %, Aldrich) as both counter and the reference electrode, while pristine VACNTs or SnO_2-VACNTs composites fabricated on Ni foams as the anode. Furthermore, 1 M $LiPF_6$ dissolved in a mixture of ethylene

carbonate (EC) and dimethyl carbonate (DEC) (v/v = 1:1) was used as an electrolyte, whereas a Celgard polypropylene film was used to separate the anode and cathode.

The electrochemical lithiation measurements were carried out using a Princeton VMP3 Bio-Logic potentiostat at room temperature, and all the potential values were measured versus Li/Li+. The lithium-ion storage behavior of the pristine VACNTs and SnO_2-VACNTs anode was characterized by cyclic voltammetry (CV) measured between 0.01 and 3 V at a scan rate of 0.2 mV/s during the first five cycles. Also, the charge/discharge characteristics of the samples were evaluated at a constant current of 0.1 A/g with cut-off potentials at 0.01 V and 3 V. Furthermore, the cycle stability of the samples was tested for 100 and 200 cycles. The rate capability of the coin cell was evaluated at different current densities such as 0.1, 0.2, 0.5, 1, 2, and 5 A/g. The spectral impedance of the cell was measured by applying a sine wave with an amplitude of 5.0 mV over the frequency range from 100 kHz to 0.05 Hz.

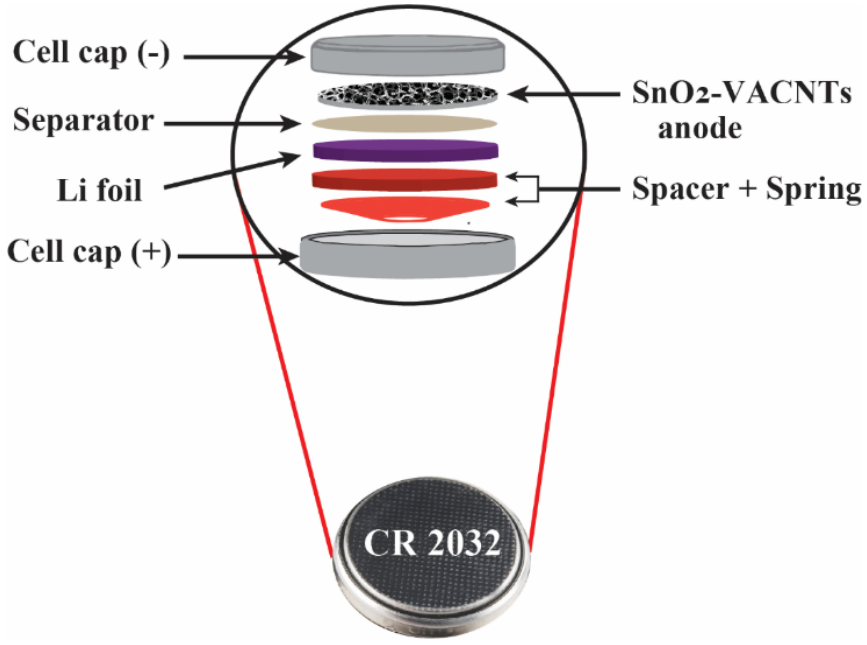

Figure 3.6. Schematic diagram showing the constituents of a CR 2032 lithium-ion coin cell.

3.4.2.2 Via miniaturized cell fabrication inside TEM

To study the lithiation/delithiation characteristics of a SnO_2-CNT nanowire, a miniaturized lithium-ion battery (LIB) was designed and fabricated inside a transmission electron microscope (TEM, FEI Tecnai F30) using TEM-scanning tunneling microscopy (STM) holder, as shown in Figure 3.7. The SnO2-CNT sample was glued to aluminum (Al) wire coated with conductive epoxy on the tip to assemble the battery. Some fresh lithium

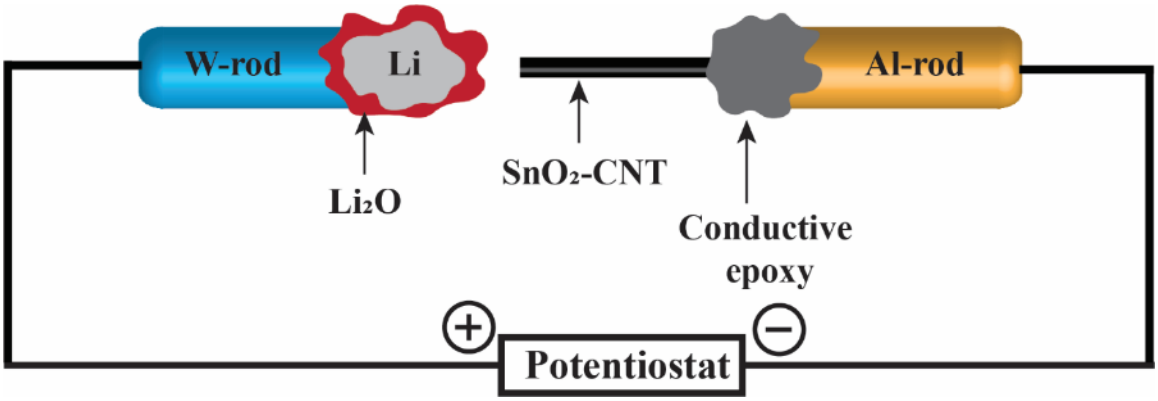

Figure 3.7. Schematic showing a design of the miniature LIB using SnO_2-CNT nanowire as an anode.

as the counter electrode and lithium-ion source was loaded at the sharp tip of a tungsten (W) wire by indenting the lithium metal inside a glovebox. The TEM-STM holder, with both the SnO_2-CNT and lithium electrodes, was transferred into the TEM, and the lithium electrode was pushed to contact the SnO_2-CNT. The lithium-ions transport was facilitated by a Li_2O solid-state electrolyte layer formed on the lithium metal surface. A bias of -2 V was applied to the SnO_2-CNT electrode with respect to the lithium electrode to initiate the lithiation, whereas the bias was reversed to facilitate the delithiation.

3.5 Electrostatic field distribution simulation

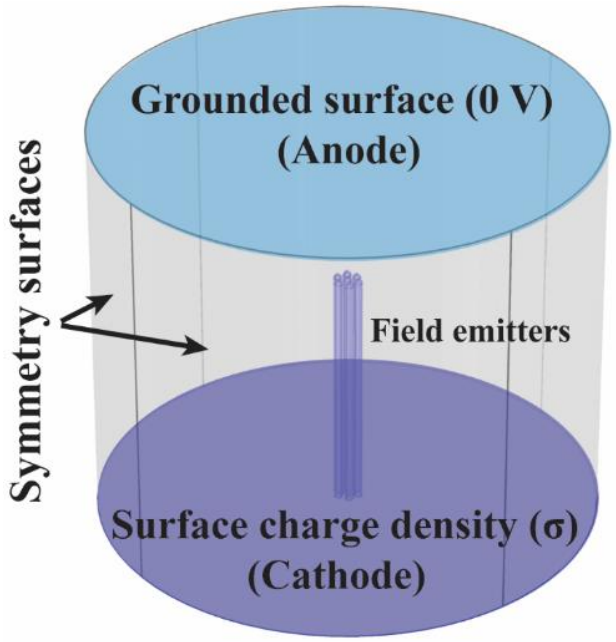

Figure 3.8. A typical domain consisting of a VACNT-based pillar emitter for electrostatic field simulation in a diode configuration method. The top surface was grounded, whereas a constant potential at the bottom surface generated a uniform macroscopic electric field of 1 V/μm in the domain.

To support the conclusion drawn from the experimental results, the electrostatic field distribution on the tip of emitters was simulated using COMSOL™ MULTIPHYSICS 5.2 software. Figure 3.8 represents a typical domain used to simulate the electrostatic field from a VACNT-based pillar field emitter in a diode configuration. The top boundary of the domain was grounded (V = 0). In contrast, the bottom surface was provided with a constant surface charge density $\sigma = \varepsilon_0 E_a$, where ε_0 is the dielectric permittivity of vacuum and E_a (1 V/μm) is a macroscopic electric field in the domain. Symmetry surfaces of the domain ensure no electric field perpendicular to these surfaces, i.e., $\mathbf{n}\cdot\mathbf{E} = 0$. The symmetry boundary condition makes the surfaces act as mirrors so that the stationary solution in the domain can be considered as that of an infinite array [13]. The VACNT emitters of different morphologies such as dense arrays, conical bundles, pillars, and Cu-filled VACNT arrays

were simulated. The emitters were assigned with similar physical properties as those of as-synthesized samples, such as the aspect ratio, inter-tube/pillar distance, and material properties of the filler metal before running the simulation. The simulated local electric field at the tip of emitters was visualized using the surface plot, and the magnitudes were recorded via the “minimum/maximum values” icon.

References

[1] Neupane S., Lastres M., Chiarella M., Li W., Su Q. and Du G., Synthesis and field emission properties of vertically aligned carbon nanotube arrays on copper. *Carbon* **2012,** 50 (7), 2641.

[2] Chen G., Neupane S., Li W., Chen L. and Zhang J., An increase in the field emission from vertically aligned multiwalled carbon nanotubes caused by NH3 plasma treatment. *Carbon* **2013,** 52, 468.

[3] Han W.-Q. and Zettl A., Coating Single-Walled Carbon Nanotubes with Tin Oxide. *Nano Letters* **2003,** 3 (5), 681.

[4] Hafner J.H., Cheung C.-L., Woolley A. and Lieber C., Structural and functional imaging with carbon nanotube AFM probes. *Progress in biophysics and molecular biology* **2001,** 77 (1), 73.

[5] Johnson D., Al Malek S., Al-Rashdi B. and Hilal N., Atomic force microscopy of nanofiltration membranes: effect of imaging mode and environment. *Journal of membrane science* **2012,** 389, 486.

[6] Tomus D. and Ng H.P., In situ lift-out dedicated techniques using FIB–SEM system for TEM specimen preparation. *Micron* **2013,** 44, 115.

[7] Adams D., Mayer T., Vasile M. and Archuleta K., Effects of evolving surface morphology on yield during focused ion beam milling of carbon. *Applied surface science* **2006,** 252 (6), 2432.

[8] Thompson L.E., Rice P.M., Delenia E., Lee V.Y., Brock P.J., Magbitang T.P., Dubois G., Volksen W., Miller R.D. and Kim H.-C., Imaging thin films of nanoporous low-k

dielectrics: Comparison between ultramicrotomy and focused ion beam preparations for transmission electron microscopy. *Microscopy and Microanalysis* **2006,** 12 (2), 156.

[9] Reimer L., Scanning electron microscopy: physics of image formation and microanalysis. *IOP Publishing*, **2000**, 1826

[10] Tanaka N., Present status and future prospects of spherical aberration corrected TEM/STEM for study of nanomaterials. *Science and Technology of Advanced Materials* **2008,** 9 (1), 014111.

[11] Rostron P., Gaber S. and Gaber D., Raman spectroscopy, review. *laser* **2016,** 21, 24.

[12] Dresselhaus M.S., Dresselhaus G., Saito R. and Jorio A., Raman spectroscopy of carbon nanotubes. *Physics reports* **2005,** 409 (2), 47.

[13] Dall'Agnol F.F. and den Engelsen D., Field Emission Simulations of Carbon Nanotubes and Graphene with an Atomic Model. *Journal of Nanomaterials & Molecular Nanotechnology* **2014,** 5, 23.

CHAPTER 4

Vertically aligned CNT arrays on stainless steel: Direct growth, structural modification, and their field emission properties

Chapter 4 presents a detailed description of the experimentations and results obtained through rigorous scientific analyses on synthesis, characterization, and field emission properties measurement of pristine and structurally modified VACNT arrays grown on the stainless steel.

4.1 Introduction

Since the discovery of carbon nanotubes (CNTs), one of the allotropes of carbon, by Iijima in 1991 [1], a vast amount of time, money, and efforts have been expended on exploiting their unique and excellent properties to develop new devices and to improve many components of current technologies. Carbon nanotubes have shown great potential in plentiful applications, including field emission (FE) emitters, lithium-ion batteries, supercapacitors, sensors, fuel cells, solar cells, and scanning probe microscopy (SPM), because of their unique physical, electronic, mechanical, and thermal properties [2-11]. The CNTs are regarded as the best field emitters in a non-oxidizing environment that can be utilized as cold field emitters in vacuum electronic devices such as FE displays, electron microscopes, X-ray sources, microwave amplifiers, and nano-electronics [11-15]. Apart from being more energy-efficient, CNT field emitters can produce a more stable electron beam, which can help accurate electron beam focusing. For such a wide range of applications, CNTs with varied properties and characteristics are instrumental. Many of these applications, such as field emission emitters, require high-quality vertically aligned

carbon nanotubes (VACNTs) directly grown on a metal substrate, which provides numerous advantages over randomly oriented CNTs (ROCNTs) and powdered forms [16-18].

The FE process involves electron transportation from the substrate through the interface between the substrate and CNT, along the CNT, and final emission out into the vacuum. Since the first report of FE from a single CNT by Rinzler et al. [19] and from a CNT film by de Heer et al. [20] in 1995, various CNTs and CNT films have been studied extensively for their FE properties. The morphology of CNTs, such as tip structure, length, degree of defects, number density, alignment, and geometrical arrangement, play a crucial role in their FE properties including turn-on and threshold electric fields, field enhancement factor, FE current density, and stability [21-25]. Besides, the direct contact of CNT emitters with the substrate is essential to enhance the EF performance by facilitating efficient electron transfer. However, CNTs are generally synthesized on a substrate coated first with a buffer layer and then a catalyst layer by different deposition techniques [26-28]. The buffer layer arguably adds an extra electrical resistance between the CNT and the substrate, limiting implementation into applications that require good electrical conductivity. Hence, it is desirable to grow VACNTs directly on the conducting metal substrate to minimize the resistance between the CNTs and the substrate.

Several groups have reported the growth of dense forest of VACNTs and ROCNTs directly on the metal substrate using different techniques [29-32]. However, most of these synthesis techniques require careful substrate surface pretreatments to nucleate CNT growth sites, which add extra steps to the growth method limiting their commercialization.

Another problem with the direct synthesis of VACNTs on the conducting substrates without an extra catalyst layer lies in non-uniform and non-reproducible CNT growth. Most importantly, those typical dense VACNT arrays suffer screening effect because of the close proximity of neighboring VACNTs, which adversely affects the field emission performance by increasing the turn-on field and decreasing the total emission current density [33].

It has been reported that a post-growth structural modification of the CNT-based emitters by coating the CNTs with a wide-bandgap semiconducting metal oxide or metal nanoparticles, such as TiO_2, ZnO, RuO_2, MgO, In, Al, and Cu, can enhance the FE properties through modifying the electronic and the physical structure of the CNT-based field emitters [34-38]. It has also been proven that coating CNT emitters with metal oxide nanoparticles can help passivate defective sites on the CNT's surface, thereby improving the FE stability remarkably. However, to our knowledge, only a few works regarding the direct synthesis of VACNT-based field emitters on the conducting substrate and their FE properties enhancement by simple post-treatment methods such as water treatment and SnO_2 coating have been reported. The post-treatment method in solution media was also advantageous for creating the morphology of VACNT arrays favorable to the FE process.

This study developed a facile and inexpensive method for directly synthesizing VACNT arrays on stainless steel (SS) substrate without any external catalyst layer using direct current (DC) plasma-enhanced chemical vapor deposition (PECVD) to enable a bulk-synthesis approach. We performed a study on the surface characterization of the SS substrate before the CNT growth. We focused on understanding the growth mechanism

and the effect of the synthesis parameters, such as growth time, growth temperature, and plasma power, on the VACNTs growth. We coated the VACNTs with a thin layer of SnO_2 nanoparticles using a facile one-step wet-chemical method. The FE characteristics of the as-synthesized, water-treated, and SnO_2 coated VACNTs were studied to understand the effect of the SnO_2 coating and the morphology change of the VACNTs array on the FE performance. Our result revealed that water treatment and SnO_2 coating could significantly improve the FE properties of the VACNTs. We also performed simulations to understand the effect of the surface modification caused by post-treatments to the VACNTs film on the FE performance. The simulation result agrees well with experimental results.

4.2 Experimental details

4.2.1 Synthesis of VACNT arrays

The SS substrates were prepared as described in section 3.1.1, and forests of VACNTs were grown using the DC PECVD method as described in section 3.2.1. In brief, the VACNT synthesis experiments were performed at different temperatures such as 650, 700, 760, or 800 ºC; meanwhile, other parameters such as time (10 min), pressure (7 Torr), plasma (70 W), the flow rate of C_2H_2 (15 sccm) and the flow rate of NH_3 (400 sccm) were kept constant throughout the experiment. Similarly, VACNTs were synthesized for different durations (2, 5, 10, 15, or 20 min) and at different plasma power (9, 40, 70, or 92 W) by keeping other parameters constant to understand the effect of growth parameters on the VACNT morphology. Furthermore, VACNT arrays were synthesized at 700 ºC for 5, 10, or 20 min at the plasma power of 75 W under the pressure of 7 Torr for water treatment

and SnO_2 coating to study FE properties. The flow rates of C_2H_2 and NH_3 were maintained at 25 and 400 sccm, respectively.

4.2.2 Water treatment and SnO_2 coating to VACNT arrays

The as-synthesized VACNT arrays were submerged into deionized water (80 mL) for nine hours at room temperature. A gentle flow of air through the deionized water facilitated the water treatment. Once the treatment time was achieved, the samples were dried by using a hot plate at 95 °C for 15 min. Also, VACNT arrays of different lengths were coated with SnO_2 nanoparticles using the wet-chemical method at room temperature, as described in section 3.2.2.

4.2.3 Field emission measurement

The FE properties of pristine VACNT arrays, water-treated VACNT arrays, and SnO_2 coated VACNT arrays of different lengths were measured using a diode configuration inside a vacuum chamber under the pressure of ~1×10^{-6} Torr, as described in section 3.4.1. The FE performance of VACNT emitters was compared according to their lengths and morphology achieved as the result of post-treatments to emitter arrays in solution media.

4.2.4 Electrostatic field simulation

Electrostatic field distribution for the VACNT emitters was simulated using COMSOL™ MULTIPHYSICS 5.2 software, as described in section 3.5. Three-dimensional (3D) models consisting of single VACNT, a dense array of VACNTs, and systems having VACNT bundles with different emitter densities were created. The parameters such as the length of VACNT = 8 μm, the diameter of VACNT = 130 nm, and

inter-VACNT distance = 0.3 μm were chosen to be reasonably close to the real VACNTs emitters system (20-min sample). An electric field of 1 V/μm was applied between the top and bottom boundaries of the simulation domain. Surface and contour plots were used to visualize the results, whereas the magnitudes of local electric fields were recorded by using a point evaluation icon.

4.3 Results and discussion

4.3.1 Surface morphology of the substrate

The study of surface morphology of the substrate before the introduction of hydrocarbon gases could provide essential information in understanding the growth mechanism of CNTs on the catalytic substrates. On-site decomposition of the hydrocarbon source (C_2H_2 in our case) and diffusion of the carbon atoms or clusters into the active nucleation sites (nano-sized catalyst islands) are critical steps in CNTs growth. Hence, abundant availability and uniform distribution of the active nucleation sites on the substrate surface greatly affected the CNT synthesis. Therefore, a detailed study of the substrate surface structure was necessary.

Figure 4.1(a) and (b) show AFM images of the surface of as-received and polished SS samples, respectively. Figure 4.1(e) and (f) are the high-resolution AFM images of the as-received and polished SS samples, respectively. Larger grains with distinct features of lateral size ranging from few microns to ~17 μm were observed on the as-received sample surface, whereas a smooth and featureless surface was observed after polishing, confirming the effectiveness of the polishing process. These grains on the as-received SS sample surface were likely a thin layer of passive chromium oxide (Cr_2O_3). Although such a layer

present on the surface of commercially available type 304 SS has advantages in corrosion resistance, it has demonstrated a poisonous effect on the metal catalyst for an adverse effect

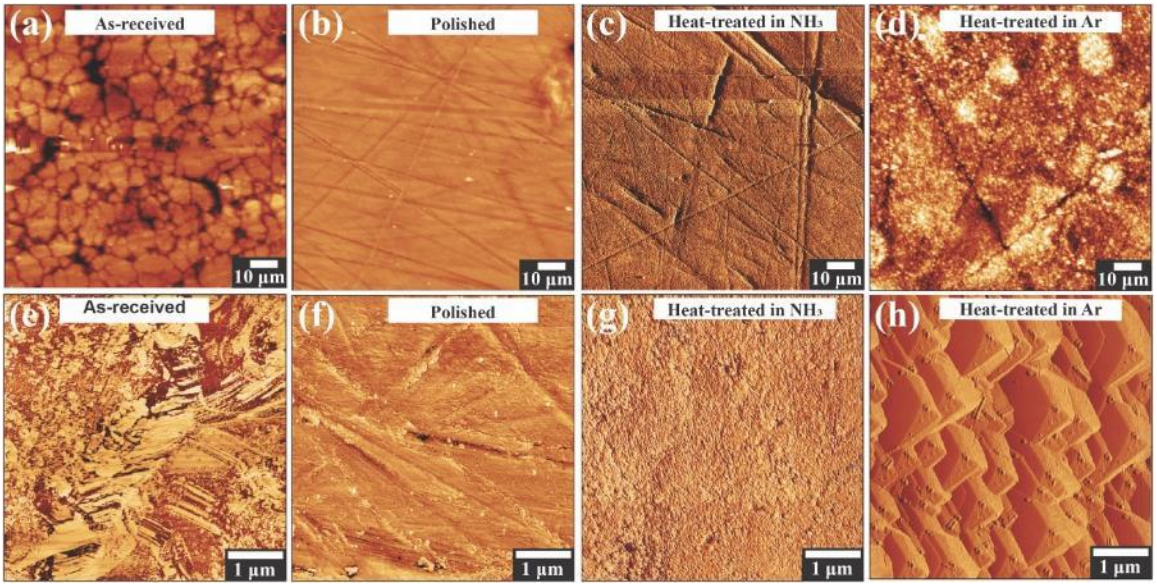

Figure 4.1. Low (100 × 100 µm scan, top row) and corresponding high (5 × 5 µm scan, bottom row) resolution AFM images of the (a, e) as-received SS sample, (b, f) polished sample, (c, g) ramping heated (760 °C) sample in NH_3 (400 sccm) environment and (d, h) ramping heated (760 °C) sample in Ar (400 sccm) environment.

on the CNT growth [32]. Apart from this, reports suggest that granular microstructures or microscale features do not help the CNTs grow; hence, it was worth removing such granular layer from the SS plate when used as the substrate for CNT growth. The polishing removed the granular structures from the surface, which likely increased the number of catalytic sites for CNT growth [30, 39-41]. Further, surface evolution during the growth period of increasing temperature, before introducing carbon source, was vital for the formation of proper catalytic sites on the SS substrate. Figure 4.1(c) and (d) (4.1(g) and (h) are their corresponding high-resolution images) represent the AFM images of the SS surfaces treated at the ramping temperature from room temperature to 760 °C at the rate of 50 ºC/min under the NH_3 and Ar (both at 400 sccm) environment, respectively. The AFM

image suggests that the heat treatment in the presence of NH_3 and Ar gas appeared to have significant effects on the surface evolution, i.e., the formation of the nano-sized catalyst

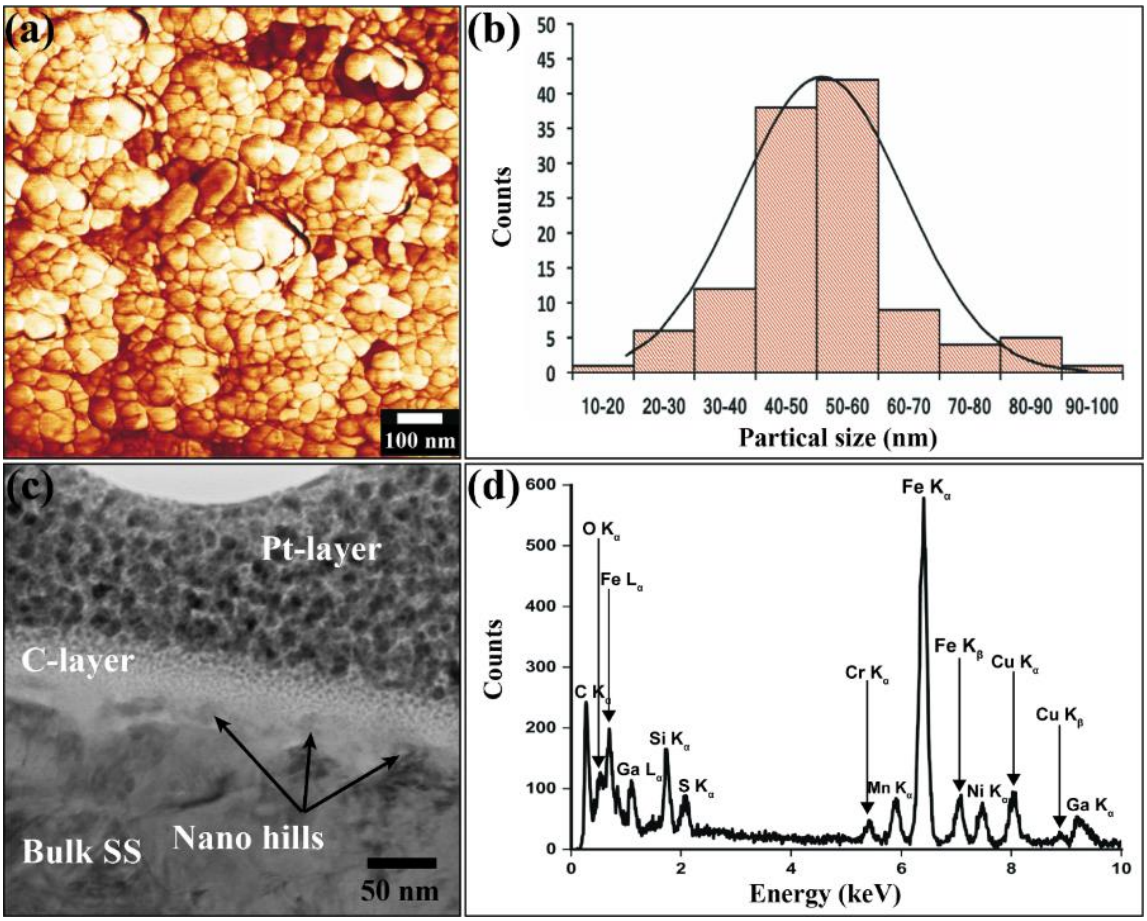

Figure 4.2. (a) High resolution (1 × 1 μm scan) AFM image of the polished and heated sample in an NH_3 environment. (b) Nanoparticles size (lateral diameter) distribution. (c) TEM image of a cross-section of the sample heated in an NH_3 environment, and (d) EDS obtained from one of the nano-hills shown in panel (c).

particles. The presence of NH_3 was critical, as it helped to create uniform nanoparticles, as shown in Figure 4.1(c) and (g), which was caused by the etching effect of the NH_3 to the SS surface [42]. On the contrary, the heat treatment under Ar caused the formation of prominent features with the dimension of more than 1 μm (see Figure 4.1(d) and (h)), which were not favorable in initiating CNT growth. Figure 4.2(a) is a high-resolution AFM image of the SS substrate treated under NH_3 gas, shows the nanoparticles uniformly distributed

on the substrate surface. Most of the nanoparticles had a lateral diameter in the range of 40–60 nm, and the average lateral diameter of the nanoparticles was found to be 51 nm.

To further investigate the morphology and composition of the SS substrate treated in the presence of NH_3, a cross-section of the sample was extracted using Ga-ion FIB and was examined by using FEI Tecnai F30 TEM operated at 300 kV and equipped with EDS technology. Figure 4.2(c) shows the cross-sectional structure of the sample coated with a platinum (Pt) layer to protect the surface features when the larger current beam milled into the specimen. In addition, an unwanted thin layer of carbon was deposited on the sample's surface during the milling process. Beneath the carbon layer, the native surface was characterized by nano-hills with a lateral diameter of about 50 nm, which agrees with the AFM results shown in Figure 4.2(a). Figure 4.2(d) represents the energy dispersive analysis of X-ray spectrum (EDS) obtained from one of the nano-hills shown in Figure 4.2(c). The EDS result showed that the major chemical constituents of the nano-hill are Fe along with Ni, Mn, and Cr, which are also the native components of the as-received SS.

The subtle change of the SS surface resulting from the high temperature and etching NH3 gas was fundamental to forming catalytically active sites for CNT nucleation. The surface evolution at the stage after the polishing and before the supply of carbon source, as revealed by AFM and TEM results (Figure 4.2(a) and (c)), was attributed to the high temperature and reducing atmosphere (NH_3), presence of oxides or carbide, and complex processes related to surface energy [31, 39]. The reduction of metal oxides and carbides to their metal phases was critical as the metal oxides and carbides are not catalytically active for the CNT synthesis. The combined effect of these processes resulted in the chemical and structural rearrangement at the surface in atomic and nanoscale, ultimately forcing the

surface to break up and hence exposing the catalytically active metal. Also, the surface breakup resulted in more surface area and crystallographic defects, which offered more active sites for dissociative adsorption and precipitation of the elemental carbon available from the dissociation of the hydrocarbon source at elevated temperature.

4.3.2 Synthesis of VACNTs on stainless steel

4.3.2.1 Effect of growth temperature

Figure 4.3(a-d) are SEM images of VACNTs synthesized at 650 °C, 700 °C, 760 °C, and 800 °C, respectively. The SEM images were taken on the samples tilted at 15° with respect to the normal of the SS substrate. These samples were synthesized by keeping the other parameters, such as flow rate of NH_3 (400 sccm), flow rate of C_2H_2 (15 sccm), plasma power (70 W), growth time (10 min), and pressure inside the tube (7 Torr), constant during the entire synthesis period. The SEM images (Figure 4.3(a-c)) show the uniform distribution and good alignment of the self-standing VACNTs. In comparison to the previous reports by Neupane *et al.* and Abad *et al.* on the synthesis of VACNTs on pristine SS substrate [43, 44], our result is significant in that well-aligned and uniform VACNT arrays thoroughly covered the SS substrate. The growth of VACNTs on SS substrate was significantly affected by the growth temperature (see graph in Figure 4.4(c)). At 650 °C, the SS substrate was covered with VACNTs of short and non-uniform length, as shown in Figure 4.3(a). The average length and diameter of the VACNTs were found to be 2.5 μm and 101 nm, respectively. The average length of the VACNTs increased to 4.2 μm and 7.8 μm for the VACNTs grown at 700 °C and 760 °C, respectively, while the average diameter was found to be 115 nm for both growth temperatures. The length of the VACNTs

synthesized at 760 °C directly on the catalytic substrate was significantly longer than those reported in the literature [43, 44]. The density of the CNTs prepared at 700 °C and 760 °C

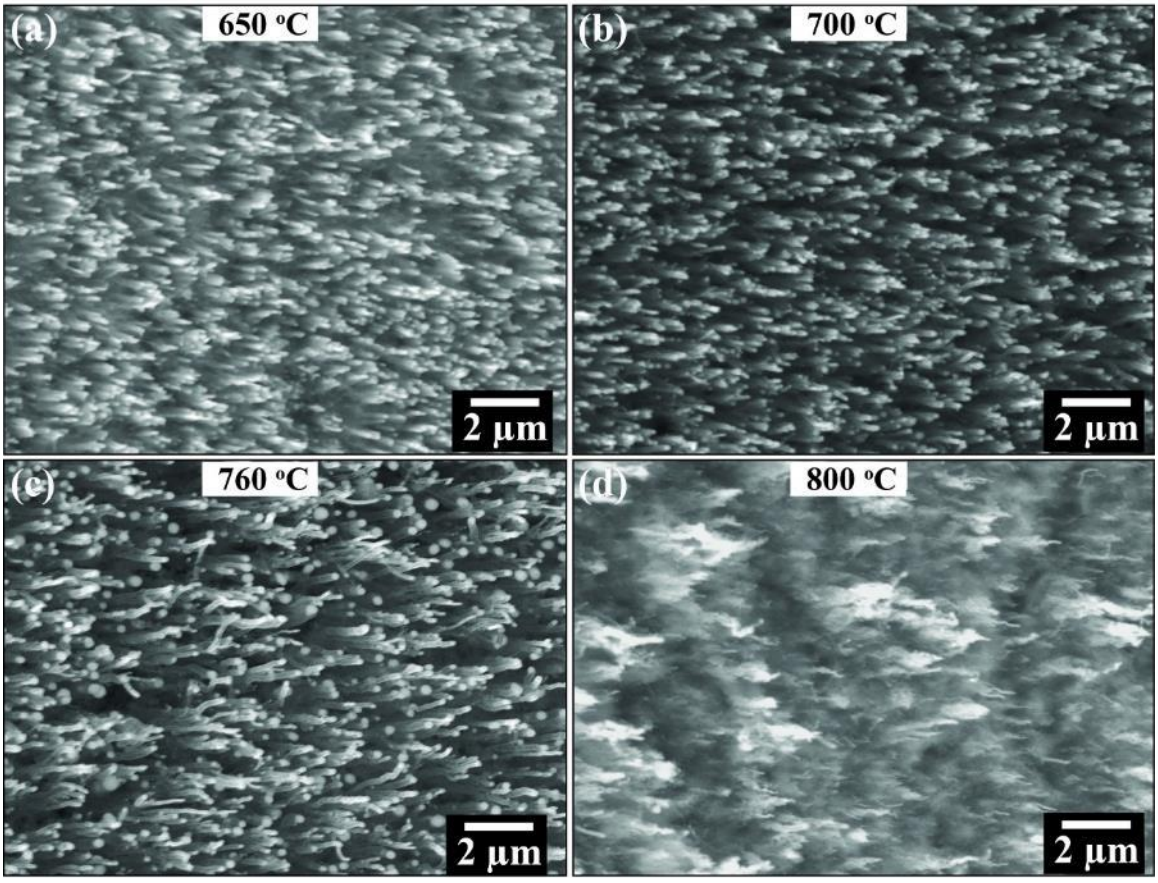

Figure 4.3. SEM images of VACNTs synthesized on SS substrate at different temperatures (a) 650 °C, (b) 700 °C, (c) 760 °C, and (d) 800 °C, by keeping other parameters such as plasma power (70 W), chamber pressure (7 Torr), growth time (10 min), flow rate of C_2H_2 (15 sccm), and flow rate of NH_3 (400 sccm) constant.

was about 9×10^8 CNTs per cm^2 as estimated from the SEM images. The average length and diameter of the VACNTs prepared at 800 °C were 8.1 µm and 106 nm, respectively. The average length did not increase significantly, which indicated saturation of the CNT length. The top surface of the sample prepared at 800 °C was covered mainly with amorphous carbon and some poorly aligned CNTs, as shown in Figure 4.3(d). The above result suggests that the CNT growth on SS substrate by the PECVD favored a specific

temperature range. It was assumed that at a lower temperature such as 650 °C, the thermal energy necessary for the reconstruction of the substrate surface to form catalytically active nano-hills was not high enough; therefore, decomposition of the hydrocarbon gas (C_2H_2) to liberate carbon at this temperature was not sufficient. The lack of a sufficient amount of carbon and active nucleation sites where catalytic diffusion and precipitation of carbon took place resulted in short, low-density VACNTs with non-uniform lengths.

The increase in temperature from 650 °C to 700 °C resulted in a more uniform, better aligned, denser, and longer VACNTs than the VACNTs synthesized at 650 °C. Upon increasing the temperature from 700 °C to 760 °C, the average length of CNTs increased significantly (by ~85%). However, no remarkable changes were observed in other parameters such as alignment and density of CNTs. The improvement in synthesis at 760 °C was mainly because of the optimum availability of carbon as a result of C_2H_2 dissociation at this temperature. On the other hand, as the temperature was further increased to 800 °C, the average length only increased by 0.3 μm. The inconsistency between the growth rate of CNT and the high decomposition rate of C_2H_2 at 800 °C led to excess carbon, which was no longer able to graphitize in forming CNT walls and ultimately decorated in the exterior of VACNTs in an amorphous form, as shown in Figure 4.3(d). The fuzzy tips of VACNTs may also be caused by the intense etching of highly energetic plasma species at the higher temperature.

Figure 4.4(a-b) represents the SEM image of the VACNT array at the scratched area where the length of CNTs was measured and the top view of the corresponding array. The sample was synthesized for 10 min at the growth temperature of 760 °C at the pressure

of 7 Torr. In the meantime, plasma power was maintained at 70 W and, C_2H_2 and NH_3 gases were fed into the chamber at the rate of 15 sccm and 400 sccm, respectively. Figure

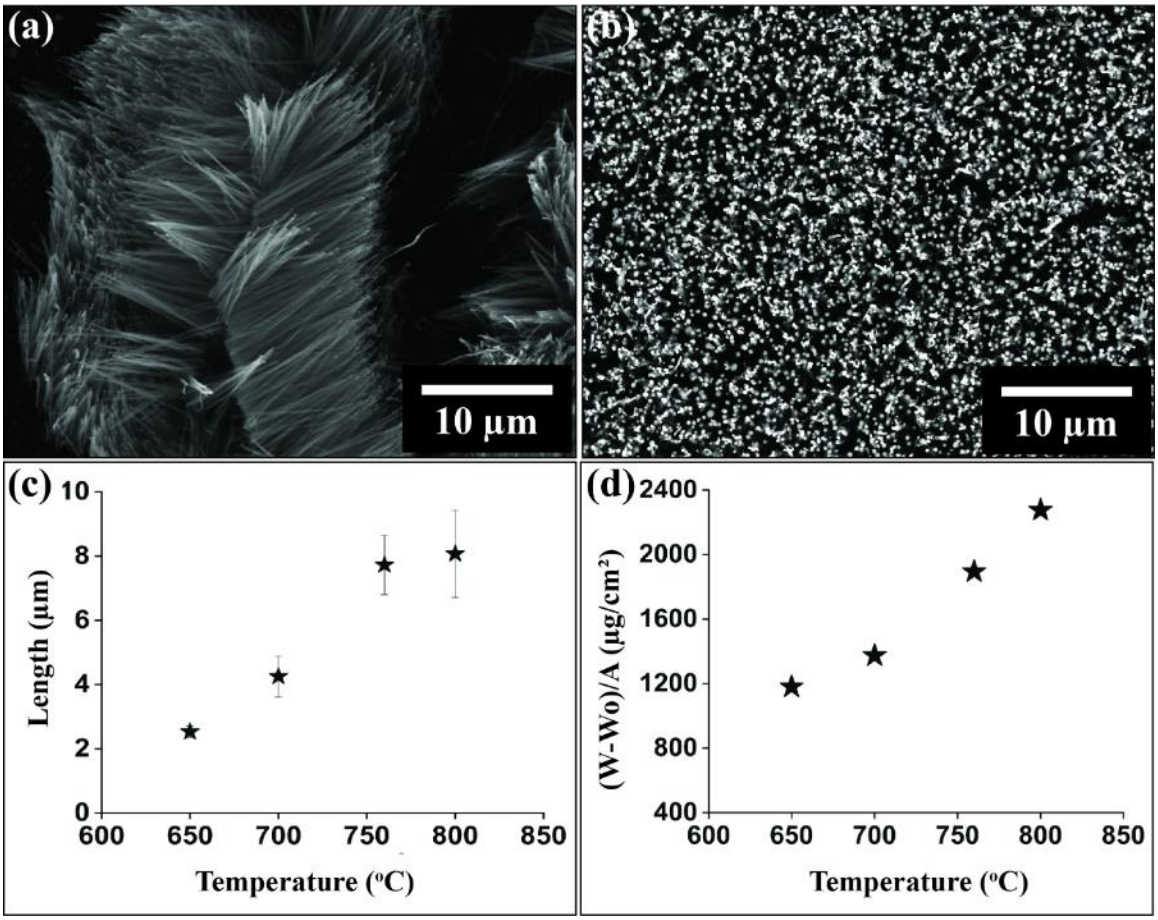

Figure 4.4. (a-b) SEM image of the VACNT array at the scratched area where the length of the CNTs were measured, and top view of the array. The growth conditions were, growth time 10 min, growth temperature 760 °C, chamber pressure 7 Torr, plasma power 70 W, flow rate of C_2H_2 15 sccm, and flow rate of NH_3 400 sccm. (c) Variation of length and (d) yield, of VACNT array with growth temperature.

4.4(c) and (d) show the length and yield of the VACNTs as a function of the growth temperature, respectively. In Figure 4.4(d), W_o is the weight of the substrate before the VACNT growth, W is the weight of the sample after the VACNT growth, and A is the surface area of the SS substrate. The graph shows that the yield increases linearly as the temperature was increased, although the high yield at 800 °C included the amorphous carbon. The yield of the VACNTs was increased by 193.12 µg/cm^2 for the increase in

temperature from 650 °C to 700 °C. Further increase in temperature from 700 °C to 760 °C resulted in the increase in yield by 520.58 μg/cm^2, which corresponds to the maximum increase in the length by 3.6 μm, as mentioned earlier. However, when the temperature increased from 760 °C to 800 °C, the increase in yield was 380.97 μg/cm^2 corresponding to the increase in length of the VACNTs by only 0.3 μm. The inconsistency in the increase in yield and length supports the conclusion that amorphous carbon was formed on the sample at 800 °C. The VACNTs synthesized directly on the catalytic SS substrate at 700 °C with the length of 4.2 μm and diameter of ~115 nm may exhibit superior field emission properties because VACNTs, with similar morphology and density, synthesized on a metal substrate coated with an external catalyst layer, were reported to show better field enhancement properties [26].

4.3.2.2 Effect of growth time

To investigate the effect of growth time on the morphology of VACNTs, PECVD experiments were performed for 5, 10, 15, and 20 min while keeping the growth temperature (760 °C), the plasma power (70 W), and the chamber pressure (7 Torr) constant, as shown in Figure 4.5. It was observed that VACNTs gained a length of about 1.20 μm in the first 3 min growth. The average length was increased to 2.20 μm, 7.80 μm, 9.80 μm, and 10.7 μm when the growth time was increased to 5 min, 10 min, 15 min, and 20 min, respectively. The VACNTs grown for 5 min (Figure 4.5(a)) or 10 min (Figure 4.5(b)) exhibited uniform length; however, a longer growth time such as 15 min (Figure 4.5(c)) or 20 min (Figure 4.5(d)) led to non-uniform length, which was also indicated by the big error bars in Figure 4.6(b). Figure 4.6(b) shows the change in length of the VACNTs

with the growth time. The linear dependency of VACNT length on growth time was expected [45]. When the growth time increased to 15 min, the average length of VACNTs

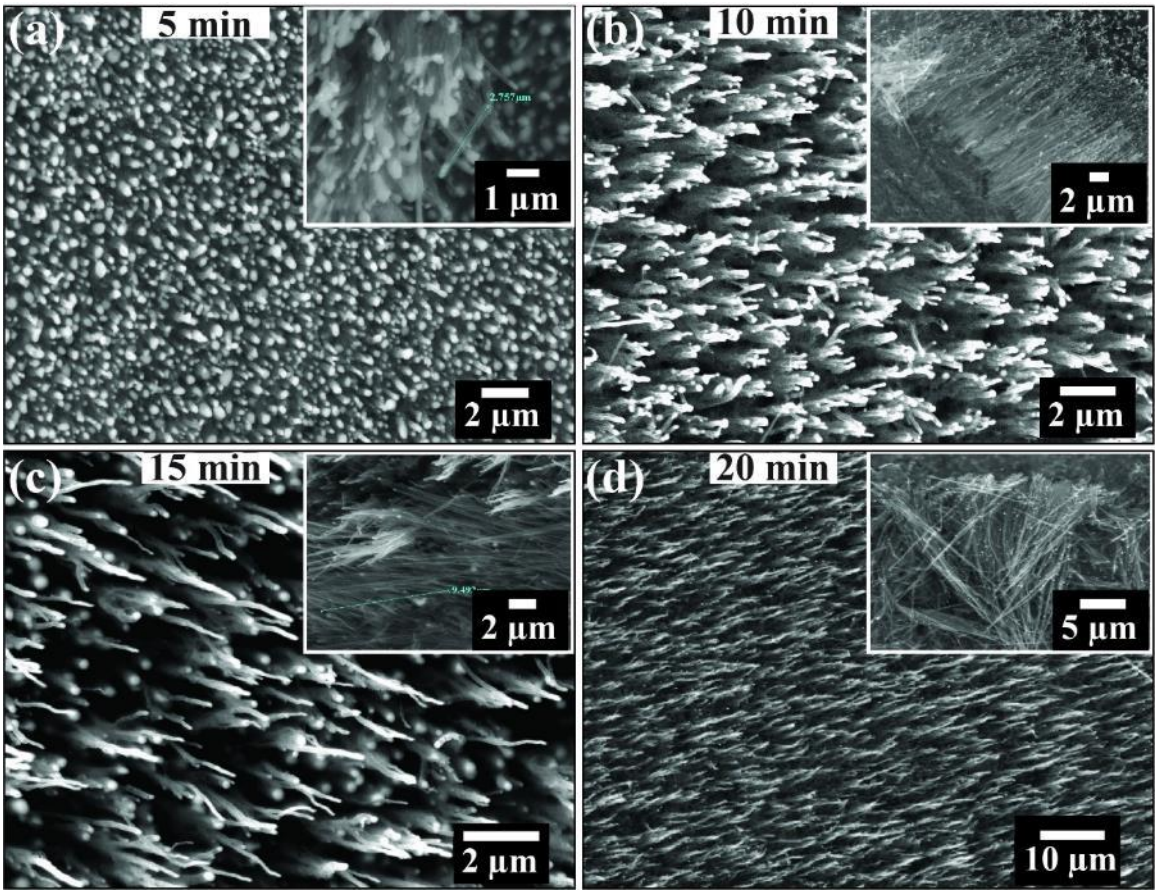

Figure 4.5. SEM images of VACNTs synthesized on SS substrate at different growth time (a) 5 min, (b) 10 min, (c) 15 min, and (d) 20 min by keeping other parameters such as growth temperature (760 °C), chamber pressure (7 Torr), plasma power (70 W), flow rate of C_2H_2 (15 sccm), and flow rate of NH_3 (400 sccm) constant. The insets are images of the scratched area of the corresponding VACNTs samples.

increased rapidly. However, a further increase in growth time (from 15 to 20 min) slowed down the growth rate caused by the gradual loss of the catalytic activity of the catalyst particles, and eventually ceased the VACNT growth [46]. The average diameter of the VACNTs grown for 5 min was about 200 nm, but as the growth time increased, the average diameter was found to be ~115 nm. The decrease in diameter may be accredited to the plasma etching the sidewall of the VACNTs or the deterioration of the catalyst particle as

the VACNT grew longer. The shorter VACNTs (i.e., grown for 5 min) were found to be filled fully or partially with catalyst materials along its length, as shown in Figure 4.6(a). However, the catalyst particles were mainly confined at the tip of VACNTs as the growth time was further increased.

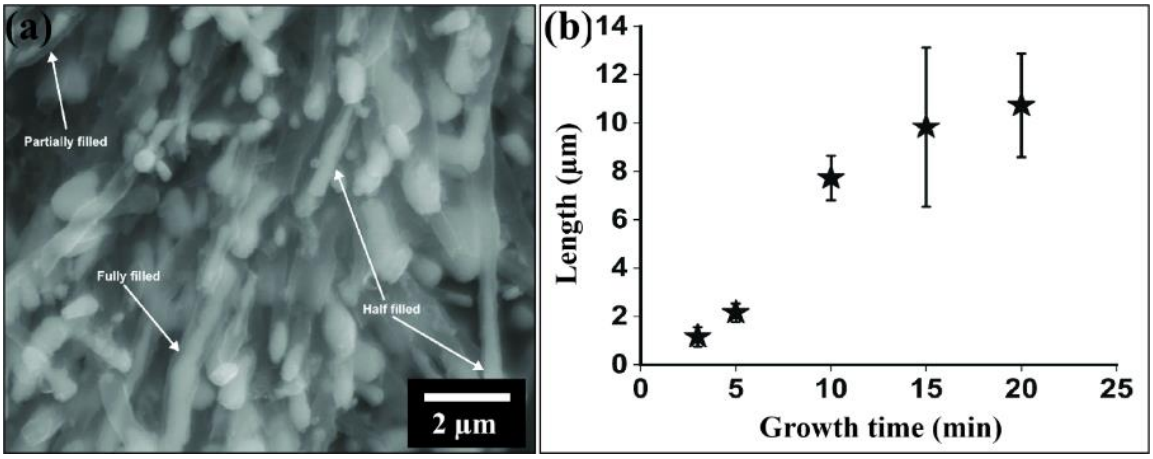

Figure 4.6. (a) SEM image of the VACNTs at the scratched area, synthesized for 5 min at growth temperature 760 °C, chamber pressure 7 Torr, flow rate of C_2H_2 15 sccm, flow rate of NH_3 400 sccm, and plasma power 70 W. (b) Variation of the VACNT length with growth time.

4.3.2.3 Effect of plasma power

Paschen's law governs the minimum potential that should be applied between the parallel plate electrodes for a given electrode distance, gas composition, and pressure [47]. Once a sufficient voltage is applied, the gas breakdown occurs forming a strong electric field and high ion flux, so-called plasma, near the cathode surface. The plasma enhances the VACNTs growth rate and aligns them along the direction of the electric field. The effect of plasma power on the morphology of VACNTs is shown in Figure 4.7. Experiments were carried out at different plasma power, such as 9, 40, 70, and 92 W, while keeping all the other parameters, such as growth temperature (760 °C), chamber pressure (7 Torr), growth time (10 min), flow rate of C_2H_2 (15 sccm), and flow rate of NH_3 (400 sccm), constant. At

a low plasma power of 9 W, sparsely scattered bright dot particles were observed on the sample which were the nucleation sites for VACNTs, as shown in Figure 4.7(a). Very few

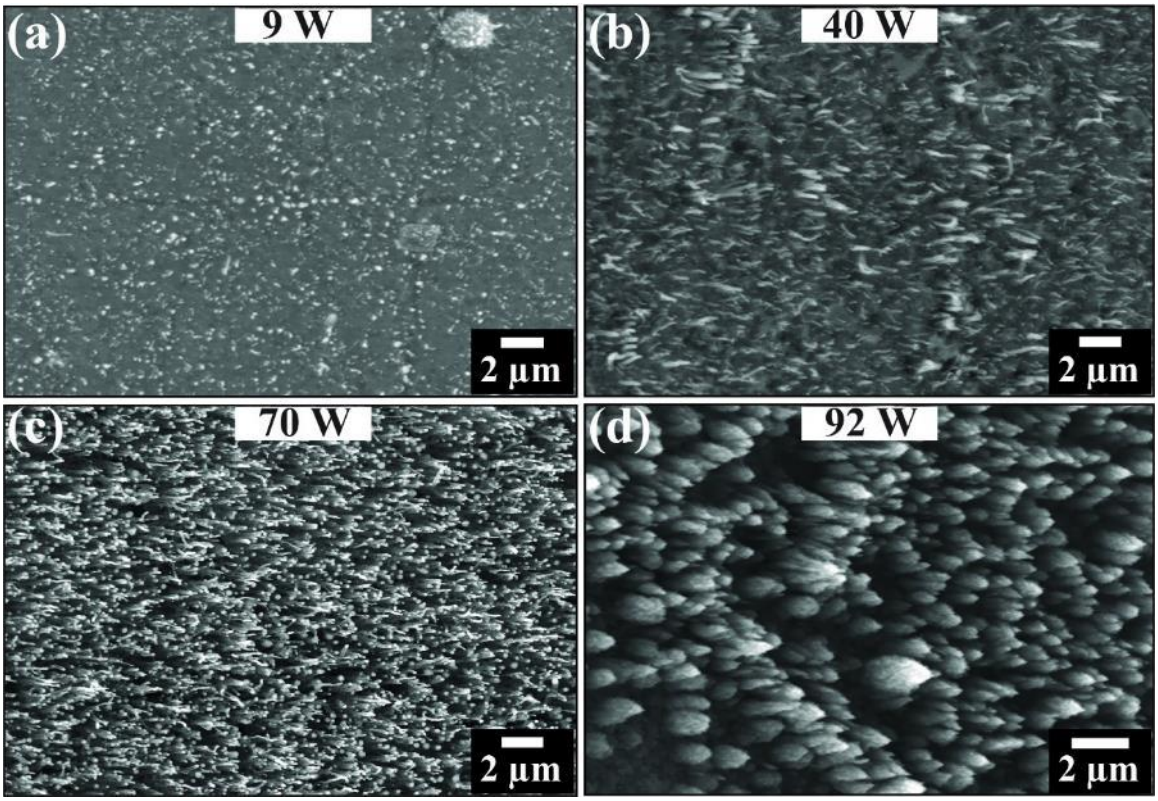

Figure 4.7. SEM images of VACNTs synthesized on SS for different plasma power (a) 9 W (b) 40 W (c)70 W, and (d)92 W, by keeping other parameters such as growth temperature (760 °C), chamber pressure (7 Torr), growth time (10 min), flow rate of C_2H_2 (15 sccm), and flow rate of NH_3 (400 sccm) constant.

and short VACNTs were also spotted on the sample at this plasma power. When the plasma power was increased to 40 W, short VACNTs of average length ~2 µm were observed. However, the density of the VACNTs was very low and a few VACNTs with a large diameter (~206 nm) were also observed, Figure 4.7(b). The length, diameter, and distribution of the VACNTs were not uniform, and the vertical alignment was not clearly presented. The result suggests that the thermal energy from the plasma and growth temperature was not sufficient to decompose C_2H_2. The plasma intensity was not strong enough to align the VACNTs along the electric field direction at the plasma power below

40 W. At the plasma power of 70 W, well-aligned VACNT arrays with an average length of ~7.8 μm were obtained (Figure 4.7(c)). When the plasma power was increased to 92 W, short and thick bush-like microstructures were observed (Figure 4.7(d)). The above results suggest that the optimum value of the plasma power was 70 W as other growth parameters remained unchanged in this experiment. It was expected that the optimum value of plasma would provide sufficient energy to dissociate C_2H_2 to generate enough carbon atoms or carbon clusters for the CNT growth and appropriate electric field to align the CNTs during their growth. High plasma power such as 92 W may have resulted in excess carbon atoms or carbon clusters, which caused the imbalance between the decomposition, diffusion, and precipitation of carbon. As a result, carbon accumulated to form microstructures instead of VACNTs, as shown in Figure 4.7(d). Hence, these results indicate that the optimal condition for synthesizing VACNTs via the PECVD method was by using the following parameters: the temperature of 760 °C, the growth time of 10 min, plasma power of 70 W, the flow rate of C_2H_2 at 15 sccm, the flow rate of NH_3 at 400 sccm, and the chamber pressure of 7 Torr.

4.3.2.4 Synthesis of VACNT field emitters

For studying the field emission properties, VACNT arrays with different lengths were synthesized for 5, 10, and 20 min at the growth conditions described in section 4.3.2.2, which include a growth temperature of 700 °C, a flow rate of C_2H_2 at 25 sccm, a flow of NH_3 at 400 sccm, a pressure of 7 Torr, and plasma power of 75 W. Figure 4.8(a-c) represents typical SEM images tilted at 15° to the normal of the SS substrate, and Figure 4.8(d-f) represents their corresponding scratched area where CNTs length was measured.

It was observed that the average length of the VACNTs was 2.1 ± 0.2 μm, 4.1 ± 0.7 μm, and 8.2 ± 1.1 μm for growth durations of 5, 10, and 20 min, respectively. Thus, a linear relationship between the VACNT's length and growth time was observed, which was in good agreement with our prediction. Also, the average diameter of the VACNTs was found

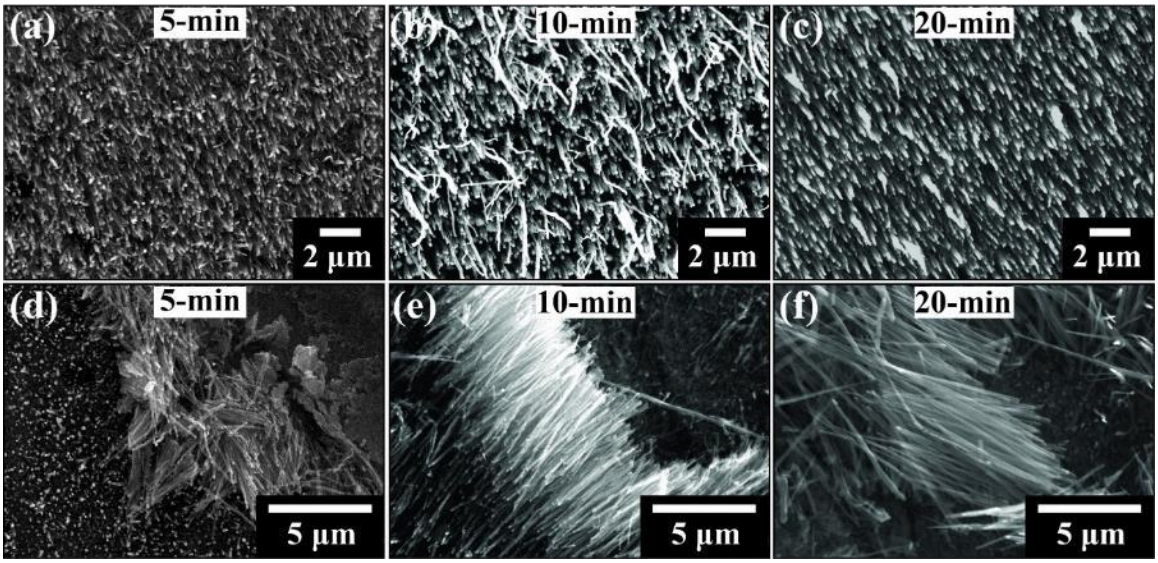

Figure 4.8. SEM images of VACNTs (tilted view and corresponding scratched area) synthesized on SS for (a) 5 min, (b) 10 min, and (c) 20 min, respectively. The other growth parameters (growth temperature of 700 °C, flow of C_2H_2 at 25 sccm, flow of NH_3 at 400 sccm, pressure of 7 Torr and plasma power of 75 W) were kept constant throughout the synthesis process. (d–f) Corresponding scratched areas showing the length of the CNTs.

to be 138.2 ± 24.5 nm, 139.7 ± 28.3 nm, and 132.1 ± 33.4 nm for the samples grown for 5 min (5-min sample), 10 min (10-min sample), and 20 min (20-min sample), respectively. We performed our experiments in the growth time range 5 to 20 min since an extended growth time (> 20 min) slowed down the growth rate of the VACNTs. The catalyst particles eventually lost their catalytic activity as the growth time increased. Moreover, prolonged exposure of the VACNTs to the intense plasma may also destroy the graphitization of the VACNTs giving rise to wall defects which can hinder the desired longer FE stability of

VACNT emitters. These results imply that growth time significantly affected the VACNTs length while synthesizing them by the PECVD method.

4.3.3 Micro/nanostructure analysis

The microstructure and chemical bonding of the VACNTs were studied by Raman spectroscopy. Typical Raman characteristic peaks at about 1348 cm^{-1} and 1590 cm^{-1} were observed. The former peak corresponds to the D-band, which is an index of disorder in the graphitic material. The later peak corresponds to the G-band, which indicates the crystallinity of the material [48]. The ratio of the D-band intensity to G-band intensity (I_D/I_G) can be used to estimate the quality of the sample. A high I_D/I_G ratio indicates the presence of structural imperfections such as pentagon and heptagon defects, as well as broken sp^2 bonds in the CNT walls [49]. In our Raman experiments, no significant variation in the I_D/I_G ratios was observed. The measured values were in the range of 0.978–0.987 for the VACNTs synthesized in the temperature range of 650–800 °C. This result indicates that the VACNTs synthesized at this temperature range have similar microstructure. The observed high values of I_D/I_G imply that the VACNTs were highly defective in structure, which may be accredited to the high growth rate of the VACNTs and the etching of VACNT walls by intense plasma. The VACNTs, synthesized by DC PECVD, with a high degree of imperfections, similar to our samples, were also reported by Baro *et al.* [49].

Low and high-resolution TEM images were also used to investigate the nanostructure of the as-synthesized VACNTs. Figure 4.9(a) represents the low-resolution TEM images of the VACNTs (the same sample as shown in Fig. 4.3(c)) which confirms the tubular structure of multi-walled CNTs with slightly different diameters. It is also

evident that each VACNT has a catalyst particle of varied sizes anchored at the tip. The TEM evidence is also in agreement with the SEM images shown in Figure 4.3, indicating the tip growth model [50]. Contrary to the melting point of their bulk counterparts, the nano-hills of metal catalysts melted at a lower temperature because of the size effect [51].

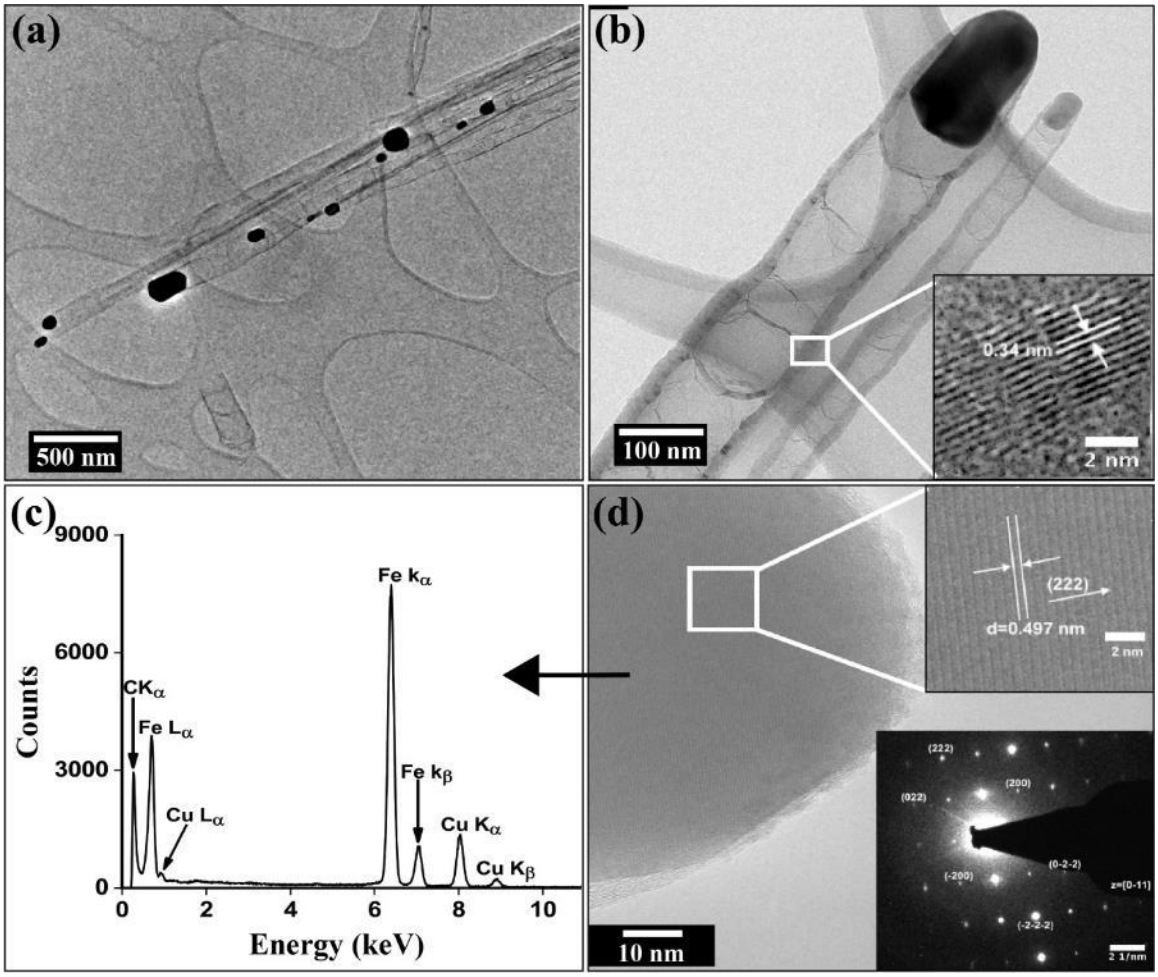

Figure 4.9. TEM images of as-synthesized VACNTs grown for 10 min at growth temperature 760 °C, chamber pressure 7 Torr, flow rate of C_2H_2 15 sccm, flow rate of NH_3 400 sccm, and plasma power of 70 W. (a) Low-resolution TEM image of CNTs with catalyst particles at the tip. (b) High-resolution TEM image showing CNTs with "bamboo-like" structure. Inset is a close- up view of the boxed area on the VACNT showing graphite layers of VACNT wall. (c) EDS spectrum showing the composition of the catalyst particle at the tip of a CNT shown in panel (d). The Cu peaks are from the TEM grid, not from the catalyst particle. (d) high-resolution TEM (HRTEM) image of the particle at the tip of VACNT enclosed by a few layers of graphitic layers. The insets on the upper and lower right sides of Figure 4.9(d) represent the HRTEM image and corresponding SAED pattern of the catalyst particle at the tip of the VACNT.

As mentioned earlier, during the synthesis process, carbon atoms or clusters of carbon atoms dissolved into the liquid-like nano-hills of metal catalyst and interacted with the metal atoms, leading to the weakening and subsequent rupturing of the bonds between the metal atoms [52]. The process may be enhanced by the ion (electron) irradiation process [53] since plasma was used as a synthesis parameter. As a result, the catalyst nano-hills were detached from the substrate and lifted off because of weak interaction between the substrate and nano-hills during the growth process. As smaller diameter VACNTs were attached to smaller catalyst particles, whereas larger VACNTs were attached to larger catalyst particles, the size of the catalyst nanoparticle (nano-hill) formed at the substrate controlled the diameter of the VACNT. The VACNTs in Figure 4.9(b) show a 'bamboo-like' structure with diameters at the bases slightly larger than at the tops.

The non-uniformity in diameter along the CNT length may be accredited to the changes in shape and size of the catalyst particles caused by the dissolution and precipitation of carbon during the growth process [50]. It has been reported that the formation of the 'bamboo-like' structure rather than a hollow tube is more favorable in the presence of a highly energetic nitrogen-rich environment [54]. In our experiment, the NH_3 plasma contained a significant amount of energetic nitrogen (N) atoms, which helped to clean the catalyst surface by proper bombardment. Hence, the bombardment can significantly increase the diffusion of carbon atoms or carbon clusters into the catalyst. At the same time, a significant number of N atoms can also diffuse into the catalyst. Upon precipitation of carbon atoms along with N atoms, the presence of N atoms led to the formation of pentagons along with the regular hexagons [55]. The N atoms can be incorporated into the VACNT wall during the synthesis process in three possible ways: (i)

insertion of an N atom into the regular hexagon by replacing one of the carbon atoms – called graphitic nitrogen atom (ii) sp^2 hybridized N atom, present at the defects of the graphitic sheet (VACNT wall) – called pyridinic nitrogen atom, and (iii) sp^3 hybridized N atom – called pyrrolic nitrogen atom, which forms pentagon instead of a regular hexagon, together with four other carbon atoms in the graphitic layers of VACNT [56].

Several researchers have reported that the N-incorporation by methods (i) and (ii) do not change the physical structure of the VACNT wall. However, N-incorporation by method (iii) has a profound effect on the tubular structure of the VACNTs, resulting in more defective, disordered, and bent VACNT [57, 58]. Hellgren *et al.* proposed a scheme to explain the formation of a 'fullerene-like' structure from the graphite layers because of the presence of sufficient nitrogen in the growth environment [59]. They suggested that incorporating sp^3-hybridized N-atoms (method (iii)) results in the formation of pentagons which help to bend the graphite layer. The N-incorporation by method (iii) eventually leads to the cross-linking between two adjacent graphitic planes through sp^3-coordinated carbon. Jang *et al.* also reported the presence of the sp^3-hybridized N–C bonds in the wall of bamboo-like CNTs more abundantly than the sp^2-hybridized N–C bonds when the nitrogen concentration is more than 5% in the growth environment [58].

The N atoms in the growth environment played a pivotal role in forming the 'bamboo-like' VACNTs shown in this study. The inset in Figure 4.9(b) represents the high-resolution TEM image of the well-graphitized multilayer of the VACNT wall. The separation between the adjacent layers was 0.340 nm which corresponds to the lattice fringe distance of the (002) graphitic plane, indicating a clear multi-walled VACNT. Figure

4.9(c) shows the EDS spectrum obtained from the catalyst particle present at the VACNT tip. The graph shows the main peaks of Fe, Cu, and C. Here, the Cu and C peaks were associated with the TEM sample grid and CNTs, respectively. The EDS spectrum suggests that the catalyst particle at the VACNT tip was pure Fe. The absence of oxygen in this spectrum rules out the possibility of the formation of Fe-oxides. Figure 4.9(d) represents the high-resolution TEM image of a catalyst particle present at the VACNT tip. The inset at the upper right side was the high magnification image of the selected area, as shown in the white box. This image shows the lattice plane distance of 0.497 nm which corresponds to the (222) lattice plane of body-centered cubic (bcc) crystal of Fe. The inset at the lower right side of Figure 4.9(d) displays the selected area diffraction (SAED) pattern of the Fe particle at the VACNT tip. The diffraction spots were indexed as (200), (220), and (222) planes of bcc Fe crystal along the [0−11] zone axis. The SAED result, along with the EDS spectrum shown in Figure 4.9(c), confirms the presence of a single crystalline Fe catalyst particle at the VACNT tip. Here, it is important to note that the Fe plays the dominant role as the catalyst during the VACNT synthesis process, as most VACNTs possess Fe at their tips.

According to the EDS taken from few other VACNT tip particles, weak signals of transition metals, such as Ni, Cr, and Mn, were also detected, dominated by the Fe. However, single-phase crystalline structures, as observed from the high-resolution TEM images, may suggest the presence of alloy (Fe-Ni-Cr-Mn) particles instead of an agglomeration of individual pure metal particles. Further research is needed to fully understand the chemical composition and crystal structure of the alloy catalyst nanoparticles. Hence, the presence of pure Fe or alloy particle at the VACNTs tip supports

the notion that catalyst nano-hills were lifted off and remained at the tip of the VACNTs during the synthesis process, as the elements mentioned above are the main constituents of the nano-hills revealed by the EDS spectrum shown in Figure 4.2(d).

Plasma-enhanced CVD (PECVD) has been demonstrated as a reliable method to synthesize uniform arrays of VACNTs on metallic and non-metallic substrates. In the VACNT synthesis by PECVD, the treatment to the polished SS under the flow of NH_3 gas generated the catalytically active nano-hills on the substrate surface. Carbon was released upon the hydrocarbon decomposition (e.g., C_2H_2) with the help of heat available from the plasma sheath and heater. The carbon dissolved and diffused into the catalyst nanoparticles. Finally, tube-like structures of carbon were formed as a result of carbon precipitation from the catalyst surface once a supersaturation was reached. The crystalline tubular structure called CNT, may or may not contain catalyst particles at the tip depending on the growth mechanism inherited, namely base growth or tip growth [50]. The electric field present in the plasma sheath helped to align the CNTs along its direction (perpendicular to the substrate surface and hence named vertical direction in our case) because VACNTs have highly anisotropic polarizability in the presence of an external field [60]. The efficient removal of amorphous carbon was also an important step to the synthesis of high-quality VACNTs. It is suggested that species like atomic hydrogen and high energy nitrogen species present in the plasma helped to etch the undesirable amorphous carbon deposited during the growth process [47]. The etching process has an advantage in keeping the catalyst particles free of amorphous carbon to get continuous access to hydrocarbon precursor gas.

4.3.4 Water treatment to VACNT arrays

It has been reported that the treatment of the self-standing high-density VACNT array with a volatile liquid helps to change the morphology of the array into individual bundles under the surface tension forces during the drying process [61, 62]. Such a particular morphology can enhance the field emission properties of VACNTs owing to their extended inter-bundle distance and the emission from the bundle as a whole [33]. It is important to mention that the bundling phenomenon can provide a platform to achieve maximum FE via minimizing charge screening effects from the surrounding VACNTs in a dense array. The as-synthesized VACNT arrays were submerged into deionized water (80 mL) for nine hours at room temperature to form bundled morphology.

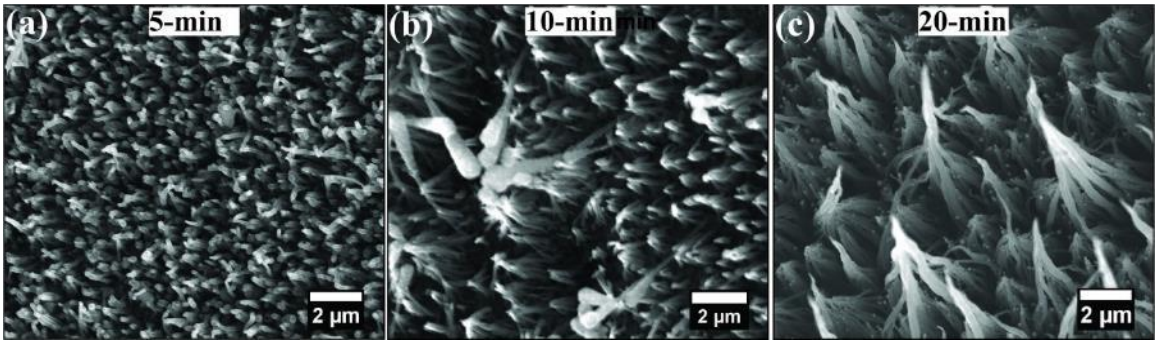

Figure 4.10. SEM images of (a) 5-min, (b) 10-min, and (c) 20-min sample showing bundling of VACNTs caused by surface tension during the drying process after treating with water for 9 h.

The water treatment to the VACNT arrays was performed in solution media, as described in section 4.2.2, which transformed the arrays into self-assembled tapered bundles of VACNTs, as shown in Figure 4.10. The change in morphology of the VACNT arrays was attributed to the surface tension of the deionized water, which caused the van der Waals forces between the deionized water and the VACNTs to pull the tip of VACNTs to each other while the roots remained attached on the substrate during the drying process

[63]. However, the bundling effect was not clearly noticeable in shorter VACNTs (Figure 4.10(a)) as they were robust enough to counter the surface tension forces, but the bundled structures were still present to some extent. It should be pointed out that the nine hours treatment to the VACNT arrays to form bundles was not strictly necessary, and the desired morphology could be accomplished within a few minute's treatments. However, the treatment was performed for nine hours to be consistent with the SnO_2 coating time on VACNTs so that the FE properties of the two different samples can be compared. The average inter-bundle distance was measured as about 3 μm for the 20-min sample, which was significantly larger than the distance between individual self-standing VACNTs of the as-synthesized samples. Apart from bundling, the water treatment might also remove amorphous carbon deposited on the sample surface during the PECVD growth process. The cleaning process could be beneficial for the FE application of VACNTs, as discussed in section 4.3.6.

4.3.5 Coating VACNT arrays with SnO_2 nanoparticles

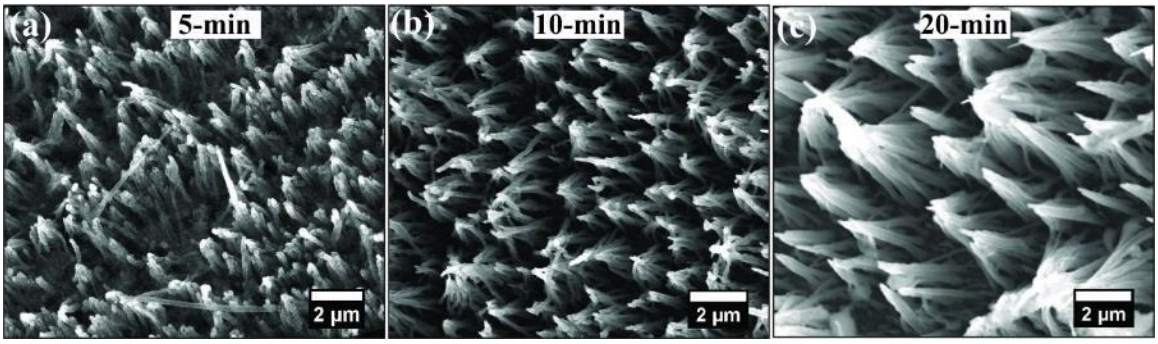

Figure 4.11. SEM images of (a) 5-min, (b) 10-min, and (c) 20-min sample showing conical bundle-like morphology of VACNTs after coating with SnO_2 nanoparticles for 9 h.

The as-synthesized VACNT arrays were coated with SnO_2 nanoparticles by using a facile wet-chemical method for different time durations such as nine and eleven hours to

understand the effect of coating time on SnO_2 nanoparticle size and coating thickness. The alignment of the VACNTs was significantly disturbed after the solution-based SnO_2 coating process compared to their pristine counterparts (i.e., the as-synthesized VACNT arrays). Figure 4.11 shows the structure change of the VACNT arrays after the SnO_2 coating process for nine hours, the original vertically standing CNTs formed cone-like bundles as the VACNT tips were attached. The bundling pattern was similar to that observed for water treatment, as shown in Figure 4.10. This bundling phenomenon was clearly presented for longer VACNTs, as shown in Figure 4.11(b-c), whereas it was not quite significant for shorter VACNTs, as shown in Figure 4.11(a).

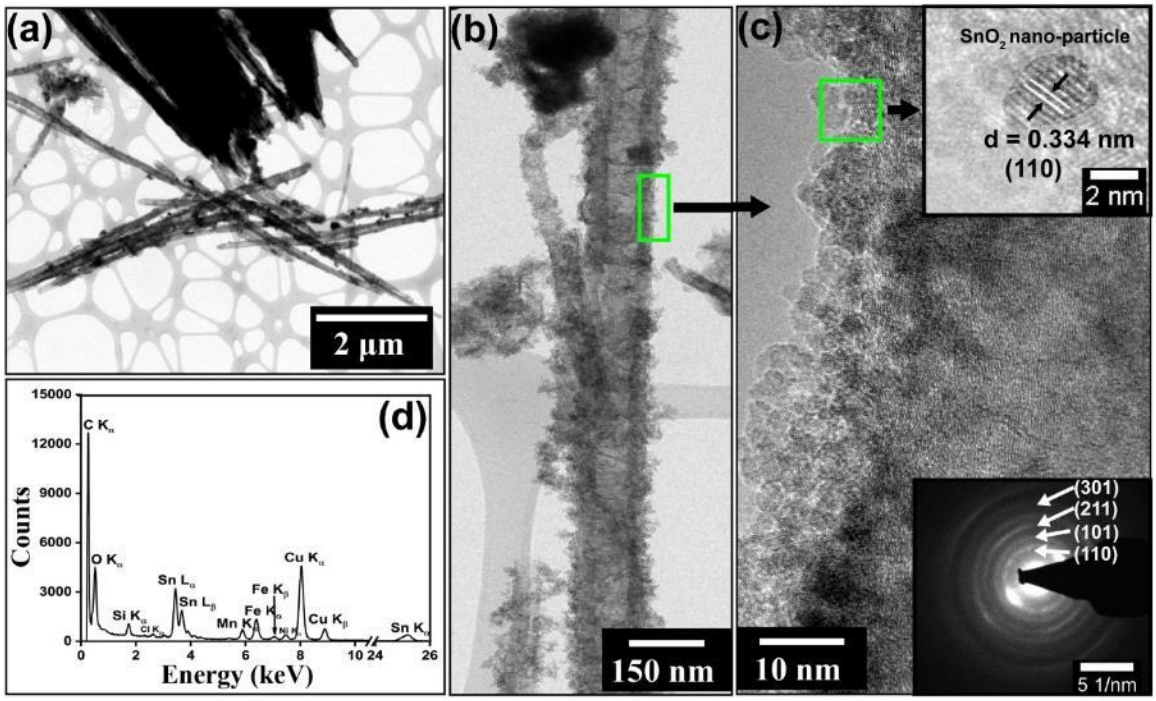

Figure 4.12. TEM images of the SnO_2 nanoparticles coated for 9 h on the surface of VACNTs grown for 10 min (a) Low-resolution TEM image of SnO_2-VACNTs bundle, (b) Magnified view of SnO_2 coated VACNT showing the SnO_2 coating layer on the VACNT surface (c) Close-up view of the boxed area indicated in (b), showing clearly the individual SnO_2 nanoparticles deposited on the VACNT surface. The inset on the top right side of (c) represents a high-resolution TEM image of a SnO_2 nanoparticle showing clear lattice fringes separated by a distance of 0.334 nm which corresponds to the (110) lattice plane of the SnO_2 crystal. The inset on the bottom right corner of (c) represents a SAED pattern showing the polycrystalline nature of SnO_2 nanoparticles layer. (d) EDS spectrum showing the composition of SnO_2-VACNTs composite.

High and low-resolution TEM images were used to study the distribution and morphology of the SnO_2 nanoparticles coated for nine and eleven hours on the surface of the VACNTs. Figure 4.12 shows TEM images of the 10-min sample after coating with SnO_2 nanoparticles for nine hours. It is clear from the TEM images that all VACNTs were thoroughly coated with SnO_2 nanoparticles forming a SnO_2-VACNT core-shell structure. Figure 4.12(a) represents a low-resolution TEM image of the SnO_2-VACNT bundle, whereas Figure 4.12(b) depicts a magnified view of a SnO_2-VACNT composite showing a coating layer of SnO_2 nanoparticles on the VACNT wall. As shown in Figure 4.12(c), the high-resolution TEM image demonstrates the individual crystalline SnO_2 nanoparticles deposited on the exterior of the VACNT wall. The average thickness of the coating was about 10 nm. The inset on the top right corner of Figure 4.12(c) displays a typical SnO_2 nanoparticle showing clear lattice fringes separated by a distance of 0.334 nm, which corresponds to the (110) lattice plane of the tetragonal SnO_2 crystal [64]. The inset at the bottom right corner of Figure 4.12(c) represents the selected area diffraction (SAD) pattern from the SnO_2-VACNT composite.

The distinct concentric rings were indexed as (110), (101), (211), and (301) corresponding to the tetragonal phases of polycrystalline SnO_2 nanoparticles. The presence of Sn and O in the EDS spectrum, as shown in Figure 4.12(d), further confirmed the presence of polycrystalline SnO_2 nanoparticles. However, the chemical analysis using EDS showed other elements, such as C, Si, Fe, Mn, Ni, and Cu, besides Sn and O in the coated multi-walled VACNT. The C signal was related to the multiwalled CNT, whereas a weak signal of Si could be from the following two sources: (1) contamination of the glass beaker as a result of reaction with the HNO_3 during the pretreatment of VACNTs or (2) interaction

of the strong C signal and Al, which is part of the collimator [65]. The strong Cu signal was from the TEM grid, whereas the weak signals of Fe, Mn, and Ni were expected from the SS substrate or the catalyst particles responsible for the VACNTs growth.

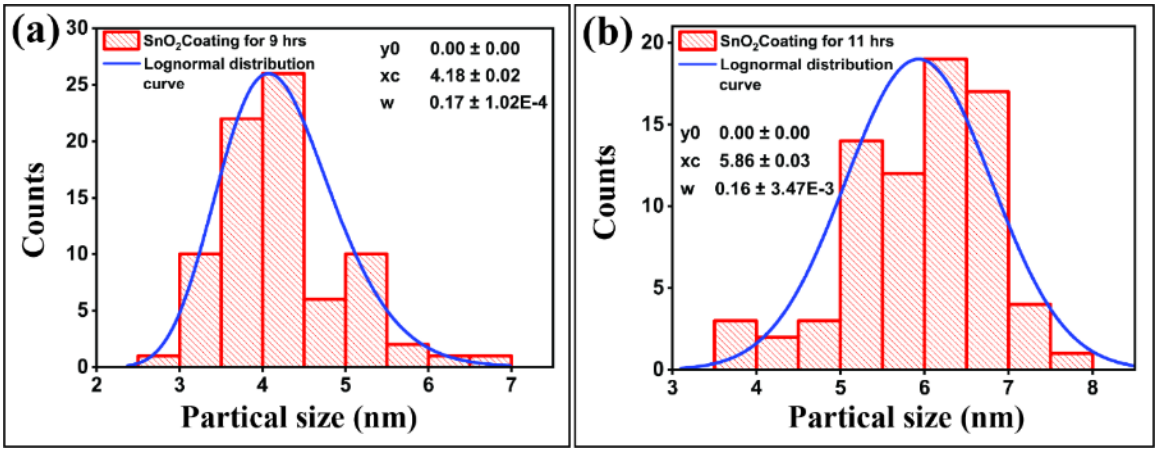

Figure 4.13. Particle size distribution of SnO_2 nanoparticles coated for (a) 9 h and (b) 11 h, on the surface of VACNTs grown for 10 min.

Figure 4.13(a-b) represents the distribution of the diameter of SnO_2 nanoparticles synthesized for nine and eleven hours, respectively. The histograms were created after a representative number of SnO_2 particles from the samples were counted. According to the diameter histogram, the average SnO_2 particle size increased with the increasing coating time. The average diameter (xc) of the SnO_2 particles for nine hours coated sample was found to be 4.18 nm with a standard deviation (w) of 0.17 nm, as shown in Figure 4.13(a). More than 90% of the particle diameters were found to be in the range from 3 to 5.5 nm. As shown in Figure 4.13(b), the average diameter (xc) of the SnO_2 particles for eleven hours coated sample was found to be 5.86 nm with the standard deviation (w) of 0.16 nm, and more than 90% of the particle diameters were observed to be in the range from 5 to 7.5 nm.

The as-synthesized multi-walled VACNTs were treated with HNO_3 before coating with SnO_2 nanoparticles to create carboxyl or hydroxyl functional groups. The hydrophilic functional groups are essential in achieving a uniform SnO_2 coating over the length of the VACNTs [66]. The synthesis of ultra-fine SnO_2 nanoparticles from an aqueous solution of $SnCl_2$ precursor can be accredited to the following chemical reaction [64]:

$$2SnCl_2 \cdot H_2O + O_2 \rightarrow 2SnO_2 + 4HCl \quad (4.1)$$

In brief, the SnO_2 phase formation mechanism and coating on the VACNT wall can be understood as follows. First, Sn^{2+} cations present in the precursor $SnCl_2$ aqueous solution were adsorbed on the negatively charged functional groups on the VACNT surface as a result of electrostatic interaction [67]. Then, the Sn^{2+} cations were oxidized to form SnO_2 nanoparticles in the presence of oxygen in the solution. The addition of a small amount of HCl in the precursor $SnCl_2$ aqueous solution was very crucial because it prevented the formation of tetratin hexhydroxide dichloride ($Sn_4(OH)_6Cl_2$) colloidal particles as a result of hydrolysis of $SnCl_2$ which would eventually lead to the formation of SnO instead of SnO_2 nanoparticles [68].

4.3.6 Field emission measurements

The field emission (FE) properties of the pristine, water treated, and SnO_2 coated VACNT arrays were measured by using a diode configuration method described in section 3.4.1 and section 4.2.3. Figure 4.14 shows the FE characteristics of the pristine and post-treated VACNT arrays. During the emission current density versus applied electric field (F–J) measurement, the first few F–J cycles showed unstable emission currents with a high fluctuation. This fluctuation can be accredited to the surface adsorbates (residual gas

molecules) present at the VACNTs tip as nano-protrusions, which lower the work function of the VACNTs tip and increase the field enhancement factor so that FE occurs at the much lower electric field than expected [69]. The emission current fluctuation can be stabilized through heating the VACNTs by applying high current densities during the first few F–J cycles to evaporate the adsorbates and the possible protruding long tubes [25]. A highly reproducible F–J characteristics of VACNT emitters were observed after the first five F–J cycles, so-called electrical conditioning.

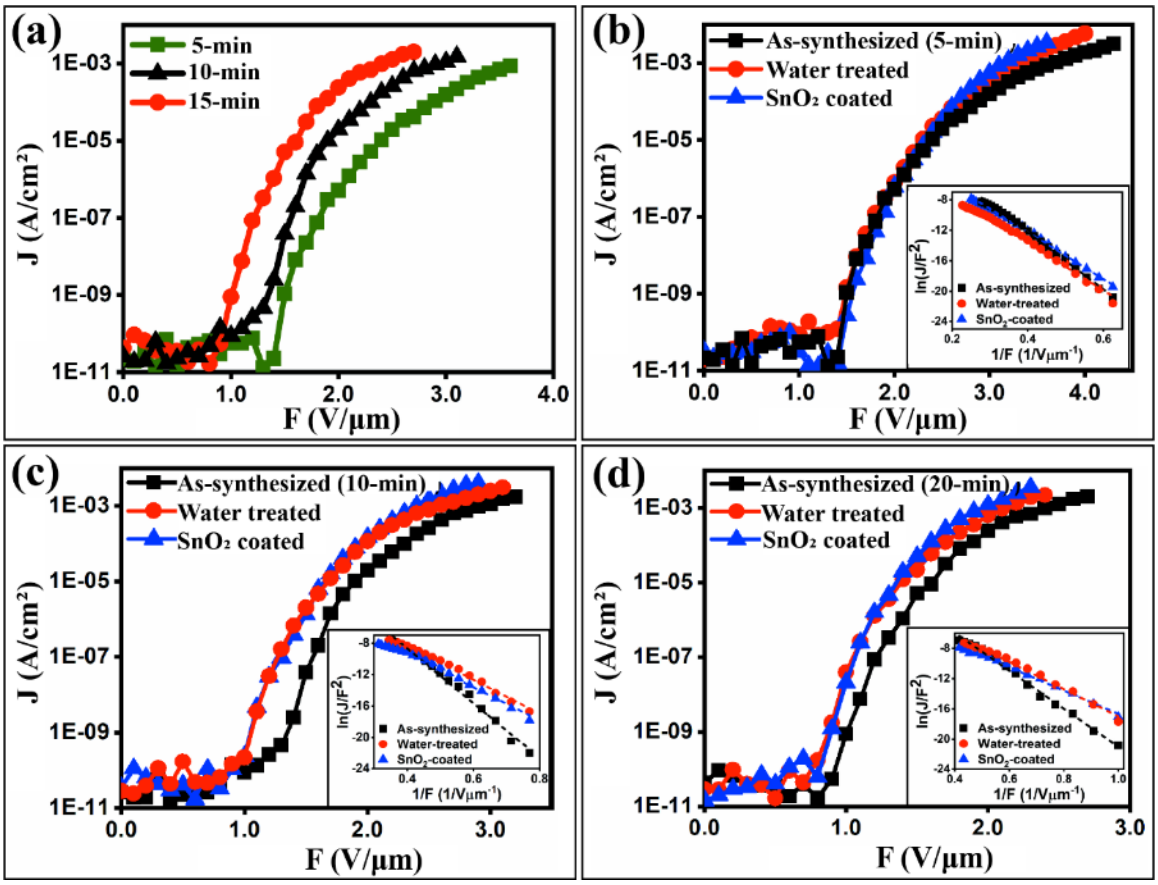

Figure 4.14. FE characteristics of as-synthesized, water-treated, and SnO_2-coated VACNTs. (a) Emission current density versus applied electric field (F–J plot) for the as-synthesized VACNTs grown for 5 min, 10 min, and 20 min. Comparative F–J plots for the as-synthesized, water-treated, and SnO_2-coated VACNTs samples synthesized for (b) 5 min, (c) 10 min, and (d) 20 min, respectively. The insets are their corresponding Fowler–Nordheim (F–N) plots.

The FE characteristics of the CNT-based field emitters were studied by the Fowler–Nordheim (F–N) equation represented by equations 2.1 and 2.2. The F–N equation helps to interpret the experimental results through the calculation of β values. However, it requires complete knowledge of the local work function of the emitters [70]. It is not easy to assess the parameter as the VACNTs possess subtle variations in the geometrical structure. It has been reported that the tip work function varies slightly for metallic (4.6 eV) and semiconducting (5.6 eV) CNTs, depending upon their helicity [71]. Different helicities and slight variation in the work function were expected in a dense mat of VACNTs array. Hence, the work function of the VACNT emitter was assumed to be 5 eV (work function of carbon) [18], and the field enhancement factors were calculated using the slopes of the fitted F–N plots, i.e., the graph of $\ln(J/F^2)$ versus 1/F, as shown in the insets of Figure 4.14(b-d). For practical applications and comparison purposes of the measured data, we define turn-on electric field (E_{TO}) and threshold electric field (E_{TH}) as the electric field required to produce the emission current densities of 1 $\mu A/cm^2$ and 1 mA/cm^2, respectively.

The FE properties of the various samples are presented in Table 4.1. Figure 4.14(a) represents the plot of emission current density versus applied electric field (F–J plot) of three pristine VACNTs samples with different average lengths. The samples demonstrated different FE characteristics according to their lengths. The E_{TO} for shorter VACNTs, such as the 5-min sample, was observed to be 2.14 V/μm, and its E_{TH} was found to be 3.53 V/μm. The E_{TO} for longer VACNTs, such as 10-min and 20-min samples, was 1.68 and 1.40 V/μm, respectively, whereas the E_{TH} was recorded as 3.00 and 2.31 V/μm, respectively. As the average length of the VACNTs was increased, better FE performance

(i.e., lower values of E_{TO} and E_{TH}) was observed, as shown in Figure 4.14(a). The field enhancement factor (β) for pristine 5-min, 10-min, and 20-min samples was calculated as 2357, 2668, and 3046, respectively. The straight lines observed in the F–N plots (insets of Figure 4.14(b-d)) indicate that the observed FE phenomenon was mainly because of the quantum mechanical tunneling process [72]. The geometrical field enhancement factor (β') of an individual VACNT emitter can be estimated by the ratio of the length to its radius [44]. In our case, the average radius of the VACNTs for the three samples mentioned above was similar, and therefore, the length was the only critical factor that can affect the β'. The increased β values for the longer VACNTs agree with the geometrical β' estimation. However, the large inconsistency in the experimental and geometrical β beta values (e.g., β = 3046 and β' = 107 for 20-min sample) suggests that the quantum tunneling was not the sole mechanism responsible for the observed FE performance. The VACNT tip may not only be the area where the FE process occurs. Chhowalla et al. suggested that a triple junction between the substrate, base of the VACNTs, and vacuum can force the electrons to be emitted to the vacuum [45].

Figure 4.14(b-d) shows the F–J plots for the pristine, water-treated, and SnO_2-coated VACNTs synthesized for 5, 10, and 20 min, respectively. The insets are their corresponding F–N plots. In the case of 5-min samples, the E_{TO} values were reasonably similar; however, the E_{TH} values were improved (decreased) as the pristine samples were treated with water and coated with SnO_2 nanoparticles. Further, the field enhancement factors were calculated as 2357, 2449, and 2486 for pristine, water-treated, and SnO_2-coated samples, respectively. For longer VACNTs, such as 10 and 20-min samples, significant improvement in the FE performance was observed after the posttreatments to

the as-synthesized VACNTs arrays, as shown in Figure 4.14(c-d). For example, the E_{TO} for the as-synthesized 10-min sample was 1.68 V/μm, which was lowered to 1.45 and 1.43 V/μm for the water-treated and SnO_2-coated samples, respectively. The E_{TH} was improved after the post-treatments; the values were measured to be 3.00, 2.58, and 2.50 V/μm for as-

Table 4.1. FE properties of as-synthesized, water-treated and SnO_2 coated VACNT emitters.

Sample	Before stability test			After stability test		
	E_{TO}(V/μm)	**E_{TH}**(V/μm)	β	**E_{TO}**(V/μm)	**E_{TH}**(V/μm)	β
5-min						
As-synthesized	2.14	3.53	2357	2.35	3.85	1991
Water-treated	2.12	3.39	2449	2.37	3.90	2044
SnO_2-coated	2.12	3.30	2486	2.34	3.80	2015
10-min						
As-synthesized	1.68	3.00	2668	1.83	3.26	2359
Water-treated	1.45	2.58	3391	1.65	2.61	2818
SnO_2-coated	1.43	2.50	3451	1.62	2.58	2826
20-min						
As-synthesized	1.40	2.31	3046	1.64	2.74	2979
Water-treated	1.19	2.20	4670	1.41	2.65	4020
SnO_2-coated	1.18	2.01	4712	1.37	2.58	4109

synthesized, water-treated, and SnO_2-coated samples, respectively. Furthermore, the field enhancement factor was increased considerably after the post treatments, and the values were 2668, 3391, and 3451 for the as-synthesized, water-treated, and SnO_2-coated samples, respectively. A very similar FE performance trend to that of the 10-min samples was observed for the 20-min samples, as shown in Figure 4.14(d). The lowest E_{TO} = 1.18 V/μm, E_{TH} = 2.01 V/μm, and the highest β = 4712 among all the samples along with the maximum

emission current density of about 7 mA/cm^2 at 2.50 V/μm were recorded for the SnO_2-coated 20-min sample.

The main reason for the enhanced FE performance from the post-treated samples was the restructuring of the VACNT array morphology into individual sharp conical bundles, as shown in Figure 4.10 and 4.11. The result also implies that a bundle emits as a whole rather than individual VACNTs. The bundling alleviates the charge screening effect by increasing the distance between the effective emitters. For example, an inter-tube distance of about 0.3 μm was measured for the pristine 20-min sample and after the water treatment and SnO_2 coating, and the inter-bundle distance was measured to be about 3 μm. An optimum ratio of CNT height and inter-tube distance (l/s) has been suggested as 1.5:1 [73] or 1:2 [72] for a high field amplification. The l/s in our case was 2.7:1 (after the post-treatments to pristine 20-min sample), which is much close to the ideal ratio compared to that for pristine sample (about 27:1). As a result, the field enhancement factor was improved significantly, and consequently, much lower values of E_{TO} and E_{TH} were observed compared to that for the pristine samples. Gupta *et al.* have reported low E_{TO} (0.6 V/μm at 1 μA/cm^2) and E_{TH} (0.7 V/μm at 10 μA/cm^2) from an array of VACNT-based square pillar of several millimeters high and 500 μm wide [74]. However, the total emission current density was rather low (4 mA/cm^2) regarding the millimeter long VACNTs because the field emission came mainly from the edge rather than the tip of the flat pillar structured emitter.

Wang *et al.* observed improved FE properties (E_{TO} = 0.73 V/μm at 10 μA/cm^2, E_{TH} = 1.29 V/μm at 10 mA/cm^2, and total emission current density of about 30 mA/cm^2) from

dense VACNT-based pillar structure (height 30 µm, diameter 20 µm, and l/s = 1:2) because of the minimum screening effect [75]. Hazra *et al.* reported extremely low E_{TO} (0.16 V/µm at 10 µA/cm^2) and impressively high emission current density of about 1.5 A/cm^2 at 0.3 V/µm from the VACNT-based pillar structure of height 132 µm and base diameter 80 µm [76]. It is important to note that such an impressive result was possible only after the plasma treatment to the VACNT pillars to create an extremely sharp tip of the pillar structure (tip diameter < 1 µm). The reported results indicate that isolated VACNT pillars have much better FE performance than uniform VACNT arrays. Our research findings agree well with the reported results. Our method for converting uniform VACNT arrays into bundled arrays is efficient and straightforward and can be easily applied to the large area of VACNT arrays. The FE performance of our bundled VACNT arrays is better or comparable to the reported results despite the low height and the smaller inter-bundle distance in an array. We expect that the bundling of VACNT arrays with low density and long length will further improve the FE performance.

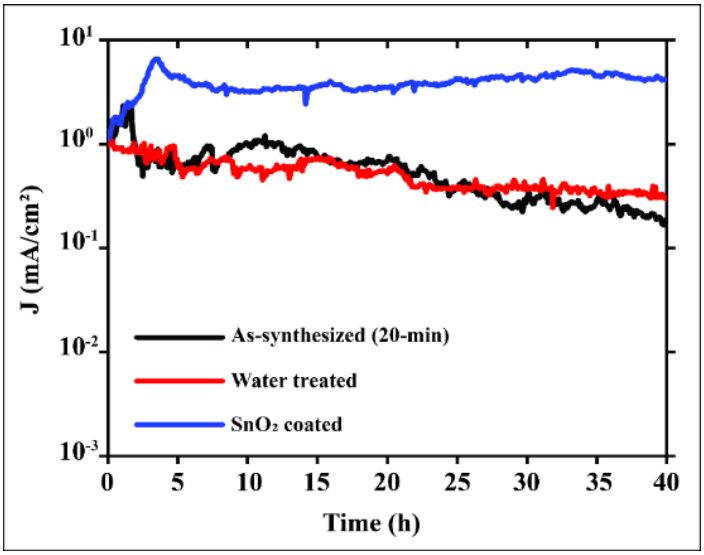

Figure 4.15. Stability comparison of the as-synthesized, water-treated, and SnO_2-coated VACNTs synthesized for 20 min.

It is also worth mentioning the F–J behavior of water-treated and SnO_2-coated (10 and 20-min) samples at the higher emission field region. At the higher applied electric field region (i.e., beyond the E_{TO}), the F–J curves for water-treated samples are saturated faster than those for the SnO_2-coated samples. As a result, the lowest E_{TH} values were observed for SnO_2-coated samples compared to water-treated and pristine samples. The slower saturation of the F–J curves for the SnO_2-coated samples at the higher field region could be ascribed to the protection against the structural failure of VACNT emitters by SnO_2 coating caused by Joules heating during the FE process.

We also performed the temporal measurement of the emission current density for pristine and post-treated 20-min samples. During the experiments, the voltage was applied so that the initial emission current density of 1 mA/cm^2 was recorded for all the samples. The applied voltage was kept constant meanwhile recording the emission current density for 40 hours. The SnO_2-coated sample showed a stable emission current during the stability test period, indicating a superior FE stability among the three samples, as shown in Figure 4.15. The emission current density from the pristine and water-treated VACNTs arrays was degraded rapidly with time than that of the SnO_2-coated sample. The mechanism for the superior FE stability of the SnO_2-coated VACNTs emitter was similar to that of CNTs coated with a thin layer of wide bandgap semiconducting material such as ZnO [77], RuO_2 [36], and TiO_2 [78]. The defective sites formed on the VACNTs caused by the intense plasma bombardment during the PECVD growth process were responsible for the poor electron emission lifetime of the pristine and water-treated VACNT arrays. In the case of SnO_2-coated VACNT emitters, however, the defects on the VACNTs were covered by the uniform SnO_2 layer. This SnO_2 layer protects the defective VACNTs from the destructive

bombardment of energetic ions and radicals created in the emission process, as well as residual oxygen molecules in the chamber. Also, it is to be noted that the FE performance from our samples, even after electrical annealing (EA) for 40 hours, did not degrade significantly (see in Table 4.1). The consistency in the FE performance after the EA implies no substantial change in the morphology of the bundled emitters, which was further confirmed by the SEM images taken after the EA process.

The CNT structure is made of sp^2 bonding between carbon atoms. The minimum energy required to remove a carbon atom from the structure is ~ 17 eV [79], and the melting point of CNTs is very high (~ 4800 K) [80]. Hence, it was tough to change the structure of CNTs, even at a large electric field. However, the eventual failure of the CNT emitters was inevitable at a specific electric field. Doytcheva *et al.* performed an in situ TEM investigation on the structural failure in freestanding multiwalled CNTs. They observed that CNTs suffered structural changes only after a certain current level but not gradually [81]. Interestingly, they observed an increase in current level at a constant voltage followed by a shortening of the CNT as a consequence of tip failure, which resulted in a current drop. We also observed similar behavior in the emission current during the first few hours for the SnO_2-coated sample, as shown in Figure 4.15, where emission current was increased first and then decreased, followed by a stable FE performance. Doytcheva *et al.* also suggested a critical current (i.e., a maximum current an individual CNT can withstand without undergoing structural failure) of 2–15 μA for CNTs with diameters in the range of 5–20 nm and a much higher critical current of 40–250 μA for CNTs with diameters about 30 nm. Hence, the critical current for a CNT increases as the diameter increase. The average diameter of the VACNTs synthesized in our experiment was in the range of about 132–140

nm, and hence, they should be able to conduct high current without structural degradation. Besides, robust contact between VACNT emitters and the substrate allowed an easy and sufficient heat transfer, which may prevent the VACNTs from damage caused by Joule heating. Therefore, the excellent emission current stability for such a long period from our sample can be attributed to the lower thermal stress, high critical current, uniform local electric field for many emission sites (bundles), strong adhesion of VACNTs to the SS substrate, and coating of emitters by crystalline SnO_2 nanoparticles.

4.3.7 Electrostatic field distribution

To further support our conclusions, we simulated the electrostatic field distribution for a single VACNT, an array of individual VACNTs, and bundled VACNTs with different numbers of VACNTs per bundle, as shown in Figure 4.16. Figure 4.16(a) represents the electrostatic field distribution at the tip of a single VACNT. The local electric field was found to be the strongest (~ 455 V/μm) compared to other such as array and bundled structures. The strongest field was evident because there were no other VACNTs to affect via the screening effect. The presence of the strongest electric field was well supported because most field penetration occurred around the single VACNT emitter, as shown in Figure 4.16(a). In the VACNTs array (Figure 4.16(b)), the local electric field at the tip of emitters was recorded as ~ 188 V/μm. The remarkable drop in the electric field strength was because of the screening effect from the neighboring VACNTs in the closely packed array. The screening effect was evident from the weak penetration of the equipotential lines between the VACNT emitters, as shown in Figure 4.16(b). On the other hand, the local electric field was 355 V/μm for the bundled structure with 9 VACNTs per bundle (Figure

4.16(c)). It was ~89% increase in the local electric field strength compared to that for the closely packed VACNT array. The significant improvement in the local electrostatic field can be attributed to the increased inter-bundle distance (0.9 μm), which can lower the screening effect [33, 82].

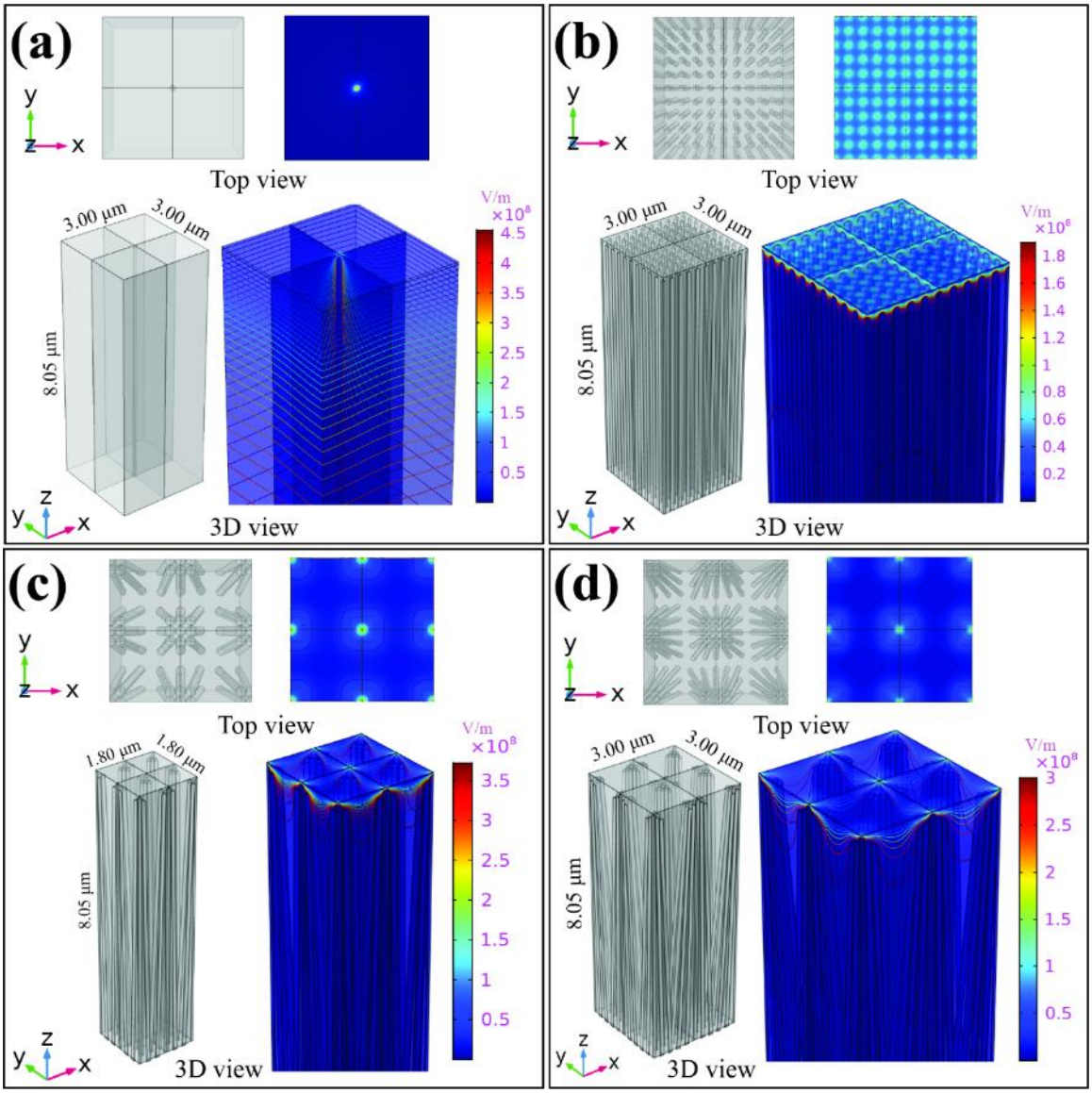

Figure 4.16. Electrostatic field distribution (simulation result) for a (a) single VACNT, (b) an array of individual VACNTs, (c) bundled VACNTs with 9 VACNTs per bundle, and (d) bundled VACNTs with 25 VACNTs per bundle.

We also simulated the local electric field distribution for the bundled structures having 17 VACNTs per bundle and 25 VACNTs per bundle (Figure 4.16(d)) to study how the number of VACNTs in a bundle affects the FE process. The maximum local electric field (E_{max}) versus emitter morphology is graphed in Figure 4.17. The graph shows that a single VACNT has the highest local electric field, and the closely packed VACNTs array has the lowest local electric field. For VACNT bundles, the array with 9 VACNTs per bundle displayed the highest local electric field, and the field decreased as the number of VACNTs in a bundle increased. Therefore, the simulation result suggests that the bundled field emitters with a smaller number of emitters per bundle (e.g., 9 VACNTs/per bundle) can deliver better FE performance than that from the dense emitters array and bundled emitters with a larger number of VACNTs per bundle. Our simulated result for pristine and post-treated VACNTs (bundled structures) agrees well with our experimental results. Our current experimental technique cannot control the number of VACNTs in a bundle. However, the bundling through simple water treatment and SnO_2 coating, as described in this work, can be a promising way to optimize the FE performance of VACNT arrays.

As the VACNTs were synthesized directly on the SS substrate without a buffer layer, the contact resistance between the substrate and CNTs was expected to be reduced substantially. The reduced contact resistance facilitated an easier electron transport in the interface between the substrate and the CNTs, through the CNTs, and finally emission into the vacuum, enhancing the overall FE performance. Also, the VACNTs synthesized by our method may be doped with nitrogen since an ammonia plasma was used during the experiment. Chen et al. conducted an XPS N 1S spectra study on CNTs treated by the NH_3 plasma and demonstrated the presence of carbon-nitrogen bonding on the CNTs wall [27].

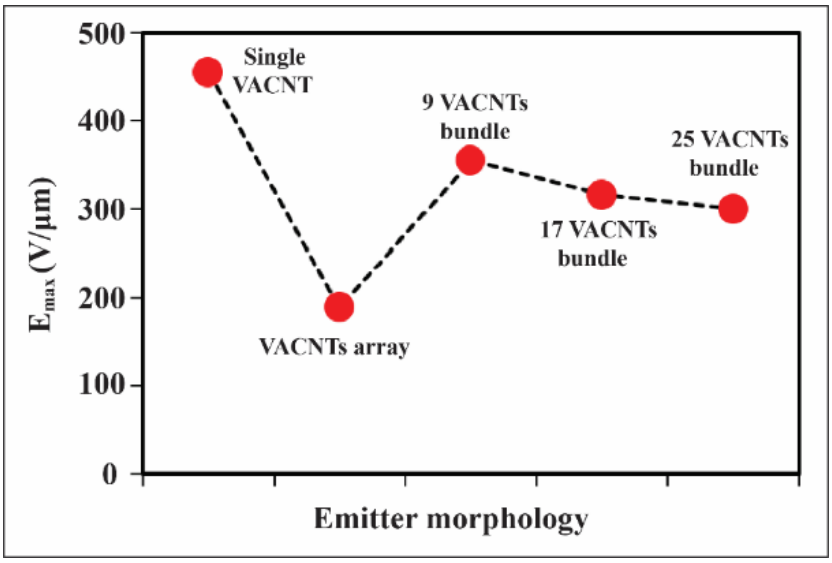

Figure 4.17. Change of electrostatic field as a function of emitter morphology.

They also revealed doped nitrogen even for untreated CNTs as they used the ammonia plasma during the synthesis process. The nitrogen doping on the VACNTs was expected in our samples as we also used ammonia plasma during the experiments. It has been reported that the FE properties of CNTs can be improved by nitrogen doping [83]. Hence, the combined effects of low contact resistance between the substrate and the VACNTs, highly conductive substrate, nitrogen-doped VACNTs, bundled morphology, and SnO_2 coating greatly enhanced the FE properties of the multiwalled VACNTs synthesized on the SS substrate by PECVD.

4.4 Conclusions

In summary, we developed a facile and effective method of synthesizing high-quality VACNT arrays directly on the stainless steel without an external metallic catalyst layer on the substrate surface using the PECVD method. The results are significantly better than those reported in previous literature regarding the uniform length, good alignment, and uniform coverage of VACNTs over the substrate surface. A careful study of surface

morphology of the substrate before VACNTs growth, as revealed by AFM and TEM images, underlines the occurrence of important surface evolution caused by ramping temperature in the presence of NH_3 gas to form the uniform nano-hills, which played a crucial role in the VACNT nucleation and growth process. The TEM analysis and EDS examination confirmed the VACNT tip particle to be pure Fe in most VACNTs. However, alloy particles of other transition metals (Ni, Cr, Mn) were also present in a few other catalyst particles. The transition metal (e.g., Fe, Ni, Cr, Mn) particle allows the dissolution and precipitation of carbon at an elevated temperature, which eventually lift-off and remains at the tip of the VACNT during the growth process, the tip-growth mechanism. Furthermore, VACNTs were successfully coated with SnO_2 nanoparticles by a facile wet-chemical method.

The FE properties of VACNTs with different lengths were compared, and the longer VACNTs (20-min sample) demonstrated better FE performance in terms of low turn-on electric field (E_{TO} = 1.40 V/μm) and low threshold electric field (E_{TH} = 2.31 V/μm) as well as higher field enhancement. The longer VACNTs resulted in a higher aspect ratio, leading to a more significant field enhancement. The post-treatment to the pristine VACNTs, such as water treatment and SnO_2-coating, significantly enhanced the FE properties (the E_{TO} and E_{TH} were 1.18 and 2.01 V/μm, respectively, for SnO_2-coated 20-min sample) because of the structural change, which significantly reduced the screening effect. The bundling effect of VACNTs on the local electric field was simulated, and the experimental and simulation results agree well. Longer VACNTs coated with SnO_2 nanoparticles presented superior FE stability among all the tested samples. The superior FE stability can be attributed to the mechanical strength enhancement and chemical

stability of the VACNT emitters. The present method of direct synthesis of VACNTs arrays on the conductive substrate such as stainless steel and their structural modification through water treatment and SnO_2 nanoparticles coating may find potential application in the field emission devices that require low bias and longer emission current stability.

References

[1] Iijima S., Helical microtubules of graphitic carbon. *Nature* **1991,** 354 (6348), 56.

[2] Bockrath M., Cobden D.H., McEuen P.L., Chopra N.G., Zettl A., Thess A. and Smalley R.E., Single-electron transport in ropes of carbon nanotubes. *Science* **1997,** 275 (5308), 1922.

[3] Qian D., Wagner G.J., Liu W.K., Yu M.F. and Ruoff R.S., Mechanics of carbon nanotubes. *Applied Mechanics Reviews* **2002,** 55 (6), 495.

[4] Hone J., Llaguno M.C., Biercuk M.J., Johnson A.T., Batlogg B., Benes Z. and Fischer J.E., Thermal properties of carbon nanotubes and nanotube-based materials. *Applied Physics A: Materials Science & Processing* **2002,** 74 (3), 339.

[5] Lin C.L., Chen C.F. and Shi S.C., Field emission properties of aligned carbon nanotubes grown on stainless steel using CH4/CO2 reactant gas. *Diamond and Related Materials* **2004,** 13 (4-8), 1026.

[6] Ng S.H., Wang J., Guo Z.P., Chen J., Wang G.X. and Liu H.K., Single wall carbon nanotube paper as anode for lithium-ion battery. *Electrochimica Acta* **2005,** 51 (1), 23.

[7] Moore J.J., Kang J.H. and Wen J.Z., Fabrication and characterization of single walled nanotube supercapacitor electrodes with uniform pores using electrophoretic deposition. *Materials Chemistry and Physics* **2012,** 134 (1), 68.

[8] Yeow J.T.W. and She J.P.M., Carbon nanotube-enhanced capillary condensation for a capacitive humidity sensor. *Nanotechnology* **2006,** 17 (21), 5441.

[9] Chen Y., Lv Z., Xu J., Peng D., Liu Y., Chen J., Sun X., Feng C. and Wei C., Stainless steel mesh coated with MnO2/carbon nanotube and polymethylphenyl siloxane as low-cost

and high-performance microbial fuel cell cathode materials. *Journal of Power Sources* **2012,** 201, 136.

[10] Wei J., Jia Y., Shu Q., Gu Z., Wang K., Zhuang D., Zhang G., Wang Z., Luo J., Cao A. and Wu D., Double- walled carbon nanotube solar cells. *Nano Lett* **2007,** 7 (8), 2317.

[11] Li J., Papadopoulos C. and Xu J., Growing Y-junction carbon nanotubes. *Nature* **1999,** 402, 253.

[12] Choi W.B., Chung D.S., Kang J.H., Kim H.Y., Jin Y.W., Han I.T., Lee Y.H., Jung J.E., Lee N.S., Park G.S. and Kim J.M., Fully sealed, high-brightness carbon-nanotube field-emission display. *Applied Physics Letters* **1999,** 75 (20), 3129.

[13] Baughman R.H., Zakhidov A.A. and Heer W.A.d., Carbon Nanotubes—the Route Toward Applications. *Science* **2002,** 297 (5582), 787.

[14] Yue G.Z., Qiu Q., Gao B., Cheng Y., Zhang J., Shimoda H., Chang S., Lu J.P. and Zhou O., Generation of continuous and pulsed diagnostic imaging x-ray radiation using a carbon-nanotube-based field-emission cathode. *Applied Physics Letters* **2002,** 81 (2), 355.

[15] Morassutto M., Tiggelaar R.M., Smithers M. and Gardeniers J.G., Vertically aligned carbon nanotube field emitter arrays with Ohmic base contact to silicon by Fe-catalyzed chemical vapor deposition. *Materials today communications* **2016,** 7, 89.

[16] Bonard J.-M., Kind H., Stöckli T. and Nilsson L.-O., Field emission from carbon nanotubes: the first five years. *Solid-State Electronics* **2001,** 45 (6), 893.

[17] Bonard J.M., Croci M., Klinke C., Kurt R., Noury O. and Weiss N., Carbon nanotube films as electron field emitters. *Carbon* **2002,** 40 (10), 1715.

[18] Kurilich M.R., Thapa A., Moilanen A., Miller J.L., Li W. and Neupane S., Comparative study of electron field emission from randomly-oriented and vertically-aligned carbon nanotubes synthesized on stainless steel substrates. *Journal of Vacuum Science & Technology B, Nanotechnology and Microelectronics: Materials, Processing, Measurement, and Phenomena* **2019,** 37 (4), 041202.

[19] Rinzler A., Hafner J., Nikolaev P., Nordlander P., Colbert D., Smalley R., Lou L., Kim S. and Tománek D., Unraveling nanotubes: field emission from an atomic wire. *Science* **1995,** 269 (5230), 1550.

[20] De Heer W.A., Chatelain A. and Ugarte D., A carbon nanotube field-emission electron source. *science* **1995,** 270 (5239), 1179.

[21] Teo K.B.K., Chhowalla M., Amaratunga G.A.J., Milne W.I., Pirio G., Legagneux P., Wyczisk F., Pribat D. and Hasko D.G., Field emission from dense, sparse, and patterned arrays of carbon nanofibers. *Applied Physics Letters* **2002,** 80 (11), 2011.

[22] Saito Y. and Uemura S., Field emission from carbon nanotubes and its application to electron sources. *Carbon* **2000,** 38 (2), 169.

[23] Melechko A.V., Merkulov V.I., McKnight T.E., Guillorn M.A., Klein K.L., Lowndes D.H. and Simpson M.L., Vertically aligned carbon nanofibers and related structures: Controlled synthesis and directed assembly. *Journal of Applied Physics* **2005,** 97 (4), 3.

[24] Lin P.H., Sie C.L., Chen C.A., Chang H.C., Shih Y.T., Chang H.Y., Su W.J. and Lee K.Y., Field emission characteristics of the structure of vertically aligned carbon nanotube bundles. *Nanoscale research letters* **2015,** 10 (1), 297.

[25] Semet V., Binh V.T., Vincent P., Guillot D., Teo K.B.K., Chhowalla M., Amaratunga G.A.J., Milne W.I., Legagneux P. and Pribat D., Field electron emission from individual carbon nanotubes of a vertically aligned array. *Applied Physics Letters* **2002,** 81 (2), 343.

[26] Neupane S., Lastres M., Chiarella M., Li W., Su Q. and Du G., Synthesis and field emission properties of vertically aligned carbon nanotube arrays on copper. *Carbon* **2012,** 50 (7), 2641.

[27] Chen G., Neupane S., Li W., Chen L. and Zhang J., An increase in the field emission from vertically aligned multiwalled carbon nanotubes caused by NH3 plasma treatment. *Carbon* **2013,** 52, 468.

[28] Okuyama H., Iwata N. and Yamamoto H., Growth of Vertically Aligned Carbon Nanotubes Depending on Thickness of Catalyst Films by Plasma-Enhanced Chemical Vapor Deposition. *Molecular Crystals and Liquid Crystals* **2007,** 472 (1), 209.

[29] Talapatra S., Kar S., Pal S.K., Vajtai R., Ci L., Victor P., Shaijumon M.M., Kaur S., Nalamasu O. and Ajayan P.M., Direct growth of aligned carbon nanotubes on bulk metals. *Nat Nanotechnol* **2006,** 1 (2), 112.

[30] Sano N., Hori Y., Yamamoto S. and Tamon H., A simple oxidation–reduction process for the activation of a stainless steel surface to synthesize multi-walled carbon nanotubes and its application to phenol degradation in water. *Carbon* **2012,** 50 (1), 115.

[31] Hashempour M., Vicenzo A., Zhao F. and Bestetti M., Direct growth of MWCNTs on 316 stainless steel by chemical vapor deposition: Effect of surface nano-features on CNT growth and structure. *Carbon* **2013,** 63, 330.

[32] Masarapu C. and Wei B., Direct Growth of Aligned Multiwalled Carbon Nanotubes on Treated Stainless Steel Substrates. *Langmuir* **2007,** 23 (17), 9046.

[33] Pandey A., Prasad A., Moscatello J., Ulmen B. and Yap Y.K., Enhanced field emission stability and density produced by conical bundles of catalyst-free carbon nanotubes. *Carbon* **2010,** 48 (1), 287.

[34] Li X., Niu J., Zhang J., Li H. and Liu Z., Labeling the Defects of Single-Walled Carbon Nanotubes Using Titanium Dioxide Nanoparticles. *J. Phys. Chem. B* **2003,** 107, 2453.

[35] Green J.M., Dong L., Gutu T., Jiao J., Conley J.F. and Ono Y., ZnO-nanoparticle-coated carbon nanotubes demonstrating enhanced electron field-emission properties. *Journal of Applied Physics* **2006,** 99 (9), 094308.

[36] Chen C.A., Lee K.Y., Chen Y.M., Chi J.G., Lin S.S. and Huang Y.S., Field emission properties of RuO2 thin film coated on carbon nanotubes. *Vacuum* **2010,** 84 (12), 1427.

[37] Chakrabarti S., Pan L., Tanaka H., Hokushin S. and Nakayama Y., Stable field emission property of patterned MgO coated carbon nanotube arrays. *Japanese Journal of Applied Physics* **2007,** 46 (7R), 4364.

[38] Sridhar S., Tiwary C., Vinod S., Taha-Tijerina J.J., Sridhar S., Kalaga K., Sirota B., Hart A.H.C., Ozden S., Sinha R.K., Harsh, Vajtai R., Choi W., Kordas K. and Ajayan P.M., Field Emission with Ultralow Turn On Voltage from Metal Decorated Carbon Nanotubes. *ACS Nano* **2014,** 8 (8), 7763.

[39] Vander Wal R.L. and Hall L.J., Carbon nanotube synthesis upon stainless steel meshes. *Carbon* **2003,** 41 (4), 659.

[40] Baddour C.E., Upham D.C. and Meunier J.-L., Direct and repetitive growth cycles of carbon nanotubes on stainless steel particles by chemical vapor deposition in a fluidized bed. *Carbon* **2010,** 48 (9), 2652.

[41] Baddour C.E., Fadlallah F., Nasuhoglu D., Mitra R., Vandsburger L. and Meunier J.-L., A simple thermal CVD method for carbon nanotube synthesis on stainless steel 304 without the addition of an external catalyst. *Carbon* **2009,** 47 (1), 313.

[42] Li G., Synthesis of well-aligned carbon nanotubes on the NH3 pretreatment Ni catalyst films. *Russian Journal of Physical Chemistry A* **2010,** 84 (9), 1560.

[43] Abad M.D., Sánchez-López J.C., Berenguer-Murcia A., Golovko V.B., Cantoro M., Wheatley A.E.H., Fernández A., Johnson B.F.G. and Robertson J., Catalytic growth of

carbon nanotubes on stainless steel: Characterization and frictional properties. *Diamond and Related Materials* **2008,** 17 (11), 1853.

[44] Neupane S., Yang Y., Li W. and Gao Y., Synthesis and enhanced electron field emission of vertically aligned carbon nanotubes grown on stainless steel substrate. *Journal of Nanoscience Letters* **2014,** 4, 14.

[45] Chhowalla M., Teo K.B.K., Ducati C., Rupesinghe N.L., Amaratunga G.A.J., Ferrari A.C., Roy D., Robertson J. and Milne W.I., Growth process conditions of vertically aligned carbon nanotubes using plasma enhanced chemical vapor deposition. *Journal of Applied Physics* **2001,** 90 (10), 5308.

[46] Bower C., Zhou O., Zhu W., Werder D.J. and Jin S., Nucleation and growth of carbon nanotubes by microwave plasma chemical vapor deposition. *Applied Physics Letters* **2000,** 77 (17), 2767.

[47] Bo Z., Yang Y., Chen J., Yu K., Yan J. and Cen K., Plasma-enhanced chemical vapor deposition synthesis of vertically oriented graphene nanosheets. *Nanoscale* **2013,** 5 (12), 5180.

[48] Dresselhaus M.S., Dresselhaus G., Saito R. and Jorio A., Raman spectroscopy of carbon nanotubes. *Physics reports* **2005,** 409 (2), 47.

[49] Baro M., Gogoi D., Pal A.R., Adhikary N.C., Bailung H. and Chutia J., Pulsed PECVD for Low-temperature Growth of Vertically Aligned Carbon Nanotubes. *Chemical Vapor Deposition* **2014,** 20 (4-5-6), 161.

[50] Meyyappan M.D., L.; Cassell, A. and Has, D., Carbon nanotube growth by PECVD: a review. *Plasma Sources Science and Technology* **2003,** 12, 205.

[51] Shibuta Y. and Suzuki T., Melting and nucleation of iron nanoparticles: A molecular dynamics study. *Chemical Physics Letters* **2007,** 445 (4-6), 265.

[52] Müller C., Golberg D., Leonhardt A., Hampel S. and Büchner B., Growth studies, TEM and XRD investigations of iron-filled carbon nanotubes. *physica status solidi (a)* **2006,** 203 (6), 1064.

[53] Banhart F., Redlich P. and Ajayan P., The migration of metal atoms through carbon onions. *Chemical physics letters* **1998,** 292 (4-6), 554.

[54] Lin C.H., Chang H.L., Hsu C.M., Lo A.Y. and Kuo C.T., The role of nitrogen in carbon nanotube formation. *Diamond and Related Materials* **2003,** 12 (10-11), 1851.

[55] Zhang X.F., Zhang X.B., Tendeloo G.V., Amelinckx M. and Beeck M.O., Carbon nano-tubes; their formation process and observation by electron microscopy. *Journal of Crystal Growth* **1993,** 130, 368.

[56] Dommele V.S., Romero-Izquirdo A., Brydson R., de Jong K.P. and Bitter J.H., Tuning nitrogen functionalities in catalytically grown nitrogen-containing carbon nanotubes. *Carbon* **2008,** 46 (1), 138.

[57] Arjmand M., Chizari K., Krause B., Pötschke P. and Sundararaj U., Effect of synthesis catalyst on structure of nitrogen-doped carbon nanotubes and electrical conductivity and electromagnetic interference shielding of their polymeric nanocomposites. *Carbon* **2016,** 98, 358.

[58] Jang J.W., Lee C.E., Lyu S.C., Lee T.J. and Lee C.J., Structural study of nitrogen-doping effects in bamboo-shaped multiwalled carbon nanotubes. *Applied Physics Letters* **2004,** 84 (15), 2877.

[59] Hellgren N., Johansson P.M., Broitman E., Hultman L. and Sundgren J.-E., Role of nitrogen in the formation of hard and elastic CNx thin films by reactive magnetron sputtering. *Physical Review B* **1999,** 59 (7), 5162.

[60] Benedict L.X., Louie S.G. and Cohen M.L., Static polarizabilities of single-wall carbon nanotubes. *Physical Review B* **1995,** 52 (11), 8541.

[61] Mashayekhi A., Hosseini S.M., Hassanpour Amiri M., Namdar N. and Sanaee Z., Plasma-assisted nitrogen doping of VACNTs for efficiently enhancing the supercapacitor performance. *Journal of Nanoparticle Research* **2016,** 18 (6), 154.

[62] Lau K.K., Bico J., Teo K.B., Chhowalla M., Amaratunga G.A., Milne W.I., McKinley G.H. and Gleason K.K., Superhydrophobic carbon nanotube forests. *Nano letters* **2003,** 3 (12), 1701.

[63] Zhang K., Li T., Ling L., Lu H., Tang L., Li C., Wang L. and Yao Y., Facile synthesis of high density carbon nanotube array by a deposition-growth-densification process. *Carbon* **2017,** 114, 435.

[64] Han W.-Q. and Zettl A., Coating Single-Walled Carbon Nanotubes with Tin Oxide. *Nano Letters* **2003,** 3 (5), 681.

[65] Rudloff-Grund J., Brenker F., Marquardt K., Kaminsky F. and Schreiber A., STEM EDX nitrogen mapping of nanoinclusions in milky diamonds from Juina, Brazil, using a windowless silicon drift detector system. *Analytical chemistry* **2016,** 88 (11), 5804.

[66] Barros E., Souza Filho A., Lemos V., Mendes Filho J., Fagan S.B., Herbst M., Rosolen J., Luengo C. and Huber J., Charge transfer effects in acid treated single-wall carbon nanotubes. *Carbon* **2005,** 43 (12), 2495.

[67] Wang Z., Chen G. and Xia D., Coating of multi-walled carbon nanotube with SnO2 films of controlled thickness and its application for Li-ion battery. *Journal of power sources* **2008,** 184 (2), 432.

[68] Fan W., Gao L. and Sun J., Tin Oxide Nanoparticle-Functionalized Multi-Walled Carbon Nanotubes by the Vapor Phase Method. *Journal of the American Ceramic Society* **2006,** 89 (8), 2671.

[69] Di Bartolomeo A., Scarfato A., Giubileo F., Bobba F., Biasiucci M., Cucolo A., Santucci S. and Passacantando M., A local field emission study of partially aligned carbon-nanotubes by atomic force microscope probe. *Carbon* **2007,** 45 (15), 2957.

[70] Dionne M., Coulombe S. and Meunier J.-L., Screening effects between field-enhancing patterned carbon nanotubes: a numerical study. *IEEE transactions on electron devices* **2008,** 55 (6), 1298.

[71] Gao R., Pan Z. and Wang Z.L., Work function at the tips of multiwalled carbon nanotubes. *Applied Physics Letters* **2001,** 78 (12), 1757.

[72] Nilsson L., Groening O., Emmenegger C., Kuettel O., Schaller E., Schlapbach L., Kind H., Bonard J. and Kern K., Scanning field emission from patterned carbon nanotube films. *Applied Physics Letters* **2000,** 76 (15), 2071.

[73] Bonard J.M., Weiss N., Kind H., Stöckli T., Forró, Lμszló and Kern K.C.t., Andre, Tuning the Field Emission Properties of Patterned Carbon Nanotube Films. *Avanced Materials* **2001,** 13 (3), 184.

[74] Gupta B.K., Kedawat G., Gangwar A.K., Nagpal K., Kashyap P.K., Srivastava S., Singh S., Kumar P., Suryawanshi S.R. and Seo D.M., High-performance field emission device utilizing vertically aligned carbon nanotubes-based pillar architectures. *AIP Advances* **2018,** 8 (1), 015117.

[75] Wang K.Y., Liao C.Y. and Cheng H.C., Field-Emission Characteristics of the Densified Carbon Nanotube Pillars Array. *ECS Journal of Solid State Science and Technology* **2016,** 5 (9), 99.

[76] Hazra K.S., Rai P., Mohapatra D.R., Kulshrestha N., Bajpai R., Roy S. and Misra D., Dramatic enhancement of the emission current density from carbon nanotube based nanosize tips with extremely low onset fields. *ACS nano* **2009,** 3 (9), 2617.

[77] Patra R., Ghosh S., Sharma H. and Vankar V.D., High stability field emission from zinc oxide coated multiwalled carbon nanotube film. *Advanced Materials Letters* **2013,** 4 (11), 849.

[78] Xu J., Xu P., Ou-Yang W., Chen X., Guo P., Li J., Piao X., Wang M. and Sun Z., Outstanding field emission properties of wet-processed titanium dioxide coated carbon nanotube based field emission devices. *Applied Physics Letters* **2015,** 106 (7), 073501.

[79] Crespi V.H., Chopra N.G., Cohen M.L., Zettl A. and Louie S.G., Anisotropic electron-beam damage and the collapse of carbon nanotubes. *Physical Review B* **1996,** 54 (8), 5927.

[80] Zhang K., Stocks G.M. and Zhong J., Melting and premelting of carbon nanotubes. *Nanotechnology* **2007,** 18 (28), 285703.

[81] Doytcheva M., Kaiser M. and Jonge N.d., In situtransmission electron microscopy investigation of the structural changes in carbon nanotubes during electron emission at high currents. *Nanotechnology* **2006,** 17 (13), 3226.

[82] Bocharov G. and Eletskii A., Theory of carbon nanotube (CNT)-based electron field emitters. *Nanomaterials* **2013,** 3 (3), 393.

[83] Doytcheva M., Kaiser M., Verheijen M.A., Reyes-Reyes M., Terrones M. and de Jonge N., Electron emission from individual nitrogen-doped multi-walled carbon nanotubes. *Chemical Physics Letters* **2004,** 396 (1-3), 126.

CHAPTER 5

VACNT-pillar arrays on stainless steel and their field emission properties

Chapter 5 describes the synthesis, characterization, and field emission properties of vertically aligned carbon nanotube (VACNT) pillar arrays on the stainless steel substrate.

5.1 Introduction

Electron sources for cold field emission are used broadly in flat panel displays, electron microscopes, x-ray tubes, microwave power amplifiers, and gas sensors [1-5]. Carbon nanotubes (CNTs) are high-performing electron field-emitters because of their high aspect ratio, small tip dimension, high electrical and thermal conductivity, as well as high mechanical and chemical stability [6-9], but they are challenging to scale up into a functional device ascribed to standard CNT synthesis routes that introduce unevenly packed arrays of CNTs and poor connection to a conductive substrate. In operation, electron field-emitters require a highly-oriented structure with well-defined packing density [10] to enhance the localized electric field, which improves the overall electron field emission (FE). More importantly, direct contact of the field-emitters with their substrate is critical for achieving high electrical and thermal conductivity. This direct contact can facilitate rapid electron transport from the substrate to the emitters during the FE process [11]. Also, a robust emitter-substrate connection can adequately dissipate any heat manifested by Joule heating during the field emission process, which can protect the emitters from field evaporation failure. Therefore, we present a novel method for growing CNT field-emitters in the form of micro-pillar structures on a conductive substrate while

preserving the number density of active emission sites, which is essential to achieving large and stable FE currents for an extended duration.

Carbon nanotubes have been studied extensively as cold cathodes for FE for more than two decades [12-16]. The FE from CNT thin film highly depends on the morphology such as length, diameter, alignment, and packing density of CNTs [17-19], growth substrate [11], and CNTs-substrate interface properties [20]. Different methods, including plasma-enhanced chemical vapor deposition (PECVD) [21], can synthesize dense forests of vertically aligned carbon nanotubes (VACNTs); yet, these forests usually lack uniformity in alignment, height, and distribution across the entire cathode, which can result in a low and unstable emission current density. It has been suggested that self-standing VACNTs have optimum total FE when the spacing between adjacent VACNTs is about double their height [10]. But it is difficult to precisely control the spacing between individual VACNTs in an array, as it requires a sophisticated, expensive, and multi-step photolithography technique for patterning the catalyst particles (Ni, Co, and Fe) on top of the substrate before synthesizing the CNTs [22, 23]. As an alternative route, nanosphere lithography (NSL) has been used to synthesize periodic arrays of VACNTs with well-controlled spacing between them [24, 25]. It has also been shown that the length and site density of the VACNTs in the periodic array can significantly influence the FE characteristics [26]. The critical aspect of the NSL was the deposition of catalyst nanodots in periodic arrays using self-assembled monolayer or bilayer of polystyrene nanospheres on a silicon substrate coated with a buffer layer. It is important to note that the VACNTs are grown on the intermediate buffer layer (for example, a chromium layer) rather than directly on the silicon substrate. The buffer layer could be detached from the substrate at

high temperatures resulting in the loss of VACNTs. Also, silicon is a low conductive material that limits the VACNT applications which demand good electrical conductivity and high emission current. It is highly desirable that the VACNTs are directly grown on a metallic substrate.

VACNT-pillar based field emission arrays (VACNT-P-FEAs) have exhibited improved FE performance [27-32]. They are relatively easier to synthesize with controlled inter-pillar distance, pillar diameter, and height, although the synthesis process relies heavily on the complex photolithographic technique. While VACNT-P-FEAs showed encouraging FE performance by increasing the effective field-emitters (VACNTs at the edges of the pillar structure) compared to the regular VACNT forests, they are associated with two main problems: the broader cross-section (typically a few μm to several tens of μm in diameter) of each pillar emitter, and the indirect connection between emitters and the substrate. The broader cross-section means that each pillar structure itself is a dense forest of VACNTs, which makes most of the field-emitters within the pillar ineffective, thereby reducing the total emission current significantly during the FE process. Hence, the overall field emission performance of VACNT-P-FEAs can be improved by synthesizing VACNT-P-FEAs directly on the metal substrates with smaller pillar dimensions (each pillar consisting of a few VACNTs) separated by an appropriated inter-pillar distance.

In chapter 5, a facile PECVD method of synthesizing micro-sized VACNT-P-FEAs directly on stainless-steel (304 type) without using external catalyst particles and a buffer layer has been devised. Nanosphere lithography with polystyrene (PS) spheres of different sizes was employed to manipulate the size of the VACNT pillar emitters. The selective

growth of individual self-standing VACNT arrays was achieved by choosing the appropriate size of the PS spheres. The method is established on the idea of exposing a limited area of the catalytic substrate surface to the carbon precursor gas by covering the surface with an inhibitor layer so that the VACNTs can be grown only on the exposed area. Further, FE measurements revealed that the turn-on and threshold electric field of the VACNT-P-FEAs grown on SS substrate patterned with 450 nm PS spheres using nanosphere lithography were lowered by about half, and the total emission current density was increased by about four-fold compared to the dense VACNT forests. A two-fold increase in the field enhancement factor for VACNT-P-FEAs showed promising candidates for FE applications. Simulations of electrostatic field distribution revealed that the higher electrostatic field localized at the tip of VACNTs resided at the edges of VACNT-P-FEAs, emphasizing that smaller individual pillar size can enhance the FE properties. These simulation results reinforce the experimental findings.

5.2 Experimental

5.2.1 Substrate preparation by Nanosphere lithography

The stainless steel (SS) substrates were prepared by employing nanosphere lithography (NLS) to enable the selective growth of VACNT pillar emitters. The details of the method have been explained in section 3.1.2. Briefly, smooth and contaminant-free SS disks of diameter ~ 1.5 cm were treated with RCA solution ($NH_4OH:H_2O_2:H_2O$) for 30 seconds to make their surface hydrophilic, required for nanosphere adhesion. The substrates were patterned with polystyrene (PS) sphere (110, 200, 450, 950, or 1500 nm in diameter) by the spin coating method. A Cr-layer (CNT inhibitor layer of 15, 50, 150, or

300 nm thick) was deposited on the PS sphere patterned substrates using e-beam evaporation. According to the PS sphere size, the samples were termed as “PS110”, “PS200”, “PS450”, “PS950”, and “PS1500”. The detailed sample nomenclature and associated parameters are shown in Table 5.1. Finally, the PS spheres were removed from the Cr-coated substrates using ultrasonication in an acetone bath for 3 minutes, which yielded open circular catalytic sites on the masked SS substrate.

Table 5.1. Table showing the sample nomenclature and associated parameters of Nanosphere lithography.

Sample	PS solution : IPA (v:v)	PS sphere size (nm)	Cr-coating thickness (nm)
PS1500	1:2	1500	300
PS950	1:4	950	300
PS450	1:10	450	150
PS200	1:15	200	50
PS110	1:20	110	15

5.2.2 Synthesis of VACNT-pillar arrays

The dense forest of VACNTs, referred to as “HD” sample in the following text, composed of individual self-standing VACNT arrays, and the masked VACNT-P-FEAs were synthesized using dc PECVD, which has been described in section 3.2.1. In brief, the SS substrates patterned by NSL were placed into the PECVD chamber evacuated to a pressure of 0.01 Torr and then heated up to 600 °C under 7 Torr of ammonia gas (400 sccm). Besides, HD samples were fabricated by using polished and cleaned SS substrates. Once the desired growth temperature was reached, DC plasma of power 70 W and acetylene gas at 25 sccm was introduced. The VACNTs were grown for 10 minutes at 600

°C for all specimens compared in this study. Finally, the samples were allowed to cool down naturally to room temperature and then removed from the chamber. A few samples were grown at higher temperatures (such as 700 °C) to check the integrity of the Cr-layer on the SS substrate.

5.2.3 Field emission measurements

The field emission properties of as-synthesized samples were measured using a diode configuration method under a high vacuum of ~1×10^{-6} Torr, as described in section 3.4.1. The field emission properties (F–J cycles) of all samples were tested for at least ten cycles to confirm the repeatability and reliability of the recorded data. Furthermore, the electrostatic field distribution of VACNT-P-FEAs was simulated using COMSOL™ MULTIPHYSICS 5.2 software on the basis of finite element methods, as described in section 3.5.

5.3 Results and discussion

5.3.1 Nanosphere lithography

Direct interaction between hydrocarbon gas and the native surface of the substrate was crucial for the direct connection of VACNTs to the substrate. Meanwhile, space-limited interaction was essential to control the VACNT pillar's morphology, which was achieved through NSL. Figure 5.1(a-b) represents the surface topography of the as-received SS substrate and its corresponding height profile along the line shown in Figure 5.1(a). As-received SS surface had a rough surface with an average roughness R_a = 55.81 nm and RMS roughness R_q = 79.92 nm. Figure 5.2 represents the topography of the SS substrate before and after the NSL using PS spheres of different sizes. As shown in Figure 5.2 (a),

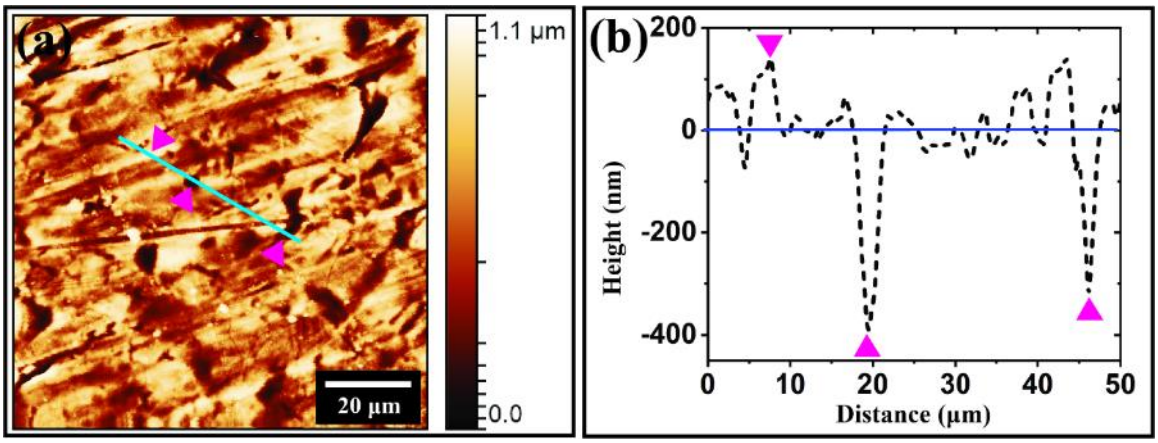

Figure 5.1. Surface characterization by AFM. (a) Surface topography of the as-received stainless steel (SS) and (b) the height profile along the line shown in Figure 5.1(a).

the as-received SS substrate was polished with sandpapers to a shiny, mirror finish. After polishing, the R_a and R_q values were reduced to 4.91 and 6.46 nm, respectively. However, a few deep and long grooves, as indicated by the triangle symbols, created during the polishing process were observed with the corresponding height profile provided in the inset of Figure 5.2(a). The polishing process was beneficial for two main reasons. First, the commercial type 304 SS is known to have a passive chromium oxide layer on its surface for corrosion resistance, which has an adverse effect during the synthesis of the CNTs [33]. Second, a smooth surface at the nano-level assists in achieving a uniform distribution of the nanoparticles, such as PS spheres, without forming clusters during the NSL process [34].

Figure 5.2(b-f) shows the AFM images of the Cr-coated SS substrates after removing the PS spheres in diameters of 1,500, 950, 450, 200, and 110 nm, respectively. The PS spheres removal created exposed regions in the SS surface, which acted as the potential templated sites for VACNT pillars or individual VACNT. The depth profiles, as shown in the insets of Figure 5.2(b-f), confirm the cavities of different sizes corresponding

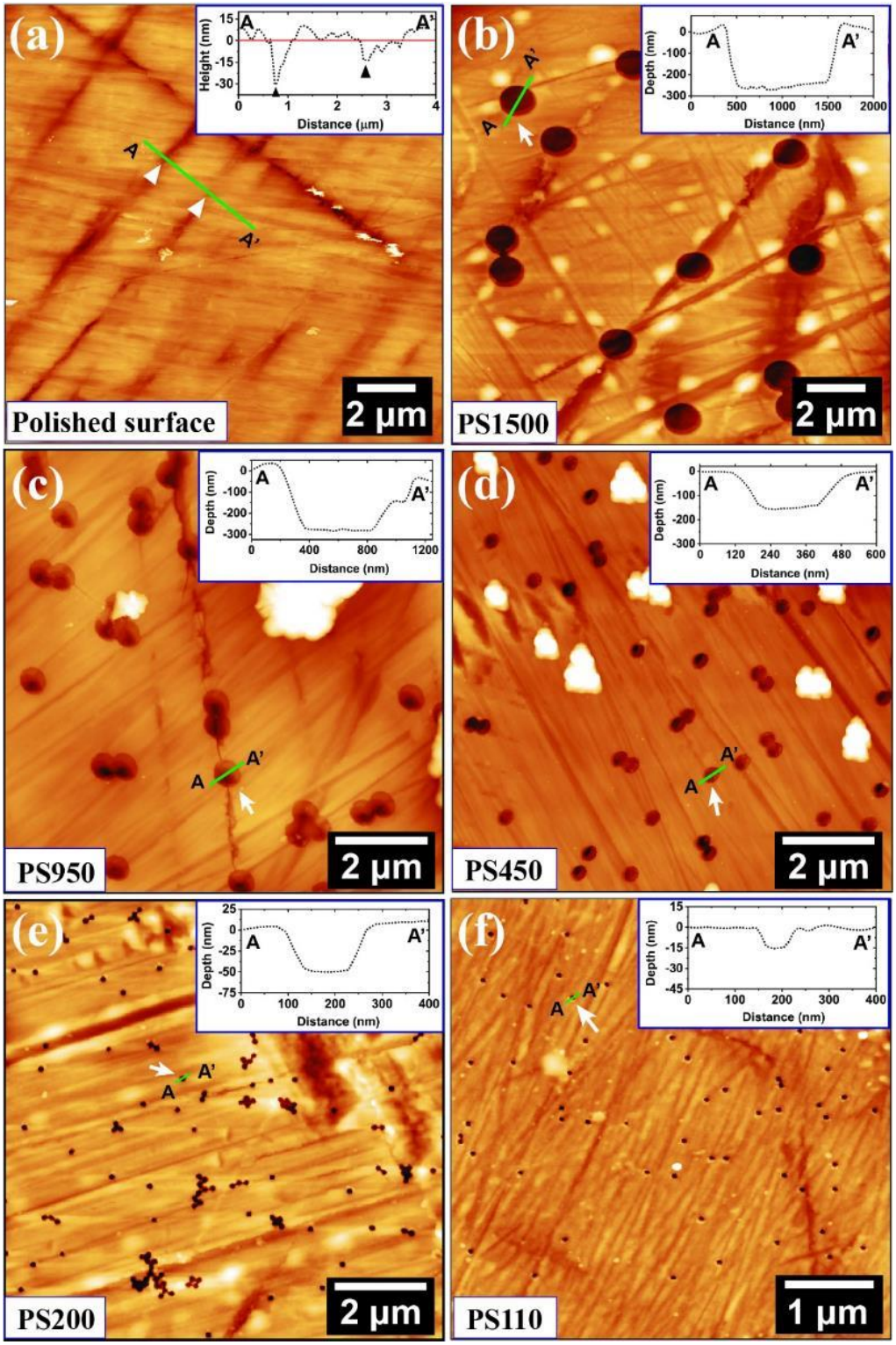

Figure 5.2. AFM images of the (a) SS substrate after polishing with sandpapers (b-f) Cr-coated SS surface, partially exposing the native substrate surface after removing the PS spheres of diameters 1500, 950, 450, 200, and 110 nm, respectively. The insets represent the height profile along the line shown in the corresponding images.

to the different PS sphere sizes. We noted that the cavity diameter was slightly smaller than the diameter of the PS spheres themselves. It was also apparent in Figure 5.2 that by optimizing the PS solution concentration, the number density of the cavities was increased as the diameter of the PS sphere was decreased, which was fundamental for keeping the number density of the VACNT field-emitters constant across the samples.

The SEM analysis further revealed that the diameter of the cavities should be smaller than the actual diameter of the corresponding PS spheres, considering that the radius of the sphere was bigger than the thickness of the Cr-layer. Figure 5.3 shows the schematics and SEM images of the Cr-coated SS substrate before and after removing the PS spheres of a nominal diameter of 200 nm. The cavity diameter (d_{cavity}) was calculated

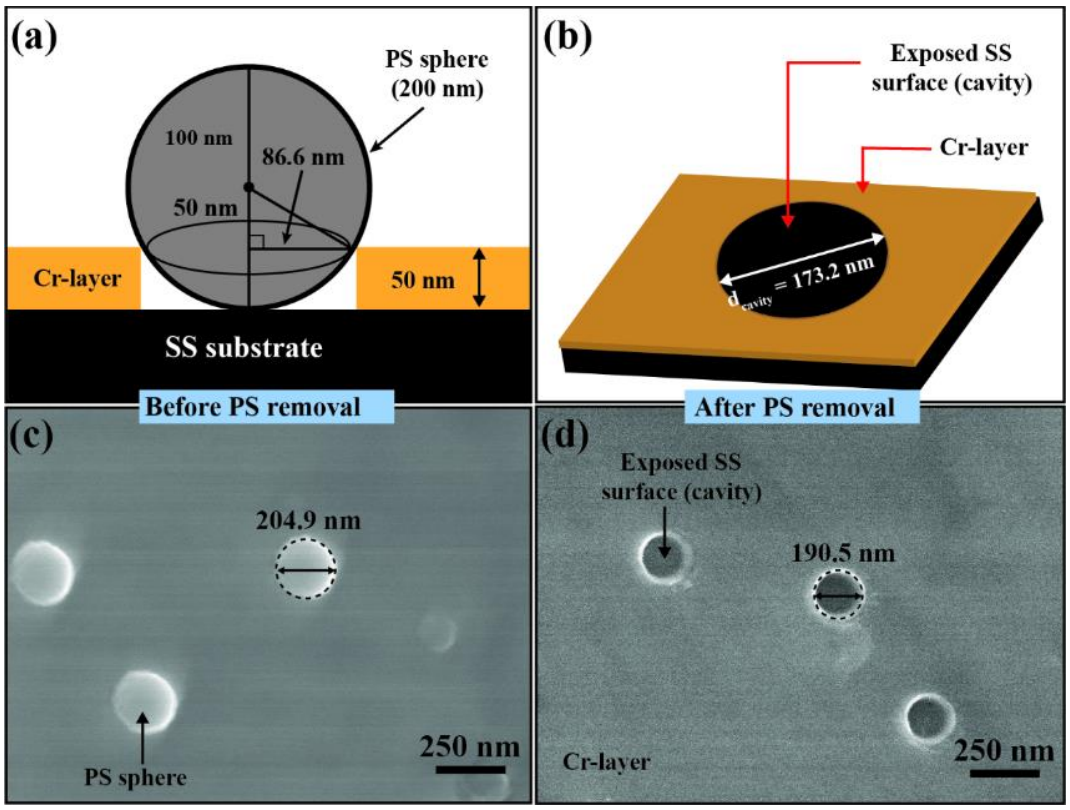

Figure 5.3. SEM analysis of the NSL. (a-b) Schematic diagrams and (c-d) SEM images of the Cr-coated SS surface before and after the removal of PS spheres.

as 173.2 nm using the 50 nm thick Cr-layer, as shown in Figure 5.3(a-b). Similarly, the values were calculated as 1200, 883.2, 424.2, and 75.4 nm for the samples PS1500, PS950, PS450, and PS110, respectively. The calculated values indicated that the diameter of the cavities should be smaller than the actual diameter of the corresponding PS spheres. One such observation is shown in Figure 5.3(c-d), where the diameter of the PS sphere was measured as 204.9 nm, but the diameter of the cavity created after removing the sphere was found to be 190.5 nm.

5.3.2 Evaluation of Cr-coating as the CNT inhibitor

Electronic structure plays a deterministic role in the catalytic activity of metals for the nucleation and growth of CNTs. Typical transition metals (Ni, Co, and Fe) having few d-vacancies (two to four) in their electronic configuration are known to interact moderately with carbon atoms via dissolving an optimal amount of carbon atoms which results in graphitization [35]. On the other hand, Cr metal with five d-vacancies in its electronic configuration is widely regarded as a poor catalyst or co-catalyst for the synthesis of CNTs [33, 36-39]. A polished SS substrate was coated partially with a Cr-layer of about 300 nm thick, as shown in Figure 5.4(a), to validate its non-catalytic behavior in our PECVD system. The word “FIU” was carved after the Cr coating with a sharp tweezer. It was then subjected to the optimized growth conditions for VACNTs (growth temperature of 600 °C, growth time of 10 minutes, flow rates of C_2H_2 and NH_3 at 25 and 400 sccm, respectively, plasma power of 70 W, and pressure of 7 Torr).

The photograph after the synthesis clearly shows two distinct regions with different color contrast, and the word “FIU” was clearly visible after the VACNTs growth, as shown

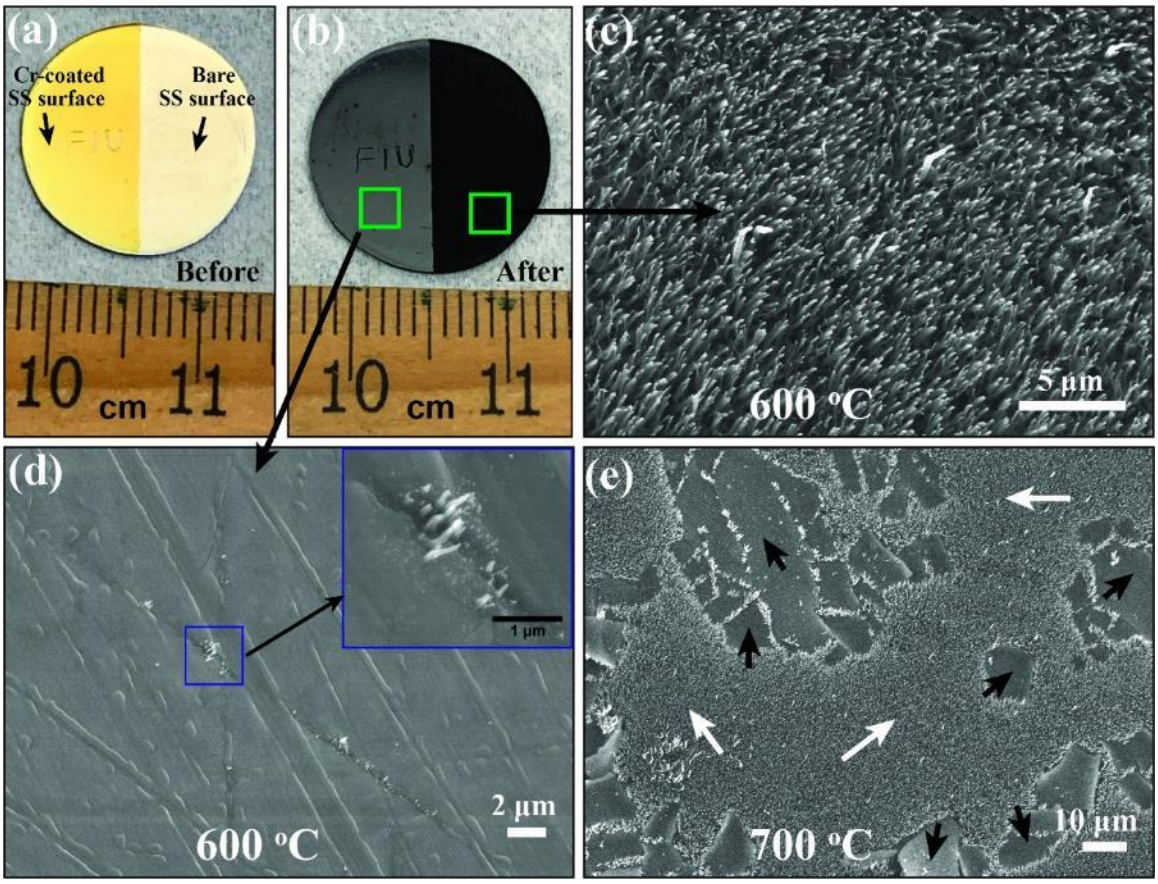

Figure 5.4. (a-b) A sequence of photographs of partially coated SS substrate with Cr showing the surface before and after the synthesis of VACNTs at 600 °C. (c-d) SEM images of the boxed areas shown in Figure 5.4(b). The inset in Figure 5.4(d) represents the magnified view of the boxed area shown in Figure 5.4(d). (e) SEM image of a sample surface after exposing to the CNT growth conditions at 700 °C. The features shown by black arrows in Figure 5.4(e) are the remnant of the Cr-layer still in contact with the SS substrate. In contrast, the large fuzzy area indicated by white arrows represents dense forest of VACNTs grown in the exposed surface of the SS substrate after the Cr-layer breakup.

in Figure 5.4(b). Figure 5.4(c-d) represents the magnified view of the boxed areas shown in Figure 5.4(b). Uniform and highly dense VACNTs were grown on the uncoated part of the SS surface. In contrast, the Cr-coated side was almost empty except a few short VACNTs observed at some grooved regions on the coated surface, as shown in the inset of Figure 5.4(d). The SEM images confirmed the successful inhibition of the growth of CNTs by the Cr-layer. In addition, the Cr-layer was found to remain intact at 600 °C. However, the Cr-layer was damaged severely at 700 °C exposing some of the SS surface,

where the dense forest of VACNTs would grow, as shown by white arrows in Figure 5.4(e). The result showed that the areas on the SS surface still covered by Cr-layer, as indicated by the black arrows in Figure 5.4(e), did not allow the growth of VACNTs. The results corroborate that the growth temperature should be less than 700 °C for the Cr-layer to remain intact with the substrate during the PECVD growth of VACNTs.

5.3.3 Synthesis and characterization of VACNT-pillar arrays

In the VACNT synthesis by PECVD, a heat treatment at 600 °C to the NSL-patterned SS substrate under a reducing environment facilitated the evolution of catalyst nano-hills on partially exposed SS surfaces [40]. The on-site decomposition, diffusion into the catalyst nano-hills, graphitization upon precipitation of the carbon atoms, and the presence of plasma (70 W) in the growth environment governed the synthesis of VACNTs [11]. Catalytically inactive Cr-layer played a crucial role in the site-limited growth of VACNT pillars. To determine the non-catalytic behavior of the Cr in our PECVD method, we performed a detailed experiment, which is described in section 5.3.2. Figure 5.5 shows the SEM images of VACNTs grown directly on the SS substrates patterned with and without PS spheres using NSL. Figure 5.5(a) shows a high-density forest (7.91×10^9 per cm^2) of well-aligned VACNTs (HD). Unlike HD, the samples shown in Figure 5.5(b-f) comprised of VACNT pillars or individual VACNT that has grown only on the exposed SS surface (cavities) created by patterning with PS spheres of diameter 1500, 950, 450, 200, and 110 nm. The insets in Figure 5.5(b-f) show the magnified view of the VACNT-pillars whose diameters are dictated by the size of the PS spheres. The number of VACNTs per pillar was proportional to the size of the PS spheres. An approximately similar density

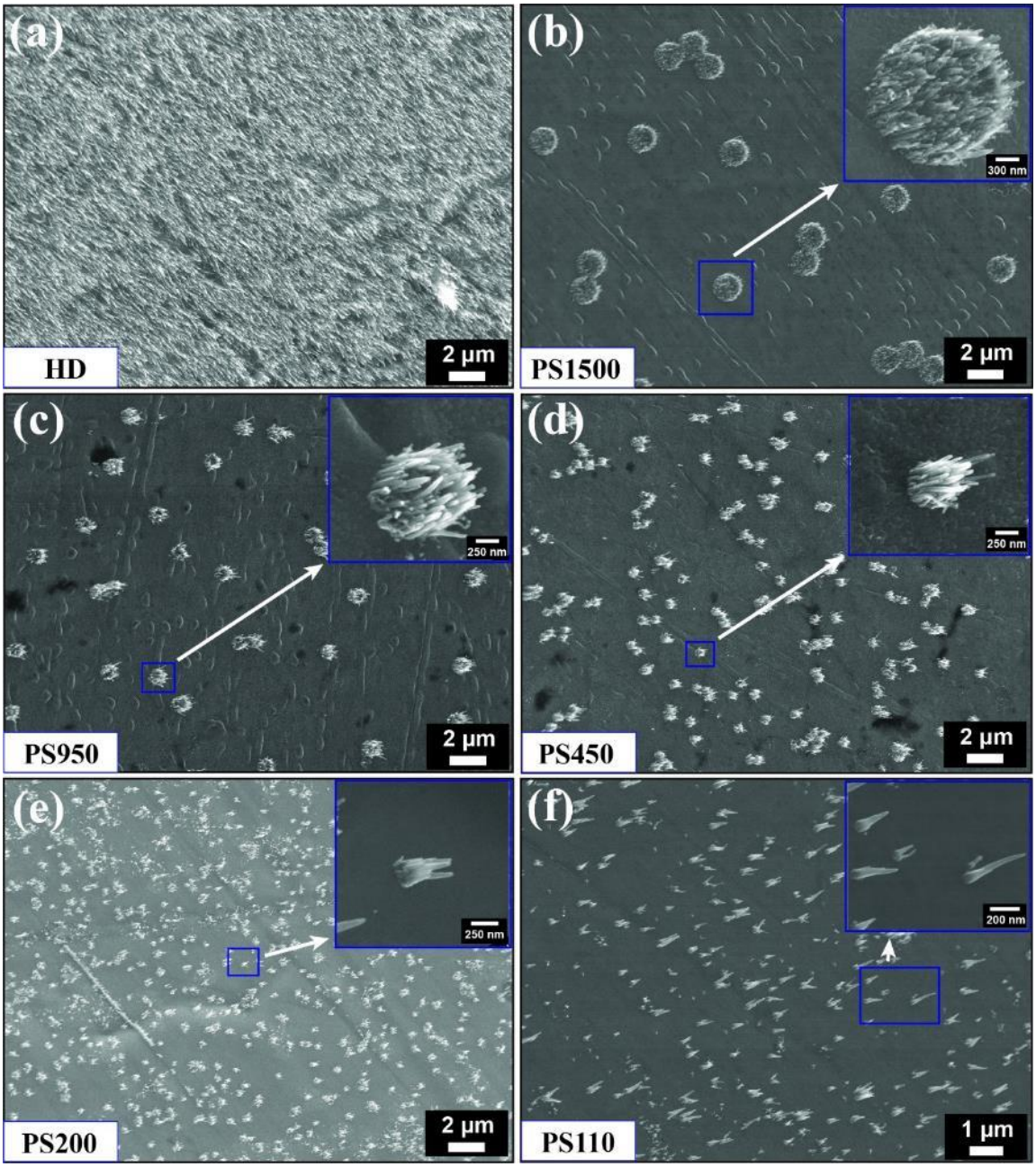

Figure 5.5. FESEM images of VACNTs synthesized on SS substrates. (a) High density (HD) VACNTs grown on polished SS surface. (b-f) VACNT pillars grown on SS after patterning the surface by PS spheres of diameter 1500 nm (PS1500), 950 nm (PS950), 450 nm (PS450), 200 nm (PS200), and 110 nm (PS110), respectively. The insets in Figure 5.5(b-f) represent the magnified view of the boxed area shown in the corresponding images.

of the VACNTs was observed for the pillar samples, such as PS1500, PS950, and PS450. The exception was the density of the VACNTs for PS200, which was slightly lower than

Table 5.2. Experimental data representing number density, counts per cavity, pillar density, length, and diameter of the VACNTs synthesized with and without NSL.

Sample	No. density ($\times 10^8$ per cm^2)	No. of VACNTs per cavity	No. of pillars in (28 × 21) μm^2 area	Length of VACNTs (μm)	Diameter of VACNTs (nm)
HD	79.1	–	–	1.48 ± 0.17	57.49 ± 9.69
PS1500	11.7	362 ± 21	19	1.49 ± 0.23	53.42 ± 7.90
PS950	11.1	197 ± 15	33	1.43 ± 0.21	55.90 ± 9.11
PS450	10.6	36 ± 5	173	1.49 ± 0.26	51.05 ± 9.09
PS200	6.2	7 ± 1	506	1.39 ± 0.23	47.92 ± 6.65
PS110	1.6	1	–	1.33 ± 0.18	56.55 ± 11.82

the other pillar samples, see Table 5.2. Eventually, we were able to achieve the synthesis of a single individual self-standing VACNT in each patterned cavity using PS110 samples, the results of which are shown in Figure 5.5(f). The length and diameter of the as-synthesized VACNTs were measured to be in a narrow range of (1.33 – 1.49) μm and (47.92 – 57.49) nm, respectively.

Assuming the shape of the cavity is circular, the maximum number of VACNTs that can be accommodated into a cavity at closely packed condition can be estimated by the following equation:

$$N = \left(\frac{d_{cavity}}{d_{VACNT}}\right)^2 \tag{5.1}$$

where d_{cavity} and d_{VACNT} represent the diameter of the cavity and VACNTs, respectively. The maximum possible number of VACNTs that can be grown in the cavity was estimated as 435, 235, 54, 9, and 1 for the samples PS1500, PS950, PS450, PS200, and PS110,

respectively. The calculation was performed on the basis of VACNT's average diameter of the sample HD. The estimation also relied on the assumption that the diameter of the HD VACNTs did not differ significantly from the other samples. The measured number of VACNTs for each specimen, as shown in Table 5.2, was lower than the calculated value from equation (5.1). The discrepancy occurred because the VACNTs were not as closely packed inside the templated cavities. Precise control over the size of catalytic sites (nano hills) was practically impossible as the activated SS substrate itself was used as the catalyst. Consequently, the pillars had VACNTs of different diameters and distributions, which prompted the templated cavities not tightly packed with VACNTs as assumed in our calculation. Nevertheless, the HD-based calculation was a good estimate of the number of VACNTs per cavity formed using different size nanospheres.

The TEM observation confirmed the tubular structure of the as-synthesized CNTs. As shown in Figure 5.6(a), CNTs were found to have particles anchored at their tips, suggesting the tip growth process [41]. The image also shows that the CNTs have different diameters, which are attributed to the different sizes of the catalyst nanoparticles [40]. Since a few graphitic layers enclosed the metal catalyst particles, the work function of the CNT tip can be expected to be close to that of the graphite, but the effect of the Fe particle on FE properties may still exist. It has been reported that metal catalysts at the tip of CNTs can be beneficial to the enhancement of the FE performance. On one hand, the metal particle can operate as an additional FE electron source [42-44]. On the other hand, it can bolster the robustness of the emitter tip to prevent radial deformations, thereby increasing the emission stability [45]. A decrease in turn-on and threshold field by 1 V/μm has been reported from CNTs with FeNi nanowires encapsulated at the tips [42]; however, it should

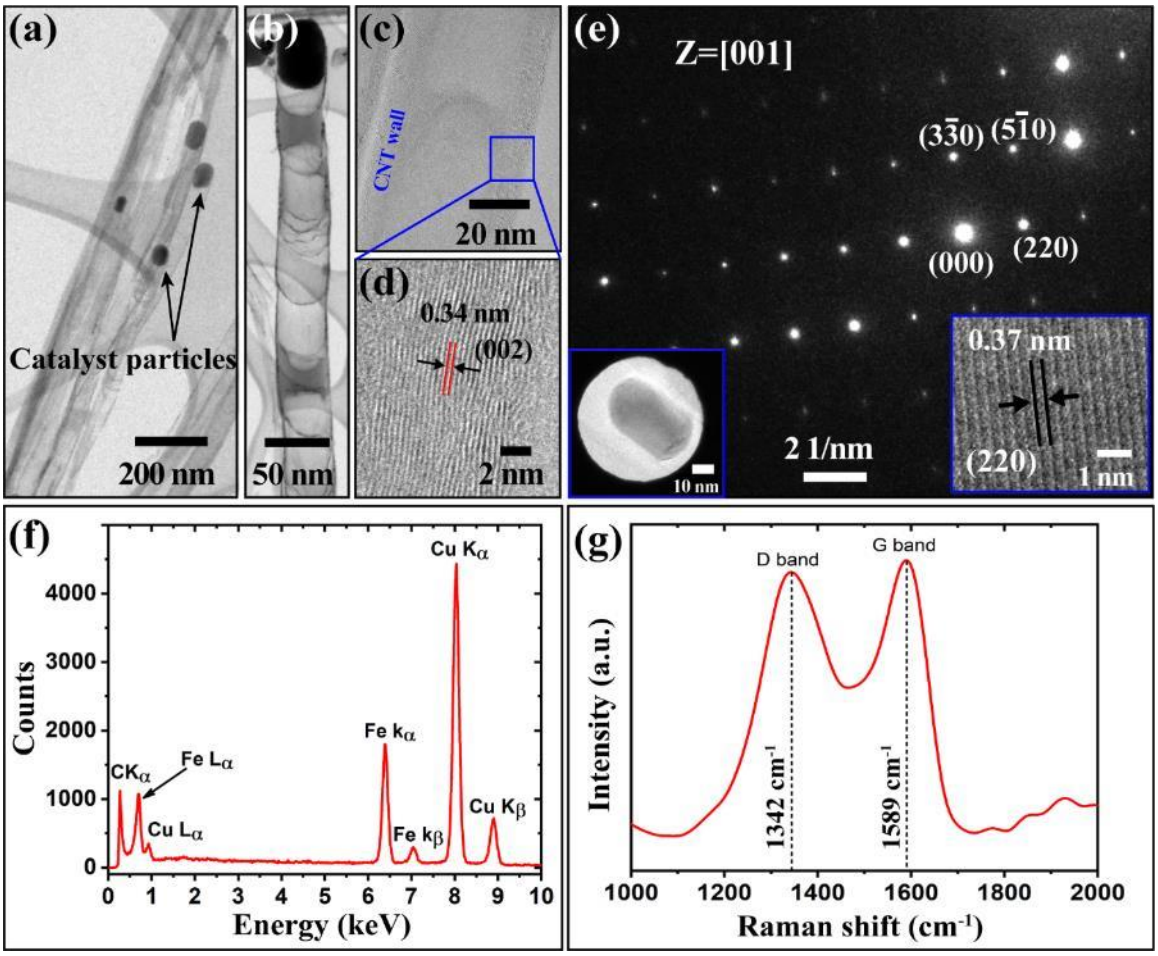

Figure 5.6. (a) Low magnification TEM image of the as-synthesized CNTs (PS1500) showing catalyst particles at the tips, (b) low magnification TEM image showing a section of CNT with "bamboo-like" structure, (c) HRTEM image of a section of CNT, (d) HRTEM image showing the lattice fringes in the CNT wall, (e) SAD pattern obtained from the Fe particle at the tip of CNT shown in the lower left inset, the bottom right inset showing an HRTEM image of the catalyst particle. (f) EDS spectrum from the Fe particle at the tip of CNT shown in the lower left inset of Figure 5.6(e) (the copper signal was from the TEM holder), and (g) Raman spectra of the as-synthesized CNTs (PS1500).

be noted that the metal particles in this work were much shorter than in the reported literature. As shown in Figure 5.6(b), the CNT walls were characterized by twisted and broken graphitic planes forming a 'bamboo-like' structure rather than a hollow cylinder, a typical characteristic of the CNTs prepared by PECVD [46]. The multilayers of graphitic planes separated by 0.34 nm, which correspond to the (002) lattice planes of graphite, were observed in the high-resolution TEM (HRTEM) images (Figure 5.6(c-d)). It has been

suggested that the growth environment consisting of energetic ions or radicals of nitrogen plays a crucial role in the formation of 'bamboo-like' CNTs [47]. The report implies that the intense NH_3 plasma used in the PECVD experiments was responsible for the 'bamboo-like' structure of the as-synthesized CNTs. The effect of "bamboo-like" VACNT-P-FEAs on FE properties has been discussed thoroughly in section 5.3.4. The selected area diffraction (SAD) pattern taken from the particle at the tip of a CNT, as shown in Figure 5.6(e), shows the diffraction spots which can be indexed as (220), $(3\bar{3}0)$, and $(5\bar{1}0)$ planes of single crystalline cubic Fe along the [001] zone axis. A distance of 0.37 nm corresponding to the (220) bcc lattice plane of Fe crystal was observed in an HRTEM image, as shown in the lower right inset of Figure 5.6(e). The EDS spectrum (Figure 5.6(f)) obtained from the particle displays the C, Fe, and Cu peaks. The C and Cu signals are associated with the CNTs and TEM sample grid/holder, respectively. The TEM results imply that the particle at the CNT tip was a bcc Fe single crystal. The tip particle analysis implies that the Fe atoms rearranged into a single crystal at the SS surface during the VACNTs growth. Thus, the VACNTs were grown directly from the SS substrate, which supports the fact that the Cr-layer did not catalyze the growth of VACNTs.

The structural defects on the CNTs synthesized using PS1500 were studied by Raman spectroscopy, as shown in Figure 5.6(g). Typical Raman characteristic peaks at about 1342 cm^{-1} (referred to as D band) and at about 1589 cm^{-1} (referred to as G band) were observed. The D band measured the graphitic lattice disorder. In contrast, the G band indexed the crystallinity of the material. These two intensities expressed as a ratio (I_D/I_G) indicated the degree of structural defects in the crystalline structure [48]. The value of I_D/I_G was found to be 1.24, which is considered a high value. The high I_D/I_G value indicates

many defects in the synthesized CNTs crystal structure. The observed high degree of defects is also a typical characteristic of the CNTs prepared by the PECVD method caused by an intense plasma bombardment on the CNT walls during the synthesis process [49]. It has been demonstrated that highly defective amorphous CNTs grown at lower temperatures, such as 600 or 650 ºC, can be beneficial for the field emission, specifically for reducing the turn-on electric field, because of the substantial field enhancement effect caused by the inhomogeneous electronic sp^2/sp^3 structures [50]. Therefore, higher field emission performance was anticipated from our samples.

5.3.4 Field emission properties

The field emission (FE) properties of the as-synthesized samples were measured using the diode configuration method under a very high vacuum. The consistency of the FE properties measurements was tested by performing at least ten cycles of emission current density versus applied field (F–J) measurements of three different samples for each growth condition. The F–J comparison includes only the cycles from run 6 to 10 because the first few cycles showed high fluctuation in the emission current. A comparison of F–J performance between the first and sixth cycle is shown in Figure 5.7(a-b). The F–J comparison revealed that the FE for the first cycle occurred unexpectedly at a much lower applied electric field with a high field enhancement in comparison to the sixth cycle. The main reason for the discrepancy between these two cycles was the nano-protrusions created as a result of the surface adsorption of residual gas molecules at the tip of the field-emitters, which decreased the work function of the emitters [51]. The field-emitters with lower work functions were expected to onset the FE much quicker than their uncontaminated

counterparts. But the adsorbed residual gas molecules usually cause unstable field emission. The unstable field emission was eliminated by field evaporating the residual gas and the protruding long emitters via electrical conditioning with high current during the first five F–J cycles [52].

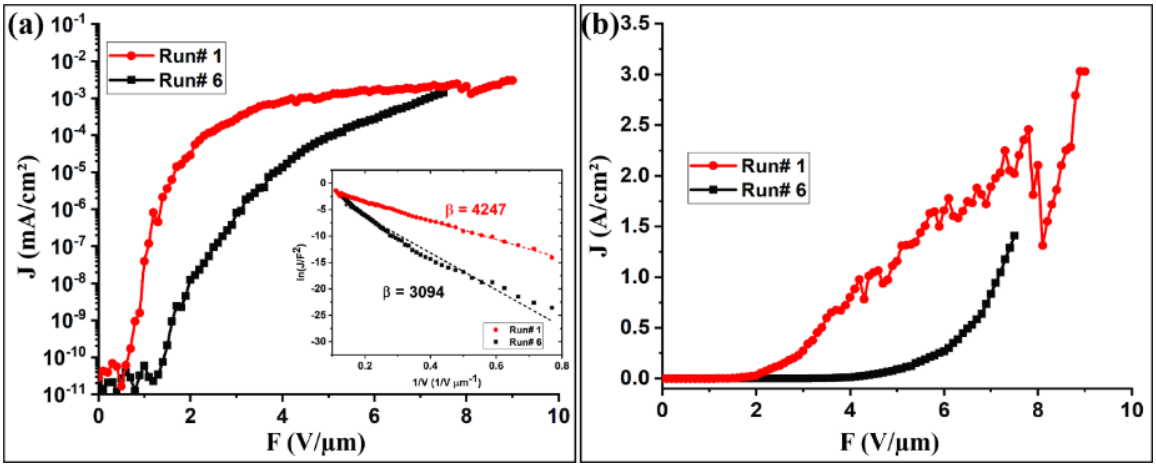

Figure 5.7. F–J comparison between the 1st and 6th cycle for the sample PS110. (a) Semi-log scale and (b) linear scale representation. The inset in Figure 5.7(a) represents the Fowler–Nordheim (F–N) plot of F–J cycles shown in Figure 5.7(a), and the difference in slope clearly indicates the disparity in field enhancement during these two cycles.

The comparison of FE properties of the samples HD, PS1500, PS950, PS450, PS200, and PS110 is shown in Figure 5.8 and Table 5.3. A turn-on electric field (E_{TO}) and a threshold electric field (E_{TH}) were defined as an applied electric field required to generate an emission current density of 1 μA/cm^2 and 1 mA/cm^2, respectively. Figure 5.8(a-b) represents the comparison of the F–J plots for different samples in semi-log and linear scale, respectively. The F–J plots revealed that the FE process of the sample PS450 initiated at a much lower applied electric field and produced a higher total current density than the other samples. Precisely, the E_{TO} and E_{TH} values for the PS450 were measured as 1.57 ± 0.21 V/μm and 2.94 ± 0.21 V/μm, respectively, and a high emission current density (J_{total}) in the range of 25 and 33 mA/cm^2 at a field of ~4 V/μm was recorded, which is more than

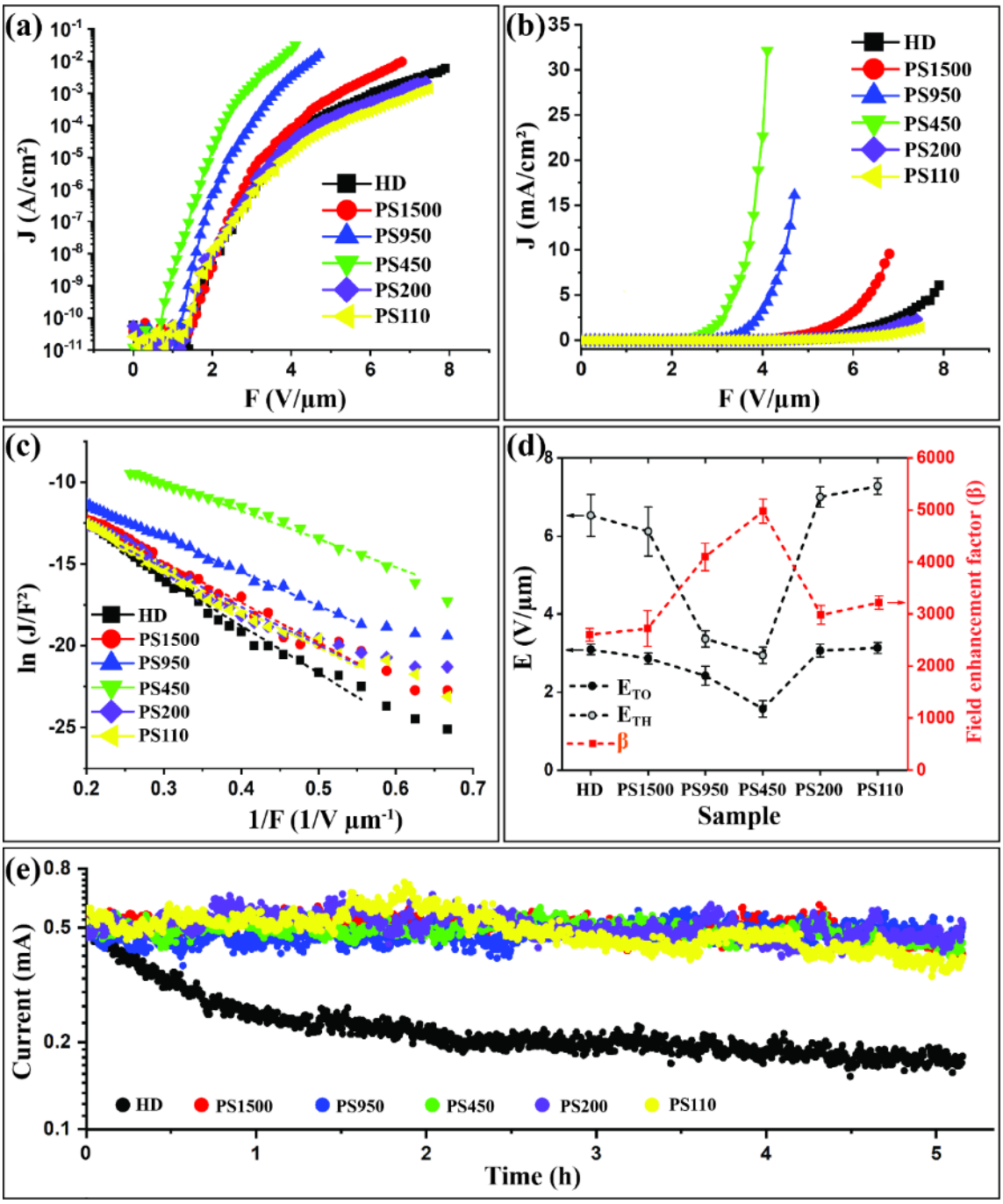

Figure 5.8. Field emission (FE) properties of the as-synthesized samples HD, PS1500, PS950, PS450, PS200, and PS110. (a) Comparative study of current density vs. applied electric field (F–J) properties represented in semi-log scale and (b) linear scale. (c) Corresponding Fowler–Nordheim (F–N) plots. (d) Variation of turn-on and threshold field, as well as field enhancement factor, of the different samples. (e) Current stability test at 0.5 mA current. The inset in Figure 5.8(b) represents the schematic of a diode configuration used to measure the FE properties of the samples.

Table 5.3. Field emission properties (Turn-on, threshold electric field, field enhancement factor, and stability) of the as-synthesized high density, VACNT-P-FEAs, and low-density self-standing VACNT samples.

Sample	E_{TO} (V/μm)	E_{TH} (V/μm)	β	Mean E_{TO}	Mean E_{TH}	Mean β	Stability at 0.5 mA		
							$\bar{I}$(mA)	σ(mA)	cf (%)
HD									
S1	2.94	6.22	2577						
S2	3.08	6.08	2500	3.09	6.53	2599	0.23	0.21	112
S3	3.26	7.29	2621						
PS1500									
S1	2.91	6.95	3103						
S2	2.81	5.43	2266	2.86	6.12	2718	0.50	0.18	16
S3	2.85	5.98	2784						
PS950									
S1	2.53	3.45	3747						
S2	2.32	3.22	4366	2.42	3.36	4100	0.48	0.16	10
S3	2.41	3.36	4186						
PS450									
S1	1.59	2.95	5234						
S2	1.51	3.01	5023	1.57	2.94	4977	0.49	0.16	12
S3	1.62	2.85	4674						
PS200									
S1	3.04	7.34	3233						
S2	3.14	6.95	2819	3.06	7.00	2980	0.51	0.19	20
S3	2.99	6.71	2889						
PS110									
S1	3.19	7.14	3094						
S2	3.11	7.57	3164	3.13	7.28	3216	0.49	0.24	36
S3	3.09	7.12	3392						

fourfold higher than that for the HD. The E_{TO} and E_{TH} values for the different samples are presented in Table 5.3, and they are also plotted in Figure 5.8(d).

The field enhancement property of the as-synthesized samples was studied by using Fowler-Nordheim (F–N) equation. The emission current density as a function of field enhancement factor (β) and applied electric field (F) can be written as [53]:

$$J = \left(\frac{A\beta^2F^2}{\phi}\right)\exp\left(-\frac{B\phi^{\frac{3}{2}}}{\beta F}\right) \tag{5.2}$$

where A (1.56×10^{-6} A V^{-2} eV) and B (6.83×10^{9} $eV^{3/2}$ V m^{-1}) are constant quantities. ϕ is the work function of the electron field-emitter. The field enhancement factors were calculated by using the slope (S) of the linearized region of the F–N plots, as shown in Figure 5.8(c), and the equation can be given as:

$$S = -\frac{B\phi^{\frac{3}{2}}}{\beta} \tag{5.3}$$

It was essential to know the work function of the emitters for understanding the local field enhancement from the VACNT emitters, and hence the overall FE process. However, subtle variations in the geometrical structure of the tip of VACNTs at the nanoscale can modify their work function [54]. The work function also depends on the helicity of CNTs-semiconducting (ϕ = 5.6 eV) and metallic (ϕ = 4.6 eV) [55]. The difficulty in keeping track

Table 5.4. Comparison of crucial FE parameters for various pillar-based CNT field-emitters reported in the literature and this work.

Substrate	**Pillar height (μm)**	**Pillar diameter (μm)**	**E_{TO} (V/μm) at 10 μA/cm^2**	**J_{total} (mA/cm^2)**	**β**	**Ref.**
Co-Ti/Ti/Al/Si	50	50	1.15	~30 at 2.5 V/μm	4362	[38]
Co-Ti/Ti/Al/Si[†]	43	20	1.08	~30 at 2.3 V/μm	5134	[38]
Ni/NiT/Ti/Si	~1.80	~2	2.5[*]	~22 at 5.5 V/μm	1824	[39]
Fe/Al/Si	15	10	2.8	~1 at 4 V/μm	1770	[56]
Fe-Ni-Co/Al/Si	2	~2.5	2.16	0.55 at 3.46 V/μm	4969	[57]
Fe/Al/Si	10	30	N/A	22.9 at 11 V/μm	3169	[29]
Fe-Cr-Al	10	30	N/A	50 at 7.47 V/μm	1671	[29]
SS	1.49	0.4	1.75	~33 at 4 V/μm	4977	This work

[†] Densified VACNT pillar emitters.
[*] Measured at 0.1 mA/cm^2.

of the variations in the structural and electronic properties of different CNTs lying in an array led us to assume the work function of the VACNT emitters to be 5.0 eV (the commonly used work function for carbon material) in our measurements [28]. The field enhancement factors were found to be 2599 ± 124, 2718 ± 345, 4100 ± 260, 4977 ± 230, 2980 ± 181, and 3216 ± 128 related to the samples HD, PS1500, PS950, PS450, PS200, and PS110, respectively. The calculated highest beta value of PS450, which is about two times higher than that for the HD, is consistent with the observed lowest values of E_{TO} and E_{TH}. Figure 5.8(d) shows the variation of beta values of the different samples.

Most FE devices require electron-emitting sources capable of generating a high emission current with a high degree of stability over an extended period. The temporal measurement of the emission current was performed for various samples at an initial current of 0.5 mA for more than 5 hours under a pressure of about 1×10^{-6} Torr. For each current versus time plot, the average current ($\bar{I}$) and the standard deviation (σ) were calculated. Moreover, the current fluctuation (cf) over the $\bar{I}$ for each plot was calculated by using the following equation:

$$cf = \frac{|I - \bar{I}|}{\bar{I}} \times 100\% \tag{5.4}$$

where I denotes the value of maximum deviated emission current from the average current value. As shown in Figure 5.8(e), the sample HD exhibited the worst emission current stability with the cf and average emission current of 112 % and 0.23 ± 0.21 mA, respectively. Unlike the HD, the rest showed improved current stability, as shown in Table 5.3. The samples PS450 and PS950 displayed superior FE stability among other samples with the cf of 12 % ($\bar{I}$ = 0.49 ± 0.16 mA) and 10 % ($\bar{I}$ = 0.48 ± 0.16 mA), respectively.

Hence, among the various samples, PS450 displayed the superior FE properties including the lowest E_{TO} = 1.57 V/μm and E_{TH} = 2.94 V/μm, as well as the highest β = 4977 and J_{total} = 33 mA/cm^2 at the field of ~4 V/μm along with improved FE stability for more than five hours. Furthermore, the key FE parameters observed for PS450 were superior or comparable to the reported values for pillar-based CNT field-emitters [29, 38, 39, 56, 57]. For a detailed comparison, Table 5.4 summarizes key FE parameters for various pillar-based CNT field emitters reported in the literature and the dissertation. It should be noted that the CNT pillar emitters reported in the literature were significantly longer than the VACNT pillar emitters reported in the current study. So, the FE properties of our VACNT-P-FEA samples can be further enhanced by growing longer VACNTs with optimized inter-pillar separation.

The poor FE performance from the dense VACNT forest was mainly caused by the compact morphology of the VACNT emitters (decreased inter-VACNTs spacing), making them vulnerable to the field screening effect [17]. Consequently, there was a delay in the onset of the emission current (i.e., high E_{To}) and premature saturation of the emission current (i.e., high E_{Th}). A reduction in threshold field by more than half and increase in saturation emission current by about 50 folds as a result of the decrease in nanotube density by an order of magnitude has been reported [17]. A ratio of inter-emitter spacing to emitter height, R/H = 1 (experimental) or 2 (theoretical), have been suggested in order to minimize the screening effect for the maximum possible field enhancement from VACNT emitter arrays [10, 58]. For the dense VACNT forest, the average emission current was very low along with a drastic decrease in emission current during the first hour of the stability test, as shown in Figure 5.8(e). Because of the significant screening effects in the dense VACNT

forest, only those VACNTs which were longer or resided at the edges of the larger gaps in the non-uniform distribution area (Figure 5.5(a)) contributed to the FE current [59]. That means the total emission current was emitted only by a few active VACNTs under the high applied field, making them vulnerable to structural failure caused by Joule's heating or current-induced dislocations, which occur only above a certain threshold of current density [60, 61]. Hence, the decrease in emission current can be attributed to the field evaporation of longer and non-uniform VACNTs during the FE stability test. However, improved emission current stability was observed after an hour of stability testing, which is a typical FE behavior for a dense forest of VACNT emitters.

The lower E_{To} and E_{Th}, the higher field enhancement factor, and improved emission stability suggest that the VACNT-P-FEAs are more favorable field-emitters than the dense arrays of VACNTs (HD) for better FE performance. The better performance from the VACNT-P-FEAs compared to the HD sample was mainly because of their isolated pillar morphology, which increased the number of active field-emitters. In other words, the pillar-type morphology of VACNT-P-FEAs increased the number of VACNTs lying at the edges of the pillar structure, which were the true sites for field emission. For a constant number density of VACNTs within a pillar-based sample, it was expected to further increase the number of active field-emitters by decreasing the pillar size, thereby increasing the overall FE properties. The data in Table 5.3 agrees with this prediction and shows that the FE performance of the VACNT-P-FEAs was indeed improved with the decrease in pillar size. It must be pointed out that PS450 exhibited the best FE performance among the samples instead of PS200 pillars with the least diameter. The result suggested that more

fundamental aspects, in addition to the pillar size, should be explored to understand the observed FE properties of the as-synthesized VACNT pillar emitters.

To understand the FE behavior of the VACNT pillar emitters and support our conclusions, we simulated the electrostatic field for VACNT-P-FEAs. Figure 5.9(a-c) represents the distribution of the local electric field at the tip of VACNT emitters for the samples PS950, PS450, and PS200, respectively. Top and 3D views show strong local electric fields allocated mainly at the edge of the pillar structures, suggesting that only the VACNTs at the pillar's edge emit electrons during the FE process. According to the simulation result, the number of active emitters in a single VACNT pillar was counted as

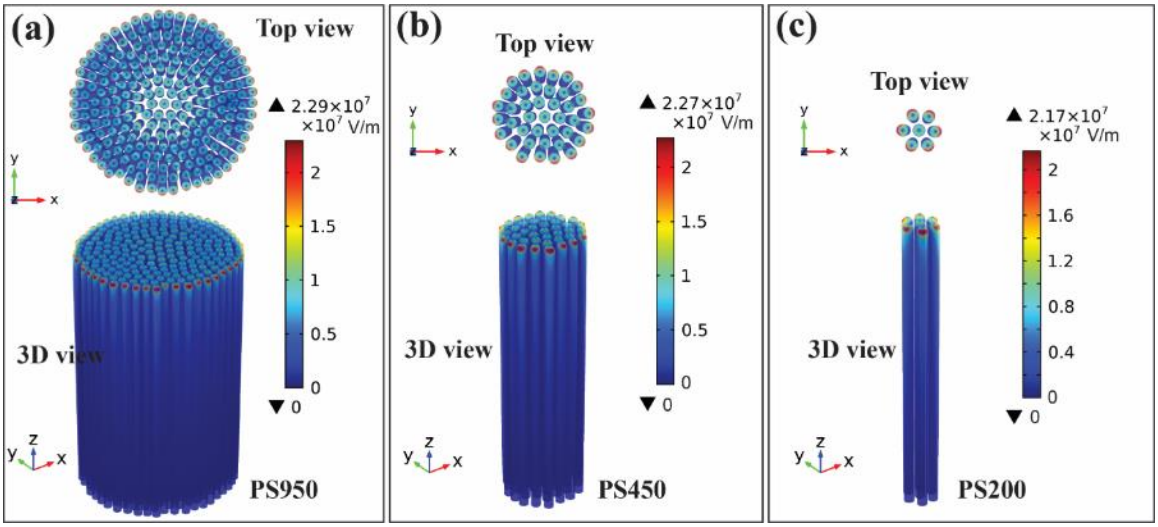

Figure 5.9. Electrostatic field distribution for VACNT-P-FEAs having different pillar diameters, referring to the sample (a) PS950, (b) PS450, and (c) PS200. The hue on the VACNT-P-FEAs represents the distribution of the electric field. The reddish regions denote the strong electric field, whereas the dark blue regions show the zero-electric field. The numbers above the scale bar correspond to the maximum electric field in the domain.

49 (~22 %), 19 (~48 %), and 6 (~86 %), corresponding to the samples PS950, PS450, and PS200, respectively. The result indicates that most VACNTs in a large pillar were inactive during field emission because of the screening effect of the densely packed VACNTs

within the pillar, whereas almost all VACNTs in a small pillar contributed to the field emission. Considering a small domain of 28 × 21 μm^2, referring to the SEM images of Figure 5.5, the number of VACNT pillars were counted as 33, 173, and 506 for PS950, PS450, and PS200, respectively (Table 5.2). According to the simulation results, the number of active emitters within the domain was estimated to be 1617, 3287, and 3036 for samples PS950, PS450, and PS200, respectively. Nilsson et al. suggested through a numerical analysis that an optimal ratio of intertube distance to the height of the CNT was about two (R/H = 2) for minimum field screening in a periodic array of VACNTs [10]. However, Yun et al. and Suh et al. demonstrated that the maximum field enhancement occurred when the value was one (R/H = 1) for a periodic array of vertically aligned carbon nanofibers/nanotubes [58, 62]. Lin et al. reported R/H = 2 for the lowest turn-on field and highest field enhancement factor from VACNT-pillars in a hexagonal array [27]. From the above results, it can be concluded that the field screening effect can be minimized, and the FE performance can be improved by maintaining the R/H ≥ 1. In the current work, the sample PS450 has an average inter-pillar spacing of 2.02 ± 0.72 μm (individual inter-pillar distance in the range of 0.73 to 3.52 μm, measured from the SEM images shown in Figure 5.5), which results in the R/H value of about 1.3. The suitable R/H value, along with the highest number of active field-emitters of the PS450, explains its superior FE performance among all the tested samples.

On the other hand, the PS200 contained a higher number of active field-emitters than PS950, but it displayed a slightly poor FE performance than PS950, as shown in Table 5.3. The weak FE performance was attributed to the field screening effect because the VACNT pillars in PS200 were too close to each other. The average inter-pillar distance for

PS200 was measured as 0.91 ± 0.24 μm (R/H = ~0.7 and individual inter-pillar distance in the range of 0.45 to 2.16 μm). In contrast, the inter-pillar distance for PS950 was more extensive (4.25 ± 1.57 μm) (R/H = ~3 and individual inter-pillar distance in the range of 1.21 to 7.23 μm). It should also be noted that the samples HD, PS110, and PS200 exhibited emission with very similar turn-on fields (3.09, 3.13, and 3.06 V/μm, respectively). Although there was reduced field screening for PS110 and PS200 owing to the larger inter-VACNTs/pillars spacing and hence high emission per VACNT, the density of field emitters in the two samples was significantly low compared to that in the HD sample (Table 5.2). The FE performance of PS200 was expected to be much better than that of PS110 since the density of VACNTs for PS200 was much higher than that for PS110. However, experimental results showed that both samples performed FE with similar turn-on and threshold fields. The discrepancy could be attributed to the morphological difference in these two samples because PS200 consisted of VACNT pillars where field screening among VACNTs within the pillar can be anticipated.

Several reports have shown that the electronic properties of CNTs can be enhanced by doping with nitrogen (N), which introduces donor states near the Fermi level [63]. As a result, N-doped CNTs show metallic properties and reduced work function, thereby showing enhanced emission efficiency [64]. Hence, it is essential to determine the doping state of our samples, which can help understand the enhanced FE performance. In our previous report [65], we performed X-ray photoelectron spectroscopy (XPS) experiments to investigate the possible bonding of N with the graphitic wall of CNTs before and after NH_3 plasma treatment by probing the N 1s core levels. We found that CNTs were characterized by the interstitial N, NO, C=N (sp^2 bonding), and C≡N (sp^3 bonding) even

before the NH_3 plasma treatment. The result indicated that CNTs were doped with N caused by the NH_3 plasma etching during the CNT growth. It has been suggested that the presence of highly energetic N atoms, radicals, or ions in the CNT growth environment creates N-doping effects by directly substituting carbon atoms on the CNT wall [66]. The samples in the current work were synthesized using the same conditions (such as hydrocarbon gas (C_2H_2), etching gas (NH_3), and PECVD) as those in our previous work [61]. Therefore, the current samples were also doped with nitrogen (N).

The incorporation of N atoms and atomic hydrogen within the graphitic network (CNT walls) plays a crucial role in the synthesis of multi-compartment CNT filament, which can be beneficial for improved FE performance. It is widely accepted that sp^3 hybridized (pyrrolic-like) nitrogen atoms bound with C atoms of the graphene layer can lead to the formation of "bamboo-like" CNTs [67, 68]. The formation of the "bamboo-like" structure may create many open graphitic edges (defects) on the outer wall of CNTs, and the edges act as additional emission sites, which can significantly enhance the FE properties [69-71]. Although we did not observe noticeable open graphitic edges in HRTEM images, the presence of such defects in nanoscale cannot be ruled out. It should also be noted that plasma bombardment on the outer wall of CNTs may also create many defects (sharp edges), which is well supported by the Raman spectra of VACNT-P-FEAs. Besides, atomic hydrogen attachment to the open graphitic edges may significantly lower the work function, enhancing the FE properties of CNTs [72]. In VACNT emitters, the tip section is supposed to be mainly responsible for the electron emission. The presence of such open graphitic edges at and around the tip with reduced work function should enhance the FE properties of our VACNT-P-FEAs.

Apart from the above-discussed factors, the higher conductivity of substrate (typically metallic substrates) plays a vital role in the FE process. The FE process involves three main stages, (i) electron introduction, (ii) electron transmission, and (iii) emission in a vacuum. In this process, the metallic substrate (SS in our case) becomes crucial since it serves as an uninterrupted source of electrons, supports efficient electron transfer to the VACNT root, and helps for adequate dissipation of heat generated by Joule's heating, thereby preserving the VACNT-metal bond and thus, a better life for field emitters [73]. Moreover, the pathway of electron transportation from the substrate to VACNTs (i.e., contact barrier) is another critical issue of scientific interest regarding the FE process. With the help of a double-barrier model, it has been shown that the width of the interfacial barrier between emitters and the substrate determines the FE properties [74]. In our work, VACNT-P-FEAs were directly grown on the SS substrate, and hence they were expected to have an ohmic connection with the substrate by Fermi level matching resulting in smaller contact resistance [75]. The ohmic contact can be attributed to the strong wettability of CNTs with SS (primary content is Fe), and in the context of our research, the contact resistance is a function of wettability instead of work function difference between CNTs and substrate [75, 76]. The presence of low contact resistance was well supported by the fact that our VACNT-P-FEAs have always shown a straight line, instead of an explicit knee, in the F–N plot (Figure 5.8(c)) [73, 74]. Because of these underlying reasons, the possibility of the contact voltage drop from our VACNT-P-FEAs during the FE process can be neglected. Therefore, the metallic nature of our field emitters (VACNT-P-FEAs on SS) contributed to the efficient electron movement and superior emission during the FE process.

5.4 Conclusions

Dense forests, micropillar arrays, and low-density arrays of self-standing VACNTs were synthesized directly, without using an external catalyst and buffer layer, on the stainless steel substrates using the PECVD method. A CNT inhibition layer (Cr-layer) combined with nanosphere lithography (NSL) enabled the growth of VACNT-P-FEAs with controlled morphologies. Compared to high-density VACNT forests, the VACNT pillars have significantly improved the electron field emission performance. The VACNT pillars synthesized on stainless steel after NSL with polystyrene spheres of 450 nm in diameter showed superior FE performance including low turn-on field (E_{To} = 1.57 V/μm), low threshold field (E_{Th} = 2.94 V/μm), high field enhancement factor (β = 4977), and high emission current density of ~33 mA/cm^2 at a field of 4 V/μm. The sample PS450 also showed a stable emission current with a high average current (0.49 mA) and a low current fluctuation (12%) for an extended period of more than five hours. The FE performance of our VACANT-P-FEA samples was better or comparable to pillar-based CNT field-emitters. The superior FE properties can be accredited to the synergistic effect of the high number of active field-emitters and an alleviated screening effect between the VACNT pillars as a result of an optimum inter-pillar distance. A simulation was performed to understand the electron field emission of the VACNT pillars. The simulation results are consistent with the experimental results. Structurally controlled VACNT-P-FEAs synthesized directly on a conducting substrate, as shown here for stainless steel, could be applied for developing next-generation high-performance miniaturized vacuum tube X-ray devices.

References

[1] de Heer W.A., Châtelain A. and Ugarte D., A Carbon Nanotube Field-Emission Electron Source. *Science* **1995,** 270 (5239), 1179.

[2] Jiang K., Carbon Nanotubes for Displaying, in: Peng H., Li Q. and Chen T. (Eds.), *Elsevier* **2017**, p. 101.

[3] Parmee R.J., Collins C.M., Milne W.I. and Cole M.T., X-ray generation using carbon nanotubes. *Nano Convergence* **2015,** 2 (1), 1.

[4] Liu B., Liu X., Yuan Z., Jiang Y., Su Y., Ma J. and Tai H., A flexible NO2 gas sensor based on polypyrrole/nitrogen-doped multiwall carbon nanotube operating at room temperature. *Sensors and Actuators B: Chemical* **2019,** 295, 86.

[5] Xing Y., Zhang Y., Xu N., Huang H., Ke Y., Li B., Chen J., She J. and Deng S., Design and realization of microwave frequency multiplier based on field emission from carbon nanotubes cold-cathode. *IEEE Transactions on Electron Devices* **2018,** 65 (3), 1146.

[6] Iijima S., Helical microtubules of graphitic carbon. *Nature* **1991,** 354 (6348), 56.

[7] Li W., Qian L., Qian S., Zhou W., Wang G., Fu C., Zhao R. and Xie S., Structure and growth thermodynamics of carbon tubes. *Science in China Series A-Mathematics* **1996,** 39 (6), 657.

[8] Qian D., Wagner G.J., Liu W.K., Yu M.F. and Ruoff R.S., Mechanics of carbon nanotubes. *Applied Mechanics Reviews* **2002,** 55 (6), 495.

[9] Bockrath M., Cobden D.H., McEuen P.L., Chopra N.G., Zettl A., Thess A. and Smalley R.E., Single-electron transport in ropes of carbon nanotubes. *Science* **1997,** 275 (5308), 1922.

[10] Nilsson L., Groening O., Emmenegger C., Kuettel O., Schaller E., Schlapbach L., Kind H., Bonard J. and Kern K., Scanning field emission from patterned carbon nanotube films. *Applied Physics Letters* **2000,** 76 (15), 2071.

[11] Talapatra S., Kar S., Pal S.K., Vajtai R., Ci L., Victor P., Shaijumon M.M., Kaur S., Nalamasu O. and Ajayan P.M., Direct growth of aligned carbon nanotubes on bulk metals. *Nat Nanotechnol* **2006,** 1 (2), 112.

[12] Rinzler A., Hafner J., Nikolaev P., Nordlander P., Colbert D., Smalley R., Lou L.,

Kim S. and Tománek D., Unraveling nanotubes: field emission from an atomic wire. *Science* **1995,** 269 (5230), 1550.

[13] De Heer W.A., Chatelain A. and Ugarte D., A carbon nanotube field-emission electron source. *science* **1995,** 270 (5239), 1179.

[14] Bonard J.-M., Croci M., Klinke C., Kurt R., Noury O. and Weiss N., Carbon nanotube films as electron field emitters. *Carbon* **2002,** 40 (10), 1715.

[15] Neupane S., Lastres M., Chiarella M., Li W., Su Q. and Du G., Synthesis and field emission properties of vertically aligned carbon nanotube arrays on copper. *Carbon* **2012,** 50 (7), 2641.

[16] Thapa A., Guo J., Jungjohann K.L., Wang X. and Li W., Density control of vertically aligned carbon nanotubes and its effect on field emission properties. *Materials Today Communications* **2020,** 22, 100761.

[17] Chhowalla M., Ducati C., Rupesinghe N.L., Teo K.B.K. and Amaratunga G.A.J., Field emission from short and stubby vertically aligned carbon nanotubes. *Applied Physics Letters* **2001,** 79 (13), 2079.

[18] Kurilich M.R., Thapa A., Moilanen A., Miller J.L., Li W. and Neupane S., Comparative study of electron field emission from randomly-oriented and vertically-aligned carbon nanotubes synthesized on stainless steel substrates. *Journal of Vacuum Science & Technology B, Nanotechnology and Microelectronics: Materials, Processing, Measurement, and Phenomena* **2019,** 37 (4), 041202.

[19] Bonard J.M., Weiss N., Kind H., Stöckli T., Forró, Lμszló and Kern K.C.t., Andre, Tuning the Field Emission Properties of Patterned Carbon Nanotube Films. *Avanced Materials* **2001,** 13 (3), 184.

[20] Lahiri I. and Choi W., Interface control: A modified rooting technique for enhancing field emission from multiwall carbon nanotube based bulk emitters. *Acta Materialia* **2011,** 59 (14), 5411.

[21] Ahmad M. and Silva S.R.P., Low Temperature Growth of Carbon Nanotubes–A Review. *Carbon* **2019,** 158, 24.

[22] Teo K., Lee S.-B., Chhowalla M., Semet V., Binh V.T., Groening O., Castignolles M., Loiseau A., Pirio G. and Legagneux P., Plasma enhanced chemical vapour deposition carbon nanotubes/nanofibres—how uniform do they grow? *Nanotechnology* **2003,** 14 (2), 204.

[23] Milne W.I., Teo K.B.K., Minoux E., Groening O., Gangloff L., Hudanski L., Schnell J.-P., Dieumegard D., Peauger F., Bu I.Y.Y., Bell M.S., Legagneux P., Hasko G. and Amaratunga G.A.J., Aligned carbon nanotubes/fibers for applications in vacuum microwave amplifiers. *Journal of Vacuum Science & Technology B: Microelectronics and Nanometer Structures Processing, Measurement, and Phenomena* **2006,** 24 (1), 345.

[24] Wang Y., Rybczynski J., Wang D.Z., Kempa K., Ren Z.F., Li W.Z. and Kimball B., Periodicity and alignment of large-scale carbon nanotubes arrays. *Applied Physics Letters* **2004,** 85 (20), 4741.

[25] Park K.H., Lee S., Koh K.H., Lacerda R., Teo K.B.K. and Milne W.I., Advanced nanosphere lithography for the areal-density variation of periodic arrays of vertically aligned carbon nanofibers. *Journal of Applied Physics* **2004,** 97 (2), 024311.

[26] Jo S.H., Tu Y., Huang Z.P., Carnahan D.L., Wang D.Z. and Ren Z.F., Effect of length and spacing of vertically aligned carbon nanotubes on field emission properties. *Applied Physics Letters* **2003,** 82 (20), 3520.

[27] Lin P.-H., Sie C.-L., Chen C.-A., Chang H.-C., Shih Y.-T., Chang H.-Y., Su W.-J. and Lee K.-Y., Field emission characteristics of the structure of vertically aligned carbon nanotube bundles. *Nanoscale research letters* **2015,** 10 (1), 297.

[28] Gupta B.K., Kedawat G., Gangwar A.K., Nagpal K., Kashyap P.K., Srivastava S., Singh S., Kumar P., Suryawanshi S.R. and Seo D.M., High-performance field emission device utilizing vertically aligned carbon nanotubes-based pillar architectures. *AIP Advances* **2018,** 8 (1), 015117.

[29] Silan J.L., Niemann D.L., Ribaya B.P., Rahman M., Meyyappan M. and Nguyen C.V., Carbon nanotube pillar arrays for achieving high emission current densities. *Applied Physics Letters* **2009,** 95 (13), 133111.

[30] Li Z., Yang X., He F., Bai B., Zhou H., Li C. and Dai Q., High current field emission from individual non-linear resistor ballasted carbon nanotube cluster array. *Carbon* **2015,** 89, 1.

[31] Sato H., Haruki K., Watanabe M., Hata K. and Saito Y., Effect of geometry of a vertically aligned carbon nanotube pillar array on its field-emission properties. *Surface and Interface Analysis* **2012,** 44 (6), 776.

[32] Wang K.-Y., Liao C.-Y. and Cheng H.-C., Field-Emission Characteristics of the Densified Carbon Nanotube Pillars Array. *ECS Journal of Solid State Science and Technology* **2016,** 5 (9), M99.

[33] Masarapu C. and Wei B., Direct Growth of Aligned Multiwalled Carbon Nanotubes on Treated Stainless Steel Substrates. *Langmuir* **2007,** 23 (17), 9046.

[34] Zhang X., Whitney A.V., Zhao J., Hicks E.M. and Van Duyne R.P., Advances in contemporary nanosphere lithographic techniques. *Journal of Nanoscience and Nanotechnology* **2006,** 6 (7), 1920.

[35] Esconjauregui S., Whelan C.M. and Maex K., The reasons why metals catalyze the nucleation and growth of carbon nanotubes and other carbon nanomorphologies. *Carbon* **2009,** 47 (3), 659.

[36] Deck C.P. and Vecchio K., Prediction of carbon nanotube growth success by the analysis of carbon–catalyst binary phase diagrams. *Carbon* **2006,** 44 (2), 267.

[37] Yuan L., Li T. and Saito K., Growth mechanism of carbon nanotubes in methane diffusion flames. *Carbon* **2003,** 41 (10), 1889.

[38] Wang K.Y., Chou C.H., Liao C.Y., Li Y.R. and Cheng H.C., Densification effects of the carbon nanotube pillar array on field-emission properties. *Japanese Journal of Applied Physics* **2016,** 55 (6S1), 06GF12.

[39] Lim Y.D., Hu L., Xia X., Ali Z., Wang S., Tay B.K., Aditya S. and Miao J., Field emission properties of SiO2-wrapped CNT field emitter. *Nanotechnology* **2017,** 29 (1), 015202.

[40] Thapa A., Neupane S., Guo R., Jungjohann K.L., Pete D. and Li W., Direct growth of vertically aligned carbon nanotubes on stainless steel by plasma enhanced chemical vapor deposition. *Diamond and Related Materials* **2018,** 90, 144.

[41] Kumar M. and Ando Y., Chemical vapor deposition of carbon nanotubes: a review on growth mechanism and mass production. *Journal of nanoscience and nanotechnology* **2010,** 10 (6), 3739.

[42] Lv R., Kang F., Zhu D., Zhu Y., Gui X., Wei J., Gu J., Li D., Wang K. and Wu D., Enhanced field emission of open-ended, thin-walled carbon nanotubes filled with ferromagnetic nanowires. *Carbon* **2009,** 47 (11), 2709.

[43] Lin W.-H. and Li Y.-Y., Field emission properties of tapered carbon nanotubes synthesized by the pyrolysis of poly(ethylene glycol) using a nickel catalyst. *Diamond and Related Materials* **2012,** 22, 124.

[44] Lee C.-K., Lee B., Ihm J. and Han S., Field emission of metal nanowires studied by first-principles methods. *Nanotechnology* **2007,** 18 (47), 475706.

[45] Hertel T., Walkup R.E. and Avouris P., Deformation of carbon nanotubes by surface van der Waals forces. *Physical Review B* **1998,** 58 (20), 13870.

[46] Meyyappan M., Delzeit L., Cassell A. and Hash D., Carbon nanotube growth by PECVD: a review. *Plasma Sources Science and Technology* **2003,** 12 (2), 205.

[47] Lin C.H., Chang H.L., Hsu C.M., Lo A.Y. and Kuo C.T., The role of nitrogen in carbon nanotube formation. *Diamond and Related Materials* **2003,** 12 (10-11), 1851.

[48] Dresselhaus M.S., Dresselhaus G., Saito R. and Jorio A., Raman spectroscopy of carbon nanotubes. *Physics reports* **2005,** 409 (2), 47.

[49] Baro M., Gogoi D., Pal A.R., Adhikary N.C., Bailung H. and Chutia J., Pulsed PECVD for Low-temperature Growth of Vertically Aligned Carbon Nanotubes. *Chemical Vapor Deposition* **2014,** 20 (4-5-6), 161.

[50] Chuang C., Huang J., Chen W., Lee C. and Chang Y., Role of amorphous carbon nanowires in reducing the turn-on field of carbon films prepared by microwave-heated CVD. *Diamond and related materials* **2004,** 13 (4-8), 1012.

[51] Di Bartolomeo A., Scarfato A., Giubileo F., Bobba F., Biasiucci M., Cucolo A., Santucci S. and Passacantando M., A local field emission study of partially aligned carbon-nanotubes by atomic force microscope probe. *Carbon* **2007,** 45 (15), 2957.

[52] Semet V., Binh V.T., Vincent P., Guillot D., Teo K.B.K., Chhowalla M., Amaratunga G.A.J., Milne W.I., Legagneux P. and Pribat D., Field electron emission from individual carbon nanotubes of a vertically aligned array. *Applied Physics Letters* **2002,** 81 (2), 343.

[53] Parveen S., Kumar A., Husain S. and Husain M., Fowler Nordheim theory of carbon nanotube based field emitters. *Physica B: Condensed Matter* **2017,** 505, 1-8.

[54] Di Bartolomeo A., Scarfato A., Giubileo F., Bobba F., Biasiucci M., Cucolo A., Santucci S. and Passacantando M., A local field emission study of partially aligned carbon-nanotubes by atomic force microscope probe. *Carbon* **2007,** 45 (15), 2957.

[55] Gao R., Pan Z. and Wang Z.L., Work function at the tips of multiwalled carbon nanotubes. *Applied Physics Letters* **2001,** 78 (12), 1757.

[56] Lin P.H., Sie C.L., Chen C.A., Chang H.C., Shih Y.T., Chang H.Y., Su W.J. and Lee K.Y., Field emission characteristics of the structure of vertically aligned carbon nanotube bundles. *Nanoscale research letters* **2015,** 10 (1), 297.

[57] Uh H.S. and Park S., Improved field emission properties from carbon nanotubes grown onto micron-sized arrayed silicon pillars with pyramidal bases. *Diamond and Related Materials* **2015,** 54, 74.

[58] Yun J., Wang R., Choi W.K., Thong J.T.L., Thompson C.V., Zhu M., Foo Y.L. and Hong M.H., Field emission from a large area of vertically-aligned carbon nanofibers with nanoscale tips and controlled spatial geometry. *Carbon* **2010,** 48 (5), 1362.

[59] Pandey A., Prasad A., Moscatello J., Ulmen B. and Yap Y.K., Enhanced field emission stability and density produced by conical bundles of catalyst-free carbon nanotubes. *Carbon* **2010,** 48 (1), 287.

[60] Kayastha V.K., Ulmen B. and Yap Y.K., Effect of graphitic order on field emission stability of carbon nanotubes. *Nanotechnology* **2007,** 18 (3), 035206.

[61] Gupta A.P., Park S., Yeo S.J., Jung J., Cho C., Paik S.H., Park H., Cho Y.C., Kim S.H. and Shin J.H., Direct synthesis of carbon nanotube field emitters on metal substrate for open-type X-ray source in medical imaging. *Materials* **2017,** 10 (8), 878.

[62] Suh J.S., Jeong K.S., Lee J.S. and Han I., Study of the field-screening effect of highly ordered carbon nanotube arrays. *Applied Physics Letters* **2002,** 80 (13), 2392.

[63] Carroll D.L., Redlich P., Blase X., Charlier J.C., Curran S., Ajayan P.M., Roth S. and Rühle M., Effects of Nanodomain Formation on the Electronic Structure of Doped Carbon Nanotubes. *Physical Review Letters* **1998,** 81 (11), 2332.

[64] Terrones M., Ajayan P.M., Banhart F., Blase X., Carroll D.L., Charlier J.C., Czerw R., Foley B., Grobert N., Kamalakaran R., Kohler-Redlich P., Rühle M., Seeger T. and Terrones H., N-doping and coalescence of carbon nanotubes: synthesis and electronic properties. *Applied Physics A* **2002,** 74 (3), 355.

[65] Chen G., Neupane S., Li W., Chen L. and Zhang J., An increase in the field emission from vertically aligned multiwalled carbon nanotubes caused by NH3 plasma treatment. *Carbon* **2013,** 52, 468.

[66] Kim J.-B., Kong S.-J., Lee S.-Y., Kim J.-H., Lee H.-R., Kim C.-D. and Min B.-K., Characteristics of nitrogen-doped carbon nanotubes synthesized by using PECVD and Thermal CVD. *Journal of the Korean Physical Society* **2012,** 60 (7), 1124.

[67] Jang J.W., Lee C.E., Lyu S.C., Lee T.J. and Lee C.J., Structural study of nitrogen-doping effects in bamboo-shaped multiwalled carbon nanotubes. *Applied Physics Letters* **2004,** 84 (15), 2877.

[68] Arjmand M., Chizari K., Krause B., Pötschke P. and Sundararaj U., Effect of synthesis catalyst on structure of nitrogen-doped carbon nanotubes and electrical conductivity and electromagnetic interference shielding of their polymeric nanocomposites. *Carbon* **2016,** 98, 358.

[69] Srivastava S.K., Vankar V.D., Sridhar Rao D.V. and Kumar V., Enhanced field emission characteristics of nitrogen-doped carbon nanotube films grown by microwave plasma enhanced chemical vapor deposition process. *Thin Solid Films* **2006,** 515 (4), 1851.

[70] Srivastava S., Vankar V.D. and Kumar V., Excellent Field Emission Properties of Short Conical Carbon Nanotubes Prepared by Microwave Plasma Enhanced CVD Process. *Nanoscale Research Letters* **2007,** 3 (1), 25.

[71] Srivastava S.K., Vankar V.D., Kumar V. and Singh V.N., Effect of Substrate Morphology on Growth and Field Emission Properties of Carbon Nanotube Films. *Nanoscale Research Letters* **2008,** 3 (6), 205.

[72] Zhi C.Y., Bai X.D. and Wang E.G., Enhanced field emission from carbon nanotubes by hydrogen plasma treatment. *Applied Physics Letters* **2002,** 81 (9), 1690.

[73] Lahiri I., Seelaboyina R., Hwang J.Y., Banerjee R. and Choi W., Enhanced field emission from multi-walled carbon nanotubes grown on pure copper substrate. *Carbon* **2010,** 48 (5), 1531.

[74] Zhang J., Wang X., Yang W., Yu W., Feng T., Li Q., Liu X. and Yang C., Interaction between carbon nanotubes and substrate and its implication on field emission mechanism. *Carbon* **2006,** 44 (3), 418.

[75] Kumari R., Tyagi P.K. and Puri N.K., Work function and electrical properties of individual multiwalled carbon nanotube: influenced by nature of catalyst and substrate. *Applied Physics A* **2018,** 124 (7), 466.

[76] Lim S.C., Jang J.H., Bae D.J., Han G.H., Lee S., Yeo I.-S. and Lee Y.H., Contact resistance between metal and carbon nanotube interconnects: Effect of work function and wettability. *Applied Physics Letters* **2009,** 95 (26), 264103.

CHAPTER 6

Cu-filled VACNT arrays on Cu disks: Synthesis, structural characterization, and their field emission properties

Chapter 6 presents the investigation on the synthesis, characterization, and field emission properties of copper filled vertically aligned carbon nanotube (Cu@VACNT) arrays on the copper substrate.

6.1 Introduction

Metals in their low-dimensional nanostructures, such as nanowires, nanorods, and nanoparticles, are fundamental for miniaturizing sophisticated mechanical, optical, and electronic devices. Since the report of single-crystal metal encapsulated in carbon nanoparticles in 1993 [1], great attention has been concentrated on synthesizing metal-carbon hybrid material, especially metal nanowires encapsulated by carbon. Carbon nanotubes (CNTs) are well known for their high tensile strength and chemical stability. The CNTs encapsulated nanowires can survive in harsh environments since the carbon shells act as protective barriers; therefore, the nanowires can be preserved in their pure form. The synergistic effect of the core metal nanowires and CNT shells, as well as the well-defined one-dimensional core-shell structure, can open up novel applications or improve the performance of existing devices. It has been shown that CNTs filled with metals have diverse applications in nanodevices such as nanomagnets [2], nanoswitches [3], nanopipettes [4], nanowelding [5], and nanothermometers [6]. Copper (Cu) is one of the most commonly used metals in electrical circuits as interconnects because of its high conductivities of heat and electricity. A weak interaction of Cu with carbon (binding energy

of 0.1 – 0.144 eV/atom) and its higher thermal and electrical conductivities make CNTs encapsulated Cu nanowires ideal materials for many of the aforementioned potential applications. In addition, vertically aligned carbon CNT (VACNT) encapsulated Cu nanowires may find potential applications in electron field emission devices since a new functionality can be achieved by combining the properties of Cu nanowires and VACNTs.

Mainly two types of methods, ex-situ and in-situ, for filling Cu into the core of CNTs have been reported. The ex-situ method involves the Cu (or any foreign materials) impregnation in the hollow interior of the CNTs after the CNT growth. Ex-situ filling methods include supercritical fluid chemical deposition (SFCD) and chemical fluid deposition (CFD) techniques [7, 8], sonication-assisted wet chemical method [9], solution infusion method [10], and electrochemical co-deposition method [11]. The different CNT ex-situ filling methods were described in a review paper [12]. The ex-situ methods require that the filling materials have low surface tension, low viscosity, high diffusivity, and adequate vapor pressure. Furthermore, an ex-situ method usually comprises multiple steps, such as CNT opening, guest material filling, and heat treatment, which can easily damage the CNTs. Another problem associated with ex-situ filling methods is that the filling rate of the CNTs remains typically low.

In contrast, the in-situ method enables the growth of CNTs and their filling with Cu simultaneously. To date, several in-situ techniques have been developed in an attempt to accomplish large scale production of Cu-filled CNTs with a well-defined structure of Cu core and high filling rate. These techniques include hydrogen arc method [13], microwave plasma-assisted chemical vapor deposition (MPCVD) [14], surfactant-assisted

hydrothermal method [15], thermal decomposition method [16, 17], laser vaporization method [18], and chemical vapor deposition (CVD) [19]. Although a variety of techniques have shown some success in filling Cu inside CNTs, there are some critical issues associated with these techniques, such as the low yield of filled CNTs, the complex and lengthy procedures, the necessity of organic/inorganic Cu salts, the lack of preferred orientation of the Cu nanowire-filled CNTs, and the contamination of unnecessary byproducts. Herein, we report a facile and controlled synthesis of large scale, vertically aligned, and mechanically self-supported pure Cu-filled CNT (Cu@VACNT) arrays directly connected to the Cu substrate. The Cu@VACNTs were grown on bulk Cu disks without the deposition of an extra metal catalyst layer via a plasma-enhanced chemical vapor deposition (PECVD) method. To the best of our knowledge, such a result achieved in the chapter has never been reported so far. A possible growth mechanism of the Cu@VACNTs has been proposed.

While the field emission properties of pristine and morphology controlled vertically aligned CNT arrays [20-27], vertically aligned metal nanowire arrays [28-31], and CNTs coated with metal or metal-oxide nanoparticles [32-36] have been studied, a little is known about the field emission behavior of the Cu@VACNT arrays. Therefore, in chapter 6, we present a comparative study of the field emission properties of the unfilled and Cu-filled VACNTs.

6.2 Experimental details

Arrays of Cu@VACNT were synthesized by the direct current (DC) PECVD method. The details of the synthesis technique have been described earlier in section 3.2.1.

In brief, Cu disks (0.6 mm thick and ~1.5 cm in diameter), polished and cleaned ultrasonically in acetone and IPA bath, were transferred into the PECVD chamber. The chamber was evacuated to a base pressure of 0.01 torr. Then, NH_3 gas was introduced into the chamber at the flow rate of 600 sccm, and the pressure inside the chamber was maintained at 7 Torr. The carbon material growth experiments were performed at different temperatures between 550 ºC and 800 ºC. A DC plasma of 90 W was applied to the Cu disks when the targeted growth temperature was reached, and then carbon precursor gas C_2H_2 was introduced at the flow rate of 25 sccm. The synthesis experiments were set for 30 min, and the as-synthesized samples could cool down naturally before being characterized for various purposes. Several substrates were heat-treated at different temperatures such as 650 ºC, 700 ºC, or 750 ºC for 10 min under the NH_3 environment at the pressure of 7 Torr to understand the surface evolution of the substrates. Here, the heat treatment conditions were the same as those for the synthesis of Cu@VACNTs, but the carbon precursor was not introduced so that the VACNTs did not grow. The surface morphology, crystal structure, degree of defects, and chemical composition of Cu@VACNTs were investigated by using various tools and techniques described previously in section 3.3. The field emission measurements were performed as described earlier in sections 3.4.1, while the electrostatic field distribution was simulated by using COMSOL™ MULTIPHYSICS 5.2, as described in section 3.5.

6.3 Results and discussion

6.3.1 Surface morphology of the Cu substrate

The surface evolution of the catalytic substrate before its interaction with carbon precursor gas at elevated temperatures was fundamental to the successful growth of CNTs based on the vapor–quasi-liquid–solid (VLS) growth mechanism [37, 38]. The critical aspect of the surface evolution was the formation of potentially active nucleation sites for the CNT growth, such as nanoparticles or nano hills, as a result of the surface break up due to the complex processes related to the surface energy [26, 39, 40]. The availability of these nanostructures at the substrate's surface can facilitate the dissociation of the carbon precursor gas and further dissolution and precipitation of the carbon atoms or clusters to synthesize CNTs.

Figure 6.1(a-b) represents the surface morphology of the as-received and polished Cu substrate, respectively. The insets in Figure 6.1(a-b) are the corresponding AFM images showing the surface profile along the line shown in the respective images. The as-received surface characterized with irregular topography was found to have an average roughness (R_a) of 76.56 nm and RMS roughness (R_q) of 97.70 nm. Apart from a few scratches, presumably because of polishing, a smooth surface with R_a = 6.93 nm and R_q = 9.03 nm was achieved after polishing, as shown in Figure 6.1(b), which can help synthesize VACNT arrays with uniform length. The EDS spectrum, comprised mainly of Cu signals, shows the elemental composition of the polished surface, as shown in Figure 6.1(c). A trace amount of Al recorded on the EDS spectrum can be assigned to the SEM sample holder. Figure 6.1(d-f) depicts the SEM images of the surface topography of the substrates after

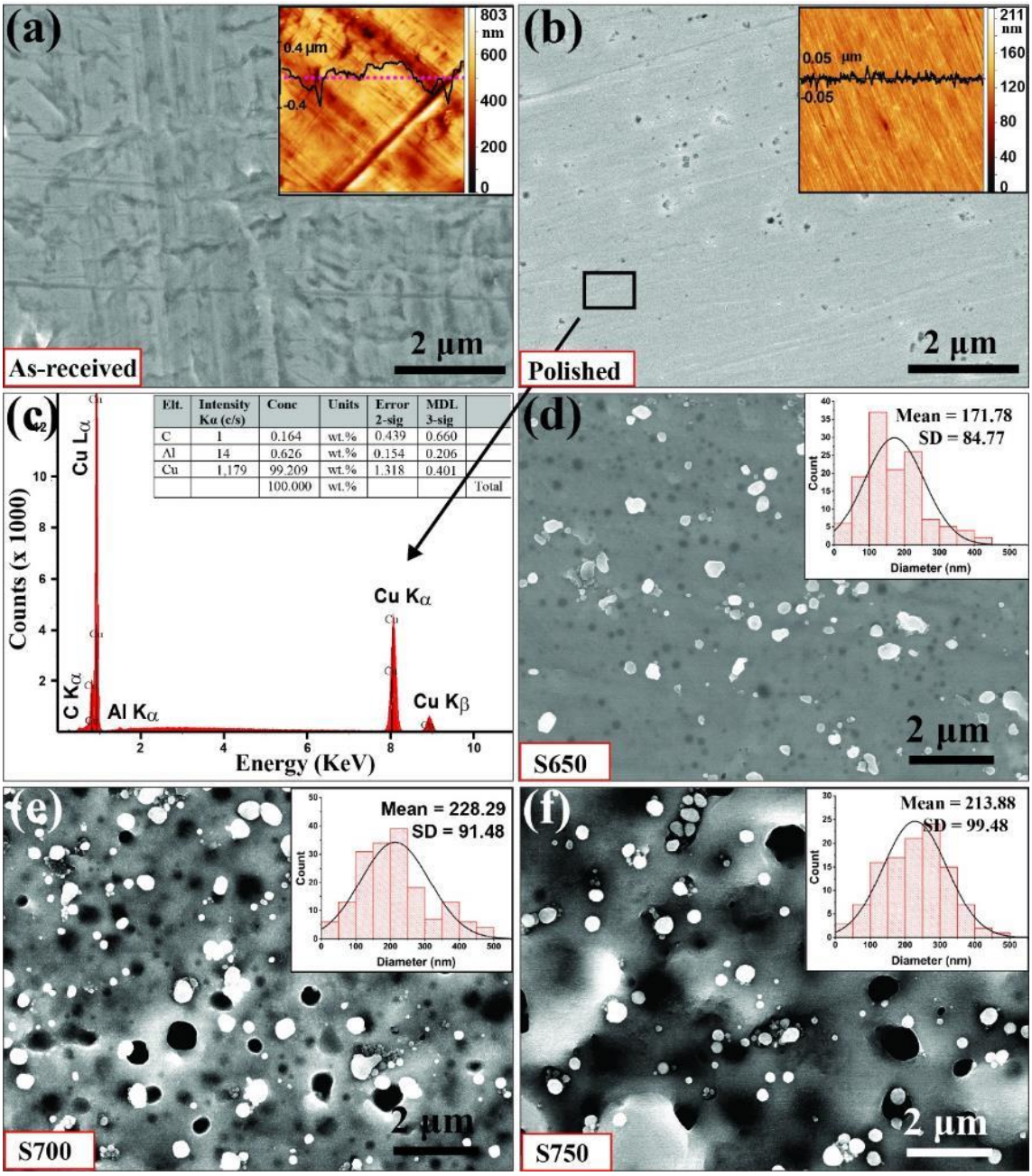

Figure 6.1. Surface morphology of Cu substrates before and after the heat treatment in an NH_3 environment. SEM images of the surface of (a) as received and (b) polished substrate. The insets in Figure 6.1(a-b) represent the AFM images showing the surface profile along the line shown in the corresponding images. (c) EDS spectrum from the polished substrate. (d-f) SEM images of the substrate after the heat treatment at temperatures 650 ºC, 700 ºC, and 750 ºC, respectively. White dots are the Cu particles and black spots are the holes formed on the surface of the Cu substrate. The insets in Figure 6.1(d-f) represents the particle size distribution of the corresponding samples.

heat treatment at 650 ºC, 700 ºC, and 750 ºC, respectively, in the NH_3 environment. Heating significantly changed the surface morphology of the substrate. The surfaces after the heat treatment contained an ensemble of nanoparticles (white dots in Figure 6.1(d-f)) along with many holes (black spots in Figure 6.1(d-f)). The formation of the nanoparticles can be attributed to the surface breakup induced by the heat under the reducing atmosphere [40]. The effect of heating on the surface modification was intensified as the temperature was raised, causing a gradual increase in the size of holes and particles, as shown in Figure 6.1(d-f). However, the particles formed at 700 ºC and 750 ºC have similar sizes. Specifically, the diameter of the nanoparticles was found to be 171.78 ± 84.77 nm, 228.29 ± 91.48 nm, and 213.88 ± 99.48 nm for samples after the heat treatment at 650 ºC, 700 ºC, and 750 ºC, respectively. Microparticles with grain sizes of more than 1 μm were not included in the statistical analysis of the particle size distribution since only the catalyst particles of nano/submicron sizes are effective in the growth of CNTs. The surface analysis suggests that temperatures have a profound effect on surface evolution that low-temperature (650 ºC) treatment causes the formation of smaller nanoparticles while high temperature (700 ºC or 750 ºC) treatment leads to more significant nanoparticles. The size of the nanoparticles will determine the diameter of the VACNTs.

6.3.2 Synthesis of Cu-filled VACNT arrays

It has been reported that CNTs cannot be synthesized directly on bulk Cu substrate without the aid of an additional catalyst because of the limited solubility of C into the Cu [25, 41]. However, some success in synthesizing multi-walled CNTs directly on Cu substrate has been reported [42-44]. The Cu substrates used for the CNT synthesis were

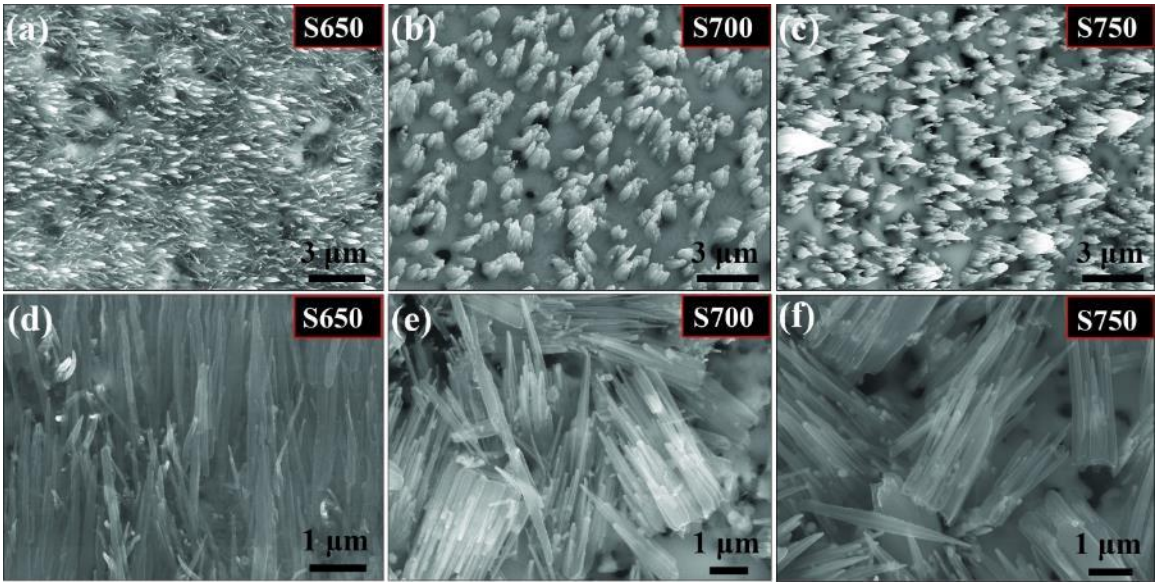

Figure 6.2. SEM images of the VACNTs synthesized on Cu substrate at the temperatures of (a) 650 ºC, (b) 700 ºC, and (c) 750 ºC for 30 min. The other growth parameters (flow rates of C_2H_2 and NH_3 at 25 sccm and 600 sccm, respectively, the pressure of 7 torr, and plasma power of 90 W) were maintained constant throughout the growth process. (d–f) Scratched areas of the samples showing the length of the CNTs.

treated with acid [44] or sulfur [42] to activate their catalytic activities. Otherwise, they would suffer either a poor CNT yield or no CNT synthesis [43]. Our experiment shows that separate extra treatment to the Cu substrate is not necessary for the PECVD synthesis of CNTs. In PECVD synthesis, the highly energetic species in the plasma can help to activate the Cu nanoparticles on the Cu substrate and keep the nanoparticles active by etching away the amorphous carbon from the nanoparticle surface. The energetic plasma species also promote hydrocarbon gas decomposition, which is the carbon source for the CNT growth.

The PECVD experiments were performed at various temperatures in the range of 550 ºC to 800 ºC to identify the growth temperatures of VACNTs on the bulk Cu substrates without extra catalyst layer decoration. The other growth parameters (including growth time of 30 min, plasma power of 90 W, pressure of 7 Torr, flow rate of 600 sccm of NH_3, and flow rate of 25 sccm of C_2H_2) were kept constant throughout the experiments. The

growth parameters were optimized through a series of experiments, and they produced VACNTs with high yield and good quality. The VACNTs grown at 550 ºC and 650 ºC are similar in terms of morphology, and hence only the sample fabricated at 650 ºC will be discussed in this work. Besides, the sample synthesized at 800 ºC did not produce VACNTs, preferably a thick layer of amorphous carbon. Figure 6.2(a-c) represents the typical SEM images (20º tilt-view) of the VACNTs synthesized directly on the Cu disks at

Table 6.1. Variation in catalyst particle size, diameter, length, and number density of VACNTs synthesized at different temperatures.

Sample	Catalyst particle size (nm)	VACNTs diameter (nm)	VACNTs length (μm)	VACNTs density (per cm^2)
S650	171.78 ± 84.77	187 ± 46	4.13 ± 1.53	4.21×10^8
S700	228.29 ± 91.48	246 ± 60	4.91 ± 1.07	3.01×10^8
S750	213.88 ± 99.48	234 ± 68	4.76 ± 1.31	3.12×10^8

650 ºC, 700 ºC, and 750 ºC, respectively. In the subsequent text, these samples will be referred to as S650, S700, and S750, respectively. Figure 6.2(d-f) shows the scratched area of corresponding samples showing the entire length of the VACNTs.

The SEM images revealed that the morphologies of the VACNT arrays were significantly affected by the different growth temperatures. Interestingly, arrays of free-standing isolated VACNTs were synthesized at low growth temperatures such as 650 ºC (Figure 6.2(a)), and arrays of bundled VACNTs were synthesized at high growth temperatures such as 700 ºC or 750 ºC (Figure 6.2(b-c)). The reason behind the two different morphologies of VACNT arrays observed in samples S650 and S700 or S750 can be described as follows. At low growth temperature (S650), individual catalyst particles,

possibly in the solid-state, catalyzed the growth of individual VACNTs to form an array of free-standing VACNTs. However, at sufficiently higher temperatures (S700 or S750), some nanoparticles adjacent to each other could coalesce to form bigger catalyst particles because of the Ostwald ripening. Subsequently, these bigger catalyst particles led to the growth of multiple VACNTs from a single catalyst site to form bundles [25]. It is also important to note that the surface of the Cu substrates was covered with a thin layer of amorphous carbon after the growth process. The carbon layer on the substrate was suggested by fewer pores on the substrates of the samples S700 and S750 (Figure 6.2(b-c)) comparing to those on the Cu substrates after heat treatment at 700 ºC and 750 ºC (Figure 6.2(d-f)). The diameter of the VACNTs was smaller for S650 as compared to that for S700 and S750. However, the length and number density of the VACNTs for all three samples were observed to be in a narrow range, as presented in Table 6.1.

It should be noted that the VACNTs synthesized at the various temperatures, as shown in Figure 6.2(a-c), were not from the Cu catalysts on the Cu substrates shown in Figure 6.1(d-f). Therefore, the densities of the VACNTs in Figure 6.2(a-c) did not match the densities of the catalyst nanoparticles in Figure 6.1(d-f). As depicted in Figure 6.1(d-f), the Cu particles were formed after the heat treatment of the Cu substrates for 10 min only. In contrast, the VACNTs, as shown in Figure 6.2(a-c), were achieved after the PECVD synthesis for 30 min. The formation of Cu particles from the surface evolution was a continuous process, and the 30 min growth time would result in more Cu particles formed on the substrate than the 10 min heat treatment. The Cu catalyst particles were responsible for the growth of VACNTs, and the density of the VACNTs should match the density of the catalyst particles.

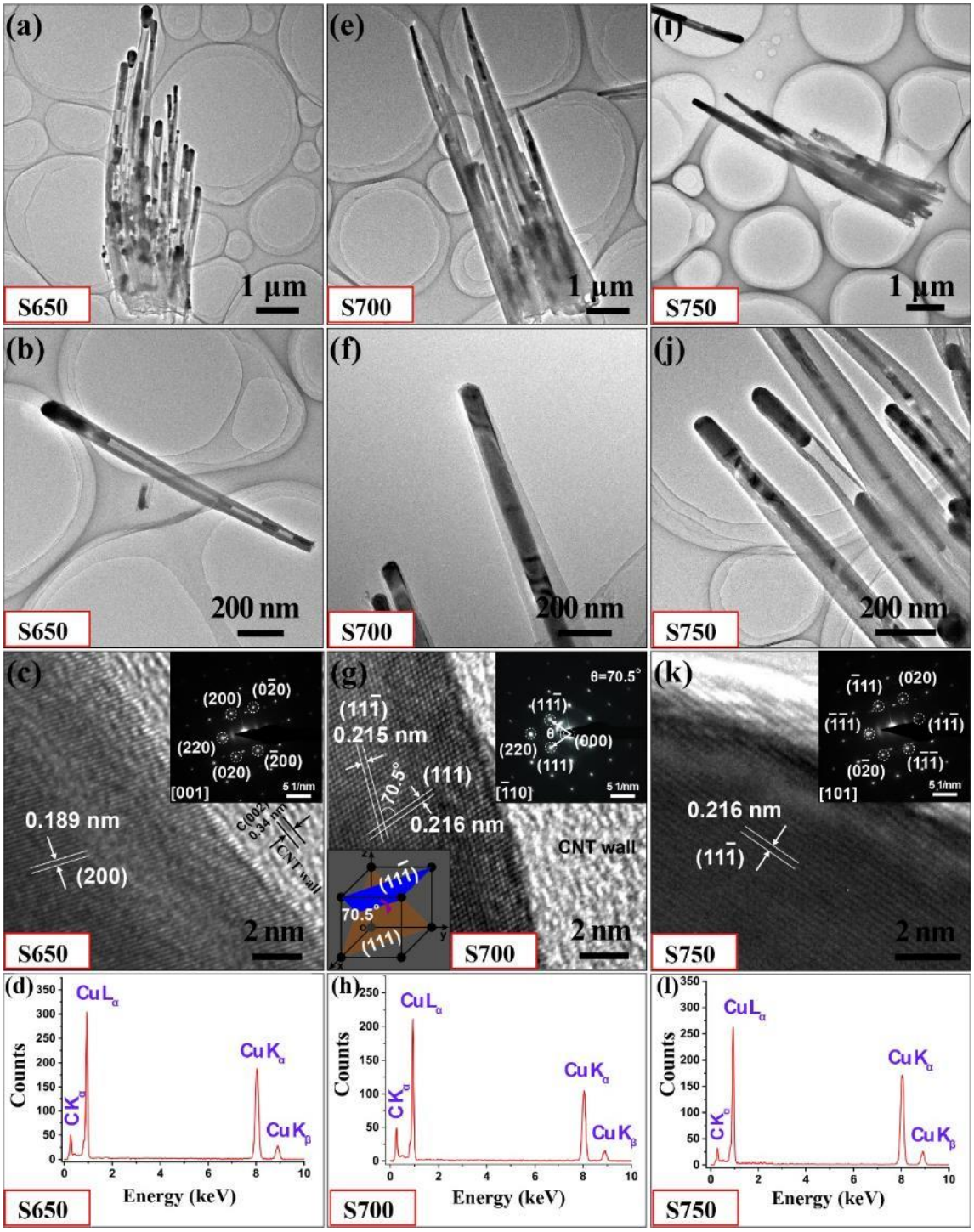

Figure 6.3. TEM images of the CNTs and EDS spectrum from the filler material of the CNTs synthesized at the temperature of (a-d) 650 ºC, (e-h) 700 ºC, and (i-l) 750 ºC. (a, e, i) Low-resolution TEM images showing the entire length of the CNTs, (b, f, j) high-magnification TEM images showing the material trapped/filled inside the CNTs, (c, g, k) high-resolution TEM images at the interface between the graphitic layers of CNTs and the filler material, and (d, h, l) EDS spectrum from the material trapped/filled inside the CNT. The insets in Figure 6.3(c, g, k) represent the SAD pattern of the material trapped/filled inside the CNT.

The nanostructure of the as-synthesized materials was investigated by using low and high-resolution TEM (HRTEM) spectroscopy, as shown in Figure 6.3. Sample S650 showed VACNTs with catalyst particles anchored at their tips, see Figure 6.3(a-b). It is noteworthy that the particles at the tips of some VACNTs were stretched down along the tube axis, forming short nanorods. A few VACNTs were also found to have discrete nanorods inside their cores. In other cases, the particles were mainly restricted at the tip of the tubes, as in typical hollow VACNTs. The HRTEM observation at the interface between the tip particle and the VACNT wall, as shown in Figure 6.3(c), shows clear multilayer lattice planes separated by 0.189 nm corresponding to the (200) lattice plane of face-centered cubic (fcc) Cu crystal. In addition, layers with an interlayer spacing of ~0.34 nm corresponding to the graphitic (002) plane of VACNTs were observed. The selected area diffraction (SAD) pattern taken from the tip particle, as shown in the inset of Figure 6.3(c), shows distinct bright spots that can be indexed as (200), (220), and (020) planes of single-crystalline fcc Cu along the [001] zone axis. As shown in Figure 6.3(d), the EDS spectrum further confirmed the identity of the tip particle as the pure single-crystalline Cu metal, where the C signal can be accredited to the VACNT shell.

The TEM examination of the sample S700, as shown in Figure 6.3(e-f), disclosed that all VACNTs were filled with foreign material from their root to the tip, forming a complete core-shell structure. The HRTEM image, as shown in Figure 6.3(g), shows two different lattice planes $(11\bar{1})$ and (111) corresponding to the fcc Cu crystal, making an angle of ~70.5º to each other. The bottom left inset in Figure 6.3(g) represents the schematic of the possible scenario of intersecting two different planes of the {111} family of the fcc Cu crystal. The top right inset in Figure 6.3(g) shows the SAD pattern, which

can be indexed as $(11\bar{1})$, (220), and (111) related to the fcc Cu crystal. As shown in Figure 6.3(h), the presence of Cu in the EDS spectrum further confirmed the core material as the single crystalline fcc Cu. The C signal was associated with the VACNT shells. The Cu@VACNTs have a tapered shape, and their Cu cores were encapsulated with a few layers of graphitic walls. In contrast, many graphitic layers were present near the root of Cu@VACNTs. Hence, it can be concluded that the VACNT walls near the tip of the Cu core were formed at the last stage of the growth process [45]. Therefore, the Cu nanowire tip should be the catalytically active site for the decomposition of carbon precursor and the dissolution-precipitation of carbon atoms or clusters to form VACNT shells.

Further increase in the growth temperature (for example, 750 ºC) led to the formation of a few partially filled VACNTs. The Cu nanowires were characterized by the voids, deformations, and dislocations forming a neck-like structure, as shown in Figure 6(i-j). However, most of the VACNTs were completely filled with Cu nanowires. The formation of voids, deformations, and dislocations along the Cu wires can be ascribed to the high temperatures. High internal energy, resulted from the high temperature, increases the atomic activity of Cu atoms in the Cu nanowires. The Cu nanowires stretch because the pre-melting occurred at the nanowire edge and on the surface [46]. The pre-melting phenomenon significantly decreases the bonding strength of the Cu atoms, leading to atomic gliding dislocations and grain boundary movement [47]. The structural transitioning process creates voids, deformations, and imperfections. The Cu@C with similar defects resulted from heating the nanowires above 800 ºC have been reported by Zhao et al. [48]. Moreover, the HRTEM, SAD pattern, and EDS spectrum (as shown in Figure 6.3(k-l)) indicated the core inside the VACNTs to be a single crystal fcc Cu.

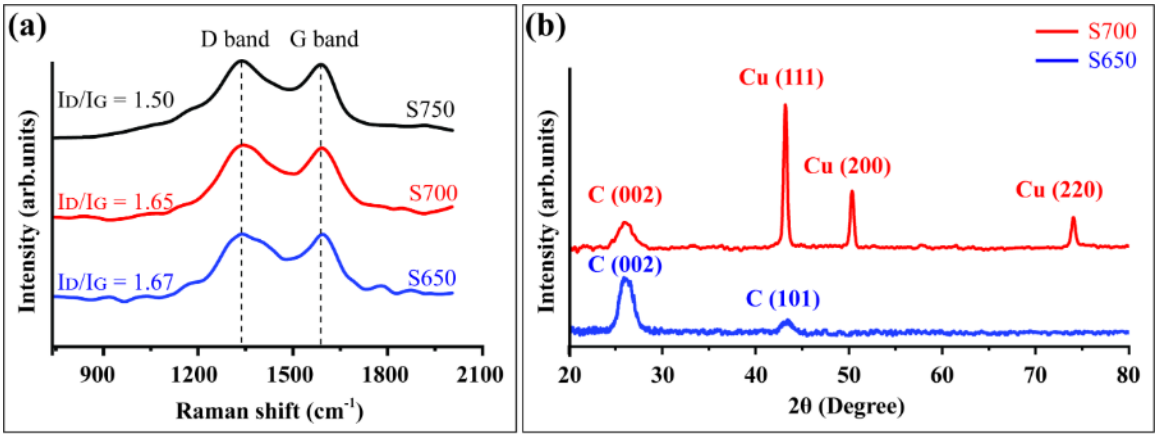

Figure 6.4. (a) Raman spectra of the multi-walled Cu-filled VACNTs synthesized at different temperatures on the Cu substrates. (b) XRD profile of the Cu-filled VACNTs synthesized at 700 ºC (S700).

Figure 6.4(a) shows the Raman spectra of the VACNTs synthesized at different temperatures corresponding to the SEM images in Figure 6.2. Two broad peaks at about 1339 cm^{-1} and 1590 cm^{-1} were observed for all the samples. The former peak corresponds to D-band which is a defect-induced feature originating from out-of-plane vibrations in breathing mode, while the later peak corresponds to the G-band which arises as a result of in-plane vibrations (E_{2g} mode) of the sp^2-hybridized carbon network [49]. The integral intensities of these bands expressed as a ratio, I_D/I_G, signifies the quality of the carbon materials. As shown in Figure 6.4(a), the value of I_D/I_G slightly decreased from 1.67 to 1.65 as the growth temperature increased from 650 ºC to 700 ºC. Further increase in growth temperature to 750 ºC resulted in the lowest I_D/I_G value of 1.50 among the three samples. The result implies that the samples grown at higher temperatures were less defective. However, the generally high value of I_D/I_G indicates a high level of defects in VACNTs. It is postulated that the high level of defects was caused by the intense plasma etching on the walls of the VACNTs during the PECVD synthesis [18].

Figure 6.4(b) represents the XRD pattern of the VACNTs synthesized at 650 ºC (S650) and Cu@VACNTs synthesized at 700 ºC (S700). The XRD spectrum for the sample S650 displayed broad diffraction peaks (2θ) at about 26º and 43º related to (002) and (101) graphitic planes [49, 50]. Interestingly, there were no distinct Cu related peaks, although TEM images verified the presence of Cu particles at the tips of VACNTs. The absence of Cu peak is ascribed to the very low content of the Cu material in the sample. The XRD profile of the S700 sample revealed the diffraction peaks matching the graphite and pure Cu metal. The prominent peaks at 43.18º, 50.34º, and 74.06º can be indexed as (111), (200), and (220) planes of the fcc Cu phase (ICDD PDF No. 04-004-8452) with space group symmetry of *Fm-3m* [45]. It is important to note that there are no characteristic peaks of impurities of metal oxides. A broad peak at about 26º can be attributed to the (002) plane of the graphitic wall of the VACNTs, which is consistent with the previous report [51]. The broadening of the peaks corresponding to graphite could indicate the defective nature of the VACNTs. Chuang et al. demonstrated that highly defective amorphous CNTs significantly enhanced the field emission compared to the crystalline counterparts by reducing the turn-on field and threshold field [52]. The improved field emission performance was attributed to the substantial field enhancement effect of the inhomogeneous electronic sp^2/sp^3 structures and the hydrogen termination on amorphous carbon structures [52]. Published reports [53, 54] have also confirmed the role of hydrogenated amorphous carbon films in enhancing the field emission properties. Therefore, higher field emission performance can be anticipated from our samples (S650 and S700). Raman and XRD results in Figure 6.4 indicated that the S650 and S700 have almost similar degrees of defects (or similar crystallinity). Hence, similar field emission

properties would be expected for both samples if they were composed of hollow carbon shells only. However, completely filled VACNTs with crystalline Cu nanowires can significantly affect field emission properties, as discussed in section 6.3.4.

6.3.3 Growth mechanism of the Cu-filled VACNTs

The role of Cu as an active catalytic metal for the synthesis of CNTs is still under debate. The Cu is considered a poor catalyst because of its extremely low carbon solubility, 0.0001 wt. % C at 1100 ºC, which prevents the formation of building blocks of CNT's wall, i.e., C–C bond [41]. However, reports of the successful growth of CNTs on bulk Cu substrate without extra catalyst in the temperature range of about 820–1000 ºC confirmed the promising catalytic activity of Cu metal [43, 44]. Moreover, Cu nanoparticles with sizes of less than 10 nm were excellent catalysts for the growth of single-walled CNTs at the temperature lower than the melting temperature of bulk Cu (1085 ºC) [55, 56]. The reports of synthesizing single/multi-walled CNTs on the Cu (bulk or nanoparticles) suggest that C atoms can dissolve into the Cu nanoparticles at temperatures lower than the melting point of bulk Cu. Although Cu particles formed after the heat treatment at different temperatures in our samples (Figure 6.1) were bigger than those mentioned above, it is reasonable to assume that C atoms dissolved into the Cu particles during the VACNT synthesis process and that Cu particles acted as the catalyst. The state of Cu particles at different temperatures is very important for understanding the growth mechanism of Cu@VACNTs. It is well known that the melting point of Cu nanoparticles can be 100–250 ºC lower than that of the bulk Cu [57]. The melting point of bulk Cu is 1085 ºC, so the melting point of Cu nanoparticles can be 835-985 ºC. It is believed that the growth temperatures (650–750 ºC)

employed in our experiment were not high enough to melt the Cu nanoparticles. Therefore, it is speculated that the Cu nanoparticles at our temperature range were in the quasi-liquid state, which implies that the growth of the Cu@VACNTs was primarily through the vapor–quasi-liquid–solid (VLS) mechanism assisted by quasi-liquid capillary adsorption [48, 57].

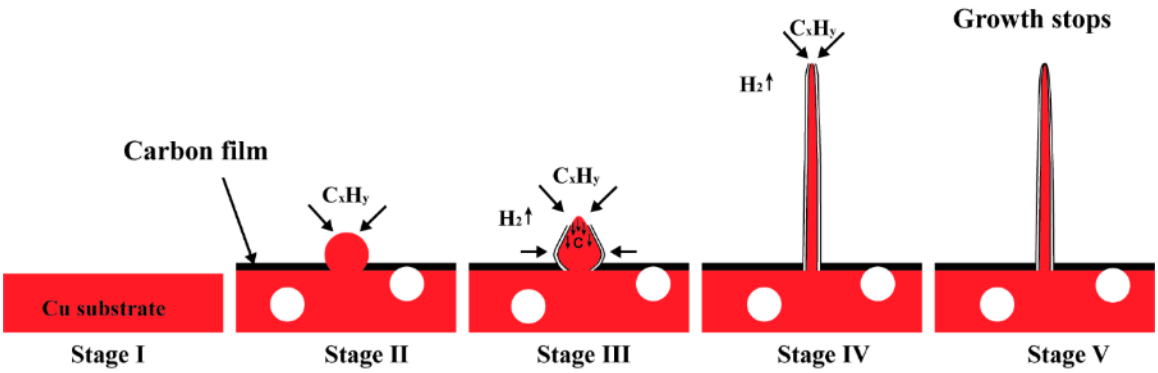

Figure 6.5. Schematic of the proposed growth mechanism for the ideal case of completely filled Cu@VACNTs.

The growth mechanism of the Cu@VACNTs is schematically described in Figure 6.5. It is important to note that the growth model is for the ideal case of completely filled VACNTs with Cu, such as in the sample S700. Initially, the precursor gas (C_2H_2) was thermally decomposed into C atoms along with energetic radicals (C_xH_y) and hydrogen gas (H_2) because of the weak catalytic activity of Cu and deposited on the surface of the substrate as a thin layer. Simultaneously, an ensemble of individual Cu particles was formed as a result of thermally induced surface breakup under the reduction environment. The surface disintegration transformed the solid Cu substrate into a highly porous morphology, as shown in stage II of Figure 6.5. The pits (porous structures) on the Cu surface can be seen in Figure 6.2(b-c) but with less frequency as compared to Figure 6.1(d-f). The result confirmed the presence of a thin layer of C deposition. In the later stage, the decomposition of the C2H2 into C atoms at the quasi-liquid Cu particle surface led to the

dissolution and precipitation of C atoms forming graphite layers on the grain boundary (stage III, Figure 6.5). Extrusion stress between the graphite layers and Cu particle transformed the catalyst particle into nanocone [58], with the tip exposed for the further decomposition of precursor gas and incorporation of C atoms. As a result, the VACNT grew longer, and simultaneously the semi-molten Cu metal was sucked into the VACNT caused by the capillary action (stage IV, Figure 6.5) [51]. During the process, the compressive pressure at the core from VACNT walls (~40 GPa) [59] could help elongate the Cu nanowire along the axes of the VACNT. The length of Cu@VACNT depends upon the continued availability of the Cu filler and the catalytic ability of the Cu nanowire's tip. That means the growth of Cu@VACNT concludes as the tip of Cu nanowire prevents further dissolution and precipitation of C atoms (stage V, Figure 6.5).

A fundamental difference in the growth mechanism of empty VACNTs grown at 650 ºC (S650) and Cu@VACNTs synthesized at higher temperatures (S700 or S750) was the state of catalyst Cu particle. The catalyst particles supporting the growth of empty VACNTs may be in the solid-state, which did not facilitate the capillary filling during the growth process. The presence of extended Cu nanorod at the tip of some of the VACNTs (Figure 6.3(a)) could be ascribed to the elongation of the catalyst particle under intense compressive pressure from graphitic layers, similar to the Ni-filled carbon nanofibers [60]. It was suggested that such a kind of filling could occur when VACNTs consisted of the solid catalyst particles at their tips [60]. If the temperature is high such as 750 ºC, the Cu filler may not be a continuous nanowire but instead of segments (with voids) caused by the high internal energy of Cu, as described in section 6.3.2.

6.3.4 Field emission measurements

The field emission (FE) properties of the hollow (S650) and Cu-filled (S700) VACNTs synthesized directly on bulk Cu substrates were measured using a diode configuration method under a pressure of about 10^{-6} Torr. The samples were subjected to the electrical conditioning during the first five current density versus applied field ($J–E_a$) cycles to evaporate the residual adsorbates, which otherwise could onset the FE much quicker than their uncontaminated counterparts [23]. Hence, $J–E_a$ cycles after the 5^{th} cycle were considered for studying the FE properties of the as-synthesized samples. Figure 6.6(a-b) depicts the comparison of $J–E_a$ properties of unfilled VACNTs and Cu@VACNTs represented on a semi-log and linear scale. A turn-on electric field (E_{TO}) and a threshold electric field (E_{TH}) were defined as an applied electric field required to produce an emission current density of 10 $\mu A/cm^2$ and 1 mA/cm^2, respectively. The measured FE properties of the as-synthesized samples are presented in Table 6.2. The $J–E_a$ plots revealed that the onset of the FE process from the Cu@VACNTs initiated at a much lower applied electric field and produced a higher total current density than the unfilled VACNTs. Precisely, the E_{TO} and E_{TH} values for the Cu@VACNTs were measured as 1.77 V/μm and 2.43 V/μm, respectively. Also, a high current density (J_{total}) in the range of about 19 and 23 mA/cm^2 at a field of about 3.3 V/μm was recorded for the Cu@VACNTs, which is about fivefold higher than that for the unfilled counterpart. The E_{TO} observed for Cu@VACNTs was significantly lower than the reported values for pure Cu nanostructures [28, 29, 31, 61, 62], amorphous carbon decorated Cu-nanowire [63], entangled CNTs [42], and VACNT arrays synthesized on Cu-substrate [25]. For a detailed comparison, Table 6.2 summarizes the key parameters of FE for various field emitters reported in the literature and the chapter 6.

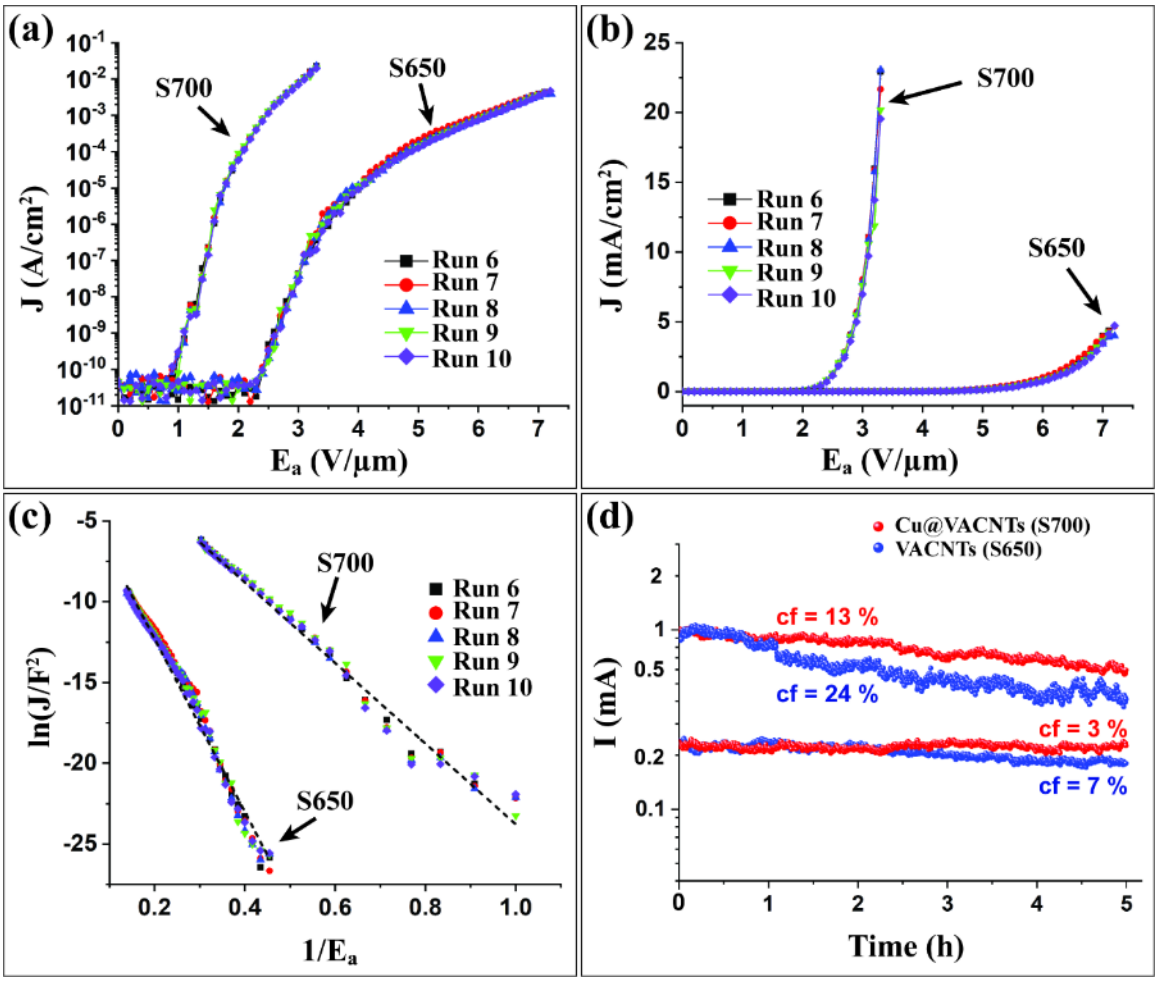

Figure 6.6. Comparative study of the FE properties of unfilled VACNTs (S650) and VACNTs filled with Cu (S700). (a) F–J plots in semi-log scale, (b) F–J plots in linear scale, (c) Fowler–Nordheim (F–N) plots, and (d) stability test at different current.

Table 6.2. Field emission properties (Turn-on, threshold electric field, field enhancement factor, and stability) of the unfilled (S650) and Cu-filled (S700) VACNTs.

Sample	E_{TO} (V/µm)	E_{TH} (V/µm)	β	Current stability	
				cf at 0.24 mA	cf at 1 mA
S650	3.96	6.10	1425	7 %	24 %
S700	1.77	2.43	3061	3 %	13 %

Fowler-Nordheim (F–N) theory can be used to approximate the FE properties of the VACNTs and their composite materials [22, 64]. The field enhancement factors (β) for the unfilled and Cu-filled VACNTs were calculated by using the F–N equation:

$$J = \left(\frac{A\,E_{local}^{2}}{\phi}\right)\exp\left(-\frac{B\,\phi^{\frac{3}{2}}}{E_{local}}\right) \tag{6.1}$$

where J is the emission current density, $A = 1.56 \times 10^{-6}$ A V^{-2} eV, $B = 6.83 \times 10^{9}$ $eV^{3/2}$ V m^{-1} [22], ϕ (5 eV [65]) is the work function of the VACNT electron field emitters, and E_{local} is the local electric field at the emission site. Equation (6.1) depends only on the local electric field E_{local}. However, in a typical FE experiment, the emission current density J is measured as a function of the applied voltage V between the anode and the cathode in a planar diode configuration. Conveniently, the local electric field at the emission site can be defined as:

$$E_{local} = \beta E_a \tag{6.2}$$

where $E_a = V/d$ is the applied macroscopic field, d is the gap between the anode and the cathode, and β is the proportionality constant [66]. Equation (6.2) shows that E_{local} depends linearly on the E_a; however, it should be noted that this linearity can deviate at very high current densities owing to the space charge or current saturation [66]. The equation (6.2) also implies that the enhancement factor β is a degree of the increase in the localized electric field at the emission site with respect to the applied macroscopic field. After substituting equation (6.2) into equation (6.1), the emission current density can be expressed as:

$$J = \left(\frac{A\beta^2 E_a^2}{\phi} \right) \exp\left(-\frac{B\phi^{\frac{3}{2}}}{\beta E_a} \right) \tag{6.3}$$

Hence, from equations (6.3), it is clear that emission current density J depends mainly on the field enhancement factor β for a constant applied field E_a. The field enhancement factors were calculated by using the slope of the F–N plots, as shown in Figure 6.6(c). The field enhancement factor β for the Cu@VACNTs was more than two times bigger than that for the unfilled VACNTs, as shown in Table 6.2, which is consistent with the observed low values of E_{TO}, E_{TH}, and high value of J_{total} for the Cu@VACNTs. Also, the observed value of field enhancement factor (β = 3061) for Cu@VACNTs was higher than most of the reported Cu-nanowires [28, 29, 31, 61], Ni-nanowires [30], Fe-nanowires [67], randomly and vertically oriented CNTs synthesized on Cu-substrate [25, 42]. The FE stability of the as-synthesized samples was verified at low (0.24 mA) and high (1mA) initial currents for 5 hours, as shown in Figure 6.6(d). For each current versus time graph, the current fluctuation (cf) over the average current ($\bar{I}$) was calculated by using the following equation:

$$cf = \frac{|I - \bar{I}|}{\bar{I}} \times 100\% \tag{6.4}$$

where I represents the value of the maximum deviated emission current from the average current value. As depicted in Figure 6.6(d), the Cu@VACNTs displayed excellent FE stability with cf values of 3 % ($\bar{I}$ = 0.22 ± 0.01 mA) at initial test current of 0.24 mA and 13 % ($\bar{I}$ = 0.79 ± 0.11 mA) at initial test current of 1 mA. The cf values for unfilled VACNTs were 7 % ($\bar{I}$ = 0.21 ± 0.02 mA) and 24 % ($\bar{I}$ = 0.62 ± 0.18 mA) at the initial test

currents of 0.24 and 1 mA, respectively. The enhanced FE stability for Cu@VACNTs could be associated with the onset of FE at the lower applied field and high field enhancement, which facilitated achieving the targeted test currents at a much lower applied field compared to the unfilled VACNTs. The emitters subjected to the lower field were less vulnerable to structural degradation because of Joules' heating, thereby producing stable emission current for an extended period of time.

Table 6.3. Comparison of key parameters of FE for various field emitters reported in the literature and this work.

Field emitters	**Alignment**	**Turn-on field @ 10 μA/cm^2 (V/μm)**	**Field enhancement factor (β)**	**Emitter height (μm)**	**References**
Cu-nanowire	Partially	4.6	443	~10.5	[31]
Cu-nanowire	Vertically	4.3	800	8–18	[29]
Cu-nanowire	Partially	12.4	713	~7	[61]
Cu-nanobat	Partially	4.0 at 1 μA/cm^2	3900	1.5	[62]
Cu-nanowire	Vertically	7.0	1041	2	[28]
aC/Cu-nanowire	Vertically	8.7	3210	~5	[63]
Cu@VACNT	Vertically	1.8	3061	4.9	This work

The low values of the turn-on field and threshold field, the high value of field enhancement factor, and improved emission stability suggest that Cu@VACNTs are more promising field emitters than empty VACNTs for FE applications. The superior FE performance of Cu@VACNTs can be understood based on the following two reasons, (i) the presence of highly conductive Cu nanowires at the core of VACNT emitters and (ii) distribution of Cu@VACNTs with bundled morphology on the substrate. Since graphitic layers encapsulated the Cu nanowires, the work function of the Cu@VACNT tips (true

emission sites) can be expected to be close to that of the graphite. Nonetheless, the effect of the Cu nanowires on FE properties may still exist. It has been suggested that metal catalysts at the tip of CNTs can improve the FE properties. Previous reports proposed that the metal particle can operate as an additional FE electron source [68-70] and reinforces the robustness of the CNT tip to prevent radial deformations, thereby enhancing the FE properties [71]. Lv et al. demonstrated a significant improvement in FE properties from CNTs with FeNi nanowires enclosed at the apices [68]. It should be noted that in the case of sample S650, the Cu particles were encapsulated only at the tips of VACNTs. However, the VACNTs in sample S700 were entirely filled with pure Cu nanowires, which can operate as much larger electron sources and bolster the robustness of the entire tube. Moreover, an efficient electron transmission from the substrate to the tips of emitters is another critical issue of scientific interest regarding the FE process. We believe that the filling of VACNTs by highly conductive Cu nanowires enhances the composite's overall electrical and thermal conductivities. The enhanced conductivities can help the efficient electron movement and adequate dissipation of heat generated by Joule's heating, thereby preserving the Cu@VACNT emitters and improving electron emission.

To support the conclusion that the filling of VACNTs by highly conductive Cu nanowires enhances the FE properties, electrostatic field distribution at the tip of an unfilled and a Cu@VACNT was simulated using COMSOL™ MULTIPHYSICS 5.2, as shown in Figure 6.7(a-b). The simulation result revealed that the local electric field at the tip of unfilled VACNT was significantly enhanced from 2.65 V/μm to 11.3 V/μm caused by the encapsulation of highly conductive Cu nanowire at the core of the carbon shells.

The enhanced local electrostatic field of Cu@VACNT emitters at their apexes aided the more accessible electron emission, thereby improving their FE properties.

Since the density of the VACNT arrays was high, the field screening effect between the adjacent VACNTs should be taken into consideration while studying their FE performance. The superior FE properties of Cu@VACNTs (S700) compared to unfilled

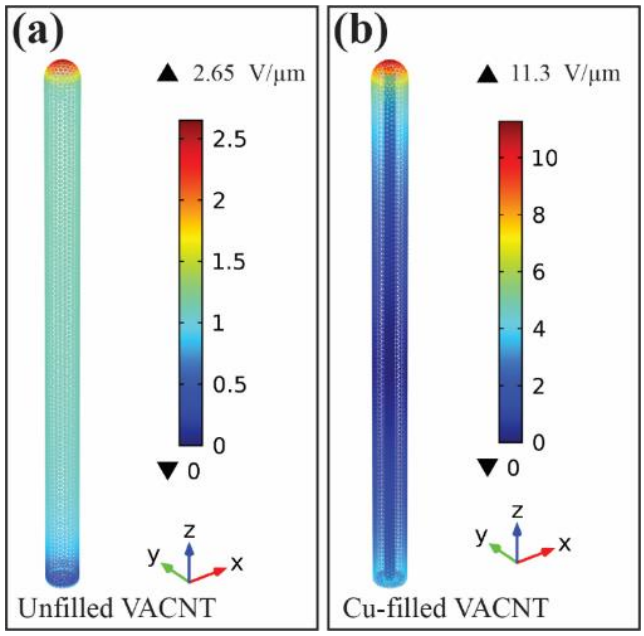

Figure 6.7. Simulation of electrostatic field distribution for (a) an unfilled VACNT and (b) a Cu@VACNT. The numbers above the scale bar represent the maximum value of the local electric field in the simulation domain.

VACNTs (S650) may also be accredited to the low field screening because of the bundled morphology of the Cu@VACNTs, as shown in Figure 6.2(b). Through a numerical analysis of a periodic array of vertically aligned CNTs, an optimal ratio of intertube distance (R) to the tube height (H) has been suggested to be about two (R/H = 2) for minimum field screening between adjacent tubes [72]. The theoretical prediction was confirmed by Lin et al. using a hexagonal array of CNT pillars with the lowest turn-on field and highest field enhancement factor [73]. It has also been demonstrated that the maximum field

enhancement occurred when the R/H value was one (R/H = 1) for a periodic array of vertically aligned carbon nanofibers [74]. These results imply that it is essential to keep the R/H ≥ 1 to reduce the field screening between VACNTs and enhance the FE properties. Although our samples lacked a general periodicity of VACNTs, there was a much larger spacing between Cu@VACNT bundles in S700 than the individual VACNTs in S650. Therefore, the Cu@VACNT bundles have a low field screening effect. In our previous report [33], we have demonstrated that a bundle of VACNTs emits electrons as a whole rather than individual VACNTs and the bundling of VACNTs can alleviate the field screening effect by increasing the distance between the effective emitters, thereby enhancing the FE performance.

The FE process involves electron transportation from the substrate through the interface between the substrate and emitters, along with the emitters, and final emission into the vacuum. For VACNT emitters, the high electrical conductivity of the substrate (typically metals) is desirable for an uninterrupted source of electrons to achieve high FE performance. High thermal conductivity of the substrate is required to dissipate the heat developed by Joule's heating during the FE process, protecting the emitters against the field evaporation by preserving the VACNT-substrate bond. Apart from the electrical and thermal conductivities of the substrate, the contact resistance between the VACNT and the substrate also plays an important role in the FE property. High contact resistance can cause resistive heating, which in turn can result in sublimation or melting of VACNTs at the higher electric field, thereby producing subdued FE properties. It has been reported that the contact resistance can be minimized by synthesizing carbon nanotubes directly on conductive substrates with work function comparable to that of the emitters [75]. In my

dissertation work, the Cu@VACNTs were directly grown on Cu disks, which have a work function of about 4.6-4.9 eV [76, 77] comparable to that of the graphite (5.0 eV). Therefore, a low contact resistance between VACNTs and the Cu disk was expected, which was well supported by the fact that the F–N plot (Figure 6.6(c)) has always exhibited straight lines for both samples without an obvious knee [78]. Hence, resistive heating problems can be avoided if the emitters are directly grown on the substrate. The superior FE performance of the Cu@VACNTs is attributed to the synergistic effect of possible ohmic contact between the substrate and Cu@VACNTs, a highly conductive substrate, low field screening because of bundled morphology, and presence of highly conductive Cu nanowires at the core of VACNT emitters.

6.4 Conclusions

In summary, we developed a simple and effective method to synthesize unfilled and filled VACNT arrays directly on bulk Cu disks via the PECVD method without using extra metal catalyst particles. The filler material was identified as a single Cu crystal. After a thorough examination of the as-synthesized samples through various techniques, the possible growth mechanism of the Cu@VACNTs has been discussed. The Cu nanoparticles formed on the Cu disk as a result of the surface reconstruction at high temperatures in the presence of a reducing environment were responsible for the growth of VACNTs. The growth temperature was the key to the successful filling of Cu inside VACNTs. The field emission experimental results indicate that the filling of Cu through the entire length of the VACNT can significantly enhance the FE properties of the VACNT field emitters. The field emission measurements revealed that the turn-on and threshold

electric field of the Cu@VACNT emitters could be lowered by more than half compared to those of the hollow VACNT emitters. The more than two-fold increase in the field enhancement factor for Cu@VACNTs showed that the Cu@VACNTs are promising candidates for field emission applications. Simulations of electrostatic field distribution revealed the localization of a higher electrostatic field at the tip of Cu@VACNTs, which underlined the importance of highly conductive metal nanowires at the core of VACNTs to the enhancement of the field emission. Directly synthesized Cu@VACNTs on the conductive Cu substrate could be applicable in vacuum micro/nano-electronic devices.

References

[1] Ruoff R.S., Lorents D.C., Chan B., Malhotra R. and Subramoney S., Single crystal metals encapsulated in carbon nanoparticles. *Science* **1993,** 259 (5093), 346.

[2] Elias A., Rodriguez-Manzo J., McCartney M., Golberg D., Zamudio A., Baltazar S., Lopez-Urias F., Munoz-Sandoval E., Gu L. and Tang C., Production and characterization of single-crystal FeCo nanowires inside carbon nanotubes. *Nano letters* **2005,** 5 (3), 467.

[3] Dorozhkin P.S., Tovstonog S.V., Golberg D., Zhan J., Ishikawa Y., Shiozawa M., Nakanishi H., Nakata K. and Bando Y., A Liquid-Ga-Filled Carbon Nanotube: A Miniaturized Temperature Sensor and Electrical Switch. *Small* **2005,** 1 (11), 1088.

[4] Svensson K., Olin H. and Olsson E., Nanopipettes for metal transport. *Physical review letters* **2004,** 93 (14), 145901.

[5] Dong L., Tao X., Zhang L., Zhang X. and Nelson B.J., Nanorobotic spot welding: controlled metal deposition with attogram precision from copper-filled carbon nanotubes. *Nano Letters* **2007,** 7 (1), 58.

[6] Gao Y. and Bando Y., Carbon nanothermometer containing gallium. *Nature* **2002,** 415 (6872), 599.

[7] Ye X.R., Lin Y., Wang C. and Wai C.M., Supercritical fluid fabrication of metal nanowires and nanorods templated by multiwalled carbon nanotubes. *Advanced Materials* **2003,** 15 (4), 316.

[8] Ye X. and Wai C., Making nanomaterials in supercritical fluids: a review. *Journal of chemical education* **2003,** 80 (2), 198.

[9] Wang D., Yang G., Ma Q., Wu M., Tan Y., Yoneyama Y. and Tsubaki N., Confinement effect of carbon nanotubes: copper nanoparticles filled carbon nanotubes for hydrogenation of methyl acetate. *Acs Catalysis* **2012,** 2 (9), 1958.

[10] Wang P., Huang B., Wei J., Qin X., Yao S. and Zhang Q., Preparation of Cu nanoparticles on carbon nanotubes by solution infusion method and calcining in ambient atmosphere. *Materials Letters* **2007,** 61 (30), 5255.

[11] Wang X., Zhang F., Xia B., Zhu X., Chen J., Qiu S., Zhang P. and Li J., Controlled modification of multi-walled carbon nanotubes with CuO, Cu2O and Cu nanoparticles. *Solid State Sciences* **2009,** 11 (3), 655.

[12] Poudel Y.R. and Li W., Synthesis, properties, and applications of carbon nanotubes filled with foreign materials: a review. *Materials Today Physics* **2018,** 7, 7.

[13] Setlur A., Lauerhaas J., Dai J. and Chang R.P., A method for synthesizing large quantities of carbon nanotubes and encapsulated copper nanowires. *Applied physics letters* **1996,** 69 (3), 345.

[14] Zhang G. and Wang E., Cu-filled carbon nanotubes by simultaneous plasma-assisted copper incorporation. *Applied physics letters* **2003,** 82 (12), 1926.

[15] Deng B., Xu A.-W., Chen G.-Y., Song R.-Q. and Chen L., Synthesis of copper-core/carbon-sheath nanocables by a surfactant-assisted hydrothermal reduction/carbonization process. *The Journal of Physical Chemistry B* **2006,** 110 (24), 11711.

[16] Haase D., Hampel S., Leonhardt A., Thomas J., Mattern N. and Büchner B., Facile one-step-synthesis of carbon wrapped copper nanowires by thermal decomposition of Copper (II)–acetylacetonate. *Surface and Coatings Technology* **2007,** 201 (22-23), 9184.

[17] Golberg D., Costa P.M., Mitome M., Hampel S., Haase D., Mueller C., Leonhardt A. and Bando Y., Copper-Filled Carbon Nanotubes: Rheostatlike Behavior and Femtogram Copper Mass Transport. *Advanced Materials* **2007,** 19 (15), 1937.

[18] Kokai F., Shimazu T., Adachi K., Koshio A. and Takahashi Y., Fabrication of completely filled carbon nanotubes with copper nanowires in a confined space. *Applied Physics A* **2009,** 97 (1), 55.

[19] Tao X., Zhang X., Cheng J., Liu F., Li Y. and Van Tendeloo G., Controllable synthesis of novel one-dimensional carbon nanomaterials on an alkali-element-modified Cu catalyst. *Nanotechnology* **2005,** 17 (1), 224.

[20] De Heer W.A., Chatelain A. and Ugarte D., A carbon nanotube field-emission electron source. *science* **1995,** 270 (5239), 1179.

[21] Rinzler A., Hafner J., Nikolaev P., Nordlander P., Colbert D., Smalley R., Lou L., Kim S. and Tománek D., Unraveling nanotubes: field emission from an atomic wire. *Science* **1995,** 269 (5230), 1550.

[22] Bonard J.-M., Croci M., Klinke C., Kurt R., Noury O. and Weiss N., Carbon nanotube films as electron field emitters. *Carbon* **2002,** 40 (10), 1715.

[23] Semet V., Binh V.T., Vincent P., Guillot D., Teo K., Chhowalla M., Amaratunga G., Milne W., Legagneux P. and Pribat D., Field electron emission from individual carbon nanotubes of a vertically aligned array. *Applied Physics Letters* **2002,** 81 (2), 343.

[24] Killian J.L., Zuckerman N.B., Niemann D.L., Ribaya B.P., Rahman M., Espinosa R., Meyyappan M. and Nguyen C.V., Field emission properties of carbon nanotube pillar arrays. *Journal of Applied Physics* **2008,** 103 (6), 064312.

[25] Neupane S., Lastres M., Chiarella M., Li W., Su Q. and Du G., Synthesis and field emission properties of vertically aligned carbon nanotube arrays on copper. *Carbon* **2012,** 50 (7), 2641.

[26] Thapa A., Guo J., Jungjohann K.L., Wang X. and Li W., Density control of vertically aligned carbon nanotubes and its effect on field emission properties. *Materials Today Communications* **2020,** 22, 100761.

[27] Li Z., Yang X., He F., Bai B., Zhou H., Li C. and Dai Q., High current field emission from individual non-linear resistor ballasted carbon nanotube cluster array. *Carbon* **2015,** 89, 1.

[28] Duan J.L., Lei D.Y., Chen F., Lau S.P., Milne W.I., Toimil-Molares M., Trautmann C. and Liu J., Vertically-aligned single-crystal nanocone arrays: Controlled fabrication and enhanced field emission. *ACS applied materials & interfaces* **2016,** 8 (1), 472.

[29] Maurer F., Dangwal A., Lysenkov D., Müller G., Toimil-Molares M.E., Trautmann C., Brötz J. and Fuess H., Field emission of copper nanowires grown in polymer ion-track membranes. *Nuclear Instruments and Methods in Physics Research Section B: Beam Interactions with Materials and Atoms* **2006,** 245 (1), 337.

[30] Joo J., Lee S.J., Park D.H., Kim Y.S., Lee Y., Lee C.J. and Lee S.-R., Field emission characteristics of electrochemically synthesized nickel nanowires with oxygen plasma post-treatment. *Nanotechnology* **2006,** 17 (14), 3506.

[31] Kim C., Gu W., Briceno M., Robertson I.M., Choi H. and Kim K., Copper Nanowires with a Five-Twinned Structure Grown by Chemical Vapor Deposition. *Advanced Materials* **2008,** 20 (10), 1859.

[32] Sreekanth M., Ghosh S., Barman S., Sadhukhan P. and Srivastava P., Field emission properties of indium-decorated vertically aligned carbon nanotubes: an interplay between type of hybridization, density of states and metal thickness. *Applied Physics A* **2018,** 124 (8), 528.

[33] Thapa A., Jungjohann K.L., Wang X. and Li W., Improving field emission properties of vertically aligned carbon nanotube arrays through a structure modification. *Journal of Materials Science* **2020,** 55 (5), 2101.

[34] Suriani A., Dalila A., Mohamed A., Mamat M., Malek M., Soga T. and Tanemura M., Fabrication of vertically aligned carbon nanotubes–zinc oxide nanocomposites and their field electron emission enhancement. *Materials & Design* **2016,** 90, 185.

[35] Sridhar S., Tiwary C., Vinod S., Taha-Tijerina J.J., Sridhar S., Kalaga K., Sirota B., Hart A.H.C., Ozden S., Sinha R.K., Harsh, Vajtai R., Choi W., Kordas K. and Ajayan P.M., Field Emission with Ultralow Turn On Voltage from Metal Decorated Carbon Nanotubes. *ACS Nano* **2014,** 8 (8), 7763.

[36] Chen C.-A., Lee K.-Y., Chen Y.-M., Chi J.-G., Lin S.-S. and Huang Y.-S., Field emission properties of RuO2 thin film coated on carbon nanotubes. *Vacuum* **2010,** 84 (12), 1427.

[37] Wagner R. and Ellis W., Vapor-liquid-solid mechanism of single crystal growth. *Applied physics letters* **1964,** 4 (5), 89.

[38] Ahmad M. and Silva S.R.P., Low Temperature Growth of Carbon Nanotubes–A Review. *Carbon* **2020,** 158, 24.

[39] Pattinson S.W., Viswanath B., Zakharov D.N., Li J., Stach E.A. and Hart A.J., Mechanism and Enhanced Yield of Carbon Nanotube Growth on Stainless Steel by Oxygen-Induced Surface Reconstruction. *Chemistry of Materials* **2015,** 27 (3), 932.

[40] Hashempour M., Vicenzo A., Zhao F. and Bestetti M., Direct growth of MWCNTs on 316 stainless steel by chemical vapor deposition: Effect of surface nano-features on CNT growth and structure. *Carbon* **2013,** 63, 330.

[41] Yemini R., Muallem M., Sharabani T., Teblum E., Gofer Y. and Nessim G.D., Patterning of forests of carbon nanotubes (CNTs) using copper overlayers as iron catalyst deactivators. *The Journal of Physical Chemistry C* **2016,** 120 (22), 12242.

[42] Katar S.L., González-Berríos A., De Jesus J., Weiner B. and Morell G., Direct Deposition of Bamboo-Like Carbon Nanotubes on Copper Substrates by Sulfur-Assisted HFCVD. *Journal of Nanomaterials* **2008,** 2008, 515890.

[43] Zhu J., Jia J., Kwong F.-l. and Ng D.H.L., Synthesis of bamboo-like carbon nanotubes on a copper foil by catalytic chemical vapor deposition from ethanol. *Carbon* **2012,** 50 (7), 2504.

[44] Kruszka B., Terzyk A.P., Wiśniewski M., Gauden P.A. and Szybowicz M., Synthesis of carbon nanotubes and nanotube forests on copper catalyst. *Materials Research Express* **2014,** 1 (3), 035040.

[45] Tao X., Zhang X., Cheng J. and Liu F., Synthesis and characterization of Cu filled carbon nanohorns. *Materials chemistry and physics* **2007,** 104 (1), 210.

[46] Sun C.Q., Dominance of broken bonds and nonbonding electrons at the nanoscale. *Nanoscale* **2010,** 2 (10), 1930.

[47] Huang P.H. and Kuo J.K., Thermal stretching of defective nanowires: the coupled effects of vacancy cluster defects, operating temperature, and wire cross-sectional area. *Applied Physics A* **2011,** 103 (4), 1083.

[48] Zhao Y., Zhang Y., Li Y. and Yan Z., A flexible chemical vapor deposition method to synthesize copper@ carbon core–shell structured nanowires and the study of their structural electrical properties. *New Journal of Chemistry* **2012,** 36 (5), 1161.

[49] Rebelo S.L., Guedes A., Szefczyk M.E., Pereira A.M., Araújo J.P. and Freire C., Progress in the Raman spectra analysis of covalently functionalized multiwalled carbon nanotubes: unraveling disorder in graphitic materials. *Physical Chemistry Chemical Physics* **2016,** 18 (18), 12784.

[50] Figueira C.E., Moreira P.F., Giudici R., Alves R.M.B. and Schmal M., Nanoparticles of Ce, Sr, Co in and out the multi-walled carbon nanotubes applied for dry reforming of methane. *Applied Catalysis A: General* **2018,** 550, 297.

[51] Ding J., Yan X., Tay B.K. and Xue Q., One-step synthesis of pure Cu nanowire/carbon nanotube coaxial nanocables with different structures by arc discharge. *Journal of Physics and Chemistry of Solids* **2011,** 72 (12), 1519.

[52] Chuang C.C., Huang J.H., Chen W.J., Lee C.C. and Chang Y.Y., Role of amorphous carbon nanowires in reducing the turn-on field of carbon films prepared by microwave-heated CVD. *Diamond and Related Materials* **2004,** 13 (4), 1012.

[53] Robertson J., Mechanisms of electron field emission from diamond, diamond-like carbon, and nanostructured carbon. *Journal of Vacuum Science & Technology B: Microelectronics and Nanometer Structures Processing, Measurement, and Phenomena* **1999,** 17 (2), 659.

[54] Xu J., Huang X., Li W., Wang L., Huang X., Chen K., Xu J. and Wilson I.H., Vacuum electron emission with low turn-on electric field from hydrogenated amorphous carbon thin films. *Applied Physics Letters* **2001,** 79 (1), 141.

[55] Zhao X., Liu Y., Cui R. and Li Y., Nucleation of copper nanoparticles on quartz as catalysts to grow single-walled carbon nanotube arrays. *Carbon* **2016,** 110, 390.

[56] Zhong G., Yang J., Sugime H., Rao R., Zhao J., Liu D., Harutyunyan A. and Robertson J., Growth of high quality, high density single-walled carbon nanotube forests on copper foils. *Carbon* **2016,** 98, 624.

[57] Zhang Q., Qian W., Yu H., Wei F. and Wen Q., Synthesis of carbon nanotubes with totally hollow channels and/or with totally copper filled nanowires. *Applied Physics A* **2007,** 86 (2), 265.

[58] Tao X., Zhang X., Cheng J., Luo Z., Zhou S. and Liu F., Thermal CVD synthesis of carbon nanotubes filled with single-crystalline Cu nanoneedles at tips. *Diamond and related materials* **2006,** 15 (9), 1271.

[59] Sun L., Banhart F., Krasheninnikov A.V., Rodriguez Manzo J., Terrones M. and Ajayan P.M., Carbon nanotubes as high-pressure cylinders and nanoextruders. *Science* **2006,** 312 (5777), 1199.

[60] He Z., Lee C.S., Maurice J.-L., Pribat D., Haghi-Ashtiani P. and Cojocaru C.S., Vertically oriented nickel nanorod/carbon nanofiber core/shell structures synthesized by plasma-enhanced chemical vapor deposition. *Carbon* **2011,** 49 (14), 4710.

[61] Chang I.-C., Huang T.-K., Lin H.-K., Tzeng Y.-F., Peng C.-W., Pan F.-M., Lee C.-Y. and Chiu H.-T., Growth of Pagoda-Topped Tetragonal Copper Nanopillar Arrays. *ACS applied materials & interfaces* **2009,** 1 (7), 1375.

[62] Wang J.-H., Yang T.-H., Wu W.-W., Chen L.-J., Chen C.-H. and Chu C.-J., Synthesis and growth mechanism of pentagonal Cu nanobats with field emission characteristics. *Nanotechnology* **2006,** 17 (3), 719.

[63] Wang S., He Y., Liu X., Huang H., Zou J., Song M., Huang B. and Liu C., Novel C/Cu sheath/core nanostructures synthesized via low-temperature MOCVD. *Nanotechnology* **2011,** 22 (40), 405704.

[64] Parveen S., Kumar A., Husain S. and Husain M., Fowler Nordheim theory of carbon nanotube based field emitters. *Physica B: Condensed Matter* **2017,** 505, 1.

[65] Gao R., Pan Z. and Wang Z.L., Work function at the tips of multiwalled carbon nanotubes. *Applied Physics Letters* **2001,** 78 (12), 1757.

[66] Nilsson L., Groening O., Groening P., Kuettel O. and Schlapbach L., Characterization of thin film electron emitters by scanning anode field emission microscopy. *Journal of Applied Physics* **2001,** 90 (2), 768.

[67] Kim D.-H., Jang H.-S., Lee H.-R., Kim C.-D. and Kang H.-D., Field emission properties of vertically aligned iron nanocluster wires grown on a glass substrate. *Applied physics letters* **2004,** 85 (1), 109.

[68] Lv R., Kang F., Zhu D., Zhu Y., Gui X., Wei J., Gu J., Li D., Wang K. and Wu D., Enhanced field emission of open-ended, thin-walled carbon nanotubes filled with ferromagnetic nanowires. *Carbon* **2009,** 47 (11), 2709.

[69] Lin W.-H. and Li Y.-Y., Field emission properties of tapered carbon nanotubes synthesized by the pyrolysis of poly(ethylene glycol) using a nickel catalyst. *Diamond and Related Materials* **2012,** 22, 124.

[70] Lee C.-K., Lee B., Ihm J. and Han S., Field emission of metal nanowires studied by first-principles methods. *Nanotechnology* **2007,** 18 (47), 475706.

[71] Hertel T., Walkup R.E. and Avouris P., Deformation of carbon nanotubes by surface van der Waals forces. *Physical Review B* **1998,** 58 (20), 13870.

[72] Nilsson L., Groening O., Emmenegger C., Kuettel O., Schaller E., Schlapbach L., Kind H., Bonard J. and Kern K., Scanning field emission from patterned carbon nanotube films. *Applied Physics Letters* **2000,** 76 (15), 2071.

[73] Lin P.-H., Sie C.-L., Chen C.-A., Chang H.-C., Shih Y.-T., Chang H.-Y., Su W.-J. and Lee K.-Y., Field emission characteristics of the structure of vertically aligned carbon nanotube bundles. *Nanoscale research letters* **2015,** 10 (1), 297.

[74] Yun J., Wang R., Choi W.K., Thong J.T.L., Thompson C.V., Zhu M., Foo Y.L. and Hong M.H., Field emission from a large area of vertically-aligned carbon nanofibers with nanoscale tips and controlled spatial geometry. *Carbon* **2010,** 48 (5), 1362.

[75] Kar R., Sarkar S., Basak C., Patsha A., Dhara S., Ghosh C., Ramachandran D., Chand N., Chopade S. and Patil D., Effect of substrate heating and microwave attenuation on the catalyst free growth and field emission of carbon nanotubes. *Carbon* **2015,** 94, 256.

[76] Mitchell E.W.J. and Mitchell J.W., The work functions of copper, silver and aluminium. *Proceedings of the Royal Society of London. Series A. Mathematical and Physical Sciences* **1951,** 210 (1100), 70.

[77] Gartland P., Berge S. and Slagsvold B., Photoelectric work function of a copper single crystal for the (100),(110),(111), and (112) faces. *Physical Review Letters* **1972,** 28 (12), 738.

[78] Zhang J., Wang X., Yang W., Yu W., Feng T., Li Q., Liu X. and Yang C., Interaction between carbon nanotubes and substrate and its implication on field emission mechanism. *Carbon* **2006,** 44 (3), 418.

CHAPTER 7

Synthesis, characterization, and measurement of electrochemical lithiation properties of SnO_2-VACNTs composite

Chapter 7 presents a detailed study of the synthesis, structural characterization, and measurement of electrochemical lithiation properties of a single SnO_2-CNT nanowire, the pristine VACNT array, and the array of SnO_2-VACNTs composite.

7.1 Introduction

Lithium-ion batteries have become an essential part of our everyday life due to their increasing applications extending from portable electronics to electric vehicles. Lithium-ion batteries (LIBs) are one of the energy storage and power devices based on electrochemical energy storage and conversion mechanism. Because of the excellent properties of LIBs, such as superior energy density, a broader operating temperature range, a low self-discharge rate, and devoid of memory effect, they are superior among other battery technologies. However, the ever-increasing demand for LIBs capable of delivering high energy and power densities with minimal volumetric constraints and safety issues requires research for novel LIB components with enhanced electrochemical properties. Carbon nanotubes (CNTs) have demonstrated the potential for application as the anode of LIBs because of their unique one-dimensional tubular structure, large surface area, short diffusion length of Li^+ ions, high electrical and thermal conductivity [1]. The CNTs are regarded as excellent materials to store lithium ions (~1000 mAh/g) [2] compared to the-state-of-art graphite anode (372 mAh/g). Several groups have researched the possibility of using CNTs as the anode material in LIBs for charge storage [3, 4]. The CNTs have been

excellent additive materials to improve the electrochemical performance of electrode materials with much improved energy conversion, storage capacities, and charge transferability [5].

Several reports have shown the experimental specific capacity of CNT anodes below 400 mAh/g [3, 6], which is a low value regarding the demands for the high energy and power densities of LIBs. One of the main reasons causing the low specific capacity of CNT anode is its conventional bilayer design. A thin layer of CNTs is glued onto a copper foil current collector with the help of a binder. The binder limits the potential application of batteries above 200 ºC, whereas the copper foil itself is not involved in the electrochemical reaction. Reports have shown that the bilayer design of LIB anode can reduce the usable capacity by ~47% [2], making LIBs essential to use free-standing, binder-free CNTs anode.

High capacity metal and semiconductor materials such as Al (800 mAh/g), Sn (994 mAh/g), Li (3860 mAh/g), Si (4000 mAh/g), and Ge (1600 mAh/g) have been explored to improve the specific and volumetric capacity of LIB anodes [7]. Despite having such high Li^+ storage capacity, colossal volume instability during the lithiation/delithiation leads to pulverization of the anode material and loss of inter-particle contact resulting in rapid capacity fading and severe safety issues. Recent research of anode materials has been motivated mainly by hybrid materials consisting of high capacity nanoparticles (<100 nm) and CNTs to address inherent concerns of bulk electrode materials [8-10]. The reduced particle size may modify the volumetric alteration mechanism, and simultaneously using CNTs can absorb the considerable stress developed during the lithiation and delithiation

process. The high electrical conductivity of CNTs can enhance the performance of LIBs since it offers a quick pathway for charged particles during the battery operation. The CNTs coated with SnO_2 nanoparticles (SnO_2-CNTs) as an anode of LIBs is an attractive strategy since the theoretical charge storage capacity of SnO_2 (781 mAh/g) is over twice as much as graphite anodes. Several groups have investigated SnO_2-CNTs composite material to explore its potential as the anode material of LIBs [10-12].

Most of the reports for fabricating SnO_2-CNTs composite as anode materials mainly focus on using wet chemical methods on randomly oriented CNTs. However, SnO_2-VACNTs can significantly improve the battery performance by offering better electrolyte accessibility and charge transfer capability due to the regular pore structure and inter-tube space of the VACNTs array [13]. Improved contact resistance between VACNTs and current collectors achieved through the direct synthesis of VACNTs on metal substrates and anisotropic conductivities of VACNTs may enhance the charge transfer and adequate dissipation of heat caused by resistive heating. A proper inter-tube distance in an array of VACNTs can alleviate the stress developed during the lithiation/delithiation process. Hence, it is essential to fabricate binder-free VACNT templates directly on metal substrates to accommodate a uniform coating of SnO_2 nanoparticles for achieving high-performance LIB anodes.

In chapter 7, SnO_2-CNTs composite has been synthesized on the stainless steel substrate. During the lithiation process of a single SnO_2-CNT nanowire, the structural evolution was examined using a miniaturized LIB designed and fabricated inside a transmission electron microscope (TEM). In situ TEM experiment revealed that the volume

of individual SnO_2 nanoparticles during the first charge cycle was significantly increased. Arrays of free-standing, binder-free VACNTs have also been synthesized directly on the 3D nickel foil. The as-synthesized VACNTs were coated with SnO_2 nanoparticles to form core-shell structures. The electrochemical lithiation performance of the pristine VACNTs and SnO_2-VACNTs anode has been evaluated in a half cell configuration. The SnO_2-VACNTs composite anode exhibited a significantly higher specific capacity of ~1891 mAh/g at the current density of 0.1 A/g than the pristine VACNTs of ~520 mAh/g. Furthermore, the SnO_2-VACNTs composite demonstrated a capacity of more than 900 mAh/g even at a high current density of 1 A/g, which is a significant improvement over the current graphite anode of LIBs.

7.2 Experimental details

The structural evolution of a single SnO_2-CNT nanowire during the lithiation process was examined using a miniaturized LIB designed and fabricated inside a TEM. The VACNTs were synthesized on the stainless steel substrate by the plasma-enhanced chemical vapor deposition (PECVD) method. A detailed explanation of the apparatus and synthesis procedure is given in section 3.2.1. The core-shell SnO_2-CNT composite was prepared by a wet-chemical method, as described in section 3.2.2. A thorough explanation of the miniaturized LIB fabrication procedure inside the TEM and the LIB testing limits are described in section 3.4.2.2. Free-standing, binder-free vertically aligned carbon nanotubes (VACNTs) were synthesized on 3D nickel (Ni, 99.99% by wt.) foam via PECVD, as described in section 3.2.1. In brief, as-received Ni foam (1.6 mm thick) was cut into circular disks of a diameter of about 1 cm. They were loaded into the PECVD

chamber after cleaning ultrasonically in acetone and isopropyl alcohol bath for 10 min, and the chamber was pumped down to the pressure of 0.01 Torr. The VACNTs were synthesized at 600 ºC for 7 min by using acetylene (25 sccm) as the carbon precursor gas in the presence of ammonia gas (400 sccm) while DC plasma of 70 W was applied at the pressure of 7 Torr. The SnO_2-VACNTs composite was prepared at room temperature by a simple wet-chemical method described in section 3.2.2. The electrochemical properties of the as-synthesized samples were measured using CR2032 coin cells in half-cell configuration with Li foil as both counter and reference electrodes. A detailed procedure of fabricating coin cells is explained in section 3.4.2.1.

7.3 Results and discussion

7.3.1 In situ TEM Lithiation study of a single SnO_2-CNT nanowire

One of the critical issues of the LIB is the tremendous volume expansion in the electrodes during the charging and discharging process, leading to serious safety concerns and rapid capacity fading. Moreover, during the first cycling process, a considerable capacity loss due to irreversible structural changes in the active material is another significant concern of the current LIBs [14]. Understanding the underlying mechanism of the structure and phase evolution of the active material during the lithiation/delithiation processes is crucial to alleviate such problems. Electron microscopy is an advanced tool for examining the structural evolution of active materials in the LIB during charging and discharging. Reliable characterization of the structural evolution of active materials using an ex situ capability is a challenge because of the active material's structural stability under

operational conditions [15]. Several in situ methods, such as scanning electron microscopy (SEM) [16], scanning probe microscopy (SPM) [17], and X-ray diffraction (XRD) [18],

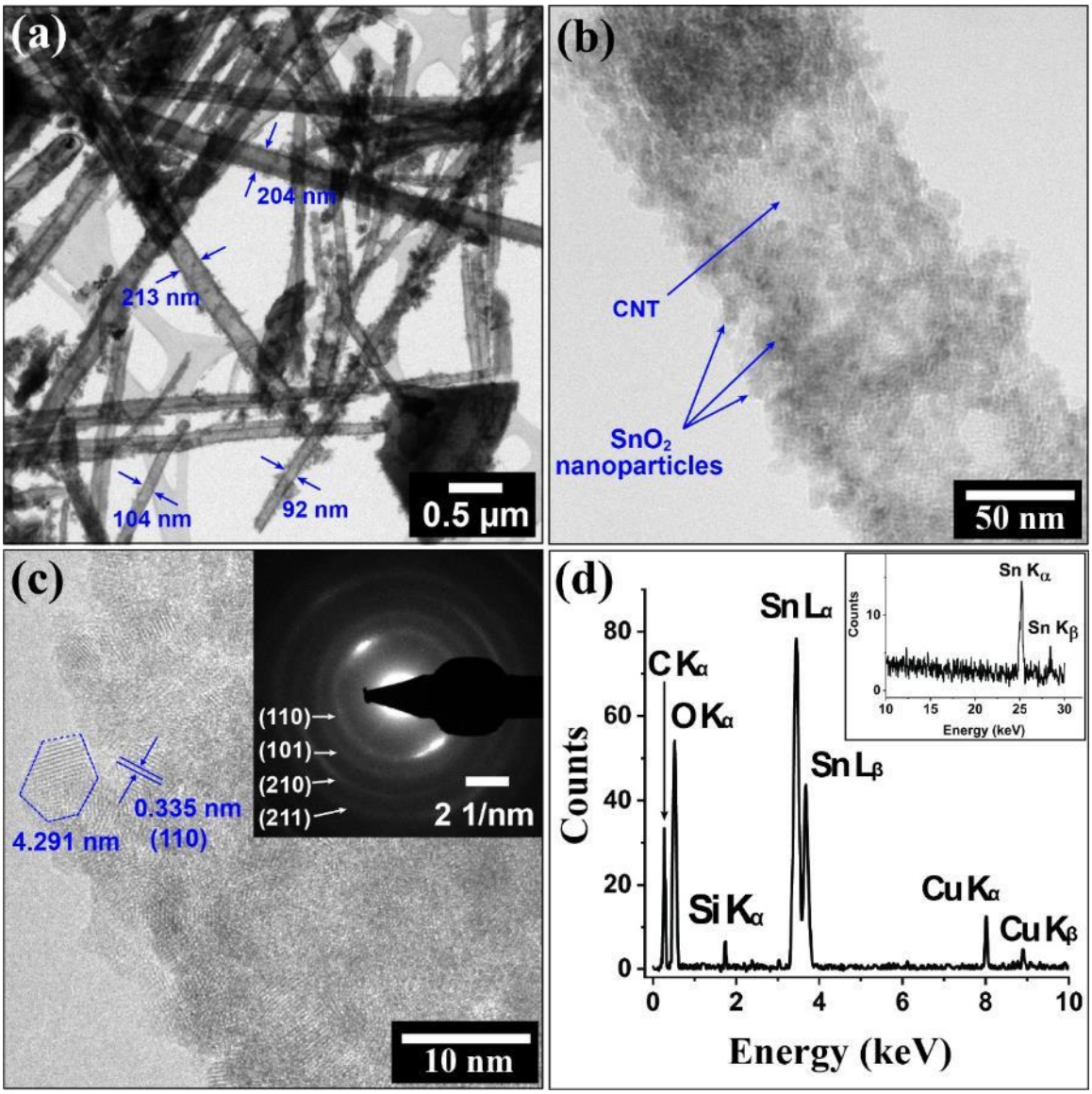

Figure 7.1. Study of nanostructure of the SnO_2-CNTs composite material synthesized on the stainless steel substrate. (a) Low-magnification, (b) high-magnification, and (c) high-resolution TEM images of the SnO_2-CNTs. The inset in figure 7.1(c) represents the SAD pattern obtained from the SnO_2-CNTs. (d) EDS spectrum from the SnO_2-CNTs composite. The Cu signal was associated with the TEM grid.

have been used to study the morphology and phase change of the active materials during the battery operation. However, a typically low spatial resolution of these techniques limits

their use. In situ TEM imaging is mostly an ideal device for investigating the structural evolution of the active materials in LIBs during their operation if suitable operation conditions can be installed [19].

Figure 7.1 shows the TEM characterization of the SnO_2-CNTs composite synthesized on the stainless steel substrate. The CNTs were synthesized at 750 ºC for 10 min using C_2H_2 (25 sccm) as the carbon precursor gas. The NH_3 gas (400 sccm) was used as a carrier gas. The plasma of 70 W at the pressure of 7 Torr was maintained during the synthesis of CNTs. The diameter of the CNTs was varied in the range of 92 nm to 213 nm, as shown in Figure 7.1(a). The length of CNTs was found to be ~8 μm long. As shown in Figure 7.1(b), the high-magnification TEM image revealed that the SnO_2 nanoparticles were coated on CNT's exterior wall. The high-resolution TEM image, as shown in Figure 7.1(c), shows the individual crystalline SnO_2 nanoparticles showing clear lattice fringes separated by a distance of 0.335 nm, which corresponds to the (110) lattice plane of the tetragonal SnO_2 crystal [20]. The size of SnO_2 particles was about 5 nm, and a typical SnO_2 nanoparticle of size 4.291 nm is shown in Figure 7.1(c). The inset of Figure 7.1(c) represents the selected area diffraction (SAD) pattern from the SnO_2-CNT composite. The distinct concentric rings can be indexed as (110), (101), (210), and (211) corresponding to the tetragonal phases of polycrystalline SnO_2 nanoparticles. The presence of Sn and O in the EDS spectrum, as shown in Figure 7.1(d), further confirmed the composite as the polycrystalline SnO_2 nanoparticles.

Figure 7.2 shows a miniaturized LIB fabricated inside the TEM using a SnO_2-CNT nanowire as an anode and lithium (Li) metal as a cathode. During the lithiation, the Li^+

ions transportation was facilitated by a Li_2O solid-state electrolyte layer formed on the Li metal surface. A bias of -2 V was applied to the SnO_2-CNT electrode vs. Li^+/Li to initiate the lithiation. Upon initial charge, the SnO_2 transformed to Sn and Li_2O according to the following reaction [19].

$$SnO_2 + 4Li^+ + 4e^- \rightarrow Sn + 2Li_2O \quad (7.1)$$

Subsequent lithiation of the SnO_2-CNT anode corresponds to the following reversible phase transformation reactions [19].

$$Sn + xLi^+ + xe^- \leftrightarrow Li_xSn \qquad (0 \leq x \leq 4.4) \quad (7.2)$$

$$C\ (nanotube) + xLi^+ + xe^- \leftrightarrow Li_xC \quad (7.3)$$

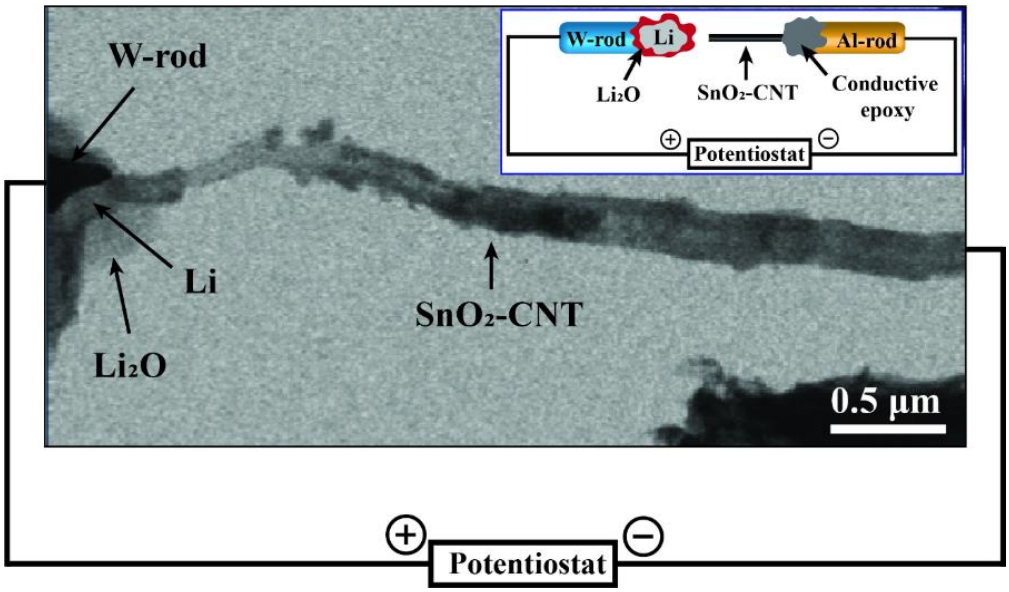

Figure 7.2. TEM image of a miniaturized LIB, showing the SnO_2-CNT nanowire in contact with the Li-cathode. The inset shows the schematic of a design of the miniature LIB using SnO_2-CNT nanowire as an anode.

Figure 7.3 shows a significant change in morphology and phase of the SnO_2 nanoparticles during the first charging process. The morphology and the crystallographic features of the SnO_2 nanoparticles are shown in Figure 7.3(a-b). Prior to the initial charge,

the size of the SnO_2 nanoparticles was ~5 nm and the distinct concentric rings on the selected area diffraction (SAD) pattern revealed the polycrystalline nature of SnO_2 nanoparticles. Figure7.3(c-d) represents the morphology and the crystallographic features

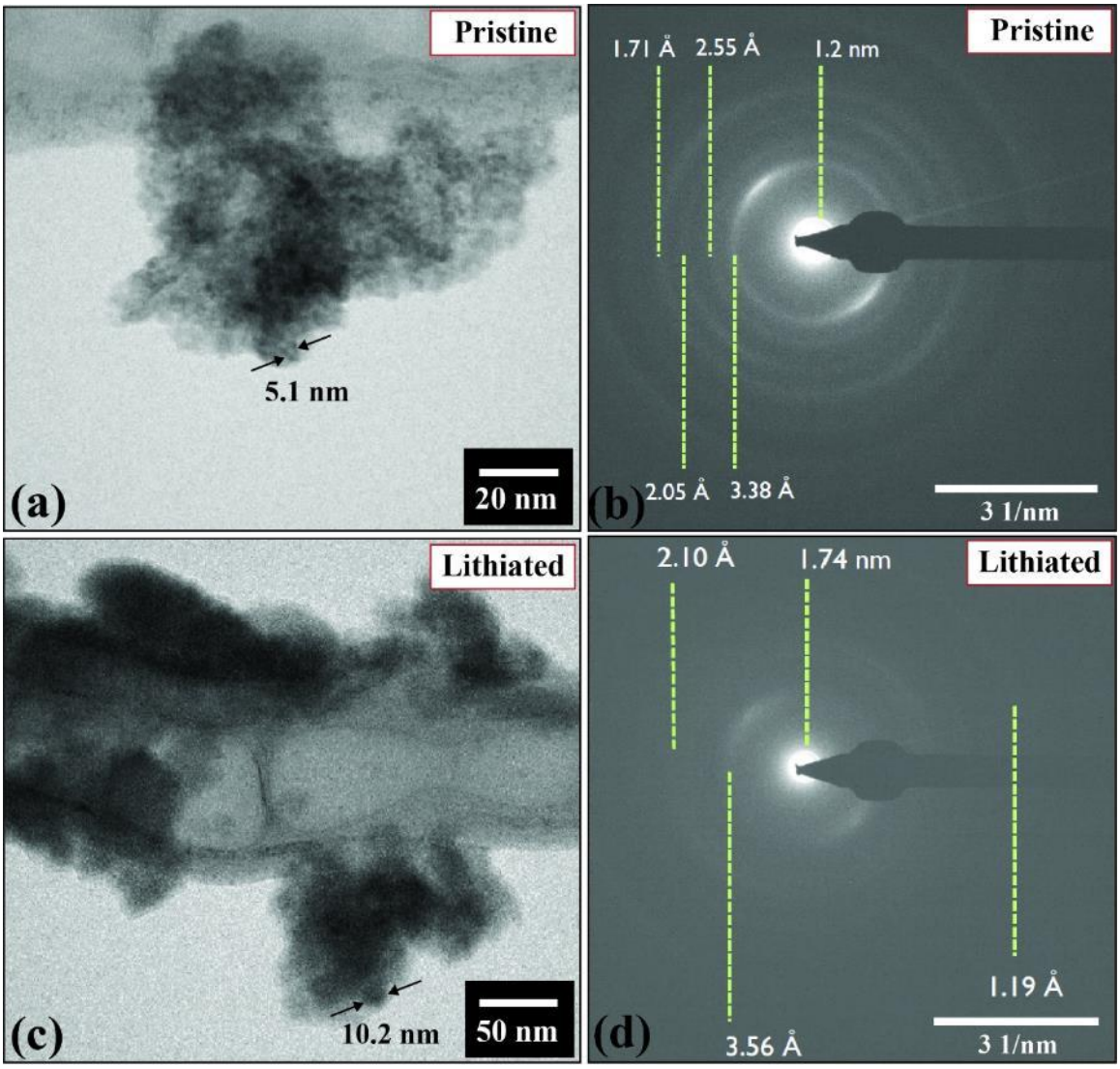

Figure 7.3. In situ TEM observation of morphology and phase evolution of a SnO_2-CNT nanowire upon lithiation. (a) TEM image showing a cluster of SnO_2 nanoparticles before lithiation and (b) corresponding SAD pattern. (c) TEM image of fully lithiated SnO_2-CNT nanowire and (d) corresponding SAD pattern. The numbers shown by dotted lines in Figure 7.3 (b) and (d) represent the lattice plane distances of SnO_2 nanocrystals in reciprocal lattice.

of the SnO_2 nanoparticles coated on the CNT after the lithiation for 3.5 minutes. Upon lithiation, the nanoparticles were significantly increased in size (~10 nm) and crystalline

nanoparticles were transformed into a matrix of amorphous (Li_2O) and crystalline particles (Li_xSn), which can be understood as a lack of clear concentric rings in the SAD pattern shown in Figure 7.3(d). The result can be attributed to the phase transformation of tetragonal SnO_2 to hexagonal Li_xSn and amorphous Li_2O after lithiation.

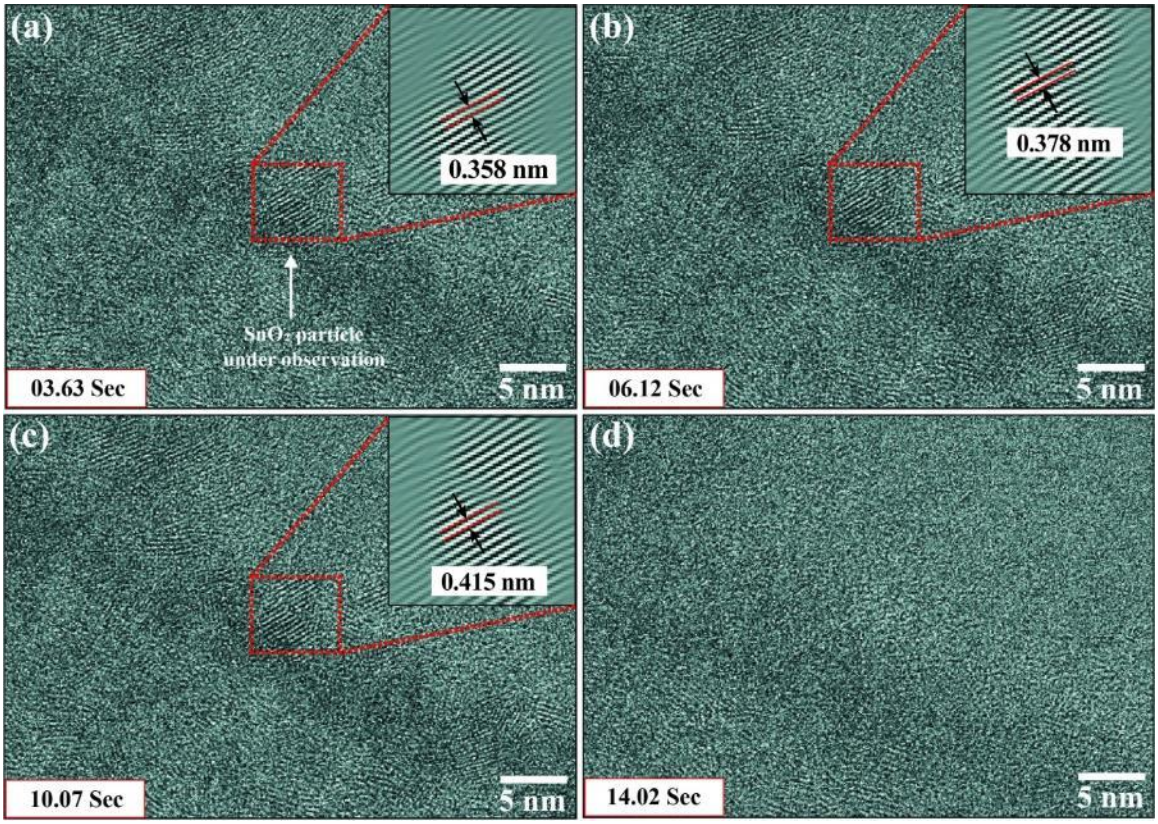

Figure 7.4. Time-resolved high-resolution TEM images from video frames of the electrochemical reaction-induced nanostructure evolution of a SnO_2 nanoparticle. The insets in Figure 7.4(a-c) represent the high-resolution TEM images of a SnO_2 nanoparticle (boxed area) showing the evolution of crystal lattice planes.

The first lithiation process is crucial for the electrode materials in LIBs since massive volume expansion occurs during the first cycle, which is reportedly one of the main reasons for substantially irreversible capacity fading. The electrochemical lithiation process of an individual SnO_2-CNT nanowire was examined using time-resolved high-resolution TEM images to understand the electrochemical lithiation behavior of the SnO_2-

CNT materials in LIBs, and the result is shown in Figure 7.4. A single SnO_2 nanoparticle, as shown in the boxed area of Figure 7.4(a-c), was tracked during the electrochemical lithiation. An inter-planar distance of 0.335 nm, which corresponds to the (110) plane of tetragonal SnO_2 crystal, increased to 0.358 nm after 3.63 seconds of initial lithiation, as shown in Figure 7.4(a). The inter planer distance further increased to 0.378 nm after the lithiation for 6.12 seconds, shown in Figure 7.4(b). The lattice separation was significantly increased by ~23 % after 10.07 seconds due to the alloying of Li-ions with Sn metals, as shown in Figure 7.4(c). After 14.02 seconds of lithiation, the crystalline SnO_2 particles were transformed nearly to the amorphous phase and became difficult to track, as shown in Figure 7.4(d). It would be interesting to see if lithiated SnO_2 nanoparticles regain their original size and crystallinity upon delithiation, critical for the LIB cycle reversibility. Hence, further experiments are necessary for the detailed understanding of the lithiation/delithiation mechanism of the SnO_2-VACNTs anode.

7.3.2 Pristine VACNTs and SnO_2-VACNT composite as the anode of LIBs

Free-standing, binder-free VACNT templates for accommodating the high capacity SnO_2 nanomaterials were synthesized directly on 3D Ni foam by the PECVD method. Figure 7.5 explains the detailed plan of the VACNT synthesis, coating with SnO_2, and fabricating the Li-ion CR2032 coin cell with the SnO_2-VACNT composite as an anode material. The on-site decomposition of hydrocarbon gas into carbon atoms, diffusion into the catalyst nanoparticles/nano-hills, and precipitation on the catalyst surface to enable the CNT graphitization are essential steps in the VACNT synthesis process. The presence of catalytically active growth sites on the substrate is crucial when a catalytic metal substrate

is preferred over the substrate coated with a thin film of transition metals. Figure 7.6 shows Ni foam's surface morphology before and after the heat treatment at 600 °C in an NH_3 environment for 6 min. As shown in Figure 7.6(a) and (c), pristine Ni foam had a relatively

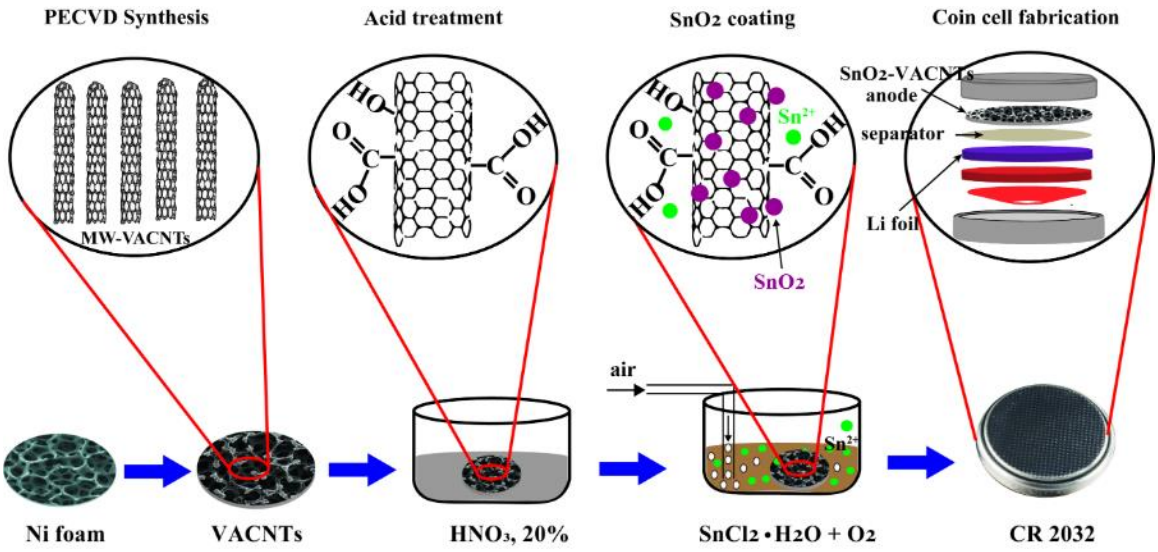

Figure 7.5. Schematic showing the detailed plan of VACNTs synthesis on Ni foam, coating with SnO_2, and fabrication of CR2032 Li-ion coin cell.

smooth surface with an average roughness R_a = 53.68 nm. After the heat treatment, the Ni foam was much rougher with R_a = 105 nm, as shown in Figure 7.6(b, d). Most importantly, uniform nano-hills were evolved on the Ni foam surface after the heat treatment under the reducing environment, which were crucial for the nucleation of the VACNTs.

Figure 7.7(a) shows a typical SEM image of a well-aligned, self-standing, and uniform array of VACNTs synthesized on the Ni foam. The inset of Figure 7.7(a) depicts a high magnification SEM image of the boxed area shown in Figure 7.7(a). The diameter of VACNTs was ranged from 150 to 270 nm, whereas the length was measured to be ~5 μm long. Figure 7.7(b) and (c) show a low and a high magnification TEM image of VACNTs, which confirmed a tubular "bamboo-like" structure of VACNTs with a catalyst

nanoparticle at the tip, a typical characteristic of the VACNTs synthesized via PECVD at a low temperature. A high-resolution TEM image depicted the lattice fringes separated by a distance of 0.34 nm in the VACNT wall, as shown in the inset of Figure 7.7(c). The high-resolution TEM image, Figure 7.7(d), revealed multilayer lattice planes separated by 0.21

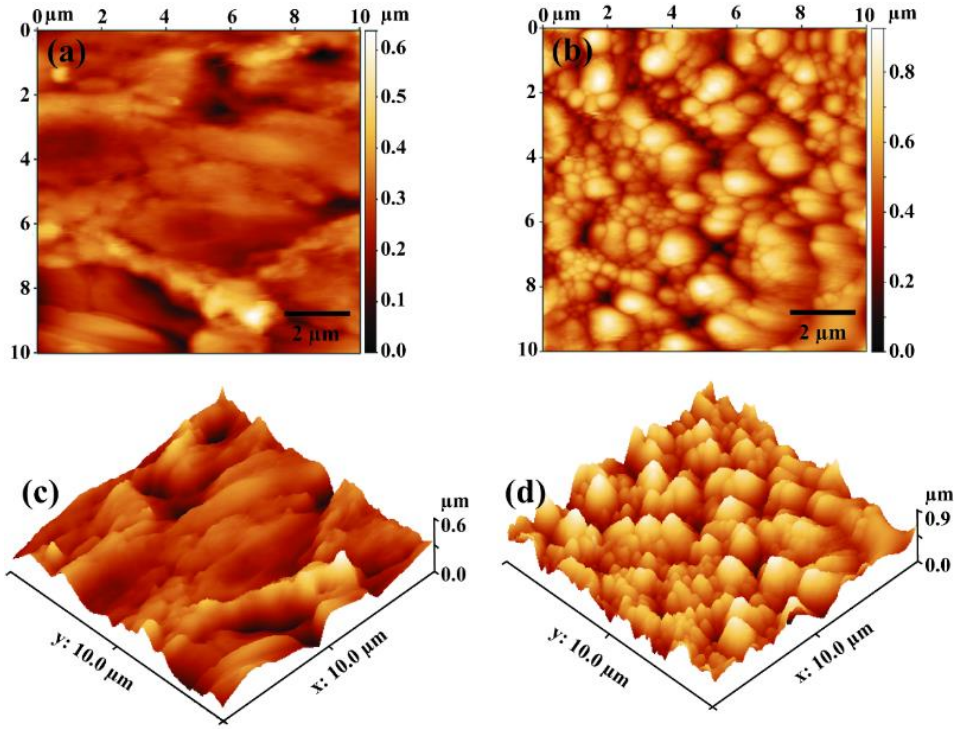

Figure 7.6. Surface evolution of the Ni foam (single strip) due to the heat treatment at 600 °C under the NH_3 environment for 6 min. AFM images of the surface of Ni foam (a) before, (b) after the heat treatment, and (c-d) their corresponding 3D view.

nm corresponding to the (111) lattice plane of face-centered cubic (fcc) Ni crystal. The typical electron diffraction pattern of the Ni nanoparticle trapped at the tip of the VACNT is shown in the upper-right inset of Figure 7.7(d). The distinct diffraction spots can be assigned to $(0\bar{2}0)$, $(\bar{1}\bar{1}1)$, and $(\bar{1}11)$ planes of pure fcc Ni along the [101] zone axis. As shown in the lower-left inset of Figure 7.7(d), the EDS spectrum confirmed the nanoparticle as a single crystalline Ni metal, where the C and Cu signals can be ascribed to the VACNT wall and TEM holder, respectively.

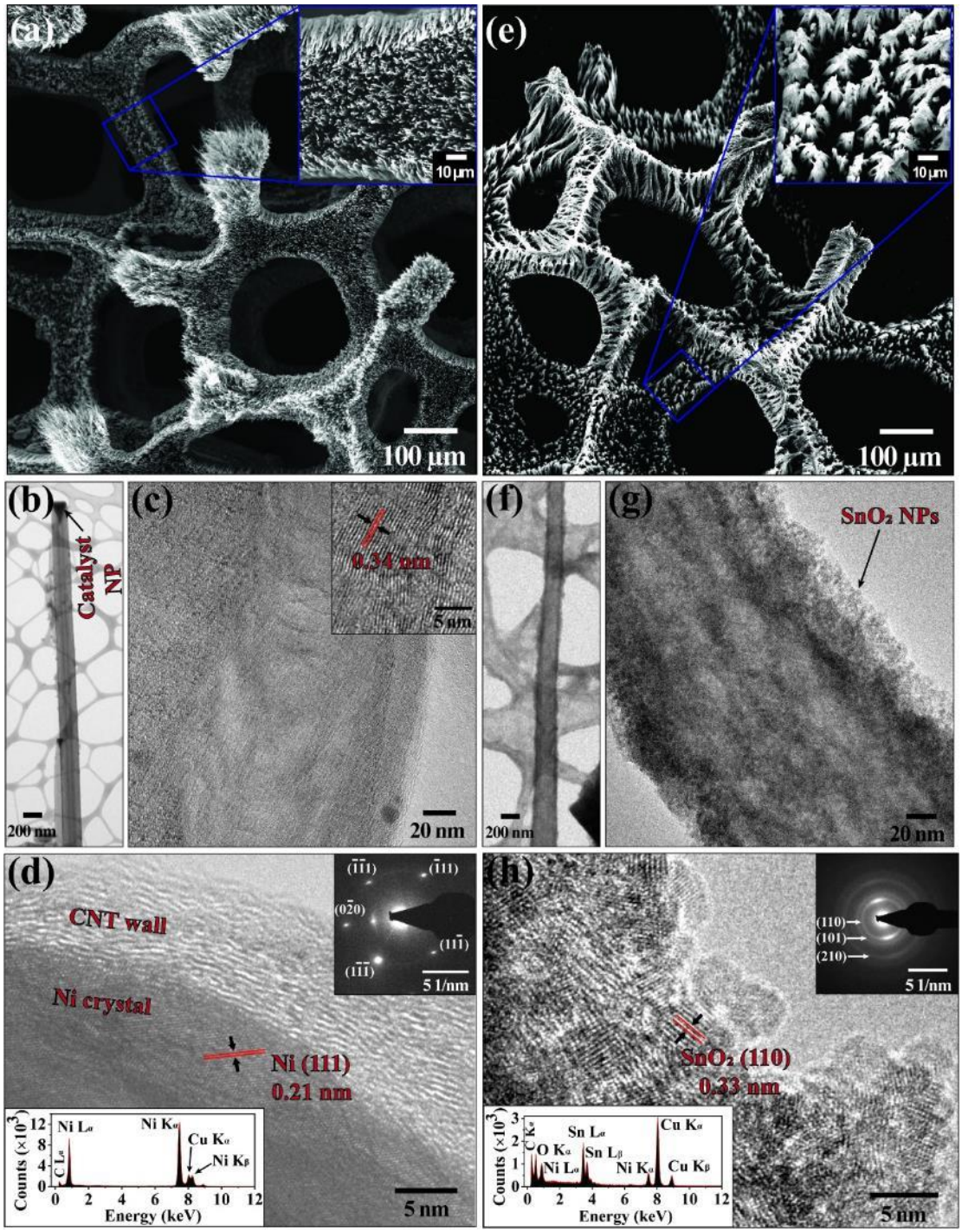

Figure 7.7. SEM and TEM characterization of the as-synthesized samples. (a, e) SEM images of VACNTs and SnO_2-VACNTs grown on the Ni foam. The insets represent the magnified view of the boxed area shown in the respective images. (b, f) Low and (c, g) high magnification TEM images of a VACNT and a SnO_2-VACNT composite. The inset in Figure 7.7(c) represents a high-resolution TEM image showing the lattice fringes in the VACNT wall. High-resolution TEM image (d) at the interface between the graphitic layers of the VACNT and the catalyst particle and (h) of the SnO_2 nanoparticles. The upper-right and lower-left insets represent the SAD pattern and EDS spectrum of the catalyst particle trapped at the tip of the VACNT and SnO_2 nanoparticles, respectively.

Figure 7.7(e) shows a uniquely bundled SnO_2-VACNTs structure created after the solution phase SnO_2 coating procedure with VACNT tips touching each other. The active material (SnO_2-VACNTs) yield was 1.02 – 1.21 mg/cm^2 for the VACNTs synthesis period of 6 min and SnO_2 coating duration of 9 hours. A low and high magnification TEM images shown in Figure 7.7(f) and (g) illustrate the coating of the VACNT by a thin layer (~20 nm) of SnO_2 nanoparticles, forming a core-shell structure. As shown in Figure 7.7(h), the high-resolution TEM image confirmed the crystalline phase of the SnO_2 nanoparticle and demonstrated lattice planes separated by 0.33 nm related to the (110) plane of the tetragonal SnO_2. The upper-right inset of Figure 7.7(h) represents the typical electron diffraction pattern of the SnO_2-VACNT composite. The concentric diffraction rings can be indexed as (110), (101), and (210) planes related to the polycrystalline phase of tetragonal SnO_2. As shown in the lower-left inset of Figure 7.7(h), the presence of Sn, O, and C in the EDS spectrum further established the material as the SnO_2-VACNT core-shell, where the signals such as Ni and Cu can be ascribed to the catalyst particle and TEM grid, respectively.

Thermogravimetric analysis (TGA) was performed to determine the SnO_2 loading on the SnO_2-VACNTs composite. Figure 7.8 (a) shows the TGA profiles of the pristine VACNTs and SnO_2-VACNTs composite sample. Both samples exhibited typical weight loss due to moisture removal below 400 °C, although the composite showed more significant weight loss, which can be accredited to the solution-based SnO_2 coating procedure. The composite displayed a rapid weight loss starting at ~463 °C, whereas the pristine VACNTs sample showed an abrupt weight loss at ~425 °C. The thermal stability of SnO_2 powder with a particle size of ~10 nm has been proven up to 900 °C [21]. The final residual weights of both samples were expected to have all the carbonaceous species

burned off by 700 °C, leaving behind the dry mass of SnO_2 and any impurities in the VACNTs [22]. The SnO_2 mass loading of the composite was determined to be about 40% of the total mass of SnO_2-VACNTs from the TGA spectra, which is the final residual mass

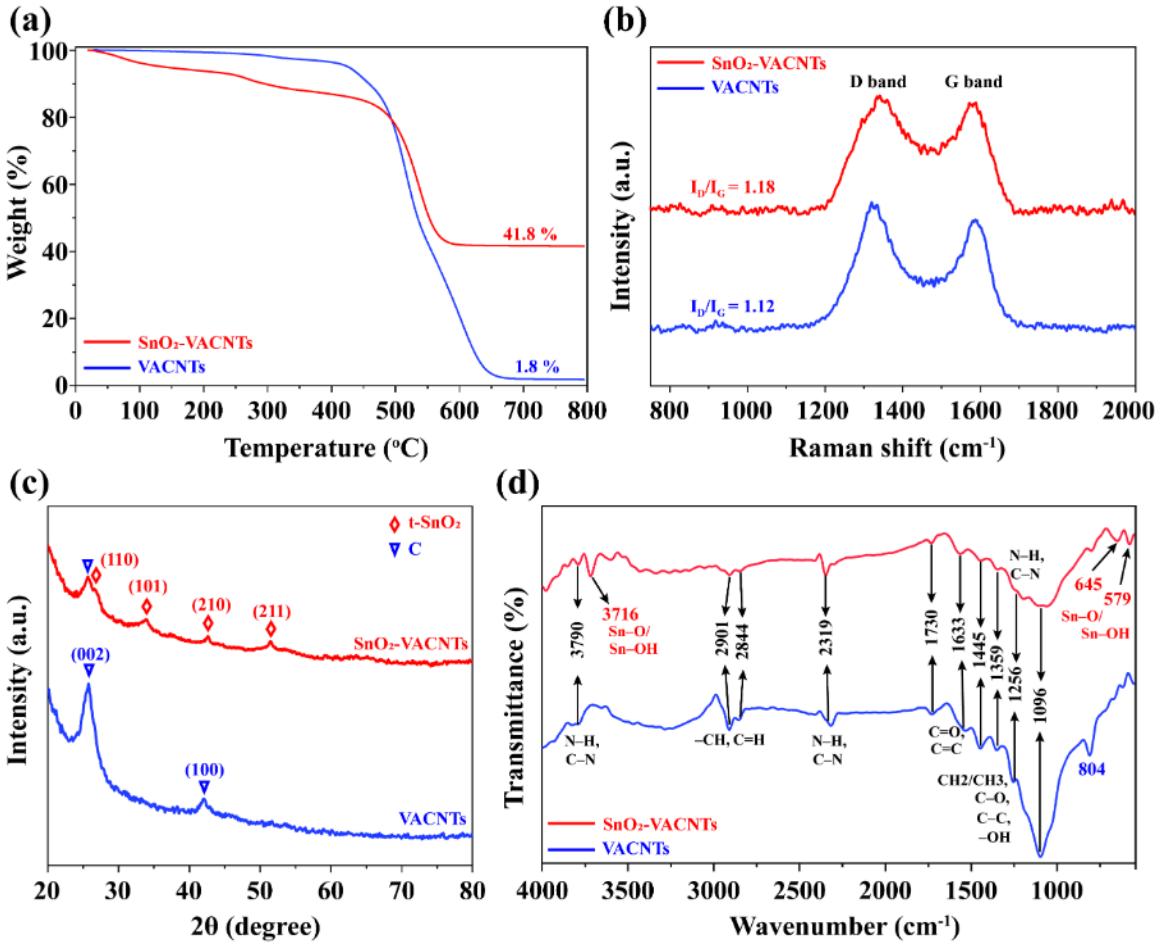

Figure 7.8. (a) TGA, (b) Raman, (c) XRD, and (d) FTIR spectra of the pristine VACNTs and SnO_2-VACNTs.

percentage remaining at 800 °C after subtracting the final mass remaining by the VACNTs. As shown by Raman spectra in Figure 7.8(b), the coating with SnO_2 slightly increased the defects on the VACNTs, which is evident from the increase in the intensity ratio of D-band and G-band (I_D/I_G) from 1.12 to 1.18 [23]. The higher defects on the SnO_2-VACNTs can be accredited to the treatment of VACNTs with HNO_3 acid before being coated with SnO_2.

It is important to note that the acid treatment was crucial to creating oxygen-containing functional groups on the VACNTs wall to assist the coating process. The crystallographic structure of the pristine VACNTs and SnO_2-VACNTs composite was characterized by XRD, as shown in Figure 7.8(c). The XRD spectra show the peaks (2θ) at ~26.6º, 33.9º, 42.6º, and 51.4º, which can be indexed as (110), (101), (210), and (211) planes of the tetragonal phase of SnO_2 nanoparticles, and the result is consistent with the previous literature [24]. The VACNT related peaks at ~26º and 42º further indicated that the test material was SnO_2-VACNTs composite.

The functional groups present on the HNO_3 treated and SnO_2 coated VACNTs were examined using FTIR analysis, as shown in Figure 7.8(d). It has been reported that chemical oxidation with HNO_3 can generate functional groups at the defect sites of the VACNTs wall [25]. The FTIR spectra of both samples revealed the C=C, C=O, C–N, and N–H stretching vibrations at various wave number positions between 4000 and 550 cm^{-1}. Peaks at ~3790 cm^{-1}, 2319 cm^{-1}, and 1256 cm^{-1}, associated with N–H and C–N band stretching, can be attributed to adsorbed H_2O and NH_3 [26]. The peaks at 2901 cm^{-1} and 2844 cm^{-1} may be associated with the –CH and C=H band stretching vibrations, respectively [27]. The signals at ~1730 cm^{-1} and 1633 cm^{-1} are related to carbonyl (C=O) stretching vibration of the carboxylic acid group and carbon structure (C=C) of VACNTs, respectively [25]. The peaks at 1445 cm^{-1}, 1359 cm^{-1}, 1096 cm^{-1}, and 804 cm^{-1} correspond to the CH_2/CH_3, C–C, C–O, and –OH band stretching, respectively [28]. The signal associated with the Sn–O or Sn–OH stretching vibrations at ~3716 cm^{-1}, 645 cm^{-1}, and 579 cm^{-1} indicated that the carbon nanomaterial contained SnO_2 nanoparticles [27, 29].

The electrochemical Li-ion storage behavior of pristine VACNTs and SnO_2-VACNTs composite anodes for LIBs was examined using lithium foil as a reference electrode. The electrochemical reactions that occurred during the cycling process were studied using cyclic voltammetry (CV) tests. Figure 7.9(a-b) shows CV curves of VACNTs

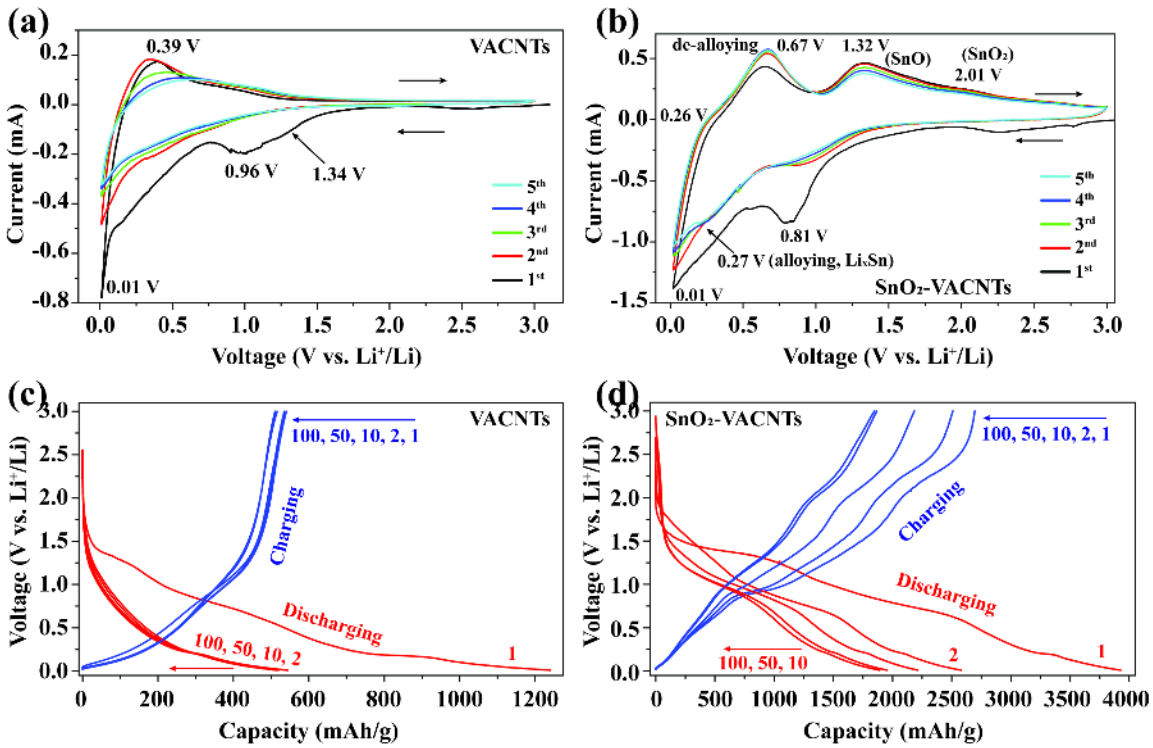

Figure 7.9. Electrochemical properties of the pristine VACNTs and SnO_2-VACNTs composite anode materials evaluated via Li-ion coin cell fabrication. (a-b) CV curves of pristine VACNTs and SnO_2-VACNTs composite with a scan rate of 0.2 mV/s measured between 0.01 and 3 V. (c-d) Charge/discharge profile of the pristine VACNTs and SnO_2-VACNTs composite at the current rate of 0.1 A/g within a voltage range between 0.01 to 3 V.

and SnO_2-VACNTs composite anodes measured between 0.01 and 3 V (versus Li^+/Li) at a scan rate of 0.2 mV/s for the first five cycles. The electrochemical reactions of pristine and hybrid anode materials in LIBs can be described by equations (7.1-7.3). For both anode materials, sharp irreversible reduction peaks (at ~0.96 V for pristine VACNTs and ~0.81 V for SnO_2-VACNTs) during the 1st CV cycle indicated the formation of solid electrolyte interphase (SEI) on the anode surfaces from the decomposition of EC and DEC. The

distinct reduction peak for the composite anode can also be accredited to the initial irreversible reduction of SnO_2 to Sn and Li_2O (equation 7.1) [30]. The reversible reduction peak at ~0.27 V for composite anode can be associated with the alloying of Li with Sn metal. Besides, reversible oxidation peaks at ~0.39 V for VACNTs can be accredited to the extraction of Li-ions from VACNTs (equation 7.3). In contrast, oxidation peaks at ~0.67, 1.32, and 2.01 V for SnO_2-VACNTs can be assigned to dealloying of Li_xSn (equation 7.2) [31] and oxidation of Sn^{+2}. The CV cycles overlapped after the 1st cycle, indicating the promising reversibility of electrochemical reactions, which may be crucial for capacity retention and long cyclability of LIBs.

The electrochemical performance of the as-synthesized electrodes was tested by the galvanostatic charge/discharge cycling at a constant current of 0.1 A/g with cut-off potentials at 0.01 V and 3 V versus Li/Li^+, as shown in Figure 7.9(c-d). The first charge and discharge capacities for VACNTs were 535 mAh/g and 1240 mAh/g. Similarly, the first charge and discharge capacities for SnO_2-VACNTs were 2695 mAh/g and 3927 mAh/g. However, discharge capacities for VACNTs and SnO_2-VACNTs in the second cycle were dropped significantly to 542 mAh/g and 2581 mAh/g, respectively. In the first discharge curves of both electrodes, a plateau is present at ~1.4 V, which may be assigned to the irreversible reduction of surface species containing oxygen on VACNTs [32]. Also, the plateau that emerged at ~0.95 V can be accredited to the formation of an SEI layer in pristine VACNTs, whereas it can be due to the formation of the SEI and Li_2O in the case of the composite electrode. Hence, the largely irreversible capacity loss between the first and second discharge cycles of electrodes was due to the irreversible reactions on the

surface of VACNTs, the formation of the solid electrolyte interphase, and the formation of amorphous Li_2O during the first cycle [32-34].

The galvanostatic cycle performance of the pristine VACNTs and SnO_2-VACNTs composite anodes was examined for 100 cycles of charge and discharge, and the results are shown in Figure 7.10(a-b). The capacity of both anode materials became stable and reversible after the initial few charge/discharge cycles. With a current density at 0.1 A/g, the LIB with VACNTs anode exhibited an excellent cyclability with coulombic efficiencies

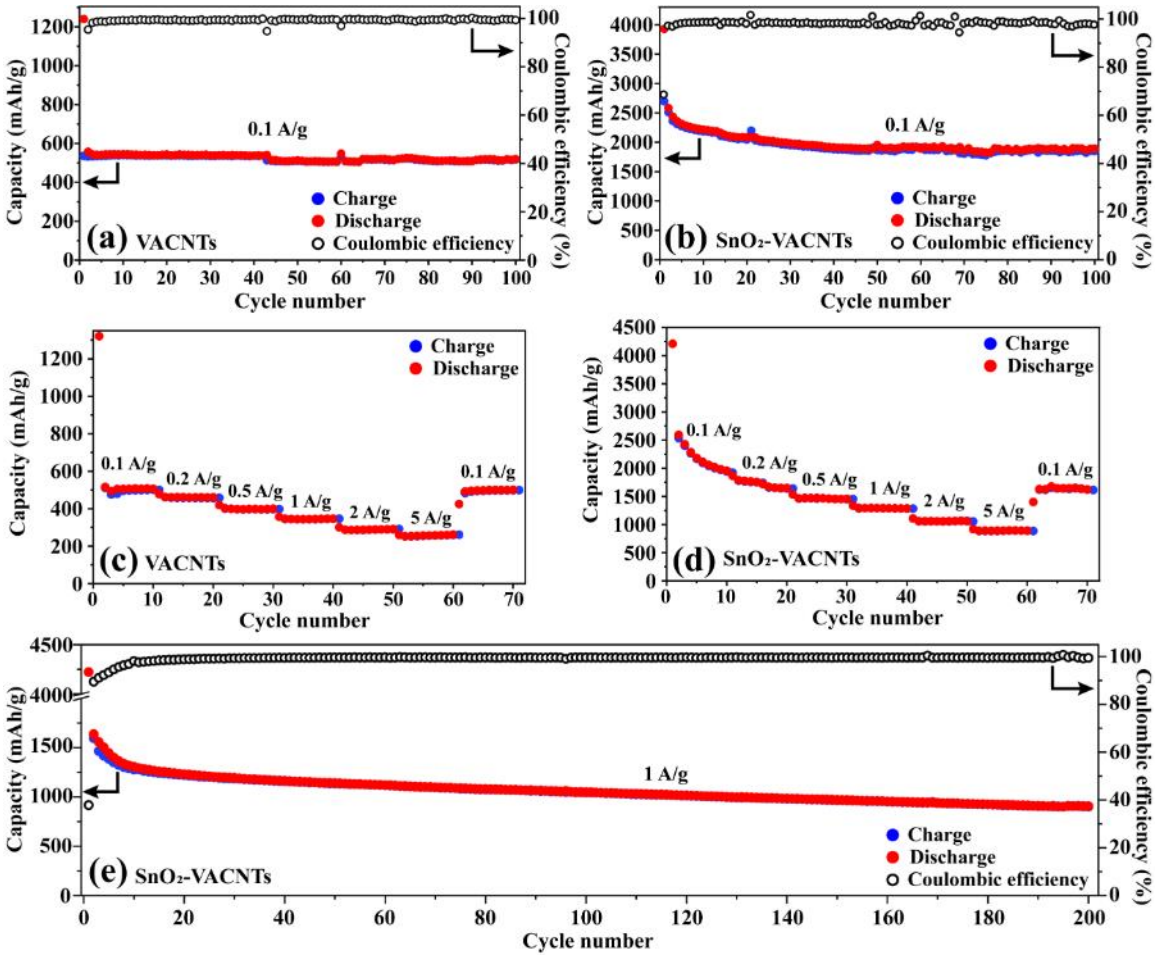

Figure 7.10. Electrochemical properties of the pristine VACNTs and SnO_2-VACNTs composite. (a-b) Cycle stability and (c-d) rate performance of the VACNTs and SnO_2-VACNTs composite, respectively. (e) Cycling performance of SnO_2-VACNTs composite at a high current density of 1 A/g with Coulombic efficiency.

of more than 99% after the first cycle. The capacity remained ~520 mA/g at 0.1 A/g after 100 cycles. In comparison, the SnO_2-VACNTs anode displayed considerably high capacity with an initial discharge capacity of 3927 mAh/g. However, the LIB with the composite anode suffered a continuous capacity fading, and after 20 cycles, it only preserved a discharge capacity of ~2085 mAh/g. Despite the initial capacity fading, it showed promising cyclability after 20 cycles and showed a discharge capacity of ~1891 mAh/g after 100 cycles. The initial poor cyclability of the LIB with the SnO_2-VACNTs anode may be attributed to the significant volume change and pulverization of SnO_2 nanoparticles, which led to the anode breakdown [34]. Moreover, both anode materials displayed excellent high-power rate capability, as shown in Figure 7.10(c-d). At current densities of 0.2, 0.5, 1, 2, and 5 A/g, the reversible capacities of the pristine VACNTs were ~458, 399, 344, 289, and 256 mAh/g, respectively. The anode retained ~95 % of its initial capacity at 0.1 A/g, as shown in Figure 7.10(c). Similarly, the SnO_2-VACNTs composite had reversible capacities of ~1696, 1463, 1294, 1065, and 894 mAh/g at current densities of 0.2, 0.5, 1, 2, and 5 A/g, respectively (Figure 7.10(d)). Besides, the composite anode retained more than 83% of its initial discharge capacity at 0.1 A/g.

Furthermore, we evaluated the composite anode's cyclability at the high current density of 1 A/g for 200 cycles, as shown in Figure 7.10(e). Similar to the performance at the low current density, the composite displayed a continuous capacity fading during the first few cycles. However, after the first ten cycles, the composite anode exhibited a highly stable cycling performance with a high specific capacity of more than 900 mAh/g at a high current density of 1 A/g after 200 cycles with an excellent coulombic efficiency, as shown in Figure 7.10(e). To examine the impact of the Ni foam on the overall Li storage capacity

of electrodes, the galvanostatic cycle performance of the heat-treated Ni foam was conducted for 100 cycles of charge and discharge at the current density of 0.1 A/g within the potential window of 0.01 to 3 V, as shown in Figure 7.11. The specific capacity of the Ni foam anode was very low (~20 mAh/g) compared to the pristine VACNTs and SnO_2-VACNTs composite anode, which confirmed that the Ni foam had little or no contribution to the electrochemical performance of the samples.

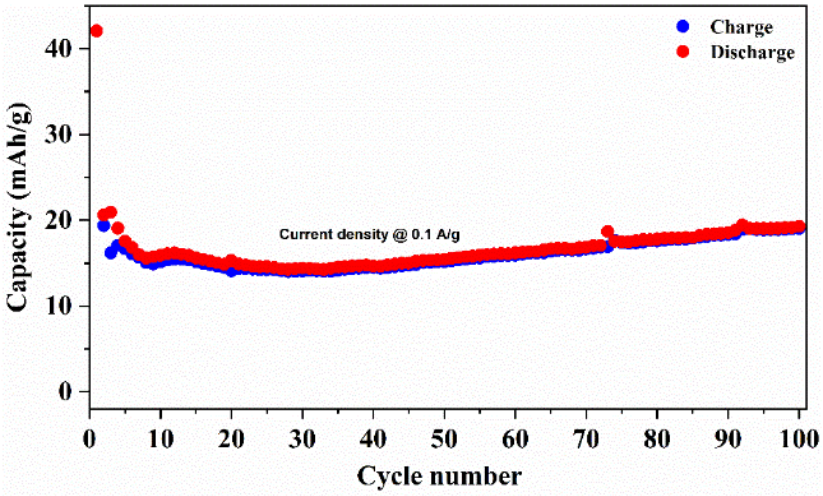

Figure 7.11. Cycling performance of the heat-treated Ni foam at a current density of 0.1 A/g. The heat treatment to the Ni foam was performed under the NH_3 environment for 6 min to create similar conditions to that of synthesizing VACNTs in the Ni foam.

Electrochemical impedance spectroscopy (EIS) measurements were performed on the pristine VACNTs and SnO_2-VACNTs composite electrodes using a sine wave of 5 mV amplitude over a frequency range of 100 kHz–50 mHz to determine the electronic conductivity and Li-ion transportation within electrodes. The Nyquist complex plane impedance measurements were carried out before and after running charge/discharge cycles, as shown in Figure 7.12. Both Nyquist plots of the VACNTs and SnO_2-VACNTs comprise a semicircle in the high-to-medium frequency region and a straight line inclined at ~45° angle to the real axis at the low-frequency region [35, 36]. The intercept at the Z'

axis at high frequency corresponds to the equivalent series resistance (R_s), which relates to the total resistance of the electrolyte, separator, and electrical contact. The depressed semicircle in the medium-frequency range describes the charge-transfer impedance (R_{ct}) on the electrode/electrolyte interface [35-38]. Moreover, the straight line at the low-frequency region of the Nyquist plot can be attributed to the Li diffusion process within the electrode [39]. Figure 7.13 shows an equivalent modified Randle's circuit to analyze

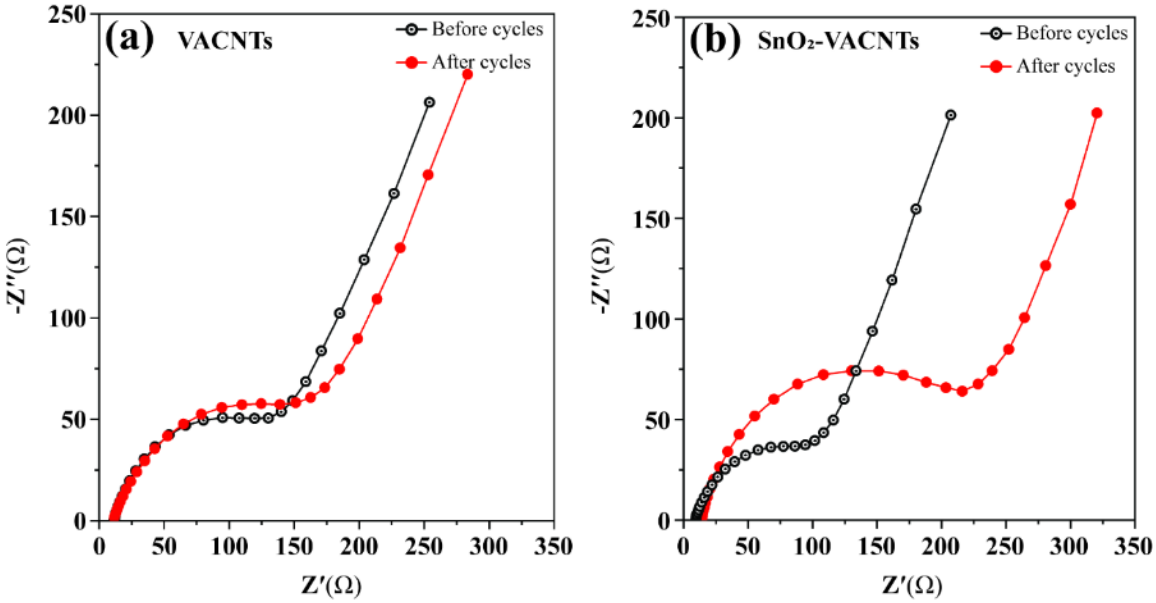

Figure 7.12. AC impedance spectra of (a) VACNTs and (b) SnO_2-VACNTs before and after the discharge-charge cyclic processes.

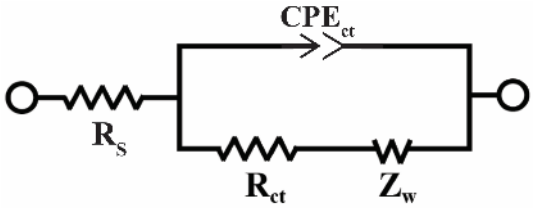

Figure 7.13. Equivalent Randle's circuit model used for fitting the experimental impedance data.

the impedance spectra. In the equivalent model circuit, CPE_{ct} and Z_w represent the double layer capacitance at intermediate frequencies and the Warburg impedance associated with Li-ion diffusion.

Table 7.1 demonstrates parameters after fitting the impedance data using equivalent Randle's circuit for the VACNTs and the SnO_2-VACNTs electrodes before and after 100 cycles of charge and discharge. Before cycling, the composite electrode exhibited lower series resistance (R_s) and charge-transfer resistance (R_{ct}) than the VACNTs electrode, indicating fast electron transport and fast faradaic reactions at the electrode surface. The depressed semicircle size in the mid-frequency range for both electrodes increased after 100 cycles, revealing higher charge transfer resistance after the cycling process. The increase of resistance may be caused by the formation and thickening of SEI and loss of

Table 7.1. Impedance parameters of VACNTs and SnO_2-VACNTs anode materials calculated from equivalent Randle's circuit.

Electrode materials		**R_s (Ω)**	**R_{ct} (Ω)**
VACNTs			
	Before cycling	11.3	113.6
	After cycling	10.8	144.2
SnO_2-VACNTs			
	Before cycling	9.4	67.8
	After cycling	13.8	165.1

active materials [40]. In the SnO_2-VACNTs electrode, the charge-transfer resistance along with series resistance after cycling increased significantly than the pristine VACNTs electrode. The increase of series resistance could be attributed to the formation and extension of the gap between the SnO_2 particle and CNT wall as a result of substantial volume expansion/contraction and pulverization of the SnO_2 during lithiation/delithiation. The continuous pulverization of the SnO_2 particle exposes a new grain surface for the fresh SEI formation, which leads to the thickening of the SEI on the anode material, increasing

charge-transfer resistance [40]. The increase in electrode resistances of the composite electrode is well supported by the continuous capacity fading during the first 20 cycles of the SnO_2-VACNTs, as shown in Figure 7.10(b).

7.4 Conclusions

In summary, arrays of VACNTs and SnO_2-VACNTs composite have been synthesized directly on stainless steel foil and 3D Ni foam using the PECVD and wet-chemical method. A miniaturized LIB was designed and fabricated inside a TEM to investigate the in situ expansion of the crystal lattice plane and phase evolution of SnO_2 nanoparticles of the SnO_2-CNT electrode during the first lithiation process. The in situ TEM experiment revealed that the lattice fringe distance of an individual SnO_2 nanoparticle was increased by ~23% of its original lattice plane separation upon alloying of Li-ions into the Sn metal particles during the first charge. Moreover, the electrochemical properties of free-standing, binder-free VACNTs and SnO_2-VACNTs anode materials were measured using Li-ion coin cells in half-cell configuration. The pristine VACNTs anode exhibited very stable cycling stability up to 100 cycles with a capacity of ~520 mAh/g at the current density of 0.1 Ah/g and excellent rate capability at various high current densities. The SnO_2-VACNTs composite electrode displayed a much higher capacity of ~1891 mAh/g at the current density of 0.1 Ah/g after 100 cycles. The composite electrode also showed a high capacity of more than 900 mAh/g at a high current density of 1 A/g after 200 cycles with excellent coulombic efficiency, showing potential anode material for future high-energy and high-power LIBs.

References

[1] Liu X.M., Huang Z.D., Oh S.W., Zhang B., Ma P.C., Yuen M.M. and Kim J.K., Carbon nanotube (CNT)-based composites as electrode material for rechargeable Li-ion batteries: a review. *Composites Science and Technology* **2012,** 72 (2), 121.

[2] Landi B.J., Ganter M.J., Cress C.D., DiLeo R.A. and Raffaelle R.P., Carbon nanotubes for lithium ion batteries. *Energy & Environmental Science* **2009,** 2 (6), 638.

[3] Kang C., Lahiri I., Baskaran R., Kim W.G., Sun Y.K. and Choi W., 3-dimensional carbon nanotube for Li-ion battery anode. *Journal of Power Sources* **2012,** 219, 364.

[4] De las Casas C. and Li W., A review of application of carbon nanotubes for lithium ion battery anode material. *Journal of Power Sources* **2012,** 208, 74.

[5] Lee J.-H., Kim G.-S., Choi Y.-M., Park W.I., Rogers J.A. and Paik U., Comparison of multiwalled carbon nanotubes and carbon black as percolative paths in aqueous-based natural graphite negative electrodes with high-rate capability for lithium-ion batteries. *Journal of power sources* **2008,** 184 (1), 308.

[6] Yehezkel S., Auinat M., Sezin N., Starosvetsky D. and Ein-Eli Y., Bundled and densified carbon nanotubes (CNT) fabrics as flexible ultra-light weight Li-ion battery anode current collectors. *Journal of Power Sources* **2016,** 312, 109.

[7] Larcher D., Beattie S., Morcrette M., Edstroem K., Jumas J.C. and Tarascon J.M., Recent findings and prospects in the field of pure metals as negative electrodes for Li-ion batteries. *Journal of Materials Chemistry* **2007,** 17 (36), 3759.

[8] Park G.D., Choi J.H., Jung D.S., Park J.-S. and Kang Y.C., Three-dimensional porous pitch-derived carbon coated Si nanoparticles-CNT composite microsphere with superior electrochemical performance for lithium ion batteries. *Journal of Alloys and Compounds* **2020,** 821, 153224.

[9] Gao C., Kim N.D., Salvatierra R.V., Lee S.-K., Li L., Li Y., Sha J., Silva G.A.L., Fei H. and Xie E., Germanium on seamless graphene carbon nanotube hybrids for lithium ion anodes. *Carbon* **2017,** 123, 433.

[10] Noerochim L., Wang J.Z., Chou S.L., Wexler D. and Liu H.K., Free-standing single-walled carbon nanotube/SnO2 anode paper for flexible lithium-ion batteries. *Carbon* **2012,** 50 (3), 1289.

[11] Zhang B., Huang J. and Kim J.K., Ultrafine Amorphous SnOx Embedded in Carbon Nanofiber/Carbon Nanotube Composites for Li-Ion and Na-Ion Batteries. *Advanced Functional Materials* **2015,** 25 (32), 5222.

[12] Ma C., Zhang W., He Y.-S., Gong Q., Che H. and Ma Z.-F., Carbon coated SnO 2 nanoparticles anchored on CNT as a superior anode material for lithium-ion batteries. *Nanoscale* **2016,** 8 (7), 4121.

[13] Jiang Y., Wang P., Zang X., Yang Y., Kozinda A. and Lin L., Uniformly embedded metal oxide nanoparticles in vertically aligned carbon nanotube forests as pseudocapacitor electrodes for enhanced energy storage. *Nano Lett* **2013,** 13 (8), 3524.

[14] Bryngelsson H., Stjerndahl M., Gustafsson T. and Edström K., How dynamic is the SEI? *Journal of Power Sources* **2007,** 174 (2), 970.

[15] Gibot P., Casas-Cabanas M., Laffont L., Levasseur S., Carlach P., Hamelet S., Tarascon J.-M. and Masquelier C., Room-temperature single-phase Li insertion/extraction in nanoscale Li x FePO 4. *Nature materials* **2008,** 7 (9), 741.

[16] Yang Y., Xie C., Ruffo R., Peng H., Kim D.K. and Cui Y., Single nanorod devices for battery diagnostics: A case study on LiMn2O4. *Nano letters* **2009,** 9 (12), 4109.

[17] Balke N., Jesse S., Morozovska A., Eliseev E., Chung D., Kim Y., Adamczyk L., Garcia R., Dudney N. and Kalinin S., Nanoscale mapping of ion diffusion in a lithium-ion battery cathode. *Nature nanotechnology* **2010,** 5 (10), 749.

[18] Courtney I.A. and Dahn J., Electrochemical and in situ X-ray diffraction studies of the reaction of lithium with tin oxide composites. *Journal of the Electrochemical Society* **1997,** 144 (6), 2045.

[19] Wang C.-M., Xu W., Liu J., Zhang J.-G., Saraf L.V., Arey B.W., Choi D., Yang Z.-G., Xiao J. and Thevuthasan S., In situ transmission electron microscopy observation of microstructure and phase evolution in a SnO2 nanowire during lithium intercalation. *Nano Letters* **2011,** 11 (5), 1874.

[20] Han W.-Q. and Zettl A., Coating Single-Walled Carbon Nanotubes with Tin Oxide. *Nano Letters* **2003,** 3 (5), 681.

[21] Noerochim L., Wang J.-Z., Chou S.-L., Li H.-J. and Liu H.-K., SnO2-coated multiwall carbon nanotube composite anode materials for rechargeable lithium-ion batteries. *Electrochimica Acta* **2010,** 56 (1), 314.

[22] Hsu R.S., Higgins D. and Chen Z., Tin-oxide-coated single-walled carbon nanotube bundles supporting platinum electrocatalysts for direct ethanol fuel cells. *Nanotechnology* **2010,** 21 (16), 165705.

[23] Dresselhaus M.S., Dresselhaus G., Saito R. and Jorio A., Raman spectroscopy of carbon nanotubes. *Physics reports* **2005,** 409 (2), 47.

[24] Lee K.M., Lee D.J. and Ahn H., XRD and TEM studies on tin oxide (II) nanoparticles prepared by inert gas condensation. *Materials Letters* **2004,** 58 (25), 3122.

[25] Ebbesen T.W., Hiura H., Bisher M.E., Treacy M.M., Shreeve-Keyer J.L. and Haushalter R.C., Decoration of carbon nanotubes. *Advanced Materials* **1996,** 8 (2), 155.

[26] Balasubramanian K. and Burghard M., Chemically functionalized carbon nanotubes. *small* **2005,** 1 (2), 180.

[27] Pandiyan R., Mahalingam S. and Ahn Y.H., Antibacterial and photocatalytic activity of hydrothermally synthesized SnO2 doped GO and CNT under visible light irradiation. *Journal of Photochemistry and Photobiology B: Biology* **2019,** 191, 18.

[28] Motshekga S., Pillai S.K. and Ray S.S., Conventional wet impregnation versus microwave-assisted synthesis of SnO 2/CNT composites. *Journal of Nanoparticle Research* **2011,** 13 (3), 1093.

[29] Zhu J., Lu Z., Aruna S., Aurbach D. and Gedanken A., Sonochemical synthesis of SnO2 nanoparticles and their preliminary study as Li insertion electrodes. *Chemistry of Materials* **2000,** 12 (9), 2557.

[30] Hernandez D., Mendoza F., Febus E., Weiner B.R. and Morell G., Binder free SnO2-CNT composite as anode material for Li-Ion battery. *Journal of Nanotechnology* **2014,** 2014, 381273.

[31] Zhang J., Zhu Y., Cao C. and Butt F.K., Microwave-assisted and large-scale synthesis of SnO 2/carbon-nanotube hybrids with high lithium storage capacity. *RSC Advances* **2015,** 5 (72), 58568.

[32] Lu W., Goering A., Qu L. and Dai L., Lithium-ion batteries based on vertically-aligned carbon nanotube electrodes and ionic liquid electrolytes. *Physical Chemistry Chemical Physics* **2012,** 14 (35), 12099.

[33] Ji L., Tan Z., Kuykendall T., An E.J., Fu Y., Battaglia V. and Zhang Y., Multilayer nanoassembly of Sn-nanopillar arrays sandwiched between graphene layers for high-capacity lithium storage. *Energy & Environmental Science* **2011,** 4 (9), 3611.

[34] Wang Z., Chen G. and Xia D., Coating of multi-walled carbon nanotube with SnO2 films of controlled thickness and its application for Li-ion battery. *Journal of power sources* **2008,** 184 (2), 432.

[35] Chen D., Sun S., Yu G., Qin L., Wang W., Jiang M. and Chen J., In-situ thermally fabricated porous and heterogeneous yolk-shell selenides wrapped in carbon as anode for high-performance hybrid lithium-ion capacitors. *Carbon* **2020,** 166, 91.

[36] Jia R., Yue J., Xia Q., Xu J., Zhu X., Sun S., Zhai T. and Xia H., Carbon shelled porous SnO2-δ nanosheet arrays as advanced anodes for lithium-ion batteries. *Energy Storage Materials* **2018,** 13, 303.

[37] Kenji F., Kazuhiko K., Kennichi I. and Masaki Y., Foliated natural graphite as the anode material for rechargeable lithium-ion cells. *Journal of Power Sources* **1997,** 69 (1), 165.

[38] Zhang S. and Shi P., Electrochemical impedance study of lithium intercalation into MCMB electrode in a gel electrolyte. *Electrochimica Acta* **2004,** 49 (9), 1475.

[39] Bulusheva L.G., Okotrub A.V., Kurenya A.G., Zhang H., Zhang H., Chen X. and Song H., Electrochemical properties of nitrogen-doped carbon nanotube anode in Li-ion batteries. *Carbon* **2011,** 49 (12), 4013.

[40] Wang L., Zhang B., Hu Y., Li X. and Zhao T., Failure analysis of LiNi0·83Co0·12Mn0·05O2/graphite–SiOx pouch batteries cycled at high temperature. *Journal of Power Sources* **2021,** 482, 228978.

CHAPTER 8

Summary and future work

8.1 Summary of the dissertation research

The dissertation presents the synthesis, characterization, and application of vertically aligned carbon nanotube (VACNT) arrays. The dissertation work is focused on the direct synthesis of VACNT arrays on various metal substrates using plasma-enhanced chemical vapor deposition (PECVD) method and their application in field emission and lithium-ion batteries (LIBs). First, we demonstrated the synthesis of high-quality VACNT arrays on the stainless steel foil without extra catalysts and showed the use of pristine and structurally modified VACNT arrays as cold cathodes for electron field emission. Second, we fabricated VACNT micro-pillars directly on the stainless steel foil and demonstrated the precise control of the pillar's size by nanosphere lithography using polystyrene spheres. Moreover, we found that the pillar size significantly affects the field emission behavior. Third, we synthesized VACNTs filled with copper nanowires inside the VACNT hollow cores. The study of field emission properties revealed that the highly conductive core nanowires enhance the field emission properties of VACNT emitters. Finally, we synthesized VACNT arrays on nickel foam and coated them with SnO_2 nanoparticles, which we tested as high-capacity anode materials in LIBs.

VACNT arrays have been synthesized in the past on conducting substrates after decorating the substrate surface with a catalyst thin layer or pretreating the substrate with chemicals. In Chapter 4, we demonstrated that high-quality VACNT arrays could be fabricated directly on the stainless steel substrate without an external metallic catalyst layer

or chemical pretreatment to the substrate using the PECVD method. We found that the occurrence of surface nano hills resulting from surface evolution due to ramping temperature in the presence of NH_3 plays a crucial role in the VACNT nucleation and growth process. The high-density VACNT emitters displayed poor field emission properties due to field screening effects. We further demonstrated that the post-treatment (water treatment and SnO_2 nanoparticles coating) to the dense VACNT arrays could result in the structural change, which could minimize the field screening effect. The VACNTs coated with SnO_2 nanoparticles presented superior field emission stability as a result of the improved mechanical strength and chemical stability of the VACNT emitters after SnO_2 coating.

The VACNT pillar emitters have been widely synthesized for field emission applications using various techniques. In Chapter 5, we demonstrated that VACNT pillar emitters could be synthesized directly on the stainless steel disk using nanosphere lithography. We showed that the pillar size could be controlled precisely by using polystyrene spheres of various sizes. We found that the field emission properties of VACNT pillar emitters strongly depend on the pillar size. The VACNT pillars synthesized after nanosphere lithography with polystyrene spheres of 450 nm in diameter showed superior field emission performance, including low turn-on field (E_{TO} = 1.57 V/μm), low threshold field (E_{TH} = 2.94 V/μm), high field enhancement factor (β = 4977), and high emission current density of ~33 mA/cm^2 at a field of 4 V/μm. This sample also showed a stable emission current with a high average current (0.49 mA) at an initial test current of 0.5 mA and a low current fluctuation (12%) for an extended period of more than 5 hours. The structurally controlled VACNT pillar emitters synthesized directly on the conducting

substrate, such as stainless steel, could be applied in developing new-generation high-performance miniaturized vacuum tube X-ray devices.

It has been shown that the interior hollow core of CNTs can be filled with foreign materials using various ex-situ and in situ methods. Chapter 6 demonstrated a simple and effective technique of synthesizing copper filled VACNT arrays via the PECVD method. We found that copper nanoparticles formed on the copper disk due to the surface reconstruction at high temperatures were responsible for the growth of VACNTs, and the growth temperature was the key to the successful filling of copper inside VACNTs. We further demonstrated that the filling of copper through the entire length of the VACNT could significantly enhance the field emission properties of the VACNT field emitters. The enhanced field emission performance of the copper-filled VACNTs can be ascribed to the overall increase in electrical and thermal conductivities of the field emitter.

Finally, arrays of VACNTs and SnO_2-VACNTs composite were synthesized directly on stainless steel foil and 3D nickel foam. The in situ TEM observation of an individual SnO_2-CNT nanowire anode in a miniaturized lithium-ion battery revealed that the crystal lattice plane distance of individual SnO_2 nanoparticles was significantly increased (~23% of its original lattice plane separation) during the first lithiation process. The electrochemical lithiation properties of pristine VACNT anode materials evaluated via lithium-ion coin cells exhibited very stable cycling performance up to 100 cycles with the capacity ~520 mAh/g at the current density of 0.1 Ah/g, and excellent rate capability at various high current densities. The SnO_2-VACNT composite electrode demonstrated a much higher capacity of ~1891 mAh/g at a current density of 0.1 A/g after 100 cycles. The

composite electrode also showed a high capacity of more than 900 mAh/g at a high current density of 1 A/g after 200 cycles, which is a significant improvement over the current graphite-based lithium-ion batteries.

8.2 Future work

The dissertation summarizes the advances achieved in fabricating VACNTs in different forms and architectures to enhance field emission and electrochemical properties. Although notable progress has been made in the respective research areas, some topics require further studies for application purposes.

Emission current density of ~1 A/cm^2 is required for applications in vacuum electronics. The aspect ratio of the field emitter is crucial for enhanced field emission properties. Therefore, longer field emitters are ideal for field emission applications. In the case of VACNT pillar emitters with different sizes, the proposed synthesis method using nanosphere lithography further needs to be optimized to accomplish VACNT pillars with long lengths (≥ 10 μm) in perfect array structures and having inter pillar distance two times bigger than their height. For this purpose, the integrity of the CNT inhibition layer (Cr-layer) is essential during VACNTs synthesis for a longer growth time (> 10 min) or at higher growth temperatures (> 600 ºC). To improve the integrity of the CNT inhibition layer, a thin buffer layer of tungsten can be deposited on the substrate before depositing the CNT inhibition layer.

A general lack of periodicity in the VACNT pillar emitters can be improved by depositing a monolayer of polystyrene spheres (e.g., 5μm in diameter) instead of random dispersion of polystyrene spheres on the substrate. The monolayer of polystyrene spheres

can be treated with plasma (NH_3 or O_2) for different durations to optimize the polystyrene sphere size, thereby controlling the VACNT pillar size and inter-pillar distance. The VACNT pillars can also be subjected to plasma treatment, which increases the aspect ratio of pillars by sharpening pillar apexes. More comprehensive studies can be conducted by changing the plasma treatment time to obtain VACNT pillars with different aspect ratio and their effect on field emission properties. The future work may also involve optimizing the synthesis procedure of copper-filled VACNTs to achieve high yield and further investigation of their field emission and electrical properties. The hybrid materials have tremendous potential in future electronic applications as interconnects since the carbon shells preserve the copper nanowire in its pure form.

As-synthesized core-shell structured SnO_2-VACNT anode material displayed promising battery performance. However, tremendous volume variability of crystalline SnO_2 nanoparticles resulted in unstable cyclability during the first few charging and discharging cycles. Future work may involve optimizing the size of SnO_2 nanoparticles to mitigate the volume expansion during the lithiation process since nanoparticles of the sub-nanometer scale can effectively modify the volume expansion mechanism. Also, increasing the mass-fraction of SnO_2 nanoparticles by depositing them both in the interior and exterior of VACNTs to enhance the capacity of SnO_2-VACNT anode materials can be an exciting prospect for future high-performance lithium-ion batteries.

VITA

ARUN THAPA

2021	Doctoral Candidate Florida International University Miami, Florida
2020	FIU DYF Award
2012	M.S., Physics Tribhuvan University Kathmandu, Nepal
2007	B.S., Physics Tribhuvan University Kathmandu, Nepal

PUBLICATIONS AND PRESENTATIONS

Arun Thapa, Xuewen Wang, Wenzhi Li, "*Synthesis and field emission properties of Cu-filled vertically aligned carbon nanotubes"*, Applied Surface Science 537 (2021) 148086

Arun Thapa, Yuba R. Poudel, Rui Guo, Katherine L. Jungjohann, Xuewen Wang, Wenzhi Li, "*Direct synthesis of micropillars of vertically aligned carbon nanotubes on stainless-steel and their excellent field emission properties"*, Carbon 171 (2021) 188-200

Rui Guo, Biplav Dahal, Arun Thapa, Yuba R. Poudel, Yunyan Liu, Wenzhi Li, "*Ambient Processed (110) Preferred $MAPbI_3$ Thin Films for Highly Efficient Perovskite Solar Cells"* – Accepted manuscript: Nanoscale Advances, (2021).

Arun Thapa, Katherine L. Jungjohann, Xuewen Wang, Wenzhi Li, "*Improving field emission properties of vertically aligned carbon nanotube arrays through a structure modification"*, Journal of Materials Science 55(5) (2020) 2101-2117.

Arun Thapa, Jing Guo, Katherine L. Jungjohann, Xuewen Wang, Wenzhi Li, "*Density control of vertically aligned carbon nanotubes and its effect on field emission properties"*, Materials Today Communications 22 (2020) 100761.

Matthew R. Kurilich, Arun Thapa, Aric Moilanen, Joyce L. Miller, Wenzhi Li, Suman Neupane, "*Comparative study of electron field emission from randomly-oriented and vertically-aligned carbon nanotubes synthesized on stainless steel substrates"*, Journal of Vacuum Science & Technology B, Nanotechnology and Microelectronics: Materials, Processing, Measurement, and Phenomena 37(4) (2019) 041202.

Arun Thapa, Suman Neupane, Rui Guo, Katherine K. Jungjohann, Doug Pete, Wenzhi Li, "*Direct growth of vertically aligned carbon nanotubes on stainless steel by plasma enhanced chemical vapor deposition"*, Diamond and Related Materials, 90 (2018) 144-153.

Arun Thapa, Amin Rabiei Baboukani, Yuba Raj Poudel, Katherine L. Jungjohann, Chunlei Wang, Wenzhi Li, "*High Capacity of Lithium-Ion Battery Anode Using Binder-Free Tin (IV) Oxide Coated Vertically Aligned Carbon Nanotubes Grown on Nickel Foam"*, Manuscript in progress.

Arun Thapa and Wenzhi Li, "*Density Control of Vertically Aligned Carbon Nanotubes Grown Directly on Stainless Steel through Nanosphere Lithography and Its Effect on Field Emission Properties"*, MRS Virtual Spring/Fall Meeting & Exhibit 2020, November 27 – December 4.

Matthew R. Kurilich, Arun Thapa, Aric Moilanen, Joyce L. Miller, Wenzhi Li, Suman Neupane, *"Electron emission from randomly oriented and vertically aligned carbon nanotubes synthesized directly on conducting surface"*, APS Meeting 2020, March 2-6, Denver, Colorado.

Arun Thapa and Wenzhi Li, *"Direct Growth of Vertically Aligned Carbon Nanotube Arrays on Stainless Steel and Their Field Emission Properties"*, APS Meeting 2019, March 4-8, Boston, Massachusetts.

Arun Thapa and Wenzhi Li, *"Direct growth of vertically aligned carbon nanotubes on stainless steel by plasma enhanced chemical vapor deposition"*, Nanoflorida annual meeting 2017, September 23-24, Florida international University, Miami, Florida.